The accretion history of dark matter halos

Camila Correa

The accretion history of dark matter halos

Thesis for the Degree of Doctor of Philosophy

Camila Anahi Correa

School of Physics
University of Melbourne

Academic advisors:
J. Stuart B. Wyithe[1] & Alan R. Duffy[1,2]

[1]School of Physics
Faculty of Science
University of Melbourne
Victoria 3010, Australia

[2]Centre for Astrophysics
and Supercomputing
Swinburne University of Technology
Victoria 3122, Australia

Submitted in total fulfillment of the requirements
of the degree of Doctor of Philosophy: 27/01/2016

Abstract

The accretion history of dark matter halos

by

Camila Anahi Correa

Thesis supervisor: Professor J. Stuart B. Wyithe

The goal of this thesis is to (i) explore the physics that drives universal accretion history of dark matter halos; (ii) determine the relation between the halos accretion history and the halos internal structure; and (iii) disentangle the impact of halos accretion history on galaxy evolution. To address these topics, we first use the extended Press-Schechter (EPS) formalism to derive the halo mass accretion history (MAH) from the growth rate of initial density perturbations. We show that the halo MAH can be well described by an exponential function of redshift in the high-redshift regime. However, in the low-redshift regime the mass history growth slows down because the growth of density perturbations is halted in the dark energy dominated era due to the accelerated expansion of the Universe. As a result, in the low-redshift regime the halo MAH can be described by a power-law function of redshift.

We complement this study with the analysis of MAHs of dark matter halos using a suite of cosmological simulations. We explore the relation between the density profile of dark matter halos and their MAHs, and confirm that the formation time, defined as the time when the virial mass of the main progenitor equals the mass enclosed within the scale radius, correlates strongly with concentration. We combine both analysis, analytic and numerical, to show that the halo MAH is the link between halo concentration and the initial density perturbation field.

The connection found between the halo MAH and its density profile reached in these studies was vital to derive a semi-analytic, physically motivated model for dark matter halo concentration as a function of halo mass and redshift. Because the semi-analytic model is based on EPS theory, it can be applied to wide ranges in mass, redshift and

cosmology. The resulting concentration-mass ($c - M$) relations are found to agree with the simulations, and because the model applies only to relaxed halos, they do not exhibit the upturn at high masses or high redshifts found by some recent works. We predict a change of slope in the $z \sim 0$ $c - M$ relation at a mass scale of $10^{11}\,\mathrm{M}_{\odot}$. We find that this is due to the change in the functional form of the halo MAH, which goes from being dominated by an exponential (for high-mass halos) to a power-law (for low-mass halos). During the latter phase, the core radius remains approximately constant, and the concentration grows due to the drop of the background density.

We then connect the evolution of dark matter halos to the evolution of galaxies. We investigate the hot hydrostatic halo formation and its dependence on feedback mechanisms. We find that in the presence of energy sources like stellar feedback, the hot halo mass, $M_{\rm hot}$, increases and the mass scale of hot halo formation is reduced. Active galactic nuclei (AGN) do not affect the hot halo as strongly. We develop a semi-analytic approach that makes use of both $M_{\rm hot}$ and the fraction of shock-heated gas, to calculate a 'critical mass scale', $M_{\rm critical}$, for hot halo formation. We find that this mass scale, where the heating rate produced by accretion shocks equals cooling, is the point in mass above which halos develop a stable hot atmosphere. In the redshift range $z = 0 - 4$, $M_{\rm critical}$ is $10^{11.7}\,\mathrm{M}_{\odot}$, but it then increases for increasing redshift, in very good agreement with our numerical results.

Finally, we investigate the physics that drives the gas accretion rate onto galaxies at the center of dark matter halos. We separately analyze the gas accretion rate onto the interstellar medium (ISM) and onto the galaxy. We find that the accretion rate onto the ISM remains roughly constant in halos larger than $10^{11.7}\,\mathrm{M}_{\odot}$, whereas the accretion rate onto the galaxy increases with increasing halo mass and flattens in the halo mass range $10^{11.7} - 10^{12.7}\,\mathrm{M}_{\odot}$, and at redshifts $z \leq 2$. The flattening is produced by the presence of the hot halo atmosphere that acts as a preventive feedback mechanism. We derive a physically motivated model of gas accretion onto galaxies that accurately reproduces the gas accretion rates from simulations. The model depends on the rate of gas cooling from the hot halo, on the fraction of shock-heated gas, and on the rate of cold gas accretion. We show that the rate of gas cooling from the hot halo is driven by the cooling radius, that it does not continuously decrease with increasing halo mass as generally thought. Instead, it decreases in the halo mass range $10^{11.5} - 10^{13}\,\mathrm{M}_{\odot}$, and then increases with increasing halo mass, meaning that high-mass halos develop a hot halo cooling flow. We find that the upturn in the cooling radius is due to the change in the gas density profile, which is characterized by an evolving radial slope with halo mass.

Declaration

I, Camila Anahi Correa, declare that this PhD thesis entitled 'The accretion history of dark matter halos' is no more than 100,000 words in length including quotes and exclusive of tables, figures, appendices, bibliography, references and footnotes. This thesis contains no material that has been submitted previously, in whole or in part, for the award of any other academic degree or diploma. Except where indicated in the Preface, this thesis is my original work.

Preface

The work presented in this thesis is that of the author, however some of the work was undertaken as part of a collaboration. All data used has been cited accordingly in the text. Specific details are listed here:

- Chapter 1, which provides a brief description of the standard cosmological framework, and introduces the physical processes that drive the formation and evolution of dark matter halos and galaxies, is entirely the work of the author. All references are cited in the text.

- Chapter 2, which derives an analytic model for halo mass accretion histories based on the extended Press-Schechter formalism, is based on the analysis presented in Correa et al. (2015a). The work was supervised by Stuart Wyithe, with input, comments and suggestions from Joop Schaye and Alan Duffy.

- Chapter 3, which analyses the halo mass accretion histories and density profiles from OWLS simulations, is presented in Correa et al. (2015b). The work was supervised by Stuart Wyithe and Alan Duffy, with input, comments and suggestions from Joop Schaye. This work utilizes data taken from a set of cosmological hydrodynamical simulations compiled by Schaye et al. (2010) as part of the OWLS project.

- Chapter 4, which analyses the halo mass accretion histories and concentration-mass relations from OWLS simulations, is based on the analysis presented in Correa et al. (2015c). The work was supervised by Stuart Wyithe and Alan Duffy, with input, comments and suggestions from Joop Schaye. This work utilizes data taken from a set of cosmological hydrodynamical simulations compiled by Schaye et al. (2010) as part of the OWLS project.

- Chapter 5, which analyses the hot halo formation in the EAGLE simulations, is

going to be presented in Correa et al. (2016, in prep.). The work was supervised by Stuart Wyithe and Alan Duffy, with input, comments and suggestions from Joop Schaye. This research utilizes data taken from a set of cosmological hydrodynamical simulations compiled by Schaye et al. (2015) as part of the EAGLE project.

- Chapter 6, which analyses the gas accretion rates onto galaxies in the EAGLE simulations, is going to be presented in Correa et al. (2016, in prep.). The work was supervised by Stuart Wyithe and Alan Duffy, with input, comments and suggestions from Joop Schaye. This work utilizes data taken from a set of cosmological hydrodynamical simulations compiled by Schaye et al. (2015) as part of the EAGLE project.

- Chapter 7, which summarizes the work presented in this thesis and discusses ideas for future work, is entirely the work of the author.

Acknowledgements

"If I can see farther it is only because I stand on the shoulders of giants" Isaac Newton (1642-1727)

I would like to thank my supervisor, Stuart Wyithe, for supervising my work and supporting (bearing?) me along the way with his sense of humor and deep understanding. Thanks Stuart for your encouragement to follow my own ideas. Since the beginning I felt free to pursue the projects I had in mind, but always knew you were there to guide these projects in the right direction, and I am mostly grateful for that. Special thanks are also to Alan Duffy, for the many encouragements and patience you had when I was learning to run cosmo simulations, and the many enlightening discussions on physics and life. Big thanks are to my third mentor, Joop Schaye, for the valuable discussions we had since my first day at Leiden until today. It is certainly true that behind every great success there is a great support, I am grateful to you, Stuart, Alan and Joop, for the work you have put into my projects, this thesis would not have been possible without it.

I would also like to thank the DRAGONS group that accompanied me since the beginning, for the enjoyable discussions we had during simulation lunches, which were also quite fun. In particular I would like to thank Greg Poole, for your encouragement and the great talks we had, that always made meditate and gave more confidence in my work. To Edoardo Tescari, Simon Mutch, Paul Geil and Hank Kim, for nice discussions over coffee about science and life. Special thanks also goes to Akila Jeeson Daniel, for your help, friendship and the fun times we had together.

I am very grateful to Rachel Webster, for the many important discussions we had during my annual review meetings. To Andrew Melatos, for your lessons about classical mechanics, science and Argentinian tango. To Michele Trenti, for the fun talks mixed between hiking, running and science.

A warm thanks goes to all my office mates from 359, Paul Angel, Antonios Katsianis, Sinem Ozbilgen and Nastaran Rezaae, for the great time we spent together. I would also like to thank Jaehong Park, Cat de Burgh-Day, Rob Barone-Nugent and Daniela Carrasco, for your good humor every day at the office, and help. In particular Rob, for the office-made drums I had to daily listen and the great running songs we shared.

I am also very thankful to Elisa Boera, Paola Oliva-Altamirano, Nicolla Pastorello and Linda Chiarello, for being so wonderful friends, for the many awesome hiking trips we

had and the support you gave me in the last year of my PhD.

I am forever thankful to Guido Moyano, for your support and fun times every day after office, when you were always there to mentally distract me from my projects, my plots and my always unfinished calculations. You always looked after me. I will always treasure the time we spent together.

Finally, I would like to thank my sister, Clara Correa, and my mother, Liliana Caballero. Clari you always encourage me to move forward and believe in me, I am very grateful for that. Mom, you always fostered my curiosity and taught me to never stop pursuing my dreams, because of that this thesis is dedicated to you.

Camila Correa

Melbourne, January 2015

Dedicated to my Mother

for her love and

measureless support

Contents

List of Figures

List of Tables

1

Introduction

This first chapter introduces the basics of cosmology and structure formation and highlights the motivation of the research conducted in the thesis.

Galaxies are the 'building blocks' of the visible universe. The concept of galaxies can be traced back to the 1700's (Wright 1750; Kant 1755), but their extra-Galactic status was confirmed by Hubble in 1929 (Hubble 1929). It was initially difficult to understand how baryons alone could have collapsed and formed galaxies until 1937, when observations of the velocity dispersion of the galaxies in clusters indicated that galaxies are embedded in large structures of unseen matter (Zwicky 1937; Babcock 1939; Rubin et al. 1978), that are much more extended than the galaxies themselves. These structures of dark matter are called *halos*, which provide the gravitational potential wells necessary for the condensation of baryons and formation of galaxies. In the following years, further evidence of dark matter came from measurements of optical and radio emissions in spiral galaxies (Rogstad & Shostak 1972; Rubin et al. 1980; Sofue & Rubin 2001) greatly strengthening the study of dark matter and dark matter halos. Further compelling evidence was found in the radial distribution of dark matter in galactic halos (e.g. Navarro et al. 1996), the observed large scale structure of the Universe (Percival et al. 2001; Eisenstein et al. 2005; Tegmark et al. 2006; Percival et al. 2010) and the anisotropies of the Cosmic Microwave Background radiation (CMB, Komatsu et al. 2011; Hinshaw et al. 2013; Sievers et al. 2013; Planck Collaboration et al. 2014).

Our understanding of the distribution, formation and evolution of dark matter halos in the Universe has progressed significantly in the last decade, through both analysis of large cosmological simulations (e.g. Wechsler et al. 2002; McBride et al. 2009; Genel et al. 2010; Fakhouri et al. 2010; Behroozi et al. 2013; van den Bosch et al. 2014) and

analytical studies (e.g. van den Bosch 2002a; Neistein et al. 2006; Correa et al. 2015a). However, a comprehensive understanding of dark matter halo formation and evolution in a cosmological context is still missing. It has been known that the mass accretion history of a halo consists of two distinct phases: an early fast phase and a later slow phase (Wechsler et al. 2002; Zhao et al. 2003; Li et al. 2007; Zhao et al. 2009), but it is still not entirely clear what drives the change of phase, or even how cosmology and the mass power spectrum impact on the overall mass growth of halos.

The accretion history of a dark matter halo directly impacts on the halo internal structure and on the evolution of the galaxies that reside in it. For instance, it has been suggested that the change of phase in the mass accretion history drives the change in the slope of the dark matter halo density profile, $\rho(r)$, varying from $\rho(r) \propto r^{-1}$ at small radii (set during rapid accretion) to $\rho(r) \propto r^{-3}$ at large radii (set during slow accretion, Zhao et al. 2003; Lu et al. 2006; Ludlow et al. 2013). However, other explanations have also been proposed to explain the universality of the halo density profile, such as mergers events (e.g., Syer & White 1996; Dekel et al. 2003), dynamical friction (e.g., Nusser & Sheth 1999), angular momentum (e.g., Williams et al. 2004) and adiabatic invariants (e.g., Avila-Reese et al. 1998; Dalal et al. 2010), but so far no general consensus has been reached.

Another fundamental problem is the efficiency of galaxy formation and its dependence on the host halo accretion history. Although initially the accretion of gas will follow that of dark matter, the presence of additional physical processes modify the manner in which galaxies grow. It has been suggested that the thermal properties of the gas accreted onto halos is responsible for the observed galaxy bimodality (namely star-forming versus quenched, Dekel & Birnboim 2006). But the interaction of gas inflow with star formation (e.g. Oppenheimer et al. 2010; Gabor & Bournaud 2014; Sánchez Almeida et al. 2014) and the process of quenching (e.g. Birnboim et al. 2007; Gabor & Davé 2012; Feldmann & Mayer 2015), is still a topic of open debate.

In view of this, the goal of this thesis is to explore the physical origin for the change of phase in the halo mass accretion history and its dependence on cosmology, to build the link between halo accretion history and density profile, and to disentangle the impact of dark matter halo mass growth on galaxy evolution. These topics constitute the scope of this work.

In this chapter we introduce the physical processes that drive the growth and evolution of dark matter halos and galaxy formation as follows:

- Cosmology. In §1.1 we provide a brief description of the standard cosmological framework, which forms the current basis to develop theories of structure formation.
- Dark matter halos. In §1.2 we explore how the density perturbations seeded by inflation have given rise to collapsed dark matter halos. We introduce the Press-

Schechter formalism in §1.2.1 and cosmological simulations in §1.2.2. We describe dark matter halo internal structure in §1.2.3.

- Galaxy formation. In §1.3 we explore the current theories of galaxy formation, that are developed within the cold dark matter framework and based on the hierarchical growth paradigm.

Finally, we highlight the motivation of the research conducted in the thesis and present a brief outline in §1.4.

1.1 Background cosmology

Cosmology is the study of the Universe, its origin and evolution. If we think about the Universe, we think about galaxies and quasars, stars and supernova explosions, unseen matter, and an infinite variety of fascinating systems that drive its enormous complexity. In spite of this, cosmologists like to think of the Universe as being rather simple, that follows simple laws and is only characterized by two forms of energy: matter (dark and baryonic matter) and dark energy. This is known as the Λ cold dark matter (ΛCDM) cosmological model (Blumenthal et al. 1984).

In 1915 Albert Einstein, as an attempt to analytically solve his equations of general relativity, considered the most simple possible universe. One that is homogeneous and isotropic on sufficiently large scales (beyond those traced by the large-scale structure of the distribution of galaxies). Homogeneity is the property of being identical everywhere in space at a fixed time, while isotropy is the property of looking the same in every direction. The Universe is clearly not exactly homogeneous, but is defined this way in an average sense over large enough scales. The combination of these two simplifying assumptions is known as the *cosmological principle*. Soon after applying this principle, Einstein found that all the solutions of his field equations required the Universe to be either expanding or contracting, in contrast to his belief at that time that the Universe was static. To obtain the static solution, he introduced a cosmological constant into his equations that opposed the gravitational attraction. However, a few years later, Einstein considered his introduction of a cosmological constant as 'the biggest blunder of my life' (quoted in Gamow 1970, see also Carroll et al. 1992), when Hubble demonstrated that the Universe is expanding, by showing that the recession velocities of galaxies are linearly related to their distances (Hubble 1929; Hubble & Humason 1931).

Hubble's discovery soon revolutionized the field of cosmology, because it implied that at the beginning the Universe should have been in an infinite-density state, the so-called *Big Bang*. Such hot and dense Universe is nowadays detected in the form of a cosmic microwave background radiation (CMB, discovered by Penzias & Wilson 1965, see also Komatsu et al. 2009; Dunkley et al. 2009). However, before the CMB radiation was re-

leased, the Universe underwent an extremely rapid expansion known as *inflation* (Guth & Pi 1982)[i]. After inflation, the Universe cooled enough for quarks to be able to condense under strong interactions and form the first primordial nucleons. Eventually, these protons and neutrons fused through the process of primordial nucleosynthesis and produced an ionised plasma of hydrogen and helium nuclei, electrons and photons. During this period, radiation was the dominant form of energy in the Universe. Photons and ordinary particles were tightly coupled together, forming a single fluid of matter and radiation. As the Universe expanded and cooled further, the plasma cooled sufficiently for hydrogen and helium nuclei to capture electrons and combine to form atomic hydrogen and helium, this period is known as *recombination*[ii]. Shortly after the number density of free electrons decreased, the decoupling of matter and radiation occurs. Recombination then led to the decoupling of photons and baryons, and the free-streaming photons, which were last scattered 380,000 years after the Big Bang, are observed today as the CMB.

Since Hubble's discovery we know that galaxies are receding from us with a velocity $\mathrm{d}\mathbf{r}/\mathrm{d}t$ proportional to their distance $\mathbf{r}$

$$\frac{\mathrm{d}\mathbf{r}}{\mathrm{d}t} = H_0\mathbf{r}. \tag{1.1}$$

The factor of proportionality, H_0, is called the *Hubble constant*. Its inverse, H_0^{-1}, gives the characteristic time for significant changes in $\mathbf{r}$, therefore H_0 is generally called the *expansion rate* of the local universe. The usual convention of writing the Hubble constant at the present day is $H_0 = 100h\ \mathrm{km\ s^{-1}\ Mpc^{-1}}$, where h is a dimensionless parameter widely used in the literature, that has a currently accepted value of $h = 0.67$ (Planck Collaboration 2015)[iii]. To measure H_0 we need galactic distances and the apparent velocity of recession of relatively nearby galaxies. The latter are easily measured from the *redshift*, z, of the galactic spectral lines $z \equiv \frac{\lambda_0}{\lambda_1} - 1$, where λ_1 is the photon wavelength that would be measured by an observer in the rest frame of the emitting galaxy and λ_0 is the wavelength measured by us.

With H_0 and Newton's constant, it is possible to form a quantity with the dimensions of mass (or energy) per unit volume called the *critical density*

[i] Guth's phrase 'an extraordinarily rapid expansion' is correct as stated, but it obscures the fact that the rate of expansion would have been even greater were it not for the vacuum energy. Inflation should be more commonly described as a period of extraordinarily *slow* expansion. For a detailed analysis see the additional cosmology topics from John Peacock (`http://www.roe.ac.uk/~jap/book/infmatch.pdf`) that will be included in the second edition of the textbook Cosmological Physics.

[ii] Note that 'recombination' is an unfortunate term, as this is the first time in the history of the Universe that the electrons combine with protons to form atoms.

[iii] Planck is the third-generation space mission, following COBE (Smoot et al. 1992) and WMAP (Bennett et al. 2003), dedicated to measurements of the CMB anisotropies. The 68% confidence limits for the cosmological parameters introduced in this chapter correspond to the second data release from Planck, calculated for the base ΛCDM model from Planck CMB power spectra, in combination with lensing reconstruction and external data (baryonic acoustic oscillation measurements and the joint light-curve analysis sample, constructed from supernovae data).

$$\rho_{\rm crit,0} = \frac{3H_0^2}{8\pi G} = 1.878 \times 10^{-29} h^2 \text{ gr cm}^{-3}, \tag{1.2}$$

that represents the energy density of the Universe at the present time needed for flatness. In eq. (1.2) and throughout this thesis, the subscript '0' denotes value as of today. It is generally convenient to express the main components, i (dark energy, baryons and dark matter and relativistic particles), of the universe is terms of the critical density as

$$\Omega_i = \frac{\rho_i}{\rho_{\rm crit}}, \tag{1.3}$$

with Ω_i defined as a density parameter. The latest works of observational cosmology (e.g. Riess et al. 1998; Spergel et al. 2007; Dunkley et al. 2009; Komatsu et al. 2009; Percival et al. 2010; Larson et al. 2011; Hinshaw et al. 2013; Planck Collaboration et al. 2014) have constrained the matter content, geometry and late-time evolution of the Universe. They have found that baryons account for the 15.73% of the total matter content in the universe, that has a density parameter of $\Omega_{\rm m,0} = 0.308 \pm 0.012$ (Planck Collaboration 2015). Here, the general inference is that the majority of the matter in the Universe (84.27%) must be in some non-baryonic form, that is only detected through its gravitational force (hence the name 'dark'). One of the most challenging tasks for modern cosmology is to determine the nature and origin of the dark matter. Candidates include the so called weakly interacting massive particles (WIMPs). Dozens of dedicated laboratory experiments are conducted to detect WIMPs (e.g. Angloher et al. 2012; Bernabei et al. 2013; Aalseth et al. 2013; CDMS Collaboration et al. 2013), along with studies of WIMPs in the galactic halo by testing their interaction with nucleons (e.g. Saab 2013), cosmic ray experiments (e.g. Aramaki et al. 2015), and γ-ray/X-ray observations that search for WIMPs annihilation signal (e.g. Lavalle & Salati 2012; Bergstrom 2012).

The total density of non-relativistic matter can then be written as the sum of densities of dark matter (DM), baryons (b), and non-relativistic neutrinos (ν), therefore $\Omega_{\rm m} = \Omega_{\rm DM} + \Omega_{\rm b} + \Omega_\nu$, where $\Omega_{\rm b,0}h^2 = 0.0223 \pm 0.0001$ and $\Omega_{\rm DM,0}h^2 = 0.1188 \pm 0.0010$ (Planck Collaboration 2015). In the case of the relativistic particles, its total density can be written as $\rho_{\rm r} = \rho_\gamma + \rho_\nu + \rho_{\rm er}$, where ρ_γ is the photon energy density ($\rho_\gamma = 4\sigma_{\rm SB}T_\gamma^4/c^3$ with $\sigma_{\rm SB}$ the Stefan-Boltzmann constant, c the speed of light) that appears to be dominated by the CMB which is, to high accuracy, a blackbody at temperature $T_\gamma = 2.73$ K. ρ_ν is the relativistic neutrino energy density and $\rho_{\rm er}$ is the energy density of 'extra radiation species'. The nature of the extra radiation species is still unknown, but it is customary to parameterize the number of extra radiation species as if they were neutrinos as $\rho_\nu + \rho_{\rm er} = \frac{7\pi^2}{120} N_{\rm eff} T_\nu^4$, where in the standard model of particle physics $N_{\rm eff} = 3.046$ (Mangano et al. 2002, also constrained by Dunkley et al. 2011 and Keisler et al. 2011), and in the standard thermal history of the universe, $T_\nu = (4/11)^{1/3} T_\gamma$ (e.g. Weinberg 1972). As a result, the

total energy density in the relativistic component is $\Omega_{\mathrm{r},0} = \frac{\rho_{\mathrm{r},0}}{\rho_{\mathrm{crit},0}} = \frac{\rho_{\gamma,0}}{\rho_{\mathrm{crit},0}}(1+0.2271N_{\mathrm{eff}}) \approx 4.2 \times 10^{-5}h^{-2}$.

Besides dark matter, another fundamental question of modern cosmology concerns the origin and nature of the second form of energy in the Universe called dark energy, also known as apparent 'vaccum energy' or 'cosmological constant' Λ. The dark energy has a density parameter of $\Omega_\Lambda = 0.6911 \pm 0.0062$ (Planck Collaboration 2015). Dark energy is energy that is not associated with particles and is therefore not diluted by the expansion of the universe. An important evidence for this dominant component is provided by the observed redshift-distance relation of high-redshift Type Ia supernovae (Kowalski & et al. 2008), that implies that the expansion of the Universe is speeding up at the present time.

1.1.1 Evolution of the Universe

To understand the evolution of the Universe since the Big Bang, it is useful to parameterize its expansion with a function called *scale factor*, $a(t)$, that is proportional to intergalactic distances and is defined to be unity at present ($a(t_0) = 1$, with $t_0 = H_0^{-1}$ the age of the Universe). If we neglect peculiar velocities, the distance between us and the galaxy i, $\mathbf{r}_i$, can be written as

$$\mathbf{r}_i = a(t)\mathbf{x}_i, \tag{1.4}$$

where the constant of proportionality, $\mathbf{x}_i$, is time independent and called the *comoving* coordinate of the galaxy. We next replace eq. (1.4) into eq. (1.1) and obtain

$$H(t) = \frac{\dot{a}(t)}{a(t)}. \tag{1.5}$$

Here, and throughout this thesis, the over dot denotes the derivate with respect to time. By definition, the Hubble parameter of the present time (eq. 1.5) is the Hubble constant.

The evolution of the Universe can be studied by solving the Einstein field equations, from which we learn that the geometry of space-time is determined by the matter/energy content of the Universe. A detailed solution of the Einstein field equations, as well of general relativity (GR), is beyond the scope of this thesis. For a detailed description of the subject the reader is refereed to the books of Schutz (2009) and Hobson et al. (2006), where he/she will find that for an homogeneous and isotropic universe. The solution of the field equations is

$$\left[\frac{\dot{a}(t)}{a(t)}\right]^2 = \frac{8\pi G}{3}\rho(t) + \frac{\Lambda c^2}{3} - \frac{Kc^2}{a^2(t)}, \tag{1.6}$$

where ρ is the matter density of the Universe, Λ is the cosmological constant, and K is the curvature of the Universe, which can either be positive (a 'closed' universe), zero ('flat', Euclidean space) or negative (an 'open' universe).

To understand eq. (1.6) it is important to briefly investigate the evolution of the energy content of the Universe. Let us then consider a uniform, perfect gas contained in a comoving volume $V \propto a^3(t)$ which expands with the Universe. Since the Universe is homogeneous and isotropic, there should not be any net heat flow across the boundaries of V. This implies that we can consider V as an adiabatic system, and since V can be chosen arbitrarily small, no GR is required to describe its thermodynamic properties. Then for our adiabatically expanding volume V the first law of thermodynamics, $\mathrm{d}U + P\mathrm{d}V = 0$, can be written as

$$V\mathrm{d}\rho + (P/c^2 + \rho)\mathrm{d}V = 0, \tag{1.7}$$

where P is pressure and, in order to consider both relativistic and non-relativistic fluids, we wrote the internal energy, U, in terms of the energy density ρc^2. Using that $V \propto a^3(t)$, and differentiating with respect to a we obtain

$$\frac{\mathrm{d}\rho}{\mathrm{d}a} = -\frac{3(P/c^2 + \rho)}{a}, \tag{1.8}$$

$$\rho \propto a^{-3(1+\omega)}. \tag{1.9}$$

To solve eq. (1.8) we introduced an arbitrary equation of state $P = \omega\rho c^2$. A non-relativistic gas is well approximated by a fluid of zero pressure ($\omega = 0$), often referred to as a dust fluid. Therefore for dust fluids eq. (1.9) gives $\rho \propto a^{-3}$. At early times, when the Universe is dominated by radiation, we can approximate the fluid as an ultra-relativistic radiation fluid for which $\omega = 1/3$, that implies $\rho \propto a^{-4}$. If the Universe is vacuum energy dominated, for which $\omega = -1$, we obtain $\rho \propto constant = \frac{\Lambda c^2}{8\pi G}$.

We next replace $\rho(t)$ in eq. (1.6) by $\rho = \rho_\mathrm{r} + \rho_\mathrm{m} = \rho_{\mathrm{r},0}a^{-4} + \rho_{\mathrm{m},0}a^{-3}$, to distinguish a non-relativistic matter component from a radiation component. We also replace $\frac{\Lambda c^2}{8\pi G}$ by $\rho_{\Lambda,0}$, which corresponds to the vacuum energy component, and obtain

$$\left[\frac{\dot{a}(t)}{a(t)}\right]^2 = H(t)^2 = \frac{8\pi G}{3}[\rho_{\mathrm{r},0}a^{-4}(t) + \rho_{\mathrm{m},0}a^{-3}(t) + \rho_{\Lambda,0}] - \frac{Kc^2}{a^2(t)}. \tag{1.10}$$

Eq. (1.10) is known as the the Friedmann equation (Friedmann 1922), and the cosmology that it describes is called Friedmann-Robertson-Walker (FRW) cosmology. If we solve eq. (1.10) for $K = 0$ (flat universe) and $z = 0$ (present time) we obtain eq. (1.2), the energy density at present time needed for flatness.

It is possible to gain intuition about the evolution of the universe from the Frierdmann

equation, by analyzing the right-hand side of eq. (1.10). If $\Lambda \geq 0$ and $K = 0$ or $K = -1$, the right-hand side is always larger than zero and $a(t)$ always increases with t (the Universe expands). If $K = +1$ and $\Lambda \geq 0$, the right-hand side becomes zero as the scale factor increases until the curvature term, K/a^2, is as large as the sum of the matter and radiation terms. Thereafter $a(t)$ decreases with t, and the Universe contracts until $a = 0$. Finally, if $\Lambda < 0$ (although not physically possible), the expansion will eventually halt and be followed by recollapse.

The Friedmann equation can be written in terms of the density parameter, Ω_i. Therefore by substituting eq. (1.3) into eq. (1.10) we obtain

$$H(t)^2 = \frac{8\pi G}{3}\rho_{\mathrm{crit},0}[\Omega_{\mathrm{r},0}a^{-4}(t) + \Omega_{\mathrm{m},0}a^{-3}(t) + \Omega_{\Lambda,0}] - \frac{Kc^2}{a^2(t)}, \tag{1.11}$$

$$H(t)^2 = H_0^2[\Omega_{\mathrm{r}}(t) + \Omega_{\mathrm{m}}(t) + \Omega_{\Lambda}(t)] - \frac{Kc^2}{a^2(t)}, \tag{1.12}$$

$$H(t)^2 = H_0^2[\Omega_{\mathrm{r}}(t) + \Omega_{\mathrm{m}}(t) + \Omega_{\mathrm{K}}(t) + \Omega_{\Lambda}(t)], \tag{1.13}$$

where in eq. (1.12) we replaced $\rho_{\mathrm{crit},0}$ by the expression (1.2) and defined $\Omega_i(t)$ as $\Omega_i = \Omega_{i,0}a^{-3(1+\omega_i)}$. In eq. (1.13) we defined $\Omega_{\mathrm{K}}(t) = -(Kc^2/H_0^2)a^2(t)$.[iv] Note that if we evaluate Friedmann equation at $t = t_0$, we find $\Omega_{\mathrm{K},0} = 1 - \Omega_{\mathrm{T},0} = 1 - (\Omega_{\mathrm{r},0} + \Omega_{\mathrm{m},0} + \Omega_{\Lambda,0})$, where $\Omega_{\mathrm{T},0}$ is the total density parameter at the present time. Also note that $\Omega_{\Lambda}(t) = \Omega_{\Lambda,0}$, since it does not have a time dependence. We then find that the curvature of space-time, K, depends on the matter density of the Universe. Therefore if $\Omega_{\mathrm{T},0} < 1$ the Universe is open, if $\Omega_{\mathrm{T},0} = 1$ the Universe is flat and if $\Omega_{\mathrm{T},0} > 1$ the Universe is closed. We can now understand the terminology 'open' and 'closed'. Open (and flat) universes expand forever, while closed universes recollapse in the future.

Throughout this thesis we will analyze how the evolution of the Universe impacts on structure formation. Rather than using time as the temporal variable, we will use redshift, z, a much more common variable in astronomy. In the previous section, we defined redshift as a function of galactic spectral lines. We now need to keep in mind that because the Universe is expanding, light waves propagating are stretched. Thus, photons with a wavelength λ_1 emitted by a galaxy at an earlier time will be observed by us with a wavelength $\lambda_{\mathrm{obs}} = \lambda_1/a(t)$. Since $a(t) < a(t_0) = 1$ in an expanding universe, $\lambda_{\mathrm{obs}} > \lambda$ and so the wavelength of the photons is redshifted. The redshift between time of the light emission and now (t_0) is $z \equiv \frac{\lambda_{\mathrm{obs}}}{\lambda_1} - 1 = \frac{1}{a(t)} - 1$. Therefore the relation between $a(t)$ and z is

$$a(t) = \frac{1}{1+z}. \tag{1.14}$$

[iv] Since Ω_{K} is a unitless parameter K has to be taken to have units of length^{-2}.

Using the above relation, the Friedmann equation as a function of redshift is

$$H(z)^2 = H_0^2[\Omega_{\mathrm{r},0}(1+z)^4 + \Omega_{\mathrm{m},0}(1+z)^3 + \Omega_{\mathrm{K},0}(1+z)^2 + \Omega_{\Lambda,0}]. \tag{1.15}$$

We now analyze eq. (1.15) in more detail. We can see that the Universe passes through a succession of epochs. At very high redshift the $\Omega_{\mathrm{r}}(t)$ term dominates, therefore eq. (1.15) is $H(z)^2 \sim H_0^2\Omega_{\mathrm{r},0}(1+z)^4$, from what we find that $a(t) \propto t^{1/2}$. This is refereed as the *radiation-dominated* epoch, that ends when $z \sim z_{\mathrm{eq}}$, with $z_{\mathrm{eq}} = 3371 \pm 23$ (Planck Collaboration 2015) the point in time when the matter and radiation content of the universe is equal. As z decreases the radiation epoch is followed by a *matter-dominated* epoch, with $H(z)^2 \sim H_0^2\Omega_{\mathrm{m},0}(1+z)^3$ and $a(t) \propto t^{2/3}$. If there is no dark energy, what follows would only depend on $\Omega_{\mathrm{K}}(t)$. For $\Omega_{\mathrm{T},0} > 1$ (and $\Omega_{\Lambda,0} \sim 0$) the expansion reaches a maximum and is followed by a contraction. In the case $\Omega_{\mathrm{T},0} < 1$, the matter epoch is followed by a *curvature* epoch with $a(t) \propto t$. Finally, for $\Omega_{\Lambda,0} > 1$, the matter epoch is followed by a *dark energy-dominated* epoch which is characterized by an exponential expansion, with $a(t) \propto \exp(H_0\Omega_{\Lambda,0}^{1/2}t)$.

1.2 Structure formation

The background cosmology discussed in the previous section describes the dynamical evolution of the Universe, but does not explain the formation of dark matter halos and galaxies. The central mechanism responsible for structure formation in the Universe is gravitational instability, caused by an inhomogeneous distribution of matter. In the currently accepted cosmological paradigm, structures are initially in the form of density perturbations, that were seeded by the amplification of quantum fluctuations during inflation. To understand the initial distribution of the density perturbations, also known as *primordial density field*, we have to analyze the CMB, which describes the statistical distribution of matter in the early Universe. Fig. 1.1 shows the anisotropies of the CMB as observed by Planck. The distinctive pattern of the angular temperature fluctuations gives a direct snapshot of the distribution of radiation and energy at the moment of decoupling. Because the CMB photons were tightly coupled with the mass density field before decoupling, the temperature fluctuations are expected to be closely related to the primordial density field at the time of decoupling. In addition, the tiny variation across the sky, less than 0.01% on average, indicates that at the time of hydrogen recombination the Universe was extremely uniform.

From the CMB we learn about the seeds of the small density fluctuations following inflation. To describe the gravitational growth of perturbations in the matter dominated era, we first consider small perturbations in the density field, $\rho(\mathbf{x}, t)$, with amplitude δ and $|\delta| \ll 1$. Here δ is defined as a relative density perturbation or *overdensity*,

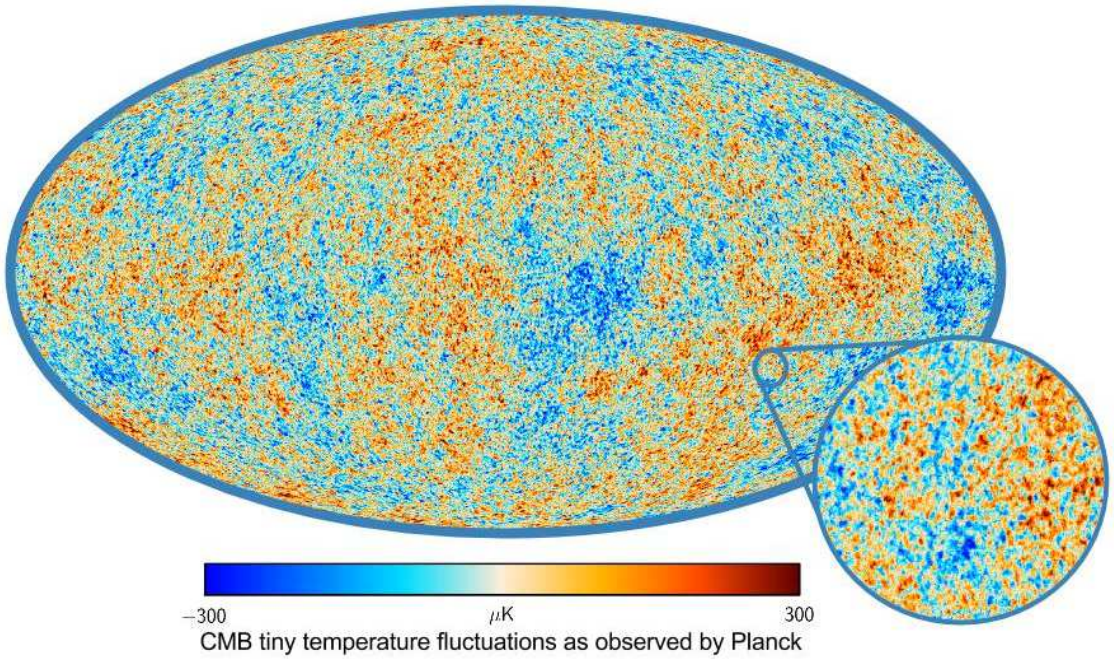

Figure 1.1: Snapshot of the oldest light in our Universe, imprinted on the sky when the Universe was just 380,000 years old. The figure shows tiny temperature fluctuations that correspond to regions of slightly different densities, representing the seeds of all future structure: the stars and galaxies of today. The expansion of the Universe has stretched out the CMB radiation by around 1000 times, which makes it look much cooler. So instead of seeing the afterglow at 3000 degrees, we see it at 2.73 K. Copyright: ESA, Planck Collaboration.

$$\delta(\mathbf{x},t) = \frac{\rho(\mathbf{x},t)}{\bar{\rho}} - 1, \tag{1.16}$$

with $\bar{\rho}$ is the mean density at position $\mathbf{x}$ and time t. It is important to note that $\mathbf{x}$ is a comoving coordinate that expands with the background Universe, and corresponds to a proper coordinate $\mathbf{r}$ as $\mathbf{x} \equiv \mathbf{r}(t)/a(t)$, with $a(t)$ the scale factor[v].

We next describe the evolution of the Universe in terms of an ideal pressure-less fluid at fixed $\mathbf{x}$ with overdensity δ. The time evolution of the fluid is given by the continuity equation (which describes mass conservation), the Euler equations (the equations of motion) and the Poisson equation (describing the gravitational field) as

$$\frac{\partial \delta}{\partial t} + \frac{1}{a}\nabla \cdot [(1+\delta)\mathbf{v}] = 0, \tag{1.17}$$

$$\frac{\partial \mathbf{v}}{\partial t} + \frac{\dot{a}}{a}\mathbf{v} + \frac{1}{a}(\mathbf{v}\cdot\nabla)\mathbf{v} = -a^{-1}\nabla\Phi, \tag{1.18}$$

$$\nabla^2\Phi = 4\pi G\bar{\rho}a^2\delta, \tag{1.19}$$

[v]The geometric meanings of $a(t)$ can be better understood if we consider and expanding or contracting sphere whose radius is $R(t) = a(t)R_0$ at time t. The scale factor relates the radius of the sphere at time t to its comoving radius, R_0, whose value does not change as the sphere expands or contracts (thus the comoving radius is just the true radius measured in units of the scale factor).

where $\mathbf{v} \equiv a\dot{\mathbf{x}}$ and $\nabla = \nabla_{\mathbf{x}}$. To work with these equations, we first differentiate eq. (1.17) once with respect to t and eq. (1.18) once with respect to $\mathbf{x}$. We combine them and neglect the nonlinear terms by assuming that both δ and $\mathbf{v}$ are small to obtain

$$\frac{\partial^2 \delta}{\partial t^2} + 2\frac{\dot{a}}{a}\frac{\partial \delta}{\partial t} = 4\pi G\bar{\rho}\delta. \tag{1.20}$$

In the above equation, the second term on the left-hand side is the Hubble drag term, which tends to suppress perturbation growth due to the expansion of the Universe, and the term on the right-hand side is the gravitational term, which causes perturbations to grow via gravitational instability. Since this is a second-order differential equation, we can find two possible solutions (or modes), a growing and a decaying mode. The growing mode, δ_+, is directly proportional to the growth factor that for a flat universe with cosmological constant results

$$D(z) = D_0 H(z) \int_z^\infty \frac{1+z'}{H(z')^3} \mathrm{d}z', \tag{1.21}$$

with $D_0 = D(z = 0) = 1$. As long as the inhomogenities are small (in the so-called *linear regime*) the density perturbation maintains its shape in comoving coordinates and grows in amplitude in proportion to $D(z)$. In the radiation-dominated regime ($z > 10^3$), $\delta(t) \propto a^2(t)$. In the matter-dominated regime ($1 < z < 10^3$), the growth factor is simply proportional to the scale factor $a(t)$. At low redshift ($z < 1$), in the dark energy-dominated regime, the density fluctuations freeze in amplitude ($D(z) \to D_0$) as their growth is suppressed by the accelerated expansion of the Universe. If we consider the difference in amplitude of the baryonic perturbations in the CMB, $\delta \sim 10^{-5}$ at the epoch of decoupling ($a_{\mathrm{dec}} \sim 10^{-3}$), and those today $\delta \sim 1$. We find that there is not enough time for the fluctuations to grow and form the structures we see today. Hence dark matter is necessary in galaxy formation, since it provides the gravitational potential for the baryons to collapse, that is not coupled to the photons.

Inflation generates a spectrum of perturbations in different $\mathbf{k}$-modes, where each defines the typical value of δ on the spatial scale $\lambda = 2\pi/k$. Mathematically, we write $\delta_{\mathbf{k}} = \int \mathrm{d}^3x \delta(\mathbf{x}) e^{-i\mathbf{k}\cdot\mathbf{x}}$, where $\delta(\mathbf{x})$ is the real-space density field. The statistical properties of the fluctuations are determined by the variance of the different $\mathbf{k}$-modes given by the linear power spectrum, $P(k) = (2\pi)^{-3}\langle|\delta_{\mathbf{k}}|^2\rangle$, where the angular brackets denote an average over the entire statistical ensemble of modes. The power spectrum is very important because it describes how much power exists at each mode k with respect to the background density. The larger the power for a given k, the more fluctuations in regions of corresponding spatial scale λ.

In the standard cosmological model, inflation produces a primordial power-law spectrum $P(k) \propto k^{ns}$, where n_s, known as the spectral index, is $n_s = 0.9667 \pm 0.0040$ (Planck

Collaboration 2015). However, the little growth of the perturbations when the Universe is dominated by radiation modifies the final power spectrum. This can be understood as follows. Fluctuations in regions of a given scale can collapse under the influence of gravity, but only if they are in *casual* contact with each other. The comoving casual horizon of the Universe can be defined as $X_{\rm H} = \int_0^t a^{-1}(t)\mathrm{d}t$, and results $X_{\rm H} \propto a(t)$ for the radiation-dominated epoch and $X_{\rm H} \propto a^{1/2}(t)$ for the matter dominated epoch. For the baryonic fluctuations entering the horizon during the radiation-dominated era, the photon pressure prevents the fluctuations to collapse further. Only scales greater than $X_{\rm H}$ can collapse. In the case of dark matter fluctuations, if the expansion rate of the Universe is faster than the collapse rate of dark matter, the fluctuations will, to first order, not be able to grow until $z_{\rm eq}$, the epoch of matter-radiation equality.

The different growth rates of perturbations on scales larger and smaller than the horizon during the radiation-dominated era modify the final power spectrum, which is characterized by a turnover at a scale that corresponds to the matter-radiation equality. Unfortunately, because we do not yet have a complete theory for the origin of the cosmological perturbations, the amplitude of $P(k)$ is not predicted a priori but rather has to be fixed by observations. Historically, the normalizing prescription of the theoretical power spectrum involves the variance of the galaxy distribution, sampled with randomly placed spheres of radii R. The predicted variance, $\langle \delta_M^2 \rangle = \sigma^2(M)$, of the density perturbation field is related to the power spectrum by

$$\sigma^2(M) \equiv \sigma^2(R) = \int_0^\infty \frac{\mathrm{d}k}{2\pi^2} k^2 P(k) \hat{W}_R^2, \tag{1.22}$$

where

$$\hat{W}_R = \frac{3}{(kR)^2}[\sin(kR) - kR\cos(kR)] \tag{1.23}$$

is the Fourier transform of the spherical top-hat window function. The value of $\sigma(R)$ can be derived from the distribution of galaxies overdensity about unity for regions of comoving size $R = 8h^{-1}\,\mathrm{Mpc}$, or from other measures including the density of clusters or amplitude of the CMB fluctuations. The most recent value of $\sigma_8 = 0.8159 \pm 0.0086$ (Planck Collaboration 2015). We then normalize the power spectrum by requiring that $\sigma(R = 8h^{-1}\,\mathrm{Mpc}) = \sigma_8$.

1.2.1 Press-Schechter formalism

The collapse of a dark matter halo occurs when fluctuations become nonlinear and the overdensity reach a critical value of the order of unity. The halo then grows in mass, either by accreting material from their neighborhood or by merging with other halos.

When the halo reaches dynamical equilibrium, generally perturbed due to the presence of substructures within the large overdense region and tidal effects of neighbouring perturbations (Lynden-Bell 1967), the halo is said to have *virialised*. At this stage the system satisfies the viral theorem, in which the internal kinetic energy is half the magnitude of the gravitational potential. According to the spherical collapse model (e.g. Gunn 1977; Bertschinger 1985; White 1996; Shen et al. 2006), the virialisation of an object occurs at a density contrast of $\delta = 18\pi^2$ in an universe with $\Omega_{\rm m} = 1$ and $\Omega_\Lambda = 0$ (Bryan & Norman 1998). Different values for the density contrasts, that give raise to different mass definitions, are discussed in Chapter 3.

It is possible to formulate the growth of virialized dark matter halos and the statistical distribution of matter by combining the notions of a Gaussian random field of density perturbations, linear gravitational growth and spherical collapse. In the primordial density field, the small overdensities are commonly refereed to as *peaks*. Using the peak formalism (Bardeen et al. 1986), we can connect these peaks to the material that later collapses to form dark matter halos. The first step is to smooth the primordial density field with a filter of a given scale, and then to select all the peaks that are above some threshold value. Fig. 1.2 shows an illustration of the method. The arrows connect dark matter halos to the overdensity field, $\delta(\mathbf{x}, t)$, that is formed by overdense regions or peaks (highlighted in red) and underdense regions or valleys. As we have seen, the peaks linearly grow over time until they reach a critical overdensity, shown in dashed line in the figure. The critical overdensity of turnaround is $\delta^0_{\rm crit} = 1.686\Omega_{\rm m}(z)^{0.0055} \simeq 1.686$. Once the peaks in $\delta(\mathbf{x}, t)$ exceed $\delta^0_{\rm crit}$, they turn around from the expansion of the Universe and collapse to form dark matter halos. Therefore, regions that have collapsed to form a dark matter halo at redshift z are associated with those regions for which

$$\delta_0 > \delta_{\rm c}(z) \equiv \frac{\delta^0_{\rm crit}}{D(z)} = \frac{1.686\Omega_{\rm m}(z)^{0.0055}}{D(z)}. \tag{1.24}$$

To relate an object of mass M with an overdensity region with characteristic radius R, so that $M = (4\pi/3)\bar{\rho}R^3$, we can use the Press-Schechter (PS) formalism (Press & Schechter 1974), which allows us to calculate dark matter halo mass functions (mass distribution), merger rates and clustering properties. In the PS formalism, we first define a smooth density field

$$\delta_{\rm S}(\mathbf{x}, R) \equiv \int \delta_0(\mathbf{x}')W(\mathbf{x} + \mathbf{x}', R){\rm d}^3x', \tag{1.25}$$

where $W(\mathbf{x}+\mathbf{x}', R)$ is a window function of radius R and $\delta_0(\mathbf{x})$ is a gaussian random field. Then, we take the ansatz that the probability of $\delta_{\rm S} > \delta_{\rm c}(z)$, $\mathscr{P}[> \delta_{\rm c}(z)]$, is the same as the fraction of mass elements that at redshift z are contained in halos with mass greater than M, $F(> M)$. This results in a number density of collapsed objects with masses in

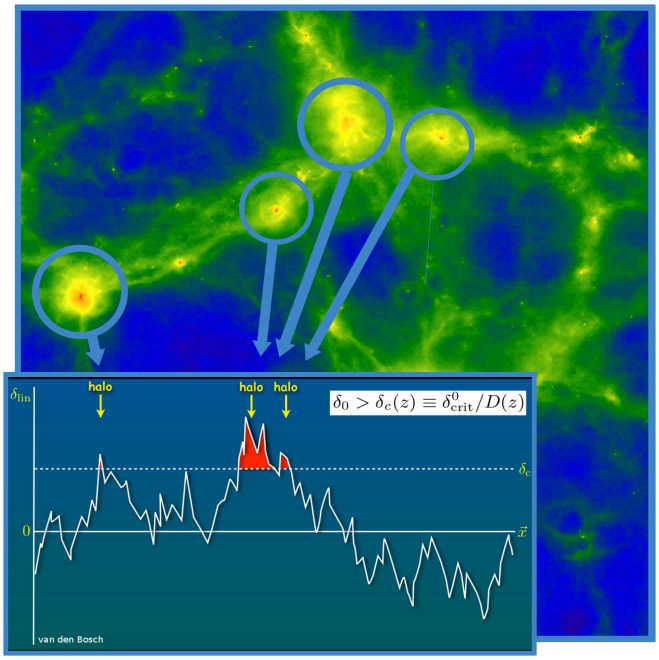

Figure 1.2: Illustrative representation of the peak formalism, where the peaks in the overdensity field grow over time until they reach a critical overdensity (dashed line), after that they turn around from the expansion of the Universe and collapse to form dark matter halos. The background image corresponds to an snapshot of the EAGLE simulations (`http://eagle.strw.leidenuniv.nl`) at $z = 0$.

the range $M, M + \mathrm{d}M$ given by

$$n(M,t)\mathrm{d}M = \sqrt{\frac{2}{\pi}}\frac{\bar{\rho}}{M^2}\frac{\delta_\mathrm{c}}{\sigma}\exp\left(-\frac{\delta_\mathrm{c}^2}{2\sigma^2}\right)\left|\frac{\mathrm{dln}\sigma}{\mathrm{dln}M}\right|\mathrm{d}M. \tag{1.26}$$

This is equation is known as the PS mass function.

Bond et al. (1991) derived an extension of the PS formalism, known as extended Press-Schechter formalism (EPS), that is based on the excursion set formalism and provides an approximate description of the statistics of merger trees using a stochastic process. The EPS formalism has been widely used in algorithms for the construction of random realizations of merger trees (e.g. Kauffmann & Haehnelt 2000; Benson et al. 2005; Cole et al. 2008; Neistein & Dekel 2008).

In the 1990s Bond, among others (Bower 1991; Kauffmann & Haehnelt 2000; Lacey & Cole 1993; Sheth & Lemson 1999; Somerville & Kolatt 1999; Cole et al. 2000, 2008; Zhang et al. 2008; Neistein & Dekel 2008), considered a spatial region of mass M_2 and radius R_2. If $\delta_\mathrm{S}(R_2) > \delta_\mathrm{c}(t_2)$, M_2 already forms a collapsed object at time t_2. Bond calculated the fraction of M_2 that was already in a collapse object of mass M_1 at an earlier time $t_1 < t_2$. This quantity provides the mass history of the halo, and thus its merger history. The most convenient way to construct the mass history of a halo is to start at the present time and follow the growth in mass backwards in time. Like following the growth of a tree, we start from the trunk and work upwards following many small

branches, even pairs of branches that merge into bigger ones as time goes on.

Throughout this thesis we define $S = \sigma^2(M)$ as a mass variable and $\omega = \delta_{\rm c}(z)$ as a time variable. We begin by following an excursion-set approach. If we relate a growth in mass M to a change in $\delta_{\rm S}$, we find that $\Delta\delta_{\rm S}$ does not depend on the value of the smooth density field $\delta_{\rm S}(\mathbf{x}, R)$ at the location $\mathbf{x}$. Instead, it only depends on $k_{\rm c} = 1/R$, the size of the region R in the $k-$space. Therefore, when $k_{\rm c}$ is increased, $\delta_{\rm S}$ executes a random change, also known as *Markovian* random walk. Then, according to the PS ansatz, the probability for a random walk, or in other words, the probability for $\delta_{\rm S}$ being greater than $\delta_{\rm c}$, is equal to the fraction of mass elements in halos greater than M as

$$f(S,\omega)\mathrm{d}S = \frac{1}{\sqrt{2\pi}}\frac{\omega}{S^{3/2}}\exp\left[-\frac{\omega^2}{2S}\right]\mathrm{d}S. \tag{1.27}$$

By knowing this, the halo mass history is constructed as follows. We begin by assuming that a halo of mass M_j (corresponding to a mass variance S_j) at time ω_j takes a small time-step $\Delta\omega$ back in time (note that $\Delta\omega < 0$). At the time $\omega_{j+1} = \omega_j + \Delta\omega$, we calculate the average mass of the halo in the past (also known as the main *progenitor*, M_{j+1} (S_{j+1})), by following an excursion set approach and computing the probability for a random walk originating at (S_j, ω_j). Hence the probability we want is given by eq. (1.27) upon replacing S by $S_{j+1} - S_j$ and ω by $\omega_{j+1} - \omega_j$. Converting from mass weighting to number weighting, we obtain the average number of progenitors at z_{j+1} in the mass interval $(M_{j+1}, M_{j+1} + dM)$ which by time z_j have merged to form a halo of mass M_j,

$$P(M_{j+1}, z_{j+1}|M_j, z_j)\mathrm{d}M_{j+1} = \frac{M_j}{M_{j+1}} f(S_{j+1}, \omega_{j+1}|S_j, \omega_j)\left|\frac{\mathrm{d}S_{j+1}}{\mathrm{d}M_{j+1}}\right|\mathrm{d}M_{j+1}. \tag{1.28}$$

As a first approximation, we assume that $P(M_{j+1}, z_{j+1}|M_j, z_j) = 0$ for $M_{j+1} < M_j/q$, so that the main progenitor always has a mass $M_{j+1} \geq M_j/q$ for a given q value. Therefore, the average mass of the main progenitor can be written as

$$M_{j+1}(z_{j+1}) = \int_{M_j/q}^{M_j} P(M|M_j, z_j) M \mathrm{d}M. \tag{1.29}$$

We then replace $P(M|M_j, z_j)$ by eq. (1.28) and obtain

$$M_{j+1}(z_{j+1}) = \int_{M_j/q}^{M_j} \frac{M_j}{M}\frac{1}{\sqrt{2\pi}}\frac{\Delta\omega}{\Delta S^{3/2}}\exp\left[-\frac{\Delta\omega^2}{2\Delta S}\right]\left|\frac{\mathrm{d}S}{\mathrm{d}M}\right| M\mathrm{d}M, \tag{1.30}$$

where $\Delta\omega = w_{j+1} - w_j$ corresponds to the redshift interval (z_{j+1}, z_j), and $\Delta S = S - S_j$. Defining $u^2 = \Delta\omega^2/2\Delta S$, the above integral yields

$$M_{j+1}(z_{j+1}) = \frac{2}{\sqrt{\pi}} M_j \int_{u_{j+1}}^{u_j} e^{-u^2} \mathrm{d}u, \tag{1.31}$$

here $u_j = \Delta\omega/\sqrt{2(S_j - S_j)} \to \infty$ and $u_{j+1} = \Delta\omega/\sqrt{2(S(M_j/q) - S_j)}$. By integrating, the halo mass history can be written in terms of the error function

$$M_{j+1}(z_{j+1}) = M_j \left[1 - \mathrm{erf}\left(\frac{\Delta\omega}{\sqrt{2S(M_j/q) - 2S_j}}\right)\right]. \tag{1.32}$$

Eq. (1.32) describes the halo mass growth as a function of redshift. For certain values of q (an arbitrary parameter that depends on the time step), Neistein et al. (2006) showed that eq. (1.32) produces halo mass histories that are in very good agreement with those taken from numerical simulations (Wechsler et al. 2002; Zhao et al. 2009).

Over the last decade, simulation-based works have analised the 'shape' of the halo mass accretion history (hereafter MAH). For example, McBride et al. (2009) used an extensive catalog of dark matter halos from the Millennium simulation, and found that about 25% of halos have MAHs that are well described by a 1-parameter exponential form, while the rest of the halos show plateaued late-time growth that is shallower than an exponential, and only a 20% Milky-Way mass to 50% cluster mass halos experience late-time growth that is steeper than an exponential. McBride et al. (2009) then concluded that these deviations from exponential growth are better fit by the function $M(z) \propto (1+z)^{\beta} e^{\gamma z}$. Similarly, Wu et al. (2013) analised a sample of 96 zoom-in simulation of $\sim 10^{14}\,\mathrm{M}_{\odot}$ halos, and compared various parametrizations for the halo MAH, concluding that the pure exponential model does not provide the curvature needed to fit the data. In addition, Behroozi et al. (2013) noted that the pure exponential parametrization of the MAH predicts that high-redshift progenitor histories cross. To fix this, they used the Bolshoi simulations and parametrize the halo MAH of a single halo mass using a double power-law times an exponential, and then parametrized the ratios of progenitor masses for other halo masses.

The general conclusion is that the halo mass accretion history seems to be well described by a power-law times an exponential, but it is still not entirely clear whether the parameters in the functional form are correlated (Wong & Taylor 2012), and even whether the functional form (power-law-exponential) is physical or an numerical artifact. Various works have found that the build-up of dark matter halos in CDM models indeed consists of an early phase of fast accretion and a late phase of slow accretion. Li (2008) proposed that the time when a halo reaches its maximum virial velocity divides its mass assembly history in two phases, where the fast accreting phase is dominated by major mergers and the slow accretion phase is dominated by minor mergers. Whereas Zhao et al. (2003) showed that the two phases are separated by the time when the halo concentration

reaches a value of ~ 4, and the typical binding energy of the halo is approximately equal to that of a singular isothermal sphere with the same circular velocity.

In view of this, in Chapter 2 we aim to provide a physical explanation for the 'shape' of the halo MAH. We further analyse eq. (1.32) as well as the analytic formulation of Neistein et al. (2006). We conclude that the change of phase in the halo MAH (from fast-growth to slow-growth) is physical and show that the halo MAH can be well described by a power-law times an exponential. In addition, we derive an analytic model that relates the halo MAH with the primordial density perturbation field and linear power spectrum. In Chapter 3 we analyse the halo MAH using a series of dark matter only cosmological simulations from the OWLS project, and investigate the connection of the halo MAH with the halo's concentration and density profile.

In the following subsection, we introduce numerical simulations. In Chapter 3 we discuss how to compute mergers trees as well as the necessary numerical convergence conditions.

1.2.2 Cosmological simulations

Numerical simulations have become an almost indispensable tool in astrophysical research. Of interest to us are cosmological simulations, whose detailed description of the evolution of the Universe has reached an impressive point of maturity and accuracy. As an illustration, Fig. 1.3 shows a 'slice' of the Universe at $z = 0$ (taken from the EAGLE simulations), together with two regions zoomed-in by a factor of 1/2 and 1/5, respectively. The figure shows a clear example of the detailed representation of the Universe that modern cosmological simulations are able to achieve.

Throughout this thesis we divide numerical simulations into two categories, N-body simulations and hydrodynamical simulations. N-body simulations focus on simulating collisionless dark matter through different particle-based methods that compute the gravitational interactions, whereas hydrodynamical simulations follow not only the gravitational interactions of dark matter but also the hydrodynamical forces on individual mass (or fluid) elements of baryonic matter. The size and resolution of numerical simulations depend on the size of the region, so that they fairly represents the object(s) of study. For example, typical sizes of simulated volumes are generally $\sim 1\,\mathrm{Mpc}$ scale for an individual galaxy, $10 - 100\,\mathrm{Mpc}$ for a galaxy population, and $> 100\,\mathrm{Mpc}$ for a galaxy cluster population. The mass resolution generally varies from $\sim 10^5\,\mathrm{M}_\odot$ up to $\sim 10^{10}\,\mathrm{M}_\odot$, on resolution scales of a few hundred parsec for individual galaxies to above the kiloparsec scale for cosmological boxes.

In N-body simulations we follow the motion of N collisionless particles, whose positions are expressed in comoving units. Since gravity is a long-range force, the force acting on a given particle depends on the position of all the other particles, that is equiv-

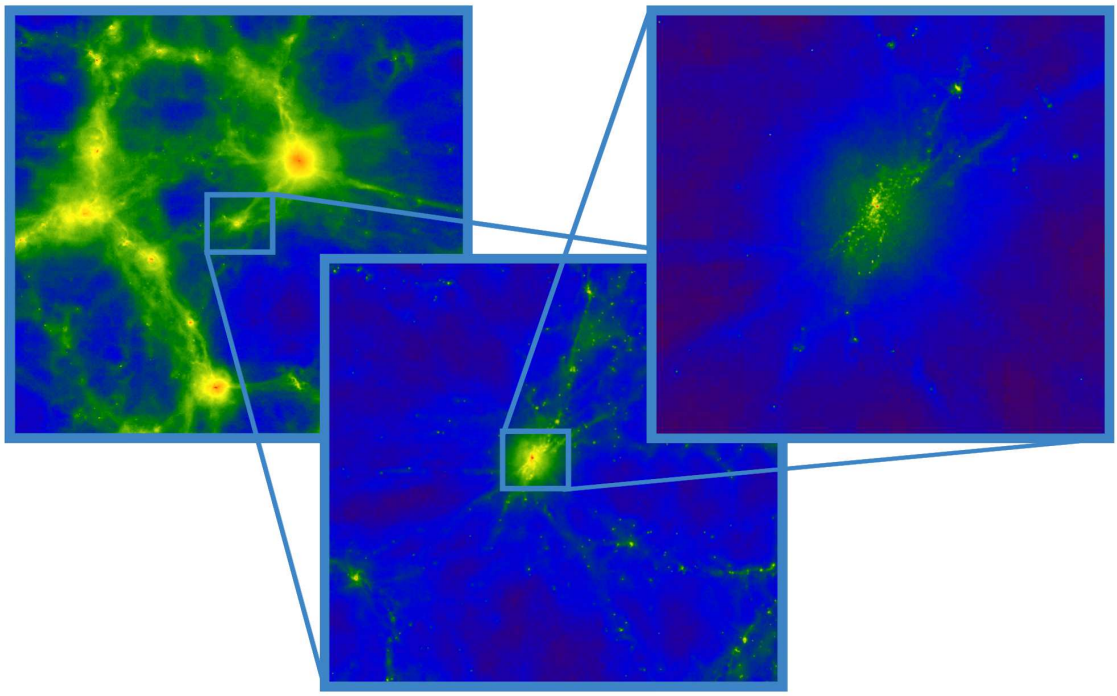

Figure 1.3: Zoom-in slices of the Universe at $z = 0$ taken from the EAGLE simulations.

alent to solve a set of $2N$ coupled first-order differential equations. To do it efficiently various methods have been implemented. (i) Tree algorithm: in this algorithm all the other particles are grouped together systematically according to their distances to the particle for which the force is to be calculated, and the force from each group is then replaced by its multipole expansion (Barnes & Hut 1986). (ii) Particle-mesh algorithm (PM): in this case the computational box (assumed to have size L) is divided into a grid of M^3 meshes with constant size L/M and the gravitational forces are computed in each grid point according to its particle distribution (e.g. Hockney & Eastwood 1988). (iii) Particle-particle-particle-mesh algorithm (Tree-PM): this method is implemented in the simulations we use throughout this thesis. As in the particle-mesh algorithm, long-range forces are computed by PM while the forces between particles with distance less then about $2L/M$ are computed directly by calculating the individual gravitational forces (see Couchman 1991). For a more detailed overview of the different techniques for cosmological simulations, the reader is refereed to Dolag et al. (2008).

An obvious limitation of N-body simulations is that objects with masses below the mass resolution are not represented in the simulation. Finite mass resolution also limits the ability to study the internal structures (density profiles, shapes, substructures) of objects with masses not much larger than the mass resolution. Typically one requires more than ~ 1000 particles in order to have a sufficiently reliable representation of the overall shape and density profile of a collapsed object.

Hydrodynamical simulations, which are more expensive to compute than N-body simulations, are divided into two different approaches: *smoothed particle hydrodynamics*

(SPH) method, where the mass of the gaseous fluid is parceled out to a discrete number of particles (Lucy 1977; Gingold & Monaghan 1977; Monaghan 1992, but see Price 2012 for a recent review), and *Eulerian* or *mesh-based* method, that typically utilizes a scheme called *adaptive mesh refinement* or AMR (Berger & Colella 1989; Stone & Norman 1992, but see Springel 2010 for a description of the most recent AMR simulation with moving mesh). In this last method, space itself is divided up into a grid, and the flow of gas between neighboring cells of this grid is computed over time. In this thesis we used N-body and SPH simulations from the OWLS (Schaye et al. 2010) and EAGLE project (Schaye et al. 2015).

The fundamental idea of SPH is to represent a fluid by a Monte Carlo sampling of its mass elements using a set of N particles. Each particle is assigned with the mass of the fluid element it represents, and in the Lagrangian formulation this mass is conserved. These particles can be used to sample any field of the fluid, so that the field value at an arbitrary position $\mathbf{x}$ can be approximated by $\langle A_i \rangle = \langle A(\mathbf{x})_i \rangle = \sum_j \frac{m_j}{\rho_j} A_j W(\mathbf{x}_i - \mathbf{x}_j, h)$, where W is a smoothing kernel of radius h. SPH, at least in its standard implementation, introduces spurious pressure forces on particles in regions where there are steep density gradients, in particular near contact discontinuities. This results in a boundary gap of the size of an SPH smoothing kernel radius, over which interactions are severely damped. In Chapter 5 we give an overview of the most basic problems of SPH and how to overcome them, whereas in Chapter 3 we focus on the resolution problems that arise when building merger trees from cosmological simulations.

1.2.3 Dark matter halo internal structure

Over the past few years large cosmological simulations have been performed to determine the properties of dark matter halos, including density profiles, shapes and accretion histories (see e.g. Springel et al. 2005; Klypin et al. 2011; Bryan et al. 2013). These properties are of particular interest, as forming galaxies depend on the structural properties of the halos in which they are embedded.

During hierarchical growth, halos acquire a density profile with a near universal shape, that can be described by the following expression

$$\rho(r) = \frac{\rho_{\rm crit}\delta_{\rm c}}{(r/r_{-2})(1 + r/r_{-2})^2}, \tag{1.33}$$

which known as the 'NFW profile' (Navarro et al. 1997, hereafter NFW). In the expression, r_{-2} is the scale radius that represents the transition from a shallow r^{-1} inner profile to a steeper r^{-3} outer profile, $\rho_{\rm crit}(z) = 3H^2(z)/8\pi G$ (with $H(z)$ given by eq. 1.15) and $\delta_{\rm c}$ is a dimensionless parameter.

A halo's physical extent is given by its virial radius, r_{200}, which is often defined as

the radius within which the mean density is 200 times the background critical density (in Chapter 3 we discuss alternative definitions of the virial radius and its impact on the halo MAH). The ratio of the virial radius and the NFW scale radius is a measure of the concentration of the density profile, and so this ratio is called the concentration parameter

$$c = \frac{r_{200}}{r_{-2}}. \tag{1.34}$$

The NFW density profile can be described by just two parameters, halo mass, M, and concentration, c. Thus, given the NFW profile, only a relation between concentration and halo mass (hereafter, the $c - M$ relation) is needed to fully specify halo structure at fixed mass. Therefore, numerous studies have been undertaken to improve the $c - M$ calibration.

Despite its importance, there is still no solid agreement on the dependence of halo concentration on halo mass and redshift. The discrepancies are generally driven by cosmology (a small change in the adopted cosmology has important effects on the structure of dark matter halos, Macciò et al. 2008) or dynamical state of the selected dark matter halos (a halo's internal structure differs significantly depending on whether it is relaxed or undergoing a merger event, Klypin et al. 2014; Ludlow et al. 2012). In Chapter 4 we explore the dynamical state of dark matter halos and their internal structure. We find that since the density profiles of unrelaxed halos are poorly captured by the NFW fitting formula, their concentration parameter is clearly affected by transient departures from equilibrium.

It has been shown that a halo concentration not only depends on halo mass but also on the halo formation time. The halo formation (or assembly) time is traditionally defined as the point in time when the halo mass reached a fraction of the total mass today. Low-mass halos typically assemble earlier, when the Universe was denser, than high-mass halos do. As a result, low-mass halos are more concentrated. It has then been concluded that concentration correlates with formation time (Bullock et al. 2001; Wechsler et al. 2002), and it has also been found that concentration correlates with the mass variance σ (e.g. Zhao et al. 2009; Prada et al. 2012; Ludlow et al. 2014; Dutton & Macciò 2014). However, the origin of these correlations is still not entirely clear. In Chapter 3 we investigate the origin for the $c - \sigma$ relation and show the halo MAH is the physical link that drives the relation. In Chapter 4 we investigate the connection between halo mass growth an concentration. We show that the change of slope in the $z \sim 0$ $c - M$ relation at a mass scale of $10^{11}\,\mathrm{M}_{\odot}$ is driven by the change in the functional form of the halo MAH, which goes from being dominated by an exponential (for high-mass halos) to a power-law (for low-mass halos). During the latter phase, the core radius remains approximately constant, and the concentration grows due to the drop of the back- ground density. In

the high-redshift regime, the halo MAH is mainly characterized by exponential growth. During this time the core radius increases simultaneously with the virial radius, hence the concentration hardly grows.

1.3 Galaxy formation

According to the classical picture of structure formation presented in §1.2, dark matter halos form at the peaks of the primordial density field. There are recent claims that the dark matter accretion rate onto halos is tightly coupled with the accretion rate of baryonic gas (Wetzel & Nagai 2015). However, unlike dark matter, gas follows more complicated physics. It cools, mixes, shocks, remains hot and eventually cools again. In this section we briefly describe the physics of gas cooling, the formation of galaxies, and its connection with the hierarchical growth paradigm of dark matter halos.

After nonlinear gravitational collapse, dark matter halos reach an equilibrium configuration, 'virialize', and the hot gas in the surrounding areas either reaches hydrostatic equilibrium in the outskirts of the halo, or is accreted and accumulates as dense, cold gas clouds to potentially form a protogalaxy at the center of the dark matter halo (White & Rees 1978; Blumenthal et al. 1986; Dubinski 1994; Mo et al. 1998). While cooling and collapsing under its own gravity, the gas clouds may fragment into small high-density cores, and eventually form stars and give rise to a visible galaxy (see McKee & Ostriker 2007 for a recent review on models of star formation).

In the hierarchical structure formation model briefly described in §1.2.1, small halos form at high redshift and cooling within them is predicted to be very efficient. This was an interesting problem in the late 1970s, when observations were clearly showing that galaxies were not very big and only a small fraction of all baryons were in cold gas or stars. The works of Silk & Rees (1998), Rees & Ostriker (1977), Binney (1977) and White & Rees (1978) suggested that collisions between gas from the intergalactic medium falling into the halo where preventing gas from cooling and producing accretion shocks. When accretion shocks occur, gas is heated and the gravitational energy of infall is converted into thermal energy. Only gas with a cooling time smaller than the dynamical time (or Hubble time) would be able to infall into the galaxy. Otherwise, it would adjust its density and temperature quasi-statically, forming a hot hydrostatic halo atmosphere, pressure supported against gravitational collapse. As a result, the general conclusion during the 1970s was that radiative cooling was limiting the mass of galaxies, but it was not completely solving the *overcooling problem*.

Years later, it was shown that there are in fact two forms of energetic sources or feedback that solve the overcooling problem from the 70s. One is the exploding stars, also known as supernovae (SN), that release large amount of energy able to expel the gas out of the galaxy (McKee & Ostriker 2007; Efstathiou 2000; Murray et al. 2005), and

produce a sort of recycling galactic fountain that acts as an extra mode of accretion onto galaxies (Oppenheimer et al. 2010; Übler et al. 2014). The other is the active phase of the central supermassive black hole (SMBH), also known as active galactic nuclei (AGN), that generates large radio jets that expand in the form of bubbles on scales > 30kpc, and are then able to heat the gas from the surrounding halo (Voit & Donahue 2005; Fabian et al. 2006; De Young 2010). This is generally referred to as "radio mode" feedback (Croton et al. 2006), which is believed to quench the diffuse gas accretion rates onto galaxies (Dubois et al. 2012).

Due to the complexity in the interaction of all the possible mechanisms (accretion shocks, SN events and AGN feedback) that modify the manner in which galaxies accrete gas, a model of galaxy gas accretion is still missing. In Chapter 5 we study how the hot halo forms and prevents gas from cooling, and in Chapter 6 we present a semi-analytic model of gas accretion rate onto galaxies.

1.4 Thesis outline

The outline of the subsequent chapters of this thesis is as follows. Chapters 2 and 3 concern the physics that drives the halo MAH and its impact on the halo internal structure. An analytic derivation of the halo MAH from the growth rate of initial density perturbations is presented in Chapter 2. This calculation shows that the halo MAH can be well described by an exponential function of redshift in the high-redshift regime. However, in the low-redshift regime the halo mass growth slows down, and can be described by a power law because the growth of density perturbations is halted in the dark energy dominated era due to the accelerated expansion of the Universe. Chapter 3 derives a semi-analytic model for the halo MAH that depends on the halo formation time and concentration, and utilizes the analytic relations from Chapter 2 to show that the halo MAH links the halo concentration with the initial density perturbation field.

Chapter 4 concerns the physical connection between the dark matter halo concentration and its assembly history. In this chapter a semi-analytic, physically motivated model for dark matter halo concentration as a function of halo mass and redshift is presented. The semi-analytic model combines the analytic model from Chapter 2 with an empirical relation between concentration and formation time obtained in Chapter 3. The model predicts a change of slope in the $z \sim 0$ concentration-mass relation at a mass scale of $10^{11}\,\mathrm{M}_{\odot}$, which is due to the change in the functional form of the halo mass history.

Chapters 5 and 6 connect the evolution of the dark matter to the evolution of baryons. Chapter 5 concerns the formation the hot hydrostatic halo formation and its impact on galaxy evolution. This chapter investigates how the presence of energy sources (like SN and AGN) increases the hot halo mass and reduces the mass scale of hot halo formation. It also derives a new semi-analytic approach to calculate a critical mass scale for hot

halo formation. Chapter 6 focuses on the physics that drives the gas accretion rate onto galaxies at the center of dark matter halos. The calculations show that the accretion rate onto the galaxy increases with increasing halo mass and flattens in the halo mass range $10^{11.7} - 10^{12.7}\,\mathrm{M}_{\odot}$ and at $z \leq 2$. A semi-analytic model of gas accretion onto galaxies is presented, that accurately reproduces the gas accretion rates from the simulations.

Finally, Chapter 7 summarizes the main findings of this thesis, discusses the impact of this study and presents ideas for future work.

2

The accretion history of dark matter halos

This chapter unravels the physics behind halo mass accretion history and the origin of the function that describes its shape.

Understanding the universal accretion history of dark matter halos is the first step towards determining the origin of their structure. In this chapter, we make use of the EPS formalism to derive the halo mass accretion history, hereafter MAH, from the growth rate of initial density perturbations. We show that the halo MAH can be well described by an exponential function of redshift in the high-redshift regime. However, in the low-redshift regime the MAH follows a power law because the growth of density perturbations is halted in the dark energy dominated era due to the accelerated expansion of the Universe. The main finding presented in this chapter is the derivation of an analytic model for halo MAH, that follows the expression $M(z) = M_0(1+z)^{af(M_0)}e^{-f(M_0)z}$, where $M_0 = M(z=0)$, a depends on cosmology and $f(M_0)$ depends on the linear matter power spectrum. The analytic model does not rely on calibration against numerical simulations, is suitable for any cosmology and is in very good agreement with the latest empirical models for the MAH in the literature. Readers unfamiliar with this topic are encouraged to first read §1.1 and §1.2 for a brief description of the standard cosmological framework, structure formation and for a better understanding of the notation used throughout this chapter. In addition, for readers interested in applying the model of halo MAH to their own studies we provide a step-by-step description on how to implement the MAH model in Appendix A as well as numerical routines online[i].

[i] Available at https://bitbucket.org/astroduff/commah and http://astro.physics.unimelb.edu.au/Research/Public-Data-Releases/COMMAH

2.1 Brief introduction

Throughout the last decade, there have been many attempts to quantify halo MAHs using catalogues of halos from numerical simulations (Wechsler et al. 2002; McBride et al. 2009; Wang & Abel 2007; Genel et al. 2010; Fakhouri et al. 2010; van de Voort et al. 2011; Faucher-Giguère et al. 2011; Johansson 2013; Benson & Bower 2011; Wu et al. 2013; Behroozi et al. 2013). Wechsler et al. (2002) characterized the MAH of halos more massive than $10^{12}\mathrm{M}_{\odot}$ at $z = 0$ using a one-parameter exponential form $e^{\beta z}$. In their work, Wechsler et al. (2002) limited their analysis to the build-up of clusters through progenitors already larger than the Milky Way halo. Similarly, McBride et al. (2009) limited their analysis to massive halos and found that a large fraction were better fitted when an additional factor of $(1 + z)^{\alpha}$ was added to the Wechsler et al. (2002) exponential parametrization, yielding a MAH of the form $M \propto (1 + z)^{\alpha} e^{\beta z}$. Wong & Taylor (2012) investigated whether the MAH can be described by a single parameter function or whether more variables are required. They utilized principal component analysis and found that despite the fact that the McBride et al. (2009) two-parameter formula presents an excellent fit to halo MAHs, the parameters α and β are not a natural choice of variables as they are strongly correlated. Recently, van den Bosch et al. (2014) studied halo MAHs extracted from N-body simulations and semi-analytical merger trees. However, so far no universal and physically motivated model of a universal halo MAH function has been provided.

An alternative method to interpret the complex numerical results and to unravel the physics behind halo mass growth, is the EPS formalism (introduced in §1.2.1). EPS theory provides a framework that allows us to connect the halo MAH to the initial density perturbations. Neistein et al. (2006) showed in their work that it is possible to create halo MAHs directly from EPS formalism by deriving a useful analytic approximation for the average halo mass growth. In this chapter we aim to provide a physical explanation for the 'shape' of the halo MAH found by earlier simulation-based works, using both the EPS theory and the analytic formulation of Neistein et al. (2006). In addition, we derive an analytic model for the halo MAH, which depends mainly on the linear power spectrum and is suitable for any cosmology.

This chapter is organized as follows. We begin with a discussion of halo mass growth and show in §2.2 that the halo MAH can be described by a power law and an exponential as originally suggested from fits to cosmological simulation data by McBride et al. (2009). We then derive a simple *analytic model* based on the EPS formalism and compare it to the latest empirical halo MAH models from the literature. We discuss how the different cosmological parameters impact on halo mass growth in §2.3. Finally, we briefly summarize the main findings of this chapter in §2.4.

2.2 On the physics behind the halo mass history

In Chapter 1 we discussed how dark matter halos initially grow from small density perturbations. As long as the density perturbations are small (in the so-called linear regime), they grow in amplitude in proportion to the linear growth factor $D(z)$, defined as

$$D(z) = D(z=0)H(z)\int_z^\infty \frac{1+z'}{H(z')^3}\mathrm{d}z', \tag{2.1}$$

with $D_0 = D(z=0) = 1$ and $H(z) = H_0[\Omega_{\mathrm{m},0}(1+z)^3 + \Omega_{\Lambda,0}]^{1/2}$. However, the density perturbations collapse to form a dark matter halo when they exceed the critical overdensity threshold value $\delta_\mathrm{c}(z) = \delta^0_\mathrm{crit}/D(z) = 1.686/D(z)$. Using the EPS formalism, Neistein et al. (2006) built dark matter halo merger trees and derived an analytic equation for the average halo MAH over an ensemble of merger trees. They defined $M_i(z_i)$ as the mass of the most massive halo (main progenitor), along the main branch of the merger tree at redshift z_i in step i, and obtained the subsequent mass via the following expression

$$M_{j+1}(z_{j+1}) = M_j\left[1 - \mathrm{erf}\left(\frac{\Delta\omega}{\sqrt{2S(M_j/q) - 2S_j}}\right)\right]. \tag{2.2}$$

In §1.2.1 of Chapter 1 we showed the mathematical derivation of this expression. However, in order to provide a physical motivation for the 'shape' of the halo MAH found in simulation-based works, in §2.2.1 we show how eq. (2.2) can be rewritten in a differential form, and show that the halo MAH is predicted to be an exponential at high redshift, and a power law at low redshift. In §2.2.2, we adopt the power-law exponential form and use it to provide a simple analytic model for halo MAHs. Finally, we compare our results with the latest models of halo mass history from the literature in §2.2.3.

2.2.1 Mass accretion in the high- and low-z regimes

To construct the MAH of a given parent halo, it is most convenient to begin with the parent halo of mass M_j at time $\omega_j = \delta_\mathrm{c}(z_j)$ and mass variance

$$S_j = \frac{1}{2\pi^2}\int_0^\infty P(k)\hat{W}^2(k;R_j)k^2\mathrm{d}k, \tag{2.3}$$

where $P(k)$ is the linear power spectrum and $\hat{W}(k;R_j)$ the Fourier transform of a top hat window function. We then go backwards in time following the merger events of its most massive progenitors. Therefore, for a small time-step $\Delta\omega$ back in time (with $\omega_j = \delta_\mathrm{c}(z_j)$ and $\Delta\omega < 0$), eq. (2.2) gives the average mass of the main progenitor M_{j+1} (S_{j+1}) by following an excursion set approach, to calculate the probability for a random walk originating at (S_j, ω_j) and executing a first upcrossing of the barrier $\omega_{j+1} = \omega_j + \Delta\omega$

at S_{j+1}.

Eq. (2.2) becomes linear in $\Delta\omega$ for small enough $\Delta\omega$. Therefore the MAH, $M_{\rm EPS}(z)$, can be constructed by iterating $M_{\rm EPS}(\Delta\omega_i + \Delta\omega_j|M_0) = M_{\rm EPS}(\Delta\omega_i|M_{\rm EPS}(\Delta\omega_j|M_0))$, where we term M_0 as the initial mass of the parent halo. The rate of change, $\mathrm{d}M_{\rm EPS}/\mathrm{d}\omega$, can be computed as

$$\frac{\mathrm{d}M_{\rm EPS}}{\mathrm{d}\omega} = \lim_{\Delta\omega\to 0}\frac{M_{\rm EPS}(\Delta\omega) - M_0}{\Delta\omega} = -M_0 \lim_{\Delta\omega\to 0}\frac{1}{\Delta\omega}\mathrm{erf}\left(\frac{\Delta\omega}{\sqrt{2(S_q - S)}}\right), \tag{2.4}$$

with $S_q = S(M_{\rm EPS}/q)$ and $S = S(M_{\rm EPS})$. Using the fact that $\lim_{x\to 0}\mathrm{erf(x)} \to 2\mathrm{x}/\sqrt{\pi}$, yields

$$\frac{\mathrm{d}M_{\rm EPS}}{\mathrm{d}\omega} = -\sqrt{\frac{2}{\pi}}\frac{M_{\rm EPS}}{\sqrt{S_q - S}}. \tag{2.5}$$

The above equation can be written in terms of redshift by replacing $\mathrm{d}\omega = \mathrm{d}(\delta^0_{\rm crit}/D(z))$ as,

$$\frac{\mathrm{d}M_{\rm EPS}}{\mathrm{d}z} = -\sqrt{\frac{2}{\pi}}\frac{M_{\rm EPS}}{\sqrt{S_q - S}}\frac{1.686\Omega_{\rm m}(z)^{0.0055}}{D(z)}\left[\frac{0.0055\mathrm{d}\Omega_{\rm m}(z)/\mathrm{d}z}{\Omega_{\rm m}(z)} - \frac{\mathrm{d}D(z)/\mathrm{d}z}{D(z)}\right]. \tag{2.6}$$

Since $0.0055(\mathrm{d}\Omega_{\rm m}(z)/\mathrm{d}z)/\Omega_{\rm m}(z) \sim 0$ and $\Omega_{\rm m}(z)^{0.0055}$ can well be approximated by 1, and eq. (2.6) can be written as

$$\frac{\mathrm{d}M_{\rm EPS}}{\mathrm{d}z} = \sqrt{\frac{2}{\pi}}\frac{M_{\rm EPS}}{\sqrt{S_q - S}}\frac{1.686}{D(z)^2}\frac{\mathrm{d}D(z)}{\mathrm{d}z}. \tag{2.7}$$

Our next step is to work with eq. (2.7) and analyse how the evolution of $M_{\rm EPS}(z)$ is governed by the growth factor. We then look for two practical approximations for the growth factor in the high- and low-redshift regimes and investigate the 'shape' of $M_{\rm EPS}(z)$ in these regimes by integrating eq. (2.7). However, in addition to the redshift dependence of the growth factor, in eq. (2.7) an extra redshift dependence is introduced through the quantity $[S_q - S]^{-1/2} = [S(M(z)/q) - S(M(z))]^{-1/2}$. Before integrating eq. (2.7), we calculate how the value of $[S(M(z)/q) - S(M(z))]^{-1/2}$ changes with redshift, in order to find a suitable first order approximation to simplify the calculations.

We replace $S = \sigma^2$ (with σ being the variance of the primordial density field) and approximate $\sigma \approx M^\gamma$, where $\gamma = -0.063$ for $M \leq 10^{12}\mathrm{M}_\odot$ and $\gamma = -0.21$ for $M > 10^{12}\mathrm{M}_\odot$, to obtain

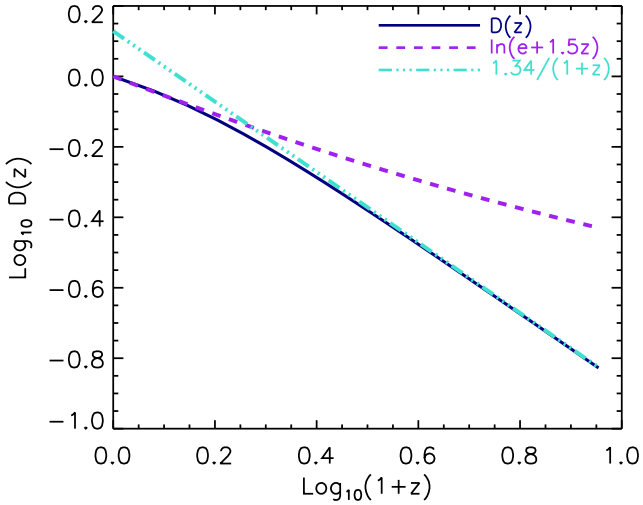

Figure 2.1: Linear growth factor against redshift. The dark blue solid line shows the growth factor obtained by performing the integral given by eq. (2.1). The purple dashed line corresponds to the low-redshift approximation in eq. (2.9). Similarly, the green dot-dashed line shows the approximation of the growth factor in the high-redshift regime.

$$\frac{[S(M(z)/q) - S(M(z))]^{-1/2}}{[S(M_0/q) - S(M_0)]^{-1/2}} = \left(\frac{M(z)}{M_0}\right)^{-\gamma}, \tag{2.8}$$

where $M_0 = M(z = 0)$. In cases where $M(z)$ is up to 2 order of magnitudes smaller than M_0, the right hand side of eq. (2.8) is close to unity ($(M(z)/M_0)^{-\gamma} = (10^{-2})^{-\gamma} \approx 1.33$ for low-mass halos and ≈ 2.63 for high-mass halos). We therefore approximate $(M(z)/M_0)^{-\gamma}$ by 1. We find that at low redshift, the approximation $[S(M(z)/q) - S(M(z))]^{-1/2} \approx [S(M_0/q) - S(M_0)]^{-1/2}$, carries a $\sim 5\%$ error for $M(z) \leq 10^{12}\mathrm{M}_\odot$ and a 15% error for $M(z) > 10^{12}\mathrm{M}_\odot$. Earlier in the accretion history, the errors may be as large as $\sim 20\%$ and 40% for $M(z) \leq 10^{12}\mathrm{M}_\odot$ and $M(z) > 10^{12}\mathrm{M}_\odot$, respectively. We demonstrate in §2.2.3 that these errors do not affect the final $M(z)$ model, which we show provides very good agreement with simulation-based MAH models.

The growth factor can be approximated with high accuracy by

$$D(z) = \begin{cases} \frac{1.34}{1+z} & \text{if} \quad z \gg 1, \\ \frac{1}{\ln(e+1.5z)} & \text{if} \quad z \ll 1, \end{cases} \tag{2.9}$$

for all cosmologies. Fig. 2.1 shows the growth factor as given by eq. (2.1) (solid dark blue line), together with the approximations in the high- and low-redshift regimes (dot-dashed green and purple lines, respectively). The high-redshift approximation for $D(z)$ is an exact solution for an Einstein-de Sitter (EdS) cosmology ($\Omega_\Lambda = 0$). However, the growth rate slows down in the cosmological constant dominated phase, so that linear

perturbations grow faster in an EdS universe.

We next estimate $M_{\rm EPS}(z)$ in the high- and low-redshift regimes by substituting the two expressions from eq. (2.9) into eq. (2.7). In the high-redshift regime (where $z \gg 1$),

$$\begin{aligned} \frac{{\rm d}M_{\rm EPS}}{M_{\rm EPS}} &= \sqrt{\frac{2}{\pi}} \frac{1}{\sqrt{S_q - S}} \frac{1.686}{D(z)^2} \frac{{\rm d}D(z)}{{\rm d}z} {\rm d}z, \\ \frac{{\rm d}M_{\rm EPS}}{M_{\rm EPS}} &= -f(M_0){\rm d}z, \end{aligned} \tag{2.10}$$

where $f(M_0) = 1/\sqrt{S(M_0/q) - S(M_0)}$ is a function of halo mass. Integrating this last equation, we obtain

$$M_{\rm EPS}(z) = M_0 e^{-f(M_0)z} \quad \text{at} \quad z \gg 1. \tag{2.11}$$

Thus, we find that to a first order approximation the halo MAH can be described by an exponential ($M(z) \sim e^{\beta z}$) in the high-redshift regime, as suggested by Wechsler et al. (2002). In the low-redshift regime, from eq. (2.10) and the bottom part of eq. (2.9), we find

$$\frac{{\rm d}M_{\rm EPS}}{M_{\rm EPS}} = -\frac{1.34}{1.8 + z} f(M_0){\rm d}z.$$

Integrating the above expression yields

$$M_{\rm EPS}(z) = M_0(1 + 0.5z)^{-1.34 f(M_0)} \quad \text{at} \quad z \ll 1. \tag{2.12}$$

Therefore, in the low-redshift regime, a power law ($M(z) \sim (1+z)^{\alpha}$) seems necessary (as suggested by McBride et al. 2009) because the growth of density perturbations is halted in the dark energy dominated era due to the accelerated expansion of the Universe.

The above conclusion is valid under the assumption that the term $(M_{\rm EPS}/M_0)^{\gamma}$ is negligible, an important and generally rough approximation. In the case where the term is included, we obtain that in the high redshift regime $M_{\rm EPS}(z) \propto z^{-1/\gamma} \approx z^{15.8}$ for low-mass halos and $M_{\rm EPS}(z) \propto z^{4.7}$ for high-mass halos. Similarly, in the low-redshift regime we find $M_{\rm EPS}(z) \propto \ln(1 + Cz)^{-1/\gamma}$, with C constant. This redshift dependence of $M_{\rm EPS}(z)$ is in agreement with the analytic model presented by Neistein et al. (2006) (see eq. A.5 of their work). Fig. 2.2 shows a comparison between the halo mass histories predicted by the analytic model of Neistein et al. (2006) (orange solid line, where we used eq. A.5 and the $q = 2.3$ case), the simulation-based model of van den Bosch et al.

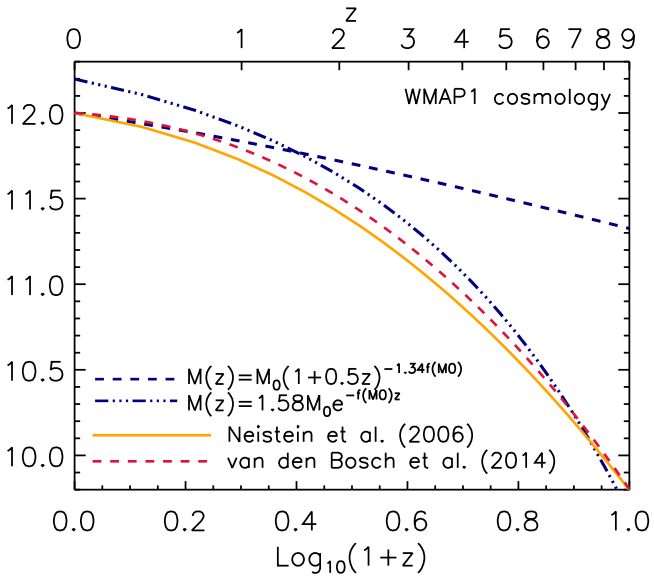

Figure 2.2: Comparison between the halo mass histories predicted by the analytic model of Neisten et al. (2006) (orange solid line), the simulation-based model of van den Bosch et al. (2014) (red dashed line) and the approximated halo mass histories given by eq. (2.12) for the low-redshift regime (blue dashed line), and by eq. (2.11) for the high-redshift regime (blue dot-dashed line).

(2014) (red dashed line) and the approximated halo mass histories given by eq. (2.12) for the low-redshift regime (blue dashed line), and by eq. (2.11) for the high-redshift regime (blue dot-dashed line). It can be seen that in the ranges of low- and high-redshift, the approximated expressions for the halo MAH (power-law and exponential) are in very good agreement with the models, from what we conclude that the functional form power-law times exponential is a fairly good approximation, able to capture the shape of the halo MAH.

It is interesting to note that regardless the functional form that describes the halo MAH, we find that the halo mass growth slows down at low redshift. Throughout this work we claim that the reason for such behavior is the accelerated expansion of the universe. To understand whether the change in growth is entirely due to cosmology, or whether it is also due to power spectrum, we investigate if the slow growth is present in universes with $\Omega_\Lambda = 0$ and $\Omega_\mathrm{m} \leq 1$. Since in both cases $D(z) = 1/(1+z)$, and the mass variance can be approximated as a power-law in mass, with γ lower than 1, we find that eq. (2.7) does not predict a transition of fast to slow growth.

2.2.2 Analytic mass accretion history model

In this subsection we provide an analytic model for the halo MAH based on the EPS formalism. This model is not calibrated against numerical simulations and allows an exploration of the physical processes involved in the halo mass growth. Based on our analysis from §2.2.1, we begin by assuming that the halo MAH can be well described by the simple form

$$M(z) = M_0(1+z)^{\alpha}e^{\beta z}. \tag{2.13}$$

The presence of the function $S(M_0)$ in both the high-redshift exponential (eq. 2.11) and the low-redshift power law (eq. 2.12) explains the correlation between α and β found by Wong & Taylor (2012). We estimate the relation between α, β and $S(M_0)$ by replacing $M_{\rm EPS}(z)$ in eq. (2.7) with the expression (2.13). Evaluating this at $z = 0$ we obtain

$$\alpha + \beta = 1.686(2/\pi)^{1/2} f(M_0) \frac{{\rm d}D}{{\rm d}z}|_{z=0}. \tag{2.14}$$

Assuming that $M(z)$ follows the relation shown in eq. (2.11) for the high-z regime we find

$$\beta = -f(M_0), \tag{2.15}$$
$$\alpha = af(M_0), \tag{2.16}$$

with $a = \left[1.686(2/\pi)^{1/2}\frac{{\rm d}D}{{\rm d}z}|_{z=0} + 1\right]$. The above equations introduce a halo MAH model directly derived from the EPS theory, where the parameters α and β are related through the variance of the smoothed density field, $S(M_0)$. The quantity q is a free parameter which can be determined by adding an extra equation that restricts the model. We do this by defining the halo formation redshift, $\tilde{z}_{\rm f}$, as the redshift where $M(\tilde{z}_{\rm f}) = M_0/q$. From eq. (2.13) we obtain

$$\frac{1}{q} = (1+\tilde{z}_{\rm f})^{af(M_0)}e^{-f(M_0)\tilde{z}_{\rm f}}, \tag{2.17}$$

where $f(M_0) = 1/\sqrt{S(M_0/q) - S(M_0)}$.

The general relation between formation time and q was introduced by Lacey & Cole (1993), using the expression

$$M(z) = M_0\left[1 - {\rm erf}\left(\frac{\delta_{\rm c}(z) - \delta_{\rm c}(0)}{\sqrt{2(S(M_0/q) - S(M_0)}}\right)\right], \tag{2.18}$$

which describes the average mass of the main progenitors in the EPS merger tree. We use eq. (2.18) to evaluate the halo mass at $\tilde{z}_{\rm f}$ and find the distribution of formation times. We follow the approach of Lacey & Cole (1993) and find

$$\delta_{\rm c}(\tilde{z}_{\rm f}) = \delta_{\rm c}(0) + \sqrt{2}f^{-1}(M_0){\rm erf}^{-1}(1 - 1/q). \tag{2.19}$$

We solve eqs. (2.17) and (2.19) and find q and $\tilde{z}_{\rm f}$ for various halo masses. We then fit the $q - M_0$ and $\tilde{z}_{\rm f} - q$ relations using a second order polynomial in $\log_{10} M$ for $\tilde{z}_{\rm f}$, and obtain the following set of equations that describe the halo MAH,

$$
\begin{aligned}
M(z) &= M_0(1+z)^{af(M_0)}e^{-f(M_0)z}, && (2.20)\\
a &= \left[1.686(2/\pi)^{1/2}\frac{\mathrm{d}D}{\mathrm{d}z}|_{z=0}+1\right], && (2.21)\\
f(M_0) &= 1/\sqrt{S(M_0/q)-S(M_0)}, && (2.22)\\
q &= 4.137\tilde{z}_{\rm f}^{-0.9476}, && (2.23)\\
\tilde{z}_{\rm f} &= -0.0064(\log_{10}M_0)^2+0.0237(\log_{10}M_0) && (2.24)\\
&\quad +1.8837.
\end{aligned}
$$

The equations that relate q, $\tilde{z}_{\rm f}$ and M_0 are calculated assuming the WMAP5 cosmology, but work for others cosmologies[ii] because the halo MAHs are mainly driven by the change in σ_8 and $\Omega_{\rm m}$. We reiterate that unlike previous models based on EPS theory (e.g. van den Bosch 2002a), the analytic model specified in the above equations was not calibrated against any simulation data.

Note that in the model the parameter q, that depends on halo mass, is not within the range $2 < q < 2.3$ required by Neistein et al. (2006) through their analysis of the distribution of the main progenitor masses. The main reason for this discrepancy is that our model is *based* on EPS formalism but *not directly derived from it* since we impose the functional form to be a power-law times an exponential, as a result the q parameter obtained is not equivalent to that of Neistein et al. (2006).

The top panel of Fig. 2.3 shows a comparison between the analytic model given by eqs. (2.20-2.24) (blue solid line), and the limiting case for the halo MAHs given by eq. (2.12) for the low-redshift regime (purple dashed line) and by eq. (2.11) for the high-redshift regime (green dot-dashed line). In the last case, we renormalized the MAH curve to match that given by the analytic model at $z = 7$. This figure demonstrates how exponential growth dominates the MAH at high redshift, and power-law growth dominates at low redshift, as concluded in the previous section.

The bottom panel of Fig. 2.3 shows the formation time obtained from eqs. (2.17) and (2.19), as a function of halo mass. As expected, larger mass halos form later. The right Y-axis shows the values of q obtained when calculating formation time, whereas the top X-axis shows the variance of the smoothed density field of a region that encloses the mass indicated by the bottom X-axis. The values of the function $f(M_0) = 1/\sqrt{S(M_0/q)-S(M_0)}$ are included in brackets. As can be seen from this figure, the larger the halo mass, the lower the variance $S(M_0)$, the larger $f(M_0)$, and so the larger the factor in the exponential that makes the halo mass halt its rapid growth at low redshift. For example, a $10^{14}\mathrm{M}_\odot$ halo has a MAH mostly characterized by an exponential growth ($\sim e^{-f(M_0)z}$)

[ii] We verified that the MAHs predicted by eqs. (2.20-2.24) are in excellent agreement with the simulations for the WMAP1/3/9 and Planck cosmologies.

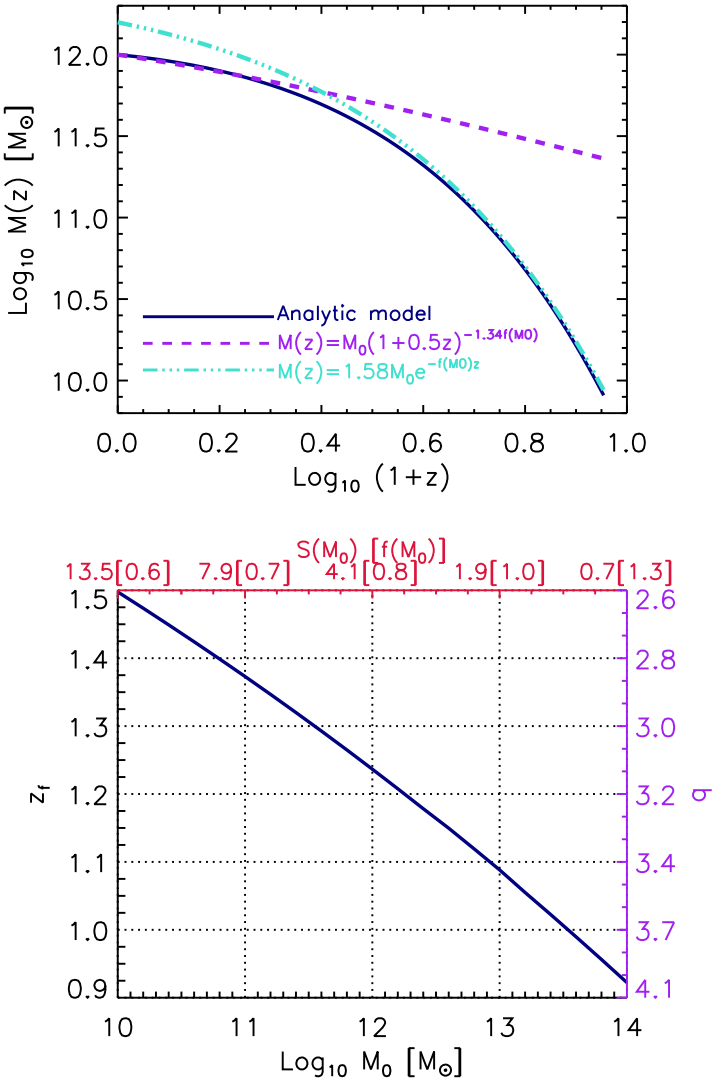

Figure 2.3: *Top panel*: comparison between halo mass histories predicted by the analytic model $M(z) = M_0(1+z)^{af(M_0)}e^{-f(M_0)z}$, given by eqs. (2.20)-(2.24) (blue solid line), and the approximated halo mass histories given by eq. (2.12), for the low-redshift regime (purple dashed line), and by eq. (2.11), for the high-redshift regime (green dot-dashed line). *Bottom panel*: formation redshift against halo mass. Here the formation redshifts were obtained by solving eqs. (2.17) and (2.19). The right Y-axis shows the values of 'q' obtained when calculating the formation redshift, whereas the top X-axis shows the variance of the smoothed density field of a region that encloses the mass indicated by the bottom X-axis. The values of the function $f(M_0) = 1/\sqrt{S(M_0/q) - S(M_0)}$ are shown in brackets.

until redshift $z = 1/f(M_0) = 0.7$, whereas a $10^{10}\mathrm{M}_\odot$ halo only has an exponential growth until redshift $z = 1.6$. Note, however, that our analytic model is not limited to the halo mass ranges shown in the bottom panel of Fig. 2.3. It can be extended to any halo masses and redshifts and the $q - M_0$ and $\tilde{z}_\mathrm{f} - M_0$ relations still hold.

In addition to the halo MAH, it is possible to calculate the accretion rate of a halo at a particular redshift. In order to do that we differentiate eq. (2.13) with respect to time and replace $\mathrm{d}z/\mathrm{d}t$ by $-H_0[\Omega_{\mathrm{m},0}(1+z)^5 + \Omega_{\Lambda,0}(1+z)^2]^{1/2}$ to obtain

$$\frac{\mathrm{d}M(z)}{\mathrm{d}t} = 71.6\ \mathrm{M}_\odot\ \mathrm{yr}^{-1} \left(\frac{M(z)}{10^{12}\mathrm{M}_\odot}\right) \left(\frac{h}{0.7}\right) f(M_0)[(1+z) - a][\Omega_{\mathrm{m},0}(1+z)^3 + \Omega_{\Lambda,0}]^{1/2}, \tag{2.25}$$

where a is given by eq. (2.21) and $f(M_0)$ is given by eq. (2.22). Note that the above formula will give the accretion rate at redshift z of a halo that has mass M_0 at redshift $z = 0$, and mass $M(z)$ at redshift z.

The physical relation derived between the parameters describing the exponential and power law behaviour implies that a single parameter accretion history formula should be seen in numerical simulations. In the following chapter we investigate the α and β parameter dependence in more detail, and we determine the intrinsic relation (which cannot be explored under the EPS formalism) between halo assembly history and inner halo structure.

2.2.3 Comparison with previous studies

In this section we briefly describe the simulation-based halo MAH models presented in van den Bosch et al. (2014) (vdB14) and McBride et al. (2009) (MB09), and contrast them with our analytic model given by eqs. (2.20-2.24). The panels in Fig. 2.4 show a comparison of our mass history model (turquoise solid lines) to the models of vdB14 (purple dashed lines) and MB09 (dark blue dot dashed lines). vdB14 used the MAHs from the Bolshoi simulation (Klypin et al. 2011) and extrapolated them below the resolution limit using EPS merger trees. They then used a semi-analytic model to transform the average or median MAH for a halo of a particular mass taken from the Bolshoi simulation, to another cosmology, via a simple transformation of the time coordinate. Using their publicly available code we calculated the mass histories of 10^9, 10^{11}, 10^{13} and $10^{15}\mathrm{M}_\odot$ halos for the WMAP1 cosmology. We find good agreement between our model and vbB14 for all halo masses. The main difference occurs for the mass histories of high-mass halos ($M_0 > 10^{13}\mathrm{M}_\odot$), where vdB14 seems to overpredict the mass growth above $z = 4$ (e.g. by a factor of ~ 6 at $z = 9$). In addition, vdB14 compared their model to those of Zhao et al. (2009) and Giocoli et al. (2012), and found that both works predict smaller halo mass growth at $z > 1.5$.

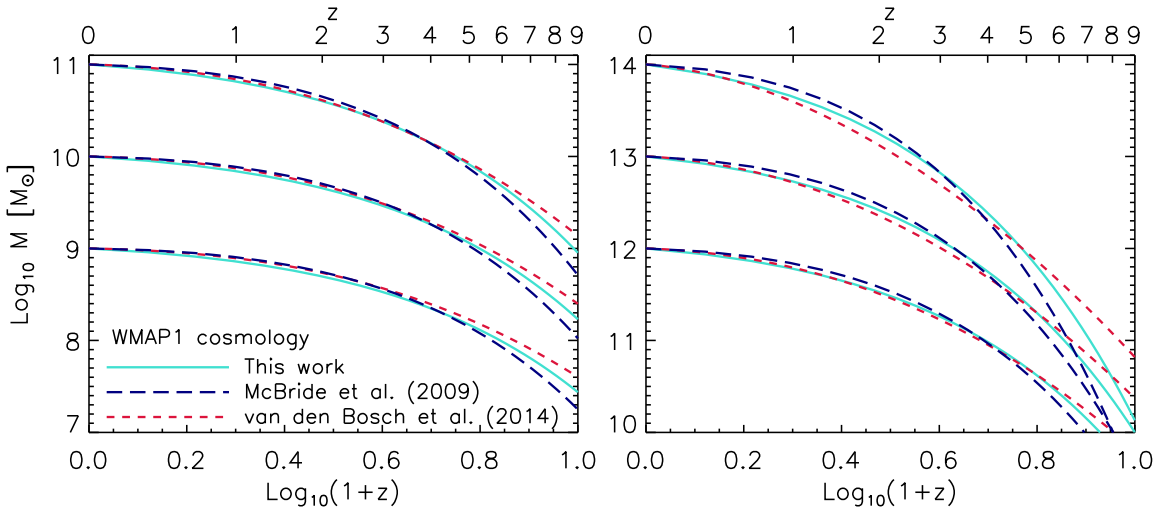

Figure 2.4: Comparison of halo mass history models. The analytic model presented in this work (turquoise solid lines) is compared with the median mass history obtained from the Bolshoi simulation and merger trees from van den Bosch et al. (2014) (purple dashed lines) and the best-fitting relations from the Millennium simulation from McBride et al. (2009) (dark blue dot dashed lines). The comparisons are shown for four halo masses and for consistency with McBride et al. (2009) we assumed in our model and in the van den Bosch et al. (2014) model the WMAP1 cosmology.

We also compare our model to the MB09 mass history curves. MB09 used the Millennium simulation (Springel et al. 2005) and separated their halo sample into categories depending on the 'shape' of the MAHs, from late-time growth that is steeper than exponential to shallow growth. We find that the fitting function that best matches our results is from their type IV category. We find good agreement with the MB09 formula.

Fig. 2.4 demonstrates that the physically motivated analytic model presented in this work yields MAHs that are in good agreement with the results obtained from numerical simulations. However, in contrast to the models based on fits to simulation results, our analytic model can be extrapolated to very low masses and is suitable for any cosmology.

2.3 Impact of cosmological parameters on halo MAH

In this section we investigate how the cosmological parameters n_s, σ_8, h, $\Omega_{\Lambda,0}$ and $\Omega_{m,0}$ (introduced in §1.1 and §1.2) impact on the growth rate of dark matter halos. We use the analytic model given by eqs. (2.20-2.24), and analyze how the variation of each cosmological parameter modifies the halo MAHs.

(i) Power spectrum index. The primordial power spectrum, as predicted by the standard cosmological model, is $P_i(k) = Ak^{n_s}$, where n_s is the spectral index that most inflationary models predict to be approximately 1 (the case of $n_s = 1$ is called the scale-invariant Harrison-Zeldovich spectrum, Harrison 1970; Zeldovich 1972). The value of n_s

is very important because it determines the shape of the power spectrum as it was set by the early universe. A change in $n_{\rm s}$ alters the power in the fluctuations of a given scale, and as a result the growth of structures changes. To investigate the impact of $n_{\rm s}$ on the halo MAH we first analyse how the linear power spectrum, $P(k)$, and variance of the primordial density field, σ, change in cases where $n_{\rm s}$ is 2, 1, 0 and -1. The top-left panel of Fig. 2.5 shows the power spectrum $P(k) = P_i(k)T^2(k)D(z)$, where $T(k)$ is the linear transfer function.[iii] We calculate different curves assuming the same values of $\Omega_{\rm m,0}$, $\Omega_{\Lambda,0}$, h and σ_8 but different values of $n_{\rm s}$, as indicated in the legend.

The top-left panel of Fig. 2.5 shows that $P(k)$ retains the primordial shape for large-scale fluctuations, $P(k) \propto k^{n_{\rm s}}$ at $k < k_{\rm eq}$, with $k_{\rm eq} \sim 0.06(\Omega_{\rm m,0}h^2){\rm Mpc}^{-1}$. On small scales, the shape of $P(k)$ changes and the slope is reduced to $P(k) \propto k^{n_{\rm s}-4}$ at $k > k_{\rm eq}$. This occurs because small-scale fluctuations enter the horizon during the radiation dominated era, and their growth is suppressed due to radiation pressure. The top-right panel of Fig. 2.5 shows that when we decrease the power index from 1 to -1, we imprint more power on large scales, and as a result $\sigma_{n_{\rm s}=-1}(M)$ is larger than $\sigma_{n_{\rm s}=1}(M)$ at high halo masses ($> 10^{14}\,{\rm M}_\odot$), but is smaller at low halo masses ($< 10^{14}\,{\rm M}_\odot$).

In §2.2.2 we defined the halo formation redshift, $\tilde{z}_{\rm f}$, as the redshift where $M(\tilde{z}_{\rm f}) = M_0/q$. We evaluate the halo MAH at $\tilde{z}_{\rm f}$ and find that $\tilde{z}_{\rm f} \sim \beta^{-1}\ln q^{-1}$, where for simplicity we approximated $M(z) \sim e^{\beta z}$ (valid at early times). We then assume that q is roughly constant with halo mass, and obtain $\tilde{z}_{\rm f} \sim f^{-1}(M_0)$. Since $f(M_0) \sim \sigma^{-1}(M_0)$, we find that the larger $\sigma(M_0)$, the larger $\tilde{z}_{\rm f}$, meaning that high-mass halos form earlier in a universe with a smaller power index, while low-mass halos form later. This can be seen in the bottom panels of Fig. 2.5 which show halo MAHs assuming $n_{\rm s} = -1$ (blue long-dashed lines), 0 (blue short-dashed lines), 1 (green solid lines) and 2 (blue solid lines). As expected, the left-bottom panel shows that halos reached $10^{12}\,{\rm M}_\odot$ quite recently (at $z = 0.54$) in a universe with $n_{\rm s} = -1$, whereas halos reached the same mass earlier (at $z = 3.1$) in a universe with $n_{\rm s} = 1$. The opposite behavior is seen in the right-bottom panel for high-mass halos.

(ii) Mass variance on an $8\,h^{-1}$Mpc scale. σ_8 is used to normalize the theoretical power spectrum by requiring that $\sigma(R) = 0.9$ at $R = 8\,h^{-1}$Mpc. Since a change in σ_8 only changes the normalization of $P(k)$, $\sigma(M)$ is shifted in proportion to the change in normalization. We then find that if we increase σ_8, $\sigma(M)$ increases for all halo masses and the exponent $\beta = -f(M_0)z$ increases, as a result $M(z)$ flattens and halos form earlier.

(iii) Hubble parameter. The Hubble parameter h gives the rate of expansion of the Universe. If we increase the rate of expansion, we not only increase the scale of upturn

[iii] We calculated $T(k)$ using the fitting relations from Eisenstein & Hu (1998) assuming no neutrinos.

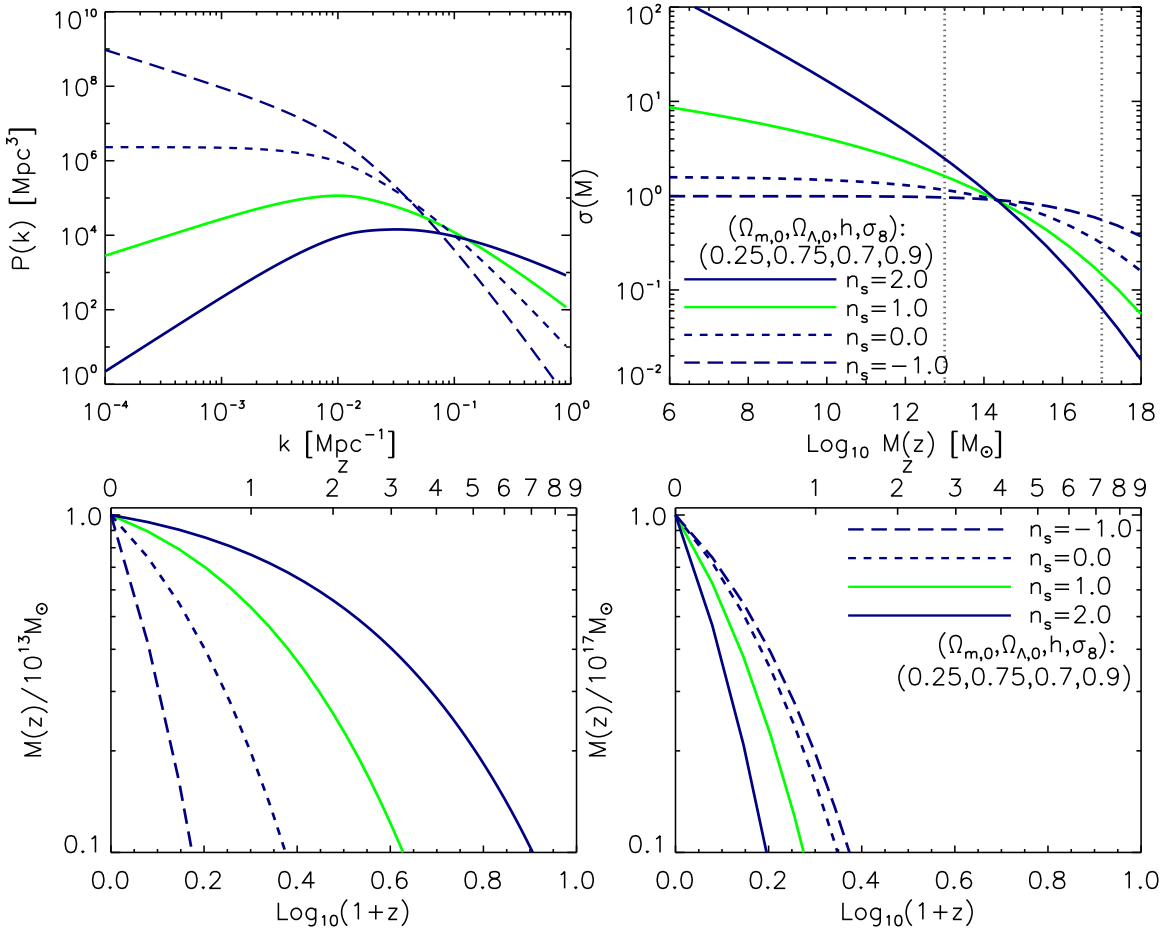

Figure 2.5: Linear power spectrum (top-left panel), mass variance (top-right panel) and MAH of halos with masses $M_0 = 10^{13}\,\mathrm{M}_\odot$ (bottom-left panel) and $M_0 = 10^{17}\,\mathrm{M}_\odot$ (bottom-right panel), calculated assuming the same value of the cosmological parameters $\Omega_{\mathrm{m},0}$, $\Omega_{\Lambda,0}$, h and σ_8, but different n_s, as indicated in the legend.

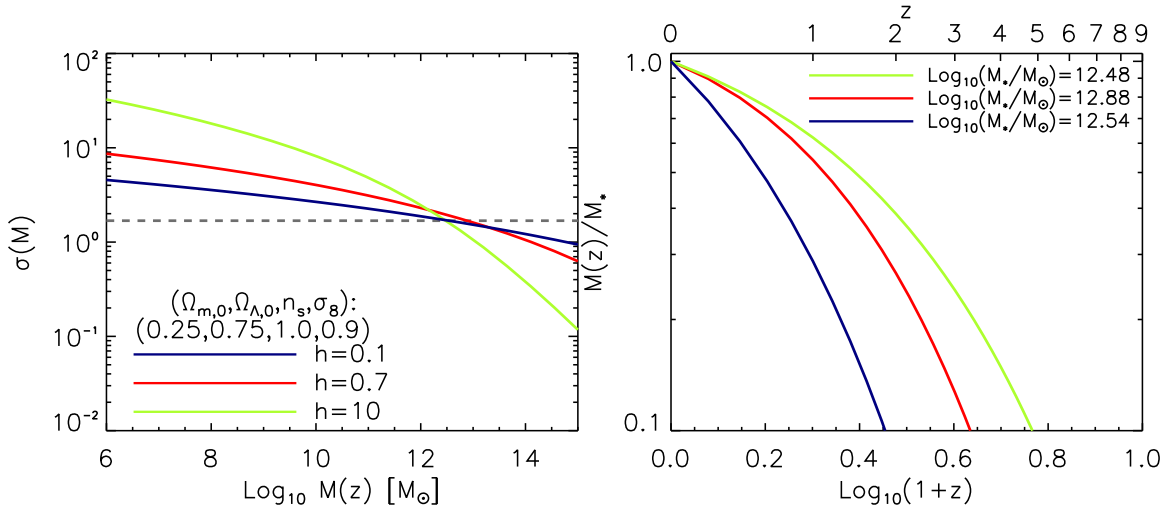

Figure 2.6: Mass variance (left-panel) and halo MAHs (right-panel) calculated assuming same value of the cosmological parameters $\Omega_{\mathrm{m},0}$, $\Omega_{\Lambda,0}$, n_s and σ_8, but different h, as indicated in the legend. In the right-panel M_* denotes the halo mass at $z = 0$ given by the intersection between grey dot line and the mass variance shown in the left-panel.

in $P(k)$ ($k_{\rm eq} \propto h^2$), but also the normalization. As a result, $\sigma(M)$ increases in low-mass halos and decreases in high-mass halos, as shown in the left-panel of Fig. 2.6. In order to analyse the change in $M(z)$ from universes with different expansion rate, we compare MAH of halos with the same value of $\sigma(M)$. We select those that intersect the dotted grey line in the left-panel of Fig. 2.6. The right-panel of the figure shows that the halo MAH changes with h, the higher h, the less steep $M(z)$. To understand this we analyse the parameter α (which depends on h) in the $M(z)$ model. If we again use $\tilde{z}_{\rm f}$ and the MAH model from eq. (2.20), we obtain

$$f^{-1}(M_0) \ln q^{-1} = \ln(1+\tilde{z}_{\rm f})[1.686(2/\pi)^{1/2} {\rm d}D/{\rm d}z|_{z=0} + 1] - \tilde{z}_{\rm f}. \tag{2.26}$$

Assuming that $\tilde{z}_{\rm f}$ is small, and approximating $\ln(1+\tilde{z}_{\rm f}) \approx \tilde{z}_{\rm f}$, we find that $\tilde{z}_{\rm f} \propto ({\rm d}D/{\rm d}z|_{z=0})^{-1}$. As a result, $\tilde{z}_{\rm f} \propto h$, from which we conclude that larger values of h lead to faster growth of structure (larger $D(z)$), and the earlier formation of dark matter halos.

(iv) Density parameter of dark energy. In §2.2.1 we show that in the low-redshift regime the halo MAH is mostly dominated by a power-law function of redshift, because the growth of the density perturbations is halted in the dark energy dominated era due to the accelerated expansion of the Universe. In this analysis we expand this explanation by comparing halo MAHs calculated under different $\Omega_{\Lambda,0}$ values.

The left-panel of Fig. 2.7 shows the growth factor calculated assuming $n_{\rm s} = 1$, $\sigma_8 = 0.9$, $h = 0.7$, $\Omega_{\rm m,0} = 1 - \Omega_{\Lambda,0}$ (flat) and $\Omega_{\Lambda,0}$ ranging from 0.1 to 0.9. In a universe with $\Omega_{\Lambda,0} = 0.9$, the dark energy dominated era begins at $z_{\Omega_\Lambda} \approx 1.08$, but in the case $\Omega_{\Lambda,0} = 0.1$, $z_{\Omega_\Lambda} \approx -0.51$, meaning that the dark energy dominated era has not yet begun. We therefore find that while growth rate factor declines at $z \leq 1.08$ when $\Omega_{\Lambda,0} = 0.9$, it grows in proportion to the scale factor ($D(z) \propto a(z)$) at all redshifts when $\Omega_{\Lambda,0} = 0.1$.

In order to analyse the change in $M(z)$ under different values of $\Omega_{\Lambda,0}$, we compare MAHs from halos at the non-linear mass scale M_*, so that $\sigma(M_*, \Omega_{\Lambda,0}) = 1.686$. $\sigma(M)$ is the main parameter governing the abundance of halos (see eq. 1.26 in §1.2.1, and see also Press & Schechter 1974; Sheth & Lemson 1999; Jenkins et al. 2001; Reed et al. 2007). In universes with different matter content (since changing $\Omega_{\Lambda,0}$ changes $\Omega_{\rm m,0}$), halos with the same $\sigma(M_*, \Omega_{\Lambda,0})$ have similar (or 'equivalent') abundance. Then, to compare MAHs of halos that are 'equivalent', we select halos with 'equivalent' abundance (a technique often employed for calculating galaxy mass evolution, e.g. van Dokkum et al. 2013; Behroozi et al. 2013).

The right-panel of Fig. 2.7 shows that when $\Omega_{\Lambda,0} = 0.1$, $M(z)$ is characterized by an exponential growth at all z (blue long-dashed line), and when $\Omega_{\Lambda,0} = 0.9$, $M(z)$ is dominated by a power-law growth at earlier times (blue solid line).

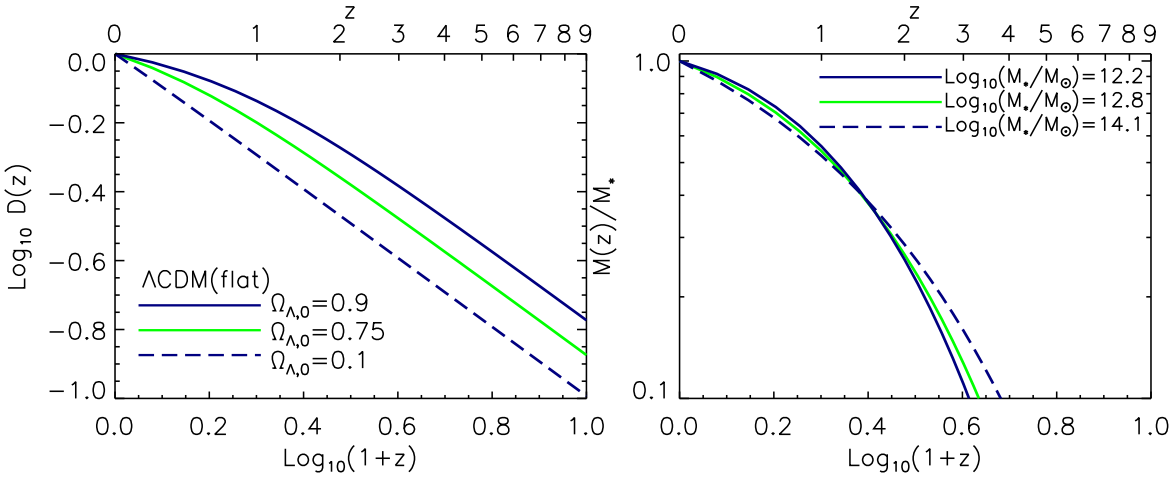

Figure 2.7: Growth rate factor (left-panel) and halo MAHs (right panels) calculated assuming $n_s = 1$, $\sigma_8 = 0.9$, $h = 0.7$ and $\Omega_{m,0} = 1 - \Omega_{\Lambda,0}$ (flat).

(v) Density parameter of matter. To analyse how the matter content in the universe changes the halo MAH, we assume $n_s = 1$, $\sigma_8 = 0.9$, $h = 0.7$, $\Omega_{\Lambda,0} = 0$ (the same result holds for $\Omega_{\Lambda,0} > 0$ in a open/close universe) and $\Omega_{m,0}$ ranging from 0.1 to 10. We find that increasing $\Omega_{m,0}$ increases $\sigma(M)$ (at fixed halo mass), and that as a result the halo MAH flattens and halos collapse earlier.

2.4 Summary

In this chapter we have demonstrated how halo mass histories are determined by the initial power spectrum of density fluctuations and the growth factor. We have found that the halo mass history can be well described by an exponential, $M(z) \sim e^{\beta z}$ (as suggested by Wechsler et al. 2002) in the high-redshift regime, but that the accretion slows to a power law at low redshift, $M(z) \sim (1+z)^{\alpha}$, because the growth of density perturbations is halted in the dark energy dominated era due to the accelerated expansion of the Universe.

We have derived an analytic mass history model based on EPS formalism, in which the parameters α and β are related to the power spectrum and depend on cosmology. We have found very good agreement between the halo mass histories predicted by our analytic model and published fits to simulation results. The reader may find a step-by-step description on how to implement the model in Appendix A, §A.1, as well as numerical routines online[iv].

In the following chapter we explore the relation between the structure of the inner dark matter halo and halo mass history using a suite of cosmological simulations. We

[iv] Available at *https://bitbucket.org/astroduff/commah*.

derive a semi-analytic model for halo mass history that combines analytic relations for the concentration and formation time with fits to simulations, to relate halo structure to the mass accretion history. In Chapter 4 we combine the semi-analytic model of halo mass history from Chapter 3 with the analytic model described in this chapter to predict the concentration-mass relation and its dependence on cosmology.

3

On the power spectrum, halo accretion history and density profile relation

This chapter explores the relation between the structure and mass accretion histories of dark matter halos.

Halo formation can be described as an 'inside out' process, where a strongly bound core collapses, followed by the gradual addition of material at the cosmological accretion rate. Through this process, halos acquire a nearly universal density profile that can be described by the NFW profile (Navarro et al. 1996, see also Chapter 1, §1.2.3). It is then generally believed that the halo MAH determines the 'universal' density profile. In this chapter we explore the relation between halo MAH and density profile. Using a suit of cosmological simulations, we find that the formation time, defined as the time when the virial mass of the main progenitor equals the mass enclosed within the scale radius, correlates strongly with concentration (as also found by Ludlow et al. 2013). We derive a semi-analytic model for halo MAH, that has the functional form $M(z) = M_0(1+z)^{\alpha}e^{\beta z}$, and the parameters α and β depend on the halo concentration. We then combine this model for the halo MAH with the analytic model derived in Chapter 2 and establish the physical link between halo concentration and the initial density perturbation field. Finally, we provide fitting formulas for the halo MAH, a step-by-step description on how to implement the semi-analytic MAH model in Appendix A, as well as numerical routines online[i].

[i] Available at http://astro.physics.unimelb.edu.au/Research/Public-Data-Releases/COMMAH

3.1 Introduction

To date, the origin of the universal shape of the halo density profile is still a topic of open debate. In the last decade many different types of arguments have been suggested. One common explanation is that the density profile results from a relaxation mechanism that produces equilibrium and is largely independent of the initial conditions and merger history (Navarro et al. 1997). On the other hand, it has also been suggested that the shape of the halo profile may be related to the shape of the matter power spectrum (Nusser & Sheth 1999). But more recently, Wang & Abel (2007) used simulations of Hot Dark Matter cosmologies to show that halos forming at the cutoff scale of the power spectrum have radial profiles that are fit by the NFW form just as well as CDM halos are at comparable resolution.

In addition to these efforts, many works have shown that the halo MAH plays an important rol in determining the halo density profile (e.g. Bullock et al. 2001; Eke et al. 2001; Wechsler et al. 2002; Zhao et al. 2003; Tasitsiomi et al. 2004; Ludlow et al. 2013). The argument is as follows. During hierarchical growth, halos form through mergers with smaller structures and accretion from the intergalactic medium. Most mergers are minor (with smaller satellite halos) and do not alter the structure of the inner halo. Major mergers (mergers between halos of comparable mass) can bring material to the centre, but they are found not to play a pivotal role in modifying the internal mass distribution (Wang & Abel 2007). Halo formation can therefore be described as an inside out process, where a strongly bound core collapses, producing an inner profile of $\rho(r) \propto r^{-1}$, followed by the gradual addition of material at the cosmological accretion rate, producing an outer profile of $\rho(r) \propto r^{-3}$ (Lu et al. 2006). The point in time when the core collapses determines the scale radius, r_{-2} (radius where $\rho(r_{-2}) \propto r^{-2}$), and so the concentration of the dark matter halo. Low-mass halos are generally more concentrated because they assembled earlier, when the Universe was denser, than high-mass halos.

Therefore, since NFW profile is determined by the halo MAH, it is then expected that halos should also follow a universal MAH profile (Dekel et al. 2003; Manrique et al. 2003; Sheth & Tormen 2004; Dalal et al. 2010; Salvador-Solé et al. 2012; Giocoli et al. 2012). This universal accretion history was recently illustrated by Ludlow et al. (2013), who showed that the halo MAHs, if scaled to certain values, follow the NFW profile. This was done by comparing the mass accretion history, expressed in terms of the critical density of the Universe, $M(\rho_{\rm crit}(z))$, with the NFW density profile, expressed in units of enclosed mass and mean density within r, $M(\langle\rho\rangle(< r))$ at $z = 0$, in a mass-density plane.

In this chapter we aim to provide a model that links the halo MAH with the halo concentration, a parameter that fully describes the internal structure of dark matter halos.

By doing so, we will gain insight into the origin of the NFW profile and its connection with the halo MAH. We also aim to find a physical explanation for the known correlation between the linear *rms* fluctuation of the density field, σ, and halo concentration.

This chapter is organized as follows. We briefly introduce the simulations used in this work in §3.2, where we explain how we calculated the merger history trees and discuss the necessary numerical convergence conditions (readers unfamiliar with numerical simulations are encouraged to first read §1.2.2 from Chapter 1). Then we provide a model for the halo MAH, which we refer to as the *semi-analytic model*. This semi-analytic model is described in §3.3, along with an analysis of the formation time definition. For this model we use the empirical McBride et al. (2009) formula. This functional form was motivated by the analytical analysis from Chapter 2, but the correlation between its two-parameters (α and β) is calibrated using numerical simulations. As a result, the semi-analytic model combines analytic relations with fits to simulations, to relate halo structure to the MAH. In §3.4.1 we show how the semi-analytic model for the halo MAH depends on cosmology and the adopted definition for halo mass. In §3.5 we provide a detailed comparison between the semi-analytic halo MAH model and the analytic model presented in Chapter 2. The parameters in this analytic model depend on the linear power spectrum and halo mass, whereas in the semi-analytic model the parameters depend on concentration and halo mass. We therefore combine the two models to establish the physical relation between the linear power spectrum and halo concentration. We expand on this relation in the following chapter (Chapter 4), where we predict the evolution of the concentration-mass relation and its dependence on cosmology. Finally, we provide a summary of formulae and discuss our main findings in §3.7.

3.2 Simulations

In this work we use a set of cosmological hydrodynamical simulations (the REF model) along with a set of dark matter only (DMONLY) simulations from the OWLS project (Schaye et al. 2010). These simulations were run with an extended version of the N-Body Tree-PM, smoothed particle hydrodynamics (SPH) code Gadget3 (last described in Springel et al. 2005). In order to assess the effects of the finite resolution and box size on our results, most simulations were run using the same physical model (DMONLY or REF) but different box sizes (ranging from $25\,h^{-1}$Mpc to $400\,h^{-1}$Mpc) and particle numbers (ranging from 128^3 to 512^3). The main numerical parameters of the runs are listed in Table 1. The simulation names contain strings of the form LxxxNyyy, where xxx is the simulation box size in comoving h^{-1}Mpc, and yyy is the cube root of the number of particles per species (dark matter or baryonic). For more details on the simulations we refer the reader to the Introduction §1.2.2.

To investigate the dependence on the adopted cosmological parameters, we include an

Table 3.1: List of simulations. From left-to-right the columns show: simulation identifier; comoving box size; number of dark matter particles (there are equally many baryonic particles); initial baryonic particle mass; dark matter particle mass; comoving (Plummer-equivalent) gravitational softening; maximum physical softening; final redshift.

Simulation	L (h^{-1}Mpc)	N	$m_{\rm b}$ ($h^{-1}{\rm M}_\odot$)	$m_{\rm dm}$ ($h^{-1}{\rm M}_\odot$)	$\varepsilon_{\rm com}$ (h^{-1}kpc)	$\varepsilon_{\rm prop}$ (h^{-1}kpc)	$z_{\rm end}$
Reference model (REF)							
L100N512	100	512^3	8.7×10^7	4.1×10^8	7.81	2.00	0
L100N256	100	256^3	6.9×10^8	3.2×10^9	15.62	4.00	0
L100N128	100	128^3	5.5×10^9	2.6×10^{10}	31.25	8.00	0
L050N512	50	512^3	1.1×10^7	5.1×10^7	3.91	1.00	0
L025N512	25	512^3	1.4×10^6	6.3×10^6	1.95	0.50	2
L025N256	25	256^3	1.1×10^7	5.1×10^7	3.91	1.00	2
L025N128	25	128^3	8.7×10^7	4.1×10^8	7.81	2.00	2
Dark matter only model (DMONLY)							
L400N512	400	512^3	–	3.4×10^{10}	31.25	8.00	0
L200N512	200	512^3	–	3.2×10^9	15.62	4.00	0
L100N512	100	512^3	–	5.3×10^8	7.81	2.00	0
L050N512	50	512^3	–	6.1×10^7	3.91	1.00	0
L025N512	25	512^3	–	8.3×10^6	2.00	0.50	0

extra set of five dark matter only simulations ($100\,h^{-1}$Mpc box size and 512^3 dark matter particles) which assume values for the cosmological parameters derived from the different releases of Wilkinson Microwave Anisotropy Probe (WMAP) and the *Planck* mission. Table 3.2 lists the sets of cosmological parameters adopted in the different simulations.

The first step towards studying the mass assembly history of halos is to identify gravitationally bound structures and build halo merger trees. We begin by selecting the largest halo in each FoF group (Davis et al. 1985) (i.e. the main subhalo of FoF groups that is not embedded inside larger halos). Halo virial masses and radii are determined using a spherical overdensity routine within the SUBFIND algorithm (Springel et al. 2001; Dolag et al. 2009) centred on the main subhalo of FoF halos. Therefore, we define halo masses as all matter within the radius r_{200} for which the mean internal density is 200 times the critical density. Throughout this work, we study the accretion history of the largest halos in each FoF group. Subhalos, defined as bound structures that reside within the virial radius of the largest 'host' halo, show distinct mass histories. The structures of subhalos are strongly affected by the potential of their host halos, as seen for example in the cessation of mass accretion onto subhalos residing in dense environments (see Wang et al. 2009 or Lacerna & Padilla 2011). Consequently, the masses of subhalos do not follow the mass history of their host halos.

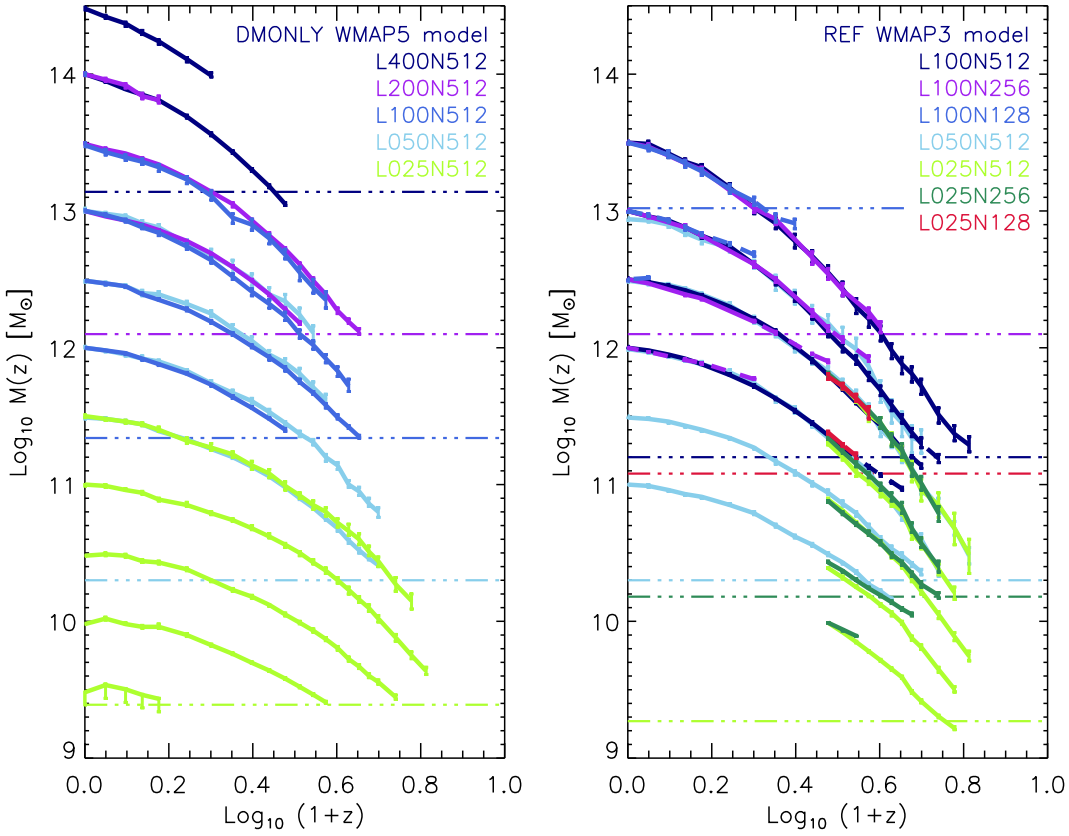

Figure 3.1: Median halo MAH as a function of redshift from simulations DMONLY (left panel) and REF (right panel) for halos in eleven and seven different mass bins, respectively. The curves show the median value, and the 1σ error bars are determined by bootstrap resampling the halos from the merger tree at a given output redshift. The different colour lines show the MAHs of halos from different simulations. We find that a necessary condition for a halo to be defined, and mass histories to converge, is that halos should have a minimum of 300 dark matter particles. The horizontal dashed dotted lines show the $300 \times m_{\rm dm}$ limit for the simulation that matches the colour, where $m_{\rm dm}$ is the respective dark matter particle mass. When following a merger tree from a given halo sample, some halos are discarded when unresolved. This introduces a bias and so an upturn in the median mass history. Therefore, mass history curves are stopped once fewer than 50% of the original sample of halos are considered. Simulations in the REF model with $25\,h^{-1}$Mpc comoving box size have a final redshift of $z = 2$, therefore the halos mass histories begin at this redshift.

Halo MAHs are obtained from the simulation outputs by building halo merger trees. The standard procedure to build a halo merger tree is to link each progenitor halo with a unique 'descendant' halo in the subsequent output (see e.g. Fakhouri et al. 2010). In this work however we do not build halo merger trees using the same method, instead *we build halo mass histories*, we identify the main branches of the halo merger trees and compute the halo mass growth.

We define the halo MAH as the mass of the most massive halo (main progenitor) along the main branch of the merger tree. The merger trees of the largest halos are then built as follows. First, at each output redshift (snapshot), we select 'resolved' halos that contain more than 300 dark matter particles. We refer to these resolved halos as descendants. We then link each descendant with a unique 'progenitor' at the previous output redshift. This is nontrivial due to halo fragmentation: subhalos of a progenitor halo may have descendants that reside in more than one halo. The fragmentation can be spurious or due to a physical unbinding event. To correct this, we link the descendant to the progenitor that contains the majority of the descendant's 25 most bound dark matter particles. Therefore, the main progenitor of a given dark matter halo is found by tracing backwards in time to the most massive halo along the main branch of its merger tree. The different mass histories are calculated by following the merger trees of a given sample of halos. At each redshift the mass histories are computed by calculating the median mass value, determined by bootstrap resampling the halos, from the merger tree. Along with the median value, the 1σ confidence interval is recorded. This is the traditional procedure to compute halo MAHs. Some studies define the halo MAH as the descendant most massive progenitor (e.g. van den Bosch 2002b; McBride et al. 2009; Fakhouri et al. 2010; Behroozi et al. 2013), or similarly, as the progenitor that contributes most to its mass (e.g. Wechsler et al. 2002; Zhao et al. 2003).

While analysing the merger trees from the simulations, we look for a numerical resolution criterion under which MAHs converge numerically. We begin by investigating the minimum number of particles halos must contain so that the merger trees lead to accurate numerical convergence. We find a necessary minimum limit of 300 dark matter particles, which corresponds to a minimum dark matter halo mass of $M_{\rm halo} \sim 2.3 \times 10^{11} {\rm M}_\odot$ in the $100\,h^{-1}$Mpc box, $M_{\rm halo} \sim 2.6 \times 10^{10} {\rm M}_\odot$ in the $50\,h^{-1}$Mpc box, and $M_{\rm halo} \sim 3.4 \times 10^{9} {\rm M}_\odot$ in the $25\,h^{-1}$Mpc box.

In a merger tree, when a progenitor halo contains less than 300 dark matter particles, it is considered unresolved and discarded from the analysis. As a result, the number of halos in the sample that contribute to the median value of the mass history decreases with increasing redshift. Removing unresolved halos from the merger tree can introduce a bias. When the number of halos that are discarded drops to more than 50% of the original sample, a spurious upturn in the median mass history occurs. To avoid this bias,

Table 3.2: Cosmological parameters.

Simulation	$\Omega_{\mathrm{m},0}$	$\Omega_{\Lambda,0}$	h	σ_8	n_s
DMONLY_WMAP1	0.25	0.75	0.73	0.90	1.000
DMONLY_WMAP3	0.238	0.762	0.73	0.74	0.951
DMONLY_WMAP5	0.258	0.742	0.72	0.796	0.963
DMONLY_WMAP9	0.282	0.718	0.70	0.817	0.964
DMONLY_*Planck*1	0.317	0.683	0.67	0.834	0.962

the median MAH curve is only built out to the redshift at which less than 50% of the original number of halos contributes to the median mass value.

Fig. 3.1 shows the effects of changing the resolution for the dark matter only and reference simulations. We first vary the box size while keeping the number of particles fixed (left panel). Then we vary the number of particles while keeping the box size fixed (right panel). The left panel (right panel) of Fig. 3.1 shows the mass history as a function of redshift for halos in eleven (seven) different mass bins for the DMONLY (REF) simulation. All halo masses are binned in equally spaced logarithmic bins of size $\Delta \log_{10} M = 0.5$. The MAHs are computed by calculating the median value of the halo masses from the merger tree at a given output redshift, the error bars correspond to 1σ confidence intervals. The different coloured lines indicate the different simulations from which the halo mass histories were calculated. The horizontal dash-dotted lines in the panels show the $300 \times m_{\mathrm{dm}}$ limit for the simulation that matches the colour. Halos in the simulation with masses lower than this value are unresolved, and hence their MAHs are not considered. The MAHs from halos whose main progenitors have masses lower than $10^{12}\mathrm{M}_\odot$ at $z = 0$ were computed from simulations with $50\,h^{-1}$Mpc and $25\,h^{-1}$Mpc comoving box sizes. In the right panel, the mass history curves obtained from the REF simulation with a $25\,h^{-1}$Mpc comoving box size have a final redshift of $z = 2$. Therefore, these halo MAHs begin at this redshift.

3.3 Semi-analytic model for the halo mass history

In the following subsections we study dark matter halo properties and provide a semi-analytic model that relates halo structure to the MAH. We begin with the NFW density profile and derive an analytic expression for the mean inner density, $\langle\rho\rangle(< r_{-2})$, within the scale radius, r_{-2}. We then define the formation redshift, and use the simulations to find the relation between $\langle\rho\rangle(< r_{-2})$ and the critical density of the universe at the formation redshift. We discuss the universality of the MAH curve and show how we can obtain a semi-analytic model for the MAH that depends on only one parameter (as expected from our EPS analysis presented in Chater 2). We then calibrate this single parameter fit using our numerical simulations. Finally, we show how the semi-analytic model for halo MAH depends on cosmology and halo mass definition.

3.3.1 Density profile

An important property of a population of halos is their spherically averaged density profile. Based on N-body simulations, Navarro et al. (1997) found that the density profiles of CDM halos can be approximated by a two parameter profile,

$$\rho(r) = \frac{\rho_{\rm crit}\delta_c}{(r/r_{-2})(1+r/r_{-2})^2}, \tag{3.1}$$

where r is the radius, r_{-2} is the characteristic radius at which the logarithmic density slope is -2, $\rho_{\rm crit}(z) = 3H^2(z)/8\pi G$ is the critical density of the universe and δ_c is a dimensionless parameter related to the concentration c by

$$\delta_c = \frac{200}{3}\frac{c^3}{[\ln(1+c) - c/(1+c)]}, \tag{3.2}$$

which applies at fixed virial mass and where c is defined as $c = r_{200}/r_{-2}$, and r_{200} is the virial radius. A halo is often defined so that the mean density $\langle\rho\rangle(< r)$ within the halo virial radius r_Δ is a factor Δ times the critical density of the universe at redshift z. Unfortunately, not all authors adopt the same definition, and readers should be aware of the difference in halo formation history and internal structure when different mass definitions are adopted (see Duffy et al. 2008; Diemer et al. 2013). We explore this in §3.4.1.2 to which the reader is referred to for further details. Throughout this work we use $\Delta = 200$. We denote $M_z \equiv M_{200}(z)$ as the halo mass as a function of redshift, $M_r \equiv M(< r)$ as the halo mass profile within radius r at $z = 0$, r_{200} as the virial radius at $z = 0$ and c as the concentration at $z = 0$. Note that the halo mass is defined as all matter within the radius r_{200} (see Table 3.3 for reference).

The NFW profile is characterized by a logarithmic slope that steepens gradually from the centre outwards, and can be fully specified by the concentration parameter and halo mass. Simulations have shown that these two parameters are correlated, with the average concentration of a halo being a weakly decreasing function of mass (e.g. NFW; Bullock et al. 2001; Eke et al. 2001; Shaw et al. 2006; Neto et al. 2007; Duffy et al. 2008; Macciò et al. 2008; Dutton & Macciò 2014; Diemer & Kravtsov 2015). Therefore, the NFW density profile can be described by a single free parameter, the concentration, which can be related to virial mass. The following relation was found by Duffy et al. (2008) from a large set of $N-$body simulations with the WMAP5 cosmology,

$$c = 6.67(M_{200}/2\times10^{12}h^{-1}{\rm M}_\odot)^{-0.092}, \tag{3.3}$$

for halos in equilibrium (relaxed). Throughout this thesis the $c-M$ relation refers to the relation between concentration and halo mass.

Table 3.3: Notation reference. Unless specified otherwise, quantities are evaluated at $z = 0$.

Notation	Definition
M_{200}	$M_r(r_{200})$, total halo mass
r_{200}	Virial radius
r_{-2}	NFW scale radius
c	NFW concentration
M_z	$M(z)$, total halo mass at redshift z
$M_r(r)$	$M(< r)$, mass enclosed within r
x	r/r_{200}
$\langle\rho\rangle(< r_{-2})$	Mean density within r_{-2}
$M_r(r_{-2})$	$M(< r_{-2})$, enclosed mass within r_{-2}
z_{-2}	Formation redshift, when M_z equals $M_r(r_{-2})$
$\rho_{\rm crit,0}$	Critical density today
$\rho_{\rm crit}(z)$	Critical density at redshift z
$\rho_{\rm m}(z)$	Mean background density at redshift z

The NFW profile can be expressed in terms of the mean internal density

$$\langle\rho\rangle(< r) = \frac{M_r(r)}{(4\pi/3)r^3} = \frac{200}{x^3}\frac{Y(cx)}{Y(c)}\rho_{\rm crit}, \tag{3.4}$$

where x is defined as $x = r/r_{200}$ and $Y(u) = \ln(1+u) - u/(1+u)$. From this last equation we can verify that at $r = r_{200}$, $x = 1$ and $\langle\rho\rangle(< r_{200}) = 200\rho_{\rm crit}$.

Evaluating $\langle\rho\rangle(< r)$ at $r = r_{-2}$, we obtain

$$\langle\rho\rangle(< r_{-2}) = \frac{M_r(r_{-2})}{(4\pi/3)r_{-2}^3} = 200c^3\frac{Y(1)}{Y(c)}\rho_{\rm crit}. \tag{3.5}$$

From this last expression we see that for a fixed redshift the mean inner density $\langle\rho\rangle(< r_{-2})$ can be written in terms of c. By substituting eq. (3.3) into (3.5), we can obtain $\langle\rho\rangle(< r_{-2})$ as a function of virial mass. Finally, we can compute the mass enclosed within r_{-2}. From eq. (3.5) we obtain

$$M_r(r_{-2}) = M_{200}\frac{Y(1)}{Y(c)}, \tag{3.6}$$

where we used $M_{200} = (4\pi/3)r_{200}^3 200\rho_{\rm crit}$.

Although the NFW profile is widely used and generally describes halo density profiles with high accuracy, it is worth noting that high resolution numerical simulations have shown that the spherically averaged density profiles of dark matter halos have small but systematic deviations from the NFW form (e.g. Navarro et al. 2004; Hayashi & White 2008; Navarro et al. 2010; Ludlow et al. 2010; Diemer & Kravtsov 2014). While there is no clear understanding of what breaks the structural similarity among halos, an alternative parametrization is sometimes used (the Einasto profile), which assumes the

logarithmic slope to be a simple power law of radius, $d\ln\rho/d\ln r \propto (r/r_{-2})^{\alpha}$ (Einasto 1965). Recently, Ludlow et al. (2013) investigated the relation between the accretion history and mass profile of cold dark matter halos. They found that halos whose mass profiles deviate from NFW and are better approximated by Einasto profiles also have accretion histories that deviate from the NFW shape in a similar way. However, they found the residuals from the systematic deviations from the NFW shape to be smaller than 10%. We therefore only consider the NFW halo density profile in this work.

3.3.2 Formation redshift

Navarro et al. (1997) showed that the characteristic overdensity ($\delta_{\rm c}$) is closely related to formation time ($z_{\rm f}$), which they defined as the time when half the mass of the main progenitor was first contained in progenitors larger than some fraction f of the mass of the halo at $z = 0$. They found that the 'natural' relation $\delta_{\rm c} \propto \Omega_{\rm m,0}(1+z_{\rm f})^3$ describes how the overdensity of halos varies with their formation redshift. Subsequent investigations have used N-body simulations and empirical models to explore the relation between concentration and formation history in more detail (Wechsler et al. 2002; Zhao et al. 2003, 2009). A good definition of formation time that relates concentration to halo mass history was found to be the time when the main progenitor switches from a period of fast growth to one of slow growth. This is based on the observation that halos that have experienced a recent major merger typically have relatively low concentrations, while halos that have experienced a longer phase of relatively quiescent growth have larger concentrations. Moreover, Zhao et al. (2009) argue that halo concentration can be very well determined at the time the main progenitor of the halo has 4% of its final mass.

The various formation time definitions each provide accurate fits to the simulations on which they are based and, at a given halo mass, show reasonably small scatter. However, our goal is to adopt a formation time definition that has a natural justification without invoking arbitrary mass fractions. To this end, we go back to the idea that halos are formed inside out, and consider the formation time to be defined as the time when the initial bound core forms. We follow Ludlow et al. (2013) and define the formation redshift as the time at which the mass of the main progenitor equals the mass enclosed within the scale radius at $z = 0$, yielding

$$z_{-2} = z[M_z = M_r(r_{-2})]. \tag{3.7}$$

From now on we denote the formation redshift by z_{-2}. Interestingly, Ludlow et al. (2013) found that at this formation redshift, the critical density of the universe is directly proportional to the mean density within the scale radius of halos at $z = 0$: $\rho_{\rm crit}(z_{-2}) \propto \langle\rho\rangle(< r_{-2})$. A possible interpretation of this relation is that the central structure of a

dark matter halo (contained within r_{-2}) is established through collapse and later accretion and mergers increase the mass and size of the halo without adding much material to its inner regions, thus increasing the halo virial radius while leaving the scale radius and its inner density ($\langle\rho\rangle(< r_{-2})$) almost unchanged (Huss et al. 1999; Wang & Abel 2007).

3.3.3 Relation between halo formation time and concentration

We now study the relation between $\rho_{\rm crit}(z_{-2})$ and $\langle\rho\rangle(< r_{-2})$ using a set of DMONLY cosmological simulations from the OWLS project that adopt the WMAP-5 cosmology. We begin by considering two samples of halos. Our complete sample contains all halos that satisfy our resolution criteria while our 'relaxed' sample retains only those halos for which the separation between the most bound particle and the centre of mass of the Friends-of-Friends (FoF) halo is smaller than $0.07R_{\rm vir}$, where $R_{\rm vir}$ is the radius for which the mean internal density is Δ (as given by Bryan & Norman 1998) times the critical density. Neto et al. (2007) found that this simple criterion resulted in the removal of the vast majority of unrelaxed halos and as such we do not use their additional criteria. At $z = 0$, our complete sample contains 2831 halos, while our relaxed sample is reduced to 2387 (84%).

To compute the mean inner density within the scale radius, $\langle\rho\rangle(< r_{-2})$, we need to fit the NFW density profile to each individual halo. We begin by fitting NFW profiles to all halos at $z = 0$ that contain at least 10^4 dark matter particles within the virial radius. For each halo, all particles in the range $-1.25 \leq \log_{10}(r/r_{200}) \leq 0$, where r_{200} is the virial radius, are binned radially in equally spaced logarithmic bins of size $\Delta \log_{10} r = 0.078$. The density profile is then fit to these bins by performing a least square minimization of the difference between the logarithmic densities of the model and the data, using equal weighting. The corresponding mean enclosed mass, $M_r(r_{-2})$, and mean inner density at r_{-2}, $\langle\rho\rangle(< r_{-2})$, are found by interpolating along the cumulative mass and density profiles (measured while fitting the NFW profile) from $r = 0$ to $r_{-2} = r_{200}/c$, where c is the concentration from the NFW fit. Then we follow the mass history of these halos through the snapshots, and interpolate to determine the redshift z_{-2} at which $M_z = M_r(r_{-2})$.

We perform a least-square minimization of the quantity $\Delta^2 = \frac{1}{N}\sum_{i=1}^{N}[\langle\rho_i\rangle(\rho_{{\rm crit},i}) - f(\rho_{{\rm crit},i}, A)]$, to obtain the constant of proportionality, A. We find $\langle\rho\rangle(< r_{-2}) = (900 \pm 50)\rho_{\rm crit}(z_{-2})$ for the relaxed sample, and $\langle\rho\rangle(< r_{-2}) = (854 \pm 47)\rho_{\rm crit}(z_{-2})$ for the complete sample. The 1σ error was obtained from the least squares fit. For comparison, Ludlow et al. (2014) found a constant value of 853 for their relaxed sample of halos and the WMAP-1 cosmology. Fig. 3.2 shows the relation between the mean inner density at $z = 0$ and the critical density of the universe at redshift z_{-2} for various DMONLY

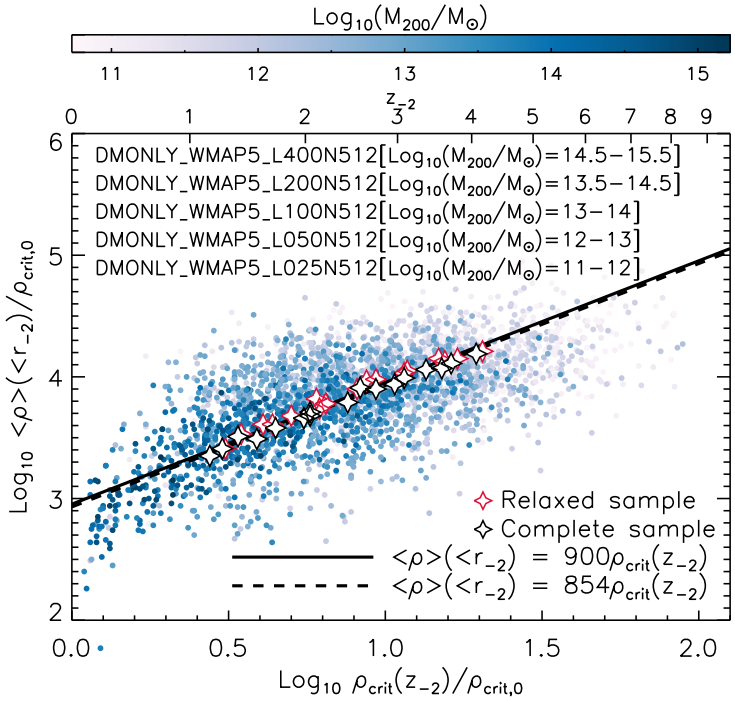

Figure 3.2: Relation between the mean density within the NFW scale radius at $z = 0$ and the critical density of the universe at the halo formation redshift, z_{-2}, for DMONLY simulations from the OWLS project. The simulations assume the WMAP-5 cosmological parameters and have box sizes of $400\,h^{-1}$Mpc, $200\,h^{-1}$Mpc, $100\,h^{-1}$Mpc, $50\,h^{-1}$Mpc and $25\,h^{-1}$Mpc. The black solid line indicates the relation shown in eq. (3.8), which only depends on cosmology through the mass-concentration relation. The black (red) star symbols show the mean values of the complete (relaxed) sample in logarithmic mass bins of width $\delta \log_{10} M = 0.2$. The black dashed and solid lines show the relations found by fitting the data of the complete and relaxed samples, respectively. The filled circles correspond to values of individual halos and are coloured by mass according to the colour bar at the top of the plot.

simulations. Each dot in this panel corresponds to an individual halo from the complete sample in the DMONLY_WMAP5 simulations that have box sizes of $400\,h^{-1}$Mpc, $200\,h^{-1}$Mpc, $100\,h^{-1}$Mpc, $50\,h^{-1}$Mpc and $25\,h^{-1}$Mpc. The $\langle\rho\rangle(< r_{-2})$-$\rho_{\rm crit}(z_{-2})$ values are coloured by mass according to the colour bar at the top of the plot. The black (red) star symbols show the mean values of the complete (relaxed) sample in logarithmic mass bins of width $\delta \log_{10} M = 0.2$. As expected when unrelaxed halos are discarded (e.g. Duffy et al. 2008), the relaxed sample contains on average slightly higher concentrations (by a factor of 1.16) and so higher formation times (by a factor of 1.1).

In Fig. 3.2 the best-fit to the data points from the relaxed sample is shown by the solid line, while the dashed line is the fit to the complete sample. The $\rho_{\rm crit}(z_{-2}) - \langle\rho\rangle(< r_{-2})$ correlation clearly shows that halos that collapsed earlier have denser cores at $z = 0$. Using the mean inner density-critical density relation for the relaxed sample,

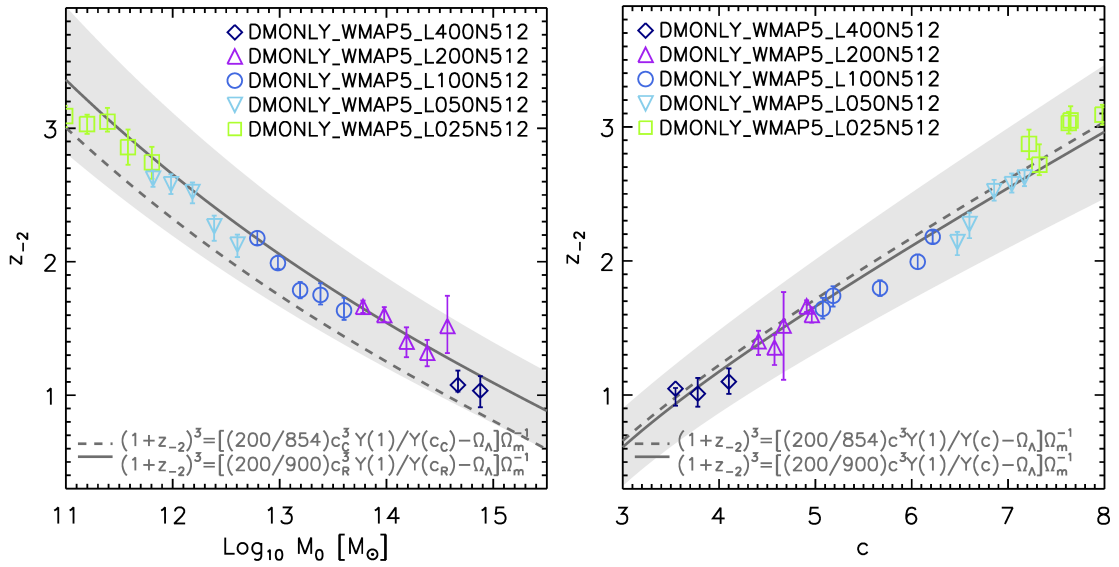

Figure 3.3: Relation between formation redshift and $z = 0$ halo mass, M_{200} (left panel), and between formation redshift, z_{-2}, and halo concentration, c (right panel). The different symbols correspond to the median values of the relaxed sample and the error bars to 1σ confidence limits. The solid line in the right panel is not a fit but a prediction of the $z_{-2} - c$ relation for relaxed halos given by eq. (3.9). Similarly, the dashed line is the prediction for the complete sample of halos, assuming a constant of proportionality between $\langle\rho\rangle(< r_{-2})$ and $\rho_{\rm crit}$ of 854, rather than the value of 900 used for the relaxed sample. The grey area shows the scatter in z_{-2} plotted in Fig. 3.7 (right panel). Similarly, the solid line in the left panel is a prediction of the $z_{-2} - M_{200}$ relation given by eqs. (3.9) and (3.3). The dashed line also shows the $z_{-2} - M_{200}$ relation assuming $\langle\rho\rangle(< r_{-2}) = 854\rho_{\rm crit}$ and the concentration-mass relation calculated using the complete sample.

$$\langle\rho\rangle(< r_{-2}) \quad = \quad (900 \pm 50)\rho_{\rm crit}(z_{-2}). \tag{3.8}$$

We replace $\langle\rho\rangle(< r_{-2})$ by eq. (3.5) and calculate the dependence of formation redshift on concentration,

$$(1 + z_{-2})^3 \quad = \quad \frac{200}{900}\frac{c^3}{\Omega_{\rm m,0}}\frac{Y(1)}{Y(c)} - \frac{\Omega_{\Lambda,0}}{\Omega_{\rm m,0}}. \tag{3.9}$$

This last expression is tested in Fig. 3.3 (left panel) where we plot the median formation redshift as a function of concentration using different symbols for different sets of simulations from the OWLS project. The symbols correspond to the median values of the relaxed sample, and the error bars indicate 1σ confidence limits. The grey solid line shows the $z_{-2} - c$ relation given by eq. (3.9), whereas the grey dashed line shows the same

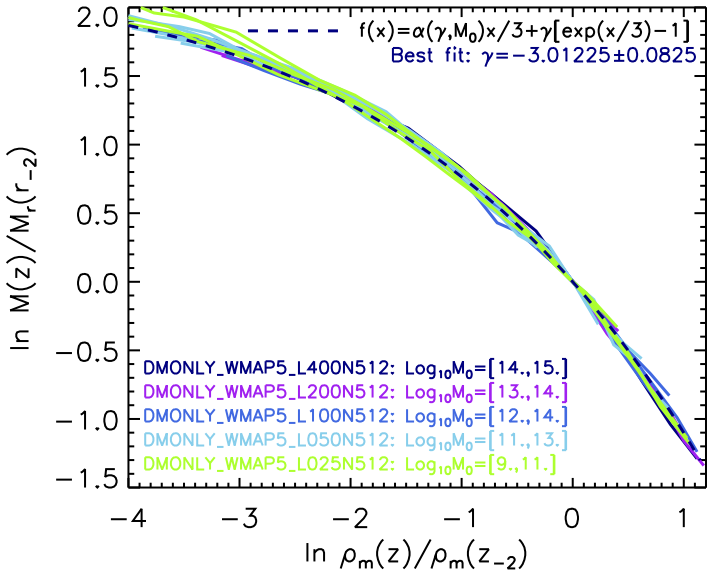

Figure 3.4: Mass histories of halos, obtained from different DMONLY_WMAP5 simulations, as indicated by the colours. The bottom left legends indicate the halo mass range at $z = 0$, selected from each simulation. For example, we selected halos between $10^9 - 10^{11}\mathrm{M}_\odot$ from the DMONLY_WMAP5_L025N512 simulation, divided them in equally spaced logarithmic bins of size $\Delta \log_{10} M = 0.2$, and calculated the median mass histories. The different curves show the median mass history of the main progenitors, normalized to the median enclosed mass of the main progenitors at $z = 0$, $M_r(r_{-2})$. The mass histories are plotted as a function of the mean background density of the universe, scaled to the mean background density at z_{-2}. The blue dashed line is a fit of expression (3.17) to the different mass history curves. The median value of the only adjustable parameter, γ, is indicated in the top-right part of the plot.

relation assuming a constant of 854 instead of 900 (as obtained for the complete sample). Similarly, using the Duffy et al. (2008) $c - M$ relation we obtain the formation redshift as a function of halo mass at $z = 0$ (right panel of Fig. 3.3). It is important to note that the $z_{-2} - c$ and $z_{-2} - M$ relations are valid in the halo mass range $10^{11} - 10^{15}\, h^{-1}\mathrm{M}_\odot$, at lower masses the $c - M$ relation begins to deviate from power-laws (Ludlow et al. 2014).

In §3.4 we analyse the scatter in the formation time−mass relation and show that it correlates with the scatter in the $c - M$ relation. Thus concluding that the scatter in formation time determines the scatter in the concentration. Also, we investigate how the scatter in halo MAH drives the scatter in formation time.

3.3.4 The mass history

Fig. 3.4 shows the MAH of halos in different mass bins as a function of the mean background density. The MAHs are scaled to $M_r(r_{-2})$ and the mean background densities are scaled to $\rho_\mathrm{m}(z_{-2}) = \rho_{\mathrm{crit},0}\Omega_{\mathrm{m},0}(1+z_{-2})^3$. The figure shows that all halo mass histories look alike. This is in agreement with Ludlow et al. (2013), who found that the MAH, expressed in terms of the critical density of the Universe, $M(\rho_\mathrm{crit}(z))$, resembles that of

the enclosed NFW density profile, $M(\langle\rho\rangle(< r))$. It is still not clear why the similarity in the shapes between $M(\rho_{\rm crit}(z))$ and $M(\langle\rho\rangle(< r))$, but it suggests that the physically motivated form $M(z) = M_0(1+z)^\alpha e^{\beta z}$, which is a result of rapid growth in the matter dominated epoch followed by a slow growth in the dark energy epoch, produces the double power-law of the NFW profile (see e.g. Lu et al. 2006). We use this feature to find a functional form that describes this unique universal curve in order to obtain an empirical expression for the mass accretion history at all redshifts and halo masses.

We are motivated by the EPS analysis of halo MAH presented in Chapter 2, where we showed through analytic calculations that the halo MAH is described by a power-law times an exponential,

$$M(z) = M_0(1+z)^\alpha e^{\beta z}, \tag{3.10}$$

and that the parameters α and β are connected via the power spectrum of density fluctuations. In this chapter however, we aim to relate halo structure to the MAH. We therefore first determine the correlation between the parameters α and β and concentration. To this end, we first find the $\alpha-\beta$ relation that results from the formation redshift definition discussed in the previous section. Thus, we evaluate the halo mass at z_{-2},

$$M_z(z_{-2}) = M_r(r_{-2}) \quad = \quad M_z(z=0)(1+z_{-2})^\alpha e^{\beta z_{-2}}. \tag{3.11}$$

Taking the natural logarithm, we obtain,

$$\ln\left(\frac{M_r(r_{-2})}{M_z(z=0)}\right) \quad = \quad \alpha\ln(1+z_{-2}) + \beta z_{-2}, \tag{3.12}$$

and hence

$$\alpha \quad = \quad \frac{\ln\left(\frac{M_r(r_{-2})}{M_z(z=0)}\right) - \beta z_{-2}}{\ln(1+z_{-2})}. \tag{3.13}$$

From this last equation we see that α can be written as a function of β, $M_r(r_{-2})$, $M_z(z=0)$ and z_{-2}. However, as $M_r(r_{-2})$ is a function of concentration and virial mass (see eq. 3.6), we can write α in terms of β, concentration and z_{-2},

$$\alpha \quad = \quad \frac{\ln(Y(1)/Y(c)) - \beta z_{-2}}{\ln(1+z_{-2})}. \tag{3.14}$$

The next step is to find an expression for β by fitting eq. (3.10) to all the data points

plotted in Fig. 3.4. We then express $M(z)$ (eq. 3.10) as a function of the mean background density. To do this, we replace $(1+z)$ by $(\rho_{\rm m}(z)/\rho_{\rm crit,0}/\Omega_{\rm m,0})^{1/3}$ and divide both sides of eq. (3.10) by $M_r(r_{-2})$, yielding

$$\frac{M_z(z)}{M_r(r_{-2})} = \frac{M_z(z=0)}{M_r(r_{-2})}\left(\frac{\rho_{\rm m}(z)}{\Omega_{\rm m,0}\rho_{\rm crit,0}}\right)^{\alpha/3}\exp\left(\beta\left[\left(\frac{\rho_{\rm m}(z)}{\Omega_{\rm m,0}\rho_{\rm crit,0}}\right)^{1/3}-1\right]\right).$$

Multiplying both denominators and numerators by $\rho_{\rm m}(z_{-2})$, we get, after rearranging,

$$\begin{aligned}\frac{M_z(z)}{M_r(r_{-2})} &= \frac{M_z(z=0)}{M_r(r_{-2})}\left(\frac{\rho_{\rm m}(z_{-2})}{\Omega_{\rm m,0}\rho_{\rm crit,0}}\right)^{\alpha/3}\left(\frac{\rho_{\rm m}(z)}{\rho_{\rm m}(z_{-2})}\right)^{\alpha/3}\exp\left(\beta\left[\left(\frac{\rho_{\rm m}(z_{-2})}{\Omega_{\rm m,0}\rho_{\rm crit,0}}\right)^{1/3}-1\right]\right)\\ &\times \exp\left(\gamma\left[\left(\frac{\rho_{\rm m}(z)}{\rho_{\rm m}(z_{-2})}\right)^{1/3}-1\right]\right), \qquad (3.15)\end{aligned}$$

where, we have defined $\gamma \equiv \beta(\rho_{\rm m}(z_{-2})/\Omega_{\rm m,0}/\rho_{\rm crit,0})^{1/3} = \beta(1+z_{-2})$. The term $\frac{M_z(z=0)}{M_r(r_{-2})} \times \left(\frac{\rho_{\rm m}(z_{-2})}{\Omega_{\rm m,0}\rho_{\rm crit,0}}\right)^{\alpha/3}\exp\left(\beta\left[\left(\frac{\rho_{\rm m}(z_{-2})}{\Omega_{\rm m,0}\rho_{\rm crit,0}}\right)^{1/3}-1\right]\right)$ in eq. (3.15) is equal to unity, which can be seen by replacing $\rho_{\rm m}(z_{-2})/\Omega_{\rm m,0}\rho_{\rm crit,0} = (1+z_{-2})^3$ and comparing with eq. (3.11). Hence eq. (3.15) becomes

$$\frac{M_z(z)}{M_r(r_{-2})} = \left(\frac{\rho_{\rm m}(z)}{\rho_{\rm m}(z_{-2})}\right)^{\alpha/3}\exp\left(\gamma\left[\left(\frac{\rho_{\rm m}(z)}{\rho_{\rm m}(z_{-2})}\right)^{1/3}-1\right]\right). \qquad (3.16)$$

Thus, based on eq. (3.16), the functional form to fit the MAHs from the simulations can be written as

$$f(\tilde{z},\gamma) = \alpha(z_{-2},c,\gamma)\tilde{z}/3+\gamma(e^{\tilde{z}/3}-1), \qquad (3.17)$$

where $f(\tilde{z},\gamma) = \ln\left(\frac{M_z(z)}{M_r(r_{-2})}\right)$ and $\tilde{z} = \ln\left[\frac{\rho_{\rm m}(z)}{\rho_{\rm m}(z_{-2})}\right]$. From eq. (3.14) we see that the parameter α is a function of z_{-2}, c and γ,

$$\alpha = \frac{\ln(Y(1)/Y(c)) - \gamma z_{-2}/(1+z_{-2})}{\ln(1+z_{-2})}. \qquad (3.18)$$

Therefore, γ is now the only adjustable parameter. We perform a χ^2-like minimization of the quantity

$$\Delta^2 = \frac{1}{N}\sum_{i=1}^{N}[\log_{10}(M_z(z_i)/M_r(r_{-2})) - f(\tilde{z}_i, \gamma)]^2, \tag{3.19}$$

and find the value of γ that best fits all halo MAHs. The sum in the χ^2-like minimization is over the N available simulation output redshifts at $z_i (i = 1, N)$, with $\tilde{z}_i = \ln\left[\frac{\rho_{\rm crit,0}\Omega_{\rm m,0}(1+z_i)^3}{\rho_{\rm m}(z_{-2})}\right]$.

Fig. 3.4 shows halo MAHs (with $M_z(z)$ scaled to $M_r(r_{-2})$) for our complete halo sample as a function of the mean background density [$\rho_{\rm m}(z)$ scaled to $\rho_{\rm m}(z_{-2})$]. The blue dashed line is the fit of expression (3.17) to all the mass history curves included in the figure. Here, the only adjustable parameter is γ. We obtained $\gamma = -3.01 \pm 0.08$, yielding

$$\beta = -3(\rho_{\rm m}(z_{-2})/\Omega_{\rm m,0}/\rho_{\rm crit,0})^{-1/3} = -3/(1 + z_{-2}). \tag{3.20}$$

Fig. 3.4 shows that the halo MAHs have a characteristic shape consisting of a rapid growth at early times, followed by a slower growth at late times. The change from rapid to slow accretion corresponds to the transition between the mass and dark energy dominated eras (see Chapter 3), and depends on the parameter β in the exponential (as can be seen from eq. 3.10). The dependence of β on the formation redshift is given in eq. (3.20), which shows that a more recent formation time, and hence a larger halo mass, results in a larger value of β, and so a steeper halo MAH curve. This last point can be seen in Fig. 3.5 from the MAHs of halos in different mass bins (coloured lines shown in the panels). The panel on the left shows the MAH curves from the DMONLY simulation outputs (coloured lines in the background), and the MAHs predicted by eqs. (3.10), (3.14) and (3.20) (red dashed lines). From these panels we see that, (i) the MAH formula works remarkably well when compared with the simulation, and (ii) the larger the mass of a halo at $z = 0$, the steeper the MAH curve at early times. In contrast, the MAH of low-mass halos is essentially governed by the power law at late times.

The halo MAHs plotted in Fig. 3.5 come from the complete sample of halos (relaxed and unrelaxed). We found no significant difference in mass growth when only relaxed halos are considered. We therefore conclude that the fact that a halo is unrelaxed at a particular redshift does not affect its halo MAH, provided the $c - M$ relation fit from the relaxed halo sample is used. This is an interesting result because while deriving the semi-analytic model of halo mass history, we assumed that the halo density profile is described by the NFW profile at all times. Therefore while the NFW is not a good fit for the density profile of unrelaxed halos (Neto et al. 2007), our semi-analytic model (based on NFW profiles) is a good fit all halos (relaxed and unrelaxed).

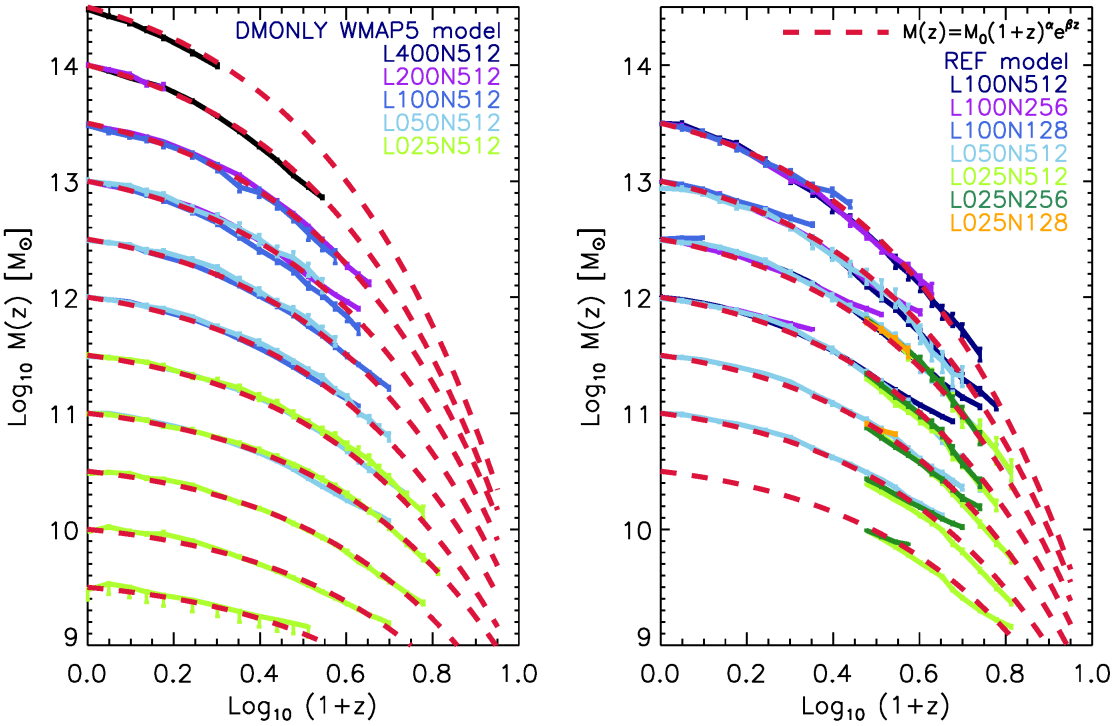

Figure 3.5: MAHs of all halos from simulations DMONLY_WMAP5 (left panel) and REF (right panel). Halo masses are binned in equally spaced logarithmic bins of size $\Delta \log_{10} M = 0.5$. The mass histories are computed by calculating the median value of the halo masses from the merger tree at a given output redshift, the error bars correspond to 1σ. The different colour lines show the MAHs of halos from different simulations as indicated in the legends, while the red dashed curves correspond to the MAHs predicted by eqs. (3.10), (3.18) and (3.20).

The right panel of Fig. 3.5 shows halo MAHs from the REF hydrodynamical simulations. We compute the halo mass as the total mass (gas and dark matter) within the virial radius (r_{200}). We find that the inclusion of baryons steepens the mass histories at high redshift, therefore the best description of $M(z)$ is given by eqs. (3.10), (3.14), (3.20), and the $c - M$ relation from the complete sample of halos, $c = 5.74(M/2 \times 10^{12} h^{-1}\mathrm{M}_{\odot})^{-0.097}$.

3.3.5 The mass accretion rate

The accretion of gas and dark matter from the intergalactic medium is a fundamental driver of both, the evolution of dark matter halos and the formation of galaxies within them. For that reason, developing a theoretical model for the mass accretion rate is the basis for analytic and semi-analytic models that study galaxy formation and evolution. In this section we look for a suitable expression for the mean accretion rate of dark matter halos. To achieve this, we take the derivative of the semi-analytic MAH model, $M(z)$, given by eq. (3.10) with respect to time and replace $\mathrm{d}z/\mathrm{d}t$ by $-H_0[\Omega_{\mathrm{m},0}(1+z)^5 + \Omega_{\Lambda,0}(1+z)^2]^{1/2}$, yielding

$$\frac{\mathrm{d}M}{\mathrm{d}t} = 71.6\,\mathrm{M}_\odot\mathrm{yr}^{-1}\,M_{12}h_{0.7}[-\alpha-\beta(1+z)][\Omega_{\mathrm{m},0}(1+z)^3+\Omega_{\Lambda,0}]^{1/2}, \quad (3.21)$$

where $h_{0.7} = h/0.7$, $M_{12} = M/10^{12}\mathrm{M}_\odot$ and α and β are given by eqs. (3.14) and (3.20), respectively. As shown in the previous section, the parameters α and β depend on halo mass (through the formation time dependence). We find that this mass dependence is crucial for obtaining an accurate description for the mass history (as shown in Fig. 3.5). However, the factor of 2 (3) change for α (β) between halo masses of 10^8 and $10^{14}\mathrm{M}_\odot$ is not significant when calculating the accretion rate. Therefore, we provide an approximation for the *mean* mass accretion rate as a function of redshift and halo mass, by averaging α and β over halo mass, yielding $\langle\alpha\rangle$=0.24, $\langle\beta\rangle$=-0.75, and

$$\langle\frac{\mathrm{d}M}{\mathrm{d}t}\rangle = 71.6\,\mathrm{M}_\odot\mathrm{yr}^{-1}\,M_{12}h_{0.7}[-0.24+0.75(1+z)][\Omega_{\mathrm{m},0}(1+z)^3+\Omega_{\Lambda,0}]^{1/2} \quad (3.22)$$

Fig. 3.6 (top panel) compares the median dark matter accretion rate for different halo masses as a function of redshift (solid lines) to the mean accretion rate given by eq. (3.22) (grey dashed lines). From the merger trees of the main halos, we compute the mass growth rate of a halo of a given mass. We do this by following the main branch of the tree and computing $\mathrm{d}M/\mathrm{d}t = (M(z_1) - M(z_2))/\Delta t$, where $z_1 < z_2$, $M(z_1)$ is the descendant halo mass at time t and $M(z_2)$ is the most massive progenitor at time $t - \Delta t$. The median value of $\mathrm{d}M/\mathrm{d}t$ for the complete set of resolved halos is then plotted for different constant halo masses. We find very good agreement between the simulation outputs and the analytic estimate given by eq. (3.22). As expected, the larger the halo mass, the larger the dark matter accretion rate.

3.3.5.1 Baryonic accretion

Next, we estimate the gas accretion rate and compare our model with similar fitting formulae proposed by Fakhouri et al. (2010) and Dekel & Krumholz (2013). The bottom panel of Fig. 3.6 shows the gas accretion rate as a function redshift for a range of halo masses ($\log_{10} M/\mathrm{M}_\odot = 11.2 - 12.8$). The grey circles correspond to the gas accretion rate measured in REF_L100N512. In this case we compute the total mass growth ($M = M_{\mathrm{gas}} + M_{\mathrm{DM}}$) from the merger trees, and then estimate the gas accretion rate by multiplying the total accretion rate by the universal baryon fraction $f_b = \Omega_{\mathrm{b},0}/\Omega_{\mathrm{m},0}$. The green solid line corresponds to our gas accretion rate model (given by $\Omega_{\mathrm{b},0}/\Omega_{\mathrm{m},0}$ times eq. 3.22). The blue dot-dashed line is the gas accretion rate proposed by Dekel & Krumholz (2013) ($\mathrm{d}M_\mathrm{b}/\mathrm{d}t = 30\mathrm{M}_\odot\mathrm{yr}^{-1} f_b M_{12}(1+z)^{5/2}$), who derived the baryonic inflow onto a halo

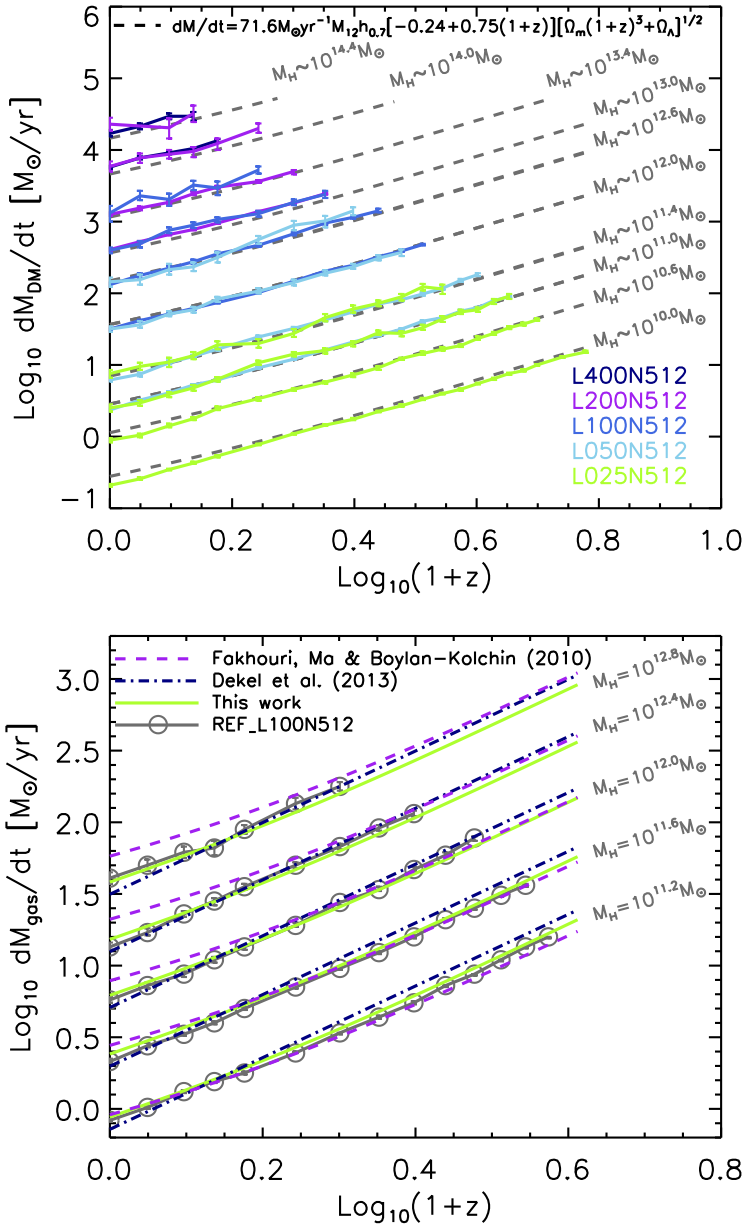

Figure 3.6: Mean accretion rate of dark matter (top panel) and gas (bottom panel) as a function of redshift for different halo masses. *Top panel*: the accretion rate obtained from the simulation outputs up to the redshift where the halo mass histories are converged. Grey dashed lines show the accretion rate estimated using eq. (3.22). *Bottom panel*: gas accretion rate obtained from the REF_L100N512 simulation (grey circles), from $\Omega_{\rm b,0}/\Omega_{\rm m,0}$ times eq. (3.22) (green solid line), and from various fitting formulae taken from the literature.

$\mathrm{d}M_\mathrm{b}/\mathrm{d}t$ from the averaged growth rate of halo mass through mergers and smooth accretion based on the EPS theory of gravitational clustering (Neistein et al. 2006; Neistein & Dekel 2008). Lastly, we compare our model with the accretion rate formula from Fakhouri et al. (2010) ($\mathrm{d}M_\mathrm{b}/\mathrm{d}t = 46.1\mathrm{M}_\odot\mathrm{yr}^{-1} f_\mathrm{b} M_{12}^{1.1}(1+1.11z)(\Omega_{\mathrm{m},0}(1+z)^3+\Omega_{\Lambda,0})^{1/2}$), plotted as the purple dashed line. Fakhouri et al. (2010) constructed merger trees of dark matter halos and quantified their merger rates and mass growth rate using the Millennium and Millennium II simulations. They defined the halo mass as the sum of the masses of all subhalos within a FoF halo. We see that our accretion rate model is in excellent agreement with the formulae from Fakhouri et al. (2010) and Dekel & Krumholz (2013). We find that the Fakhouri et al. (2010) formula generally overpredicts the gas accretion rate in the low-redshift regime (e.g. it overpredicts it by a factor of 1.4 at $z = 0$ for a $10^{12}\mathrm{M}_\odot$ mass halo). The Dekel & Krumholz (2013) formula underpredicts (overpredicts) the gas accretion rate in the low- (high-) redshift regime for halos with masses larger (lower) than $10^{12}\mathrm{M}_\odot$.

3.4 Analysis of scatter

3.4.0.1 Scatter in formation times and concentrations

We now analyse the scatter in the formation time−mass relation and show it relates to the scatter in the concentration−mass relation. In §3.3.3 we show that the formation time is related to halo concentration through the $\langle\rho\rangle(<r_{-2}) - \rho_\mathrm{crit}(z_{-2})$ relation plotted in Fig. 3.2. Through first order error propagation, we look for the corresponding scatter in the formation time,

$$900\rho_\mathrm{crit}(z_{-2}) = \langle\rho\rangle(<r_{-2}), \tag{3.23}$$

$$900\delta(\rho_\mathrm{crit}(z_{-2})) = \delta(\langle\rho\rangle(<r_{-2})), \tag{3.24}$$

$$\frac{900}{200}\delta[\Omega_m(1+z_{-2})^3+\Omega_\Lambda] = \delta\left(c^3\frac{Y(1)}{Y(c)}\right), \tag{3.25}$$

$$3\Omega_m(1+z_{-2})^2 z_{-2}\left(\frac{\delta z_{-2}}{z_{-2}}\right) = \frac{\langle\rho\rangle(<r_{-2})}{900\rho_0}\left(\frac{\delta c}{c}\right)\left(3-\frac{c^2}{(1+c)^2}\frac{1}{Y(c)}\right), \tag{3.26}$$

where we used $\delta(c^3/Y(c)) = 3c^2\delta c/Y(c) - c^4\delta c/[Y(c)^2(1+c)^2]$. Eq. (3.26) relates the scatter in formation time ($|\delta z_{-2}|/z_{-2}$) to the scatter in the concentration ($|\delta c|/c$).

The grey shaded areas in the panels in Fig. 3.3 show the scatter in z_{-2}, while the panels in Fig. 3.7 show the scatter in the $c-M$ relation (left panel) and in the $z_{-2}-M$ relation (right panel). The grey contours in Fig. 3.7 enclose 68% of the distribution while

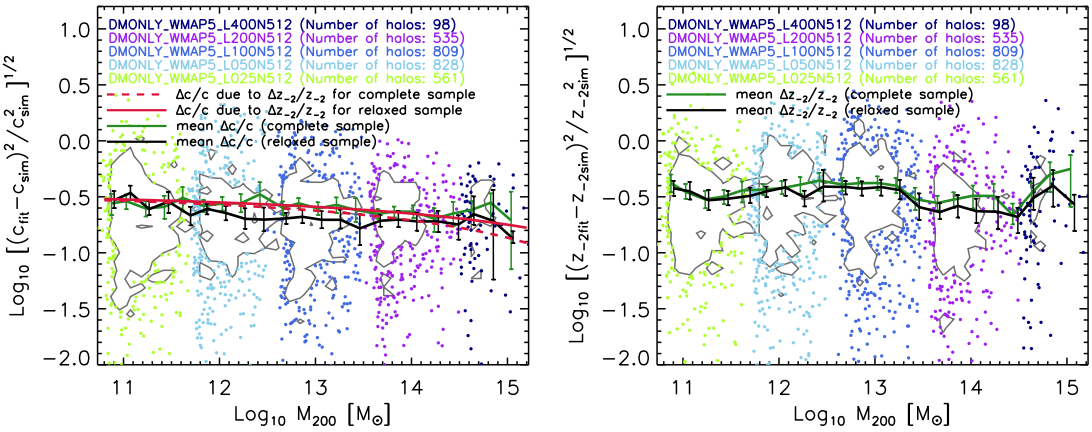

Figure 3.7: Scatter in the concentration−mass relation (left panel) and the formation redshift−mass relation (right panel). *Left panel*: Y-axis shows the difference between the concentration predicted by Duffy et al. (2008) (see eq. 3.3) and the actual concentration from the simulation output. This difference is divided by the concentration from the simulation output and plotted against virial halo mass. The different colours of the points indicate that the concentration outputs were obtained from DMONLY_WMAP5 simulations with different box sizes. The grey contours enclose 68% of the distribution while the individual points show the remaining 32%. The black (green) solid line shows the mean relative scatter in the concentration-mass relation per halo mass bin of the relaxed (complete) sample. The red dashed line is an analytic estimate of the scatter obtained by propagating the scatter in the formation redshift−mass relation to the concentration−mass relation (eq. 3.26). *Right panel*: same as the left panel but the scatter is obtained from the difference in the formation redshift predicted from eq. (3.9) and the simulation output. The black (green) solid line shows the median value in the scatter as a function of mass of the relaxed (complete) sample.

the individual points show the remaining 32%. The black (green) solid line shows the mean scatter in the formation time per halo mass bin for the relaxed (complete) sample. The presence of unrelaxed halos does not have any significant effect on either the scatter in the formation time or the mass histories. The average scatter in formation time is $\langle|\delta z_{-2}|/z_{-2}\rangle = 0.324$ ($\langle|\delta z_{-2}|/z_{-2}\rangle = 0.356$) for the relaxed (complete) sample.

The left panel of Fig. 3.7 shows that the average scatter in the concentration−mass relation is $\langle|\delta c|/c\rangle = 0.257$ for the full sample and $\langle|\delta c|/c\rangle = 0.218$ for the relaxed sample. In agreement with previous work (see e.g. Neto et al. 2007), the scatter in the concentration of the relaxed halo sample is lower than the scatter of the full sample. The extra scatter in the full sample is produced by the deviation of the density profiles from the NFW form for halos experiencing ongoing mergers and for artificially linked halos.

Assuming $\langle|\delta z_{-2}|/z_{-2}\rangle = 0.324$, $\langle|\delta c|/c\rangle$ can be obtained as a function of halo mass by applying eq. (3.26). This analytic estimate is plotted in the left panel for the relaxed sample (red dashed line). We find very good agreement between the scatter in concentration from eq. (3.26), and the median value plotted in black for the relaxed sample, and in green for the complete sample. Therefore, we conclude that the scatter in formation time

determines the scatter in the concentration. However, at higher masses and redshifts the fraction of relaxed halos decreases (e.g. Ludlow et al. 2012) and it has been found that the concentration-mass relation of the complete halo sample exhibits a strong flattening and upturn (Klypin et al. 2011; Prada et al. 2012). As a result, at high masses and redshifts the scatter in the concentration will probably depend on other variables besides the scatter in formation time.

In the following subsection we find that the scatter in the accretion history determines the scatter in the formation time.

3.4.0.2 Scatter in halo mass histories

In this section we analyse the scatter found when computing mass histories from the simulation outputs. We analytically estimate the scatter in the mass history due to both the scatter in the concentration and formation times (estimated in §3.4.0.1). We then compare this to the scatter obtained from the simulation outputs.

To compute the scatter in the mass history we perform a first order error propagation in $M(z)$ (eq. 3.10),

$$\delta M(z)/M(z) = \delta\alpha \ln(1+z) + z\delta\beta, \tag{3.27}$$

where $\delta\alpha$ ($\delta\beta$) is the scatter in α (β) due to the scatter in c and z_{-2}. From eq. (3.14) we first compute $\delta\alpha$ due to the scatter in z_{-2},

$$\begin{aligned}
\delta\alpha &= \delta(-\beta z_{-2}/\ln(1+z_{-2})) \\
&= \frac{-z_{-2}\delta\beta - \beta\delta z_{-2}}{\ln(1+z_{-2})} - \beta z_{-2}\delta[\ln(1+z_{-2})]^{-1} \\
&= -\frac{z_{-2}\beta(1+z_{-2}\ln(1+z_{-2}))}{(1+z_{-2})\ln(1+z_{-2})}\left(\frac{\delta z_{-2}}{z_{-2}}\right),
\end{aligned} \tag{3.28}$$

where in the last line we used $\delta\beta = \frac{-\beta z_{-2}}{(1+z_{-2})}\left(\frac{\delta z_{-2}}{z_{-2}}\right)$, which follows from eq. (3.20). Similarly, we calculate the scatter in α due to the scatter in c,

$$\begin{aligned}
\delta\alpha &= \delta(\ln(Y(1)/Y(c))/\ln(1+z_{-2}) \\
&= -\frac{\delta Y(c)}{Y(c)}\frac{1}{\ln(1+z_{-2})} \\
&= -\frac{c^2}{(1+c)^2 Y(c)\ln(1+z_{-2})}\left(\frac{\delta c}{c}\right),
\end{aligned} \tag{3.29}$$

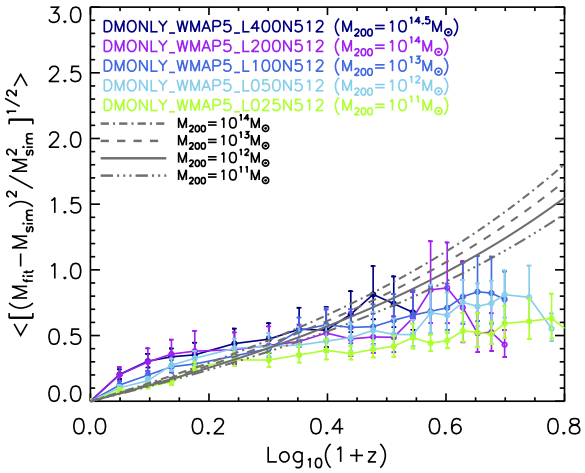

Figure 3.8: Mean scatter in the halo mass history against redshift for different halo masses M_{200}. The y-axis shows the mean value of the difference between the mass history ($M_{\rm fit}$) predicted by eqs. (3.10), (3.14) and (3.20), and the mass history ($M_{\rm sim}$) from the simulation output. The difference is divided by the $M_{\rm sim}$ from the simulation output. The different coloured lines correspond to the different DMONLY_WMAP5 simulations as indicated in the legends. The grey lines show the analytic estimates of the mass history curves given by eqs. (3.27), (3.28) and (3.29).

where in the last step we used $\delta Y(c) = \frac{c^2}{(1+c)^2}\left(\frac{\delta c}{c}\right)$. Finally, we substitute $\delta\beta = \frac{-\beta z_{-2}}{(1+z_{-2})}\left(\frac{\delta z_{-2}}{z_{-2}}\right)$ and eqs. (3.28) and (3.29) into eq. (3.27). From §3.4.0.1 we adopt the average scatter in z_{-2} and c for the complete sample, that is $\langle|\delta c|/c\rangle = 0.25$ and $\langle\delta z_{-2}/z_{-2}\rangle = 0.35$, and compute $\langle|\delta M(z)/M(z)|\rangle$ as a function of redshift. Fig. 3.8 shows the scatter measured from the simulation outputs (coloured lines) and from the analytic estimates (grey dashed lines). The different coloured lines correspond to the median values of the scatter from simulations with different box sizes. We calculate these by averaging the difference between the mass history predicted by eqs. (3.10), (3.14) and (3.20) (for a given halo with mass M_{200} at $z = 0$), and each $M(z)$ given by the merger trees from the complete halo sample. The good agreement we find between the median values of the scatter and the analytic estimate seems to indicate that the scatter in the concentration comes from the scatter in the formation time, which in turn comes from the scatter in the halo mass history. However, despite our efforts this is not entirely certain, since there are large deviation at $z > 2$ and therefore other variables may modify the scatter in the mean density profile of halos. We plan to analyse the origin of the scatter in more detail in future work.

3.4.1 Dependence on cosmology and mass definition

We have developed a semi-analytic model that relates the inner structure of a halo at redshift zero to its mass history. The model adopts the NFW profile, computes the

mean inner density within the scale radius, and relates this to the critical density of the universe at the redshift where the halo virial mass equals the mass enclosed within r_{-2}. This relation enables us to find the formation redshift - halo mass dependence and to derive a one parameter model for the halo mass history. In this section we consider the effects of cosmology and mass definition on the semi-analytic model.

3.4.1.1 Cosmology dependence

The adopted cosmological parameters affect the mean inner halo densities, concentrations, formation redshifts and halo MAHs. In this section we investigate how the parameters in the semi-analytic model (such as formation redshift) change with cosmology. To do so, we have run a set of dark matter only simulations with different cosmologies. Table 3.2 lists the sets of cosmological parameters adopted by the different simulations. Specifically, we assume values for the cosmological parameters derived from measurements of the cosmic microwave background by the WMAP and the *Planck* missions (Spergel et al. 2003, 2007; Komatsu et al. 2009; Hinshaw et al. 2013; Planck Collaboration et al. 2014).

In Chapter 2 we investigate how the variation of the cosmological parameters $n_{\rm s}$, σ_8, h, $\Omega_{\rm m,0}$ and $\Omega_{\Lambda,0}$ impact on the halo MAH using the analytic model. We find that in universes with larger σ_8 and $\Omega_{\rm m,0}$ halos form earlier. Similarly, in universes with larger $n_{\rm s}$ low-mass halos form earlier, but high-mass halos form later. Finally, in universes with larger values of h, the growth of structures is faster and the formation of halos is earlier.

It has been shown that halos that formed earlier are more concentrated (Navarro et al. 1997; Bullock et al. 2001; Eke et al. 2001; Kuhlen et al. 2005; Macciò et al. 2007; Neto et al. 2007). Macciò et al. (2008) explored the dependence of halo concentration on the adopted cosmological model for field galaxies. They found that dwarf-scale field halos are more concentrated by a factor of 1.55 in WMAP1 compared to WMAP3, and by a factor of 1.29 for cluster-sized halos. This clearly reflects the fact that halos of a fixed $z = 0$ mass assemble earlier in a universe with higher $\Omega_{\rm m,0}$, higher σ_8 and/or higher n_s.

The halo formation redshift can be related to the power at the corresponding mass scale, and therefore depends on both σ_8 and n_s. The parameter σ_8 sets the power at a scale of $8\,h^{-1}$Mpc, which corresponds to a mass of about $1.53 \times 10^{14} h^{-1} {\rm M}_\odot (\Omega_{\rm m,0}/\Omega_{\rm m,0,WMAP5})$, and a wavenumber of k_8. This last quantity is given by the relation $M = (4\pi\rho_{\rm m}/3)(2\pi/k)^3$. For a power-law spectrum $P(k) \propto k^n$, the variance can be written as $\sigma^2(k)/\sigma_8^2 = (k/k_8)^{n+3}$. Therefore, the change in σ between WMAP5 and WMAP1 for a given halo mass that corresponds to a wavenumber k is

$$\frac{\sigma_{\rm WMAP1}(k)}{\sigma_{\rm WMAP5}(k)} = \frac{\sigma_{8,\rm WMAP1}}{\sigma_{8,\rm WMAP5}} \left(\frac{k}{k_8}\right)^{(n_{\rm s,WMAP1} - n_{\rm s,WMAP5})/2} . \tag{3.30}$$

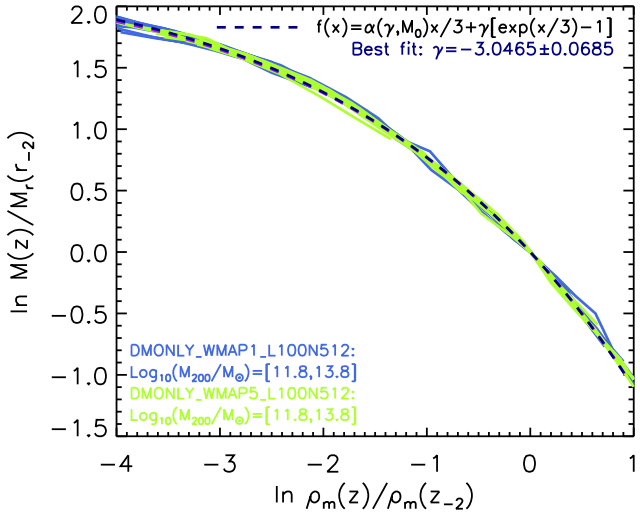

Figure 3.9: MAHs of halos, obtained from simulations with the WMAP1 cosmology (DMONLY_WMAP1_L100N512, blue solid lines) and the WMAP5 cosmology (DMONLY_WMAP5_L100N512, green solid lines). The curves show the median mass history of the main progenitors, normalized to the median enclosed mass, $M_r(r_{-2})$, of the main progenitors at $z = 0$. The MAHs are plotted as a function of the mean background density of the universe, scaled to the mean background density at z_{-2}. The blue dashed line is a fit of expression (3.17) to the different mass history curves. The median value of the only adjustable parameter, γ, is indicated in the top-right part of the plot. We find that γ is insensitive to cosmology.

A halo mass of $10^{12}\mathrm{M}_\odot$ corresponds to a wavenumber of $k_{1.3} \sim 6k_8$. The total change in the mean power spectrum at this mass scale is $\frac{\sigma_{\rm WMAP1}(k_{1.3})}{\sigma_{\rm WMAP5}(k_{1.3})} = 1.27$. This is proportional to the change of the formation redshift,

$$(1 + z_{\rm f,WMAP1}) = 1.27(1 + z_{\rm f,WMAP5}). \tag{3.31}$$

Next, we test how this change affects the halo MAH. We haven shown that the MAH profile is well described by the expression $M(z) = M_z(z = 0)(1 + z)^\alpha e^{\beta z}$, where α and β both depend on the formation redshift. In the MAH model presented in §3.3.4 there are two best-fitting parameters that can be cosmology dependent. One is the constant value $A = 900$ in eq. (3.8) that relates the mean inner density to the critical density at z_{-2}, and the other is the constant value $\gamma = -3$ in eq. (3.20) that defines the β parameter.

To investigate the cosmology dependence of A, we analyse the $\langle\rho\rangle(< r_{-2}) - \rho_{\rm crit}(z_{-2})$ relation in the simulations with different cosmologies. We do the same as in §3.3.3. First we fit the NFW profile to dark matter halos to obtain c and r_{-2}, and calculate the cumulative mass, M_{-2}, and density, $\langle\rho\rangle(< r_{-2})$, from $r = 0$ to $r = r_{-2}$. Then we follow the halo MAHs through the snapshots and interpolate to calculate z_{-2}, the redshift for which $M(z)$ is equal to M_{-2}. Finally, we obtain the best-fit $\langle\rho\rangle(< r_{-2}) - \rho_{\rm crit}(z_{-2})$ relation. We find that the parameter $A_{\rm cosmo}$, where cosmo is WMAP1, WMAP3, WMAP5, WMAP9 or Planck, changes with cosmology. We show this in the top panel of Fig. 3.10. We find $A_{\rm WMAP1} = 787\pm52.25$, $A_{\rm WMAP3} = 850\pm39.60$, $A_{\rm WMAP5} = 903\pm48.63$,

$A_{\rm WMAP9} = 820 \pm 51.03$ and $A_{\rm Planck} = 798 \pm 43.73$. We do not find good agreement with Ludlow et al. (2013), who found $A_{\rm WMAP1} = 853$ for WMAP1 cosmology. This is due to the fact that we are only analyzing the $\langle\rho\rangle(< r_{-2}) - \rho_{\rm crit}(z_{-2})$ relation in the high-mass regime ($M = 10^{12.8} - 10^{13.8}{\rm M}_\odot$), due to the limitations of the box size ($L = 100\,h^{-1}$Mpc). With a more complete halo population, we may obtain better agreement. We conclude that the $A_{\rm cosmo}$ parameter depends on cosmology, at least for the halo mass ranges we are considering.

Next, we analyse how the change of the formation redshift due to cosmology affects β, defined as $\beta = -3/(1 + z_{\rm f})$. We find from Fig. 3.9 that the constant value, -3, is insensitive to cosmology. Fig. 3.9 shows the same analysis as Fig. 3.4, but for halo MAHs obtained from simulations with the WMAP1 and WMAP5 cosmology as indicated in the legends. We fit expression (3.17) to the mass history curves from different cosmologies and obtained the same adjustable parameter γ. We therefore conclude that $\gamma = -3$ is insensitive to cosmology.

If we then consider that the change in β between WMAP1 and WMAP5 is $\beta_{WMAP1} = -3/(1 + z_{\rm f,WMAP1}) = -3/1.27/(1 + z_{\rm f,WMAP5}) = \beta_{WMAP5}/1.27$, the change in the halo MAH between the WMAP5 and WMAP1 cosmologies, for a halo mass of $10^{12}{\rm M}_\odot$ at $z = 0$, corresponds to

$$\begin{aligned} \log_{10}\frac{M(z)_{\rm WMAP1}}{M(z)_{\rm WMAP5}} &= \log_{10} e^{(\beta_{\rm WMAP1} - \beta_{\rm WMAP5})z} \\ &\approx -0.12\beta_{\rm WMAP1} z, \\ &\approx 0.1z. \end{aligned} \tag{3.32}$$

In the last step we replaced $\beta_{\rm WMAP1}$ by $-3/(1 + z_{\rm f,WMAP1}) = -0.75$ for a $10^{12}{\rm M}_\odot$ halo. We obtained $z_{\rm f,WMAP1}$ from the $\langle\rho\rangle(< r_{-2}) - \rho_{\rm crit}(z_{-2})$ relation suitable for the WMAP1 cosmology (see top panel of Fig. 3.10) and the $c - M$ relation from Neto et al. (2007).

Next, we test the change in halo MAH. For example, if a halo had a mass of $10^{11.4}{\rm M}_\odot$ at $z = 2$ in the WMAP5 cosmology, it would have had a mass of $10^{11.6}{\rm M}_\odot$ in the WMAP1 cosmology. The value of σ_8 has a particularly large effect at high redshift, because structure formation proceeds faster in the WMAP1 cosmology, as shown by the above expression. This last point can also be seen in the two panels of Fig. 3.10. The top panel is the same as the right panel of Fig. 3.3, and shows the formation redshift, z_{-2}, as a function of halo mass (obtained from simulations with different cosmologies). We see that there are large differences between the WMAP5 and WMAP1 cosmologies due to the changes in σ_8 and n_s. Interestingly, there is only a small difference between the Planck and WMAP1 cosmologies (in agreement with Ludlow et al. 2014 and Dutton & Macciò 2014), and also between the Planck and WMAP9 cosmologies for which we

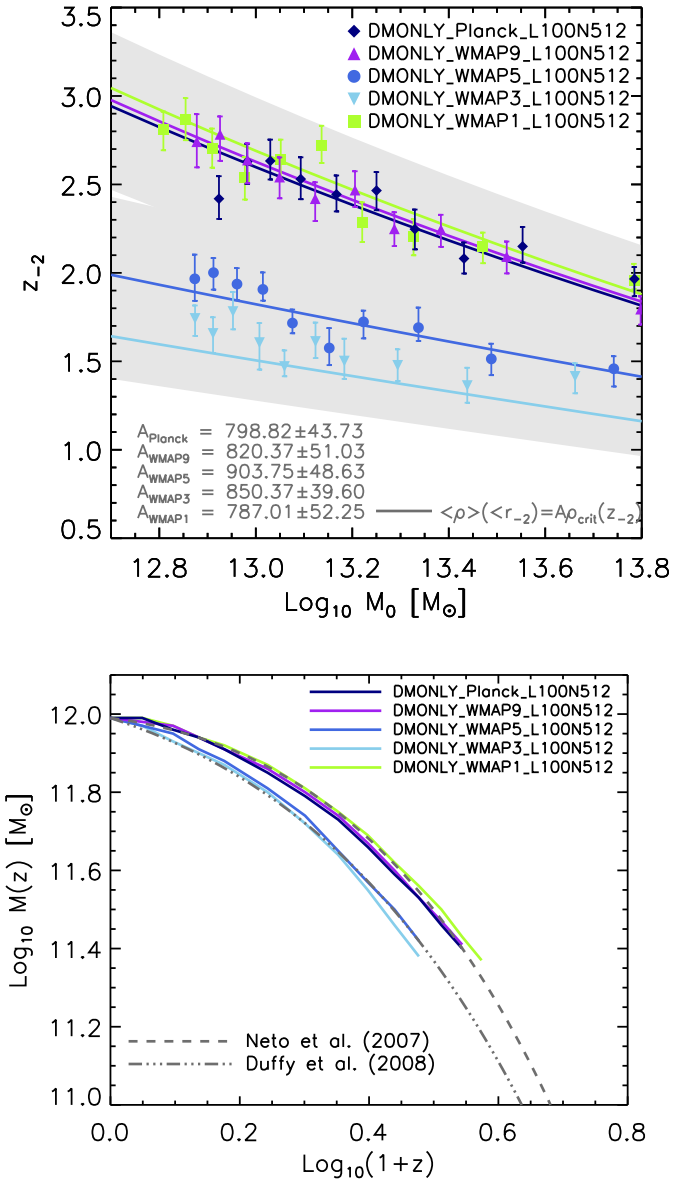

Figure 3.10: *Top panel*: Relation between formation redshift (z_{-2}) and halo mass at $z = 0$ (M_0). The different symbols correspond to median values, the error bars to 1σ confidence limits and the grey area to the scatter. These were computed from the dark matter only simulations that assumed a WMAP3 (light blue line), WMAP5 (blue line), WMAP1 (green line), WMAP9 (purple line) and Planck cosmology (dark blue line). The solid lines are not fits, but predictions of the $z_{-2} - M_{\rm halo}$ relation given by eq. (3.9). We also indicated the different values of the constant of proportionality A obtained by fitting the $\langle\rho_{-2}\rangle - \rho_{\rm crit}(z_{-2})$ relation. *Bottom panel*: halo mass history of a halo of $10^{12}{\rm M}_\odot$ at $z = 0$ from DMONLY simulations with different cosmologies. The grey curves show that as long as a suitable concentration-mass relation is assumed for the cosmology under consideration, eqs. (3.44), (3.45) and (3.46) give a good estimate of the mass history curve.

found $(1+z_{\rm f})_{\rm Planck} = 1.01(1+z_{\rm f})_{\rm WMAP9}$ for a $10^{12}{\rm M}_\odot$ halo. The bottom panel of Fig. 3.10 shows the mass history of $10^{12}{\rm M}_\odot$ halos at $z=0$ from DMONLY simulations with different cosmologies. As predicted, the change in mass history between the WMAP5 and WMAP1 cosmologies is $\log_{10}\frac{M(z)_{\rm WMAP1}}{M(z)_{\rm WMAP5}} \sim 0.1z$. While little difference is found between the WMAP9 and Planck ($\Delta M(z) \sim 10^{-3}z$).

We found that as long as a suitable $c-M$ relation and value for the A parameter are assumed for the cosmology being considered, eqs. (3.44), (3.45) and (3.46) provide a good estimate of the mass history curve. This can seen in the bottom panel of Fig. 3.10 by comparing the different halo MAHs. For the WMAP5 and WMAP3 cosmologies we assumed the $c-M$ relation found by Duffy et al. (2008), whereas we used the relation from Neto et al. (2007) for the other cosmologies. For a step-by-step description of how to use the mass history models (analytic and semi-analytic) that were presented in Chapter 2 and §3.3.4, respectively, see Appendix A.

3.4.1.2 Mass definition dependence

So far our calculations have been based on a halo mass defined as the mass of all matter within the radius r_{200} at which the mean internal density $\langle\rho\rangle(<r_{200})$ is a factor of $\Delta=200$ times the critical density of the universe, $\rho_{\rm crit}$ (from now on we denote this halo mass by M_{200}). In the literature a number of values have been used for Δ. Some authors opt to use $\Delta=200$ (e.g., Jenkins et al. 2001) or $\Delta=200\Omega_{\rm m}(z)$ (e.g. NFW), while others (e.g., Bullock et al. 2001) choose $\Delta=\Delta_{\rm vir}$ according to the spherical virialization criterion of Bryan & Norman (1998). These definitions can lead to sizeable differences in c for a given halo and, as discussed, the differences are also cosmology-dependent.

In this section we study how the structural properties and MAHs depend on the adopted mass definition. We analyse halo MAHs of relaxed halos using three different halo mass definitions. First, we use M_{200}. Secondly, we use $M_{\rm mean}$, which is the mass within the radius $r_{\rm mean}$ for which the mean internal density is 200 times the mean background density. Finally, $M_{\rm vir}$ is the mass within the radius $r_{\rm vir}$ for which the mean internal density is $\Delta_{\rm vir}$ times the critical density as determined by Bryan & Norman (1998). Note that halo masses and radii are determined using a spherical overdensity routine within the SUBFIND algorithm (Springel et al. 2001) centred on the main subhalo of the FoF halos (Davis et al. 1985). We perform all calculations for the three different halo definitions, taking the halo centre to be the location of the particle in the FoF group for which the gravitational potential is minimum.

Eq. (3.8) shows that the formation redshift is directly proportional to the mean density within the scale radius ($(1+z_{-2})^3 \propto \langle\rho\rangle(<r_{-2})$), but the constant of proportionality depends on the mass definition that is adopted. Therefore, a change in the mass definition

changes the formation time as

$$\frac{(1+z_f)_{\Delta_1}}{(1+z_f)_{\Delta_2}} \approx \left(\frac{\langle\rho\rangle(<r_{-2})_{\Delta_1}}{\langle\rho\rangle(<r_{-2})_{\Delta_2}}\right)^{1/3}, \tag{3.33}$$

where $\Delta_{1,2}$ refers to different overdensity criteria. That is, from eq. (3.5), $\langle\rho\rangle(<r_{-2})$ changes according to the mass definition as $\langle\rho\rangle(<r_{-2})_\Delta = \Delta \times \rho_{\rm crit,0} c_\Delta^3 Y(1)/Y(c_\Delta)$. Then $\langle\rho\rangle(<r_{-2})_{\Delta_1=200}$ refers to the mean internal density within r_{-2}, obtained by defining the mean internal density at the virial radius to be $200\rho_{\rm crit,0}$. If we consider $\Delta_1 = 200$ and $\Delta_2 = {\rm mean} = 200\Omega_{\rm m}$, and that there is a factor of 0.55 difference between the concentrations c_{200} and $c_{\rm mean}$ for a $10^{12}{\rm M}_\odot$ halo, then we obtain (using eq. 3.33) the relation $(1+z_{\rm f})_{200} \approx (0.255\Omega_{\rm m,0}^{-1})^{1/3}(1+z_{\rm f})_{\rm mean}$, where we have used the fact that $\langle\rho\rangle(<r_{-2})_{\rm mean} \sim (\Omega_{\rm m,0}/0.255)\langle\rho\rangle(<r_{-2})_{200}$[ii]. This implies that the change in the halo mass history due to different halo mass definitions is

$$\begin{aligned}
\log_{10}\frac{M(z)_{200}}{M(z)_{\rm mean}} &= \log_{10}(1+z)^{\alpha_{200}-\alpha_{\rm mean}} \\
&\quad + \log_{10} e^{(\beta_{200}-\beta_{\rm mean})z} && (3.34)\\
&\approx 0.956\alpha_{200}\log_{10}(1+z) && (3.35)\\
&\quad + [1-(0.255/\Omega_{\rm m,0})^{1/3}]\log_{10}(e)\beta_{200}z \\
&\approx 0.0543z, && (3.36)
\end{aligned}$$

where in step (3.35) we replaced $\alpha_{200} - \alpha_{\rm mean} \approx 0.956\alpha_{200}$, which is valid for a $10^{12}{\rm M}_\odot$ halo, and $\alpha_{200} = 0.2501$ and $\beta_{200} = -0.8147$.

The difference in MAH given by eq. (3.36) can be seen in Fig. 3.11, which shows how the halo MAH is affected by the halo mass definition. The green line in Fig. 3.11 shows the MAH assuming the M_{200} mass definition. The purple line shows the $M_{\rm vir}$ definition, and the dark blue line shows the $M_{\rm mean}$ definition. The different dashed lines correspond to the MAHs $M(z) = M(z=0)(1+z)^\alpha e^{\beta z}$, where the difference lies in the mass definition that changes the mean inner density and the $c-M$ relation (for a relaxed halo sample). Duffy et al. (2008) studied how the halo mass definition changes the $c-M$ relation, and provided the parameters of the different $c-M$ relations. They found that the concentration of a relaxed $M_{\rm mean}$ halo is 80% larger than the concentration of a relaxed M_{200} halo. We adopt those fits in our calculations of the $M(z)$ estimate and conclude that, as long as we use a $c-M$ relation that is consistent with the adopted halo mass definition, the expressions (3.10), (3.14) and (3.20) accurately reproduce the halo mass history.

[ii] In this last step we used the approximation that $\langle\rho\rangle(<r_{-2})_\Delta = \Delta \times c^3 Y(1)/Y(c)\rho_{\rm crit,0} \approx \Delta \times 0.643 c^{2.28}\rho_{\rm crit,0}$

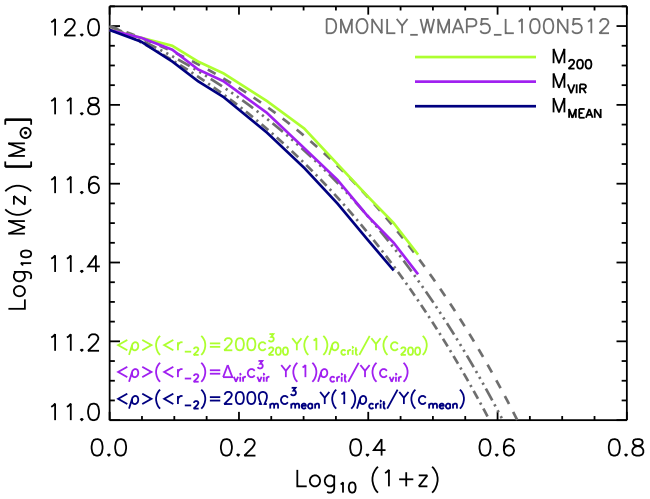

Figure 3.11: Mass history of a $10^{12}\mathrm{M}_{\odot}$ halo as a function of redshift. The different coloured lines show the change in the mass history when different halo mass definitions are used. The green line shows the mass history of a halo of $M_{200} = 10^{12}\mathrm{M}_{\odot}$ at $z = 0$, whereas the dark blue (purple) line shows the mass history of a halo of $M_{\rm mean} = 10^{12}\mathrm{M}_{\odot}$ ($M_{\rm vir} = 10^{12}\mathrm{M}_{\odot}$) at $z = 0$. The dashed lines show the mass history predicted by eqs. (3.44), (3.45) and (3.46). The difference lies in the formation redshift definition which is affected by the change in the mean inner density (see eq. 3.8). The value of $\langle\rho\rangle(< r_{-2})$ changes with the value of Δ we used in the definition of halo mass. The $c-M$ relation correspond to the mass definition under consideration.

The analytic estimate given by eq. (3.36) predicts that the difference in mass history due to the change in the mass definition (M_{200} versus $M_{\rm mean}$) is $\Delta \log_{10} M(z) \approx 0.0543z$. This can be seen in Fig. 3.11, where $\Delta \log_{10} M(z) = 0.1086$ at $z = 2$ ($M_{\rm mean}(z = 2) = 10^{11.3035}\mathrm{M}_{\odot}$ and $M_{200}(z = 2) = 10^{11.4117}\mathrm{M}_{\odot}$). Note that Fig. 3.11 is not showing $M_{200}(z)$, $M_{\rm mean}(z)$ and $M_{\rm vir}(z)$ for the same stack of halos. We select halos that have masses (either M_{200}, $M_{\rm mean}$ or $M_{\rm vir}$) equal to $10^{12}\,\mathrm{M}_{\odot}$ at $z = 0$ (within 0.2 dex) and compare their MAHs. In the case we select the *same* stack of halos, $M_{200}(z)$ should be smaller than $M_{\rm mean}(z)$.

3.5 Comparison between semi-analytic and analytic models

In this section we compare the semi-analytic model derived in §3.3.4, with the analytic model for halo mass history derived in Chapter 2. Note that while the semi-analytic model is obtained through fits to simulations, the analytic model is based on the EPS theory without calibration against simulations, and only depends on the power spectrum of the primordial density perturbations.

Fig. 3.12 shows a comparison between the models for various halo masses

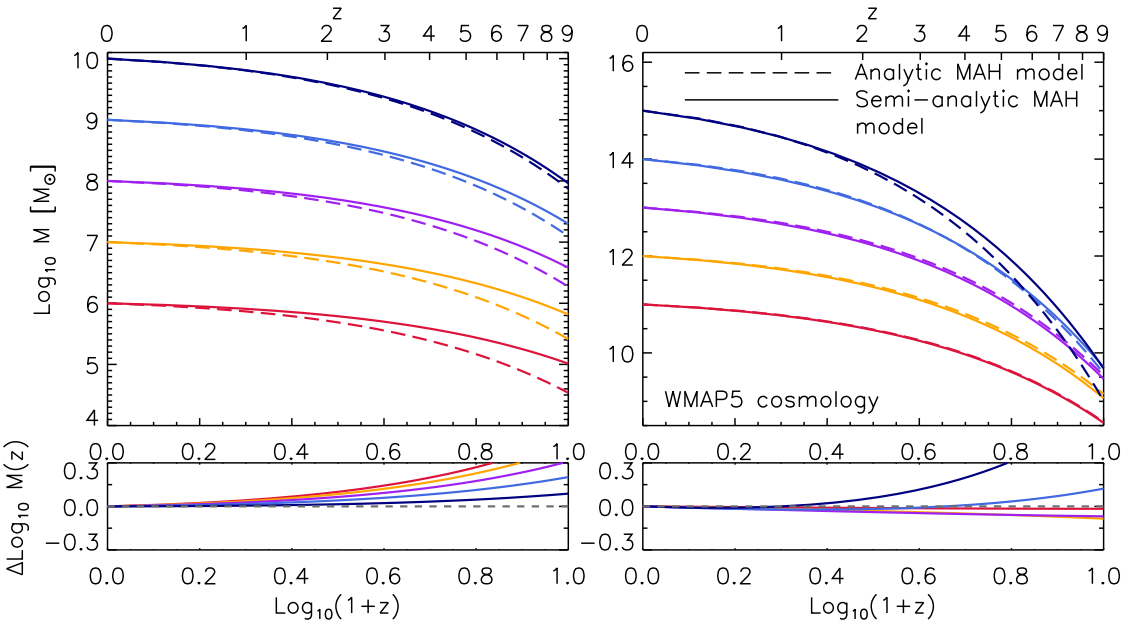

Figure 3.12: The top panels show a comparison between the semi-analytic (solid lines) and the analytic model (dashed lines) for halo mass history. The bottom panels show the residuals between the models. The different coloured lines correspond to the models for various halo masses in range $\log_{10}[M_0/\mathrm{M}_\odot] = 6 - 15$.

($\log_{10}[M_0/\mathrm{M}_\odot] = 6 - 15$). As can be seen from the figure, the models mostly agree on the MAHs of halos with final masses between 10^{10} and $10^{14}\mathrm{M}_\odot$. However, there are a few factors of difference in the MAHs of larger and smaller halos, and the difference increases towards high redshift. We find that in the analytic model the halo mass decreases quite abruptly at high redshift for halos with final masses $> 10^{14}\mathrm{M}_\odot$. For instance, there is a factor of 9 difference at $z = 5$ between the models for a $10^{15}\mathrm{M}_\odot$ halo. This difference is probably due to the progenitor definition. In the analytic model, the progenitor is defined as the halo with mass a factor of q lower ($q \sim 4$ for $M_0 > 10^{14}\mathrm{M}_\odot$) at redshift z_f ($z_f \sim 0.9$), whereas in the semi-analytic model, the progenitor is the halo that contains most of the 25 most bound dark matter particles in the following snapshot.

Fig. 3.12 also shows that the semi-analytic model overpredicts the MAHs of halos with final masses $< 10^{9}\mathrm{M}_\odot$. This is expected because the parameters α and β in the semi-analytic model depend on the $c - M$ relation adopted. In this case we are using Duffy et al. (2008) relation, which is calibrated in the mass range $10^{10} - 10^{14}\mathrm{M}_\odot$, for lower masses the $c - M$ relation deviates from a simple power-law (Ludlow et al. 2014).

Next, we combine these two models (semi-analytic and analytic) to establish the physical link between a halo concentration and the linear *rms* fluctuation of the primordial density field. From Fig. 3.12 we have found that there are a few factors of difference between the models. We now focus on the mass range $10^{11} - 10^{14}\mathrm{M}_\odot$, where the factor of difference is less than 1.5. We set the mass history curve to be the same in the two models, that is

$$M(z)_{\rm Analytic} = M(z)_{\rm Semi-analytic} \tag{3.37}$$

for all redshifts. We then evaluate this equality at redshift 1 and obtain,

$$f(M_0)\left(0.92\frac{{\rm d}D}{{\rm d}z}|_{z=0} - 0.3\right) \;\; = \;\; \alpha_{\rm S}(c)\ln(2) + \beta_{\rm S}(c). \tag{3.38}$$

In this last equation, $\alpha_{\rm S}(c)$ and $\beta_{\rm S}(c)$ are given by eqs. (3.18) and (3.20), respectively, and depend on concentration, D is the linear growth factor and $f(M_0)$ depends on the rms of the primordial density field, σ. We approximate various terms in eq. (3.38), including $f(M_0) \sim 1.155(\sigma(M_0)^2)^{0.277}$ and $Y(1)/Y(c) \sim 0.643c^{-0.71}$, and obtain

$$c = 3\sigma^{0.946} + 2.3, \tag{3.39}$$

which is suitable for a WMAP5 cosmology. Note that eq. (3.39) is not a fit to any simulation data, it has been derived from eq. (3.38). Fig. 3.13 shows the $c-\sigma$ relation at $z = 0$. In this figure we compare the predicted relation (solid line), as given by eq. (3.39) (obtained by equaling the analytic and semi-analytic models), with the simulation outputs (coloured symbols). The different symbols correspond to the median values of the relaxed sample of halos and the error bars to 1σ confidence limits. The good agreement between the analytic prediction and the simulation outputs clearly shows that the halo MAH is the physical connection in the $c-\sigma$ correlation.

3.6 Halo accretion history and assembly bias

The Markovian nature of the EPS formalism implies that the environment of halos of given mass should be independent of their assembly histories (White 1996). However, statistical analysis of formation time distributions demonstrated that halos in dense environments (i.e. in close pairs) have slightly earlier assembly times than typical objects of the same mass (Sheth & Tormen 2004). The dependence of halo clustering on halo MAH at fixed mass is known as *assembly bias* (Gao et al. 2005; Wechsler et al. 2006; Gao & White 2007; Wu et al. 2008; Lacerna & Padilla 2011, 2012; Zentner et al. 2014).

Recently, Hearin et al. (2015) investigated the correlations between the mass accretion rates, ${\rm d}M/{\rm d}t$, of nearby halos, and found that since these halos reside in the same large scale tidal field, the environment regulates their ${\rm d}M/{\rm d}t$. As a result, slow-accreting halos cluster more strongly than fast-accreting halos of the same mass. However, assembly bias implies that early-forming halos cluster more strongly than late-forming halos of the same mass. Then, we can conclude that strong clustered halos, that reside in preferentially denser environments and form earlier, have lower ${\rm d}M/{\rm d}t$ at $z = 0$, than late-forming

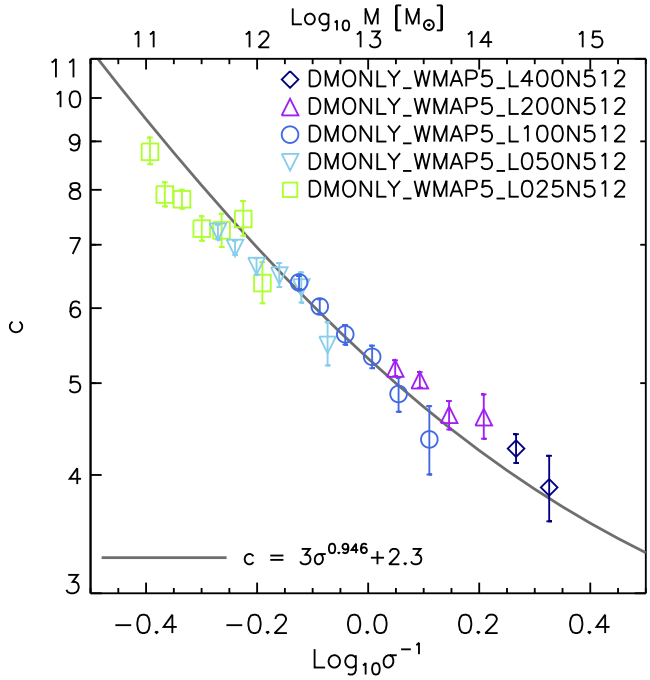

Figure 3.13: Comparison between the $\sigma - c$ relation at $z = 0$ predicted by the combination of the mass history models (solid line), and the simulation outputs (coloured symbols).

halos of the same mass.

In this section we investigate whether the MAH model derived in §3.3.4 is able to predict the drop in the accretion rates of strong clustered halos. To do so, we assume that the formation time, z_{-2}, is an 'indirect measure' of clustering and an independent parameter in the model. We calculate the accretion rate history of a halo of mass M_0 at $z = 0$ as

$$\begin{aligned}
\frac{\mathrm{d}M(M_0, z_{-2}, z)}{\mathrm{d}t} &= 71.6\,\mathrm{M}_\odot\mathrm{yr}^{-1}\, M_{12}(M_0, z_{-2}, z) h_{0.7}[-\alpha(M_0, z_{-2}) - \beta(z_{-2})(1+z)] \\
&\times [\Omega_{\mathrm{m},0}(1+z)^3 + \Omega_{\Lambda,0}]^{1/2}, \qquad (3.40) \\
M_{12}(M_0, z_{-2}, z) &= (M_0/10^{12}\,\mathrm{M}_\odot)(1+z)^{\alpha(M_0,z_{-2})} e^{\beta(z_{-2})z}, \qquad (3.41) \\
\alpha(M_0, z_{-2}) &= [\ln(Y(1)/Y(c(M_0)) - \beta z_{-2}]/\ln(1+z_{-2}), \qquad (3.42) \\
\beta(z_{-2}) &= -3/(1+z_{-2}). \qquad (3.43)
\end{aligned}$$

We next compare the accretion rate histories of halos that have the same mass at $z = 0$, but formed at different times. Fig. 3.14 shows the accretion rates (left panel) and mass histories (right panel) of halos that have masses of $10^{12}\,\mathrm{M}_\odot$ at $z = 0$. The different coloured lines correspond to various formation times as indicated in the legend. We find that as the formation time increases, $\mathrm{d}M/\mathrm{d}t$ at low-z decreases, as suggested by

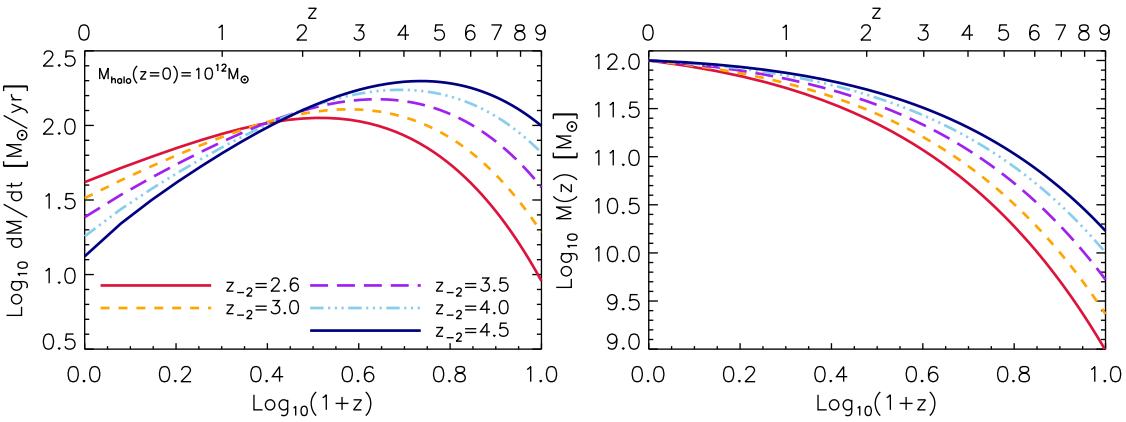

Figure 3.14: Accretion rate histories (left panel) and mass histories (right panel) as a function of redshift of halos that have masses of $10^{12}\,\mathrm{M}_{\odot}$ at $z = 0$, but formed at $z_{-2} = 2.6$ (solid red line), $z_{-2} = 3.0$ (dashed orange line), $z_{-2} = 3.5$ (dashed purple line), $z_{-2} = 4.0$ (dot-dashed light blue line) and $z_{-2} = 4.5$ (solid blue line).

Hearin et al. (2015). Halos forming earlier, have larger $\mathrm{d}M/\mathrm{d}t$ at high-z, that reaches a maximum value at the halo formation time. At $z < 1.6$, early-forming halos have lower accretion rates than late-forming halos.

In Chapter 6 we investigate the correlation between gas accretion onto galaxies and the host halo dark matter accretion rate. We believe that if both rates are tightly coupled as recently suggested (Wetzel & Nagai 2015), the relation between halo MAH and its formation time can potentially predict the mass and redshift dependence of large-scale *galactic conformity*[iii] (Hearin et al. 2015).

3.7 Summary and conclusion

In this chapter we have demonstrated that there is an intrinsic relation between halo assembly history and inner halo structure, and that the mass history is the physical connection between the inner halo structure and the power spectrum of initial density fluctuations.

We examined the density profiles and mass growth histories of a large sample of halos and their progenitors within the OWLS simulations. We separated our halo sample into a 'relaxed' sample, and a 'complete' sample that includes both relaxed and unrelaxed halos. We confirmed the finding of Ludlow et al. (2013) that for relaxed halos the mean enclosed density within the NFW scale radius (r_{-2}), $\langle\rho\rangle(< r_{-2})$, is directly proportional to the critical density of the Universe at the formation redshift, z_{-2}, defined as the time at which the mass of the main progenitor equals the mass enclosed within the scale radius at $z = 0$, $\langle\rho\rangle(< r_{-2}) = 900\rho_{\mathrm{crit}}(z_{-2})$.

[iii] Galactic conformity (first introduced by Weinmann et al. 2006), is the tendency of neighboring galaxies to have similar specific star formation rates, colors, gas fractions and morphologies.

Regarding the halo internal structure, we have found that on average, halo concentrations differ by a factor of 1.16 between the relaxed and complete samples. The lower individual concentrations of unrelaxed halos (due to spurious subhalos or ongoing mergers that do not result in an accurate fit for an NFW density profile) produce incorrect enclosed halo masses and therefore lower formation times (by a factor of 1.1). However, on average, the $z_{-2} - c$ relation does not change, thus indicating that the halo MAH is not affected by the fact that a halo is out of equilibrium at a particular redshift.

We have found that formation time decreases with increasing mass (at a non-linear rate). This means that high-mass halos are still accreting mass rapidly in the present epoch, while low-mass halos typically accreted their mass early. Thus, the $z_{-2} - c$ relation provides the physical link between the halo MAH and internal structure. This result led us to provide a semi-analytic model for the halo MAH, which uses a direct, analytic correlation between the parameters α and β in the mass history (eq. 3.44) and concentration,

$$M(z) = M_0(1+z)^{\alpha}e^{\beta z}, \tag{3.44}$$

$$\alpha = [\ln(Y(1)/Y(c)) - \beta z_{-2}]/\ln(1+z_{-2}), \tag{3.45}$$

$$\beta = -3/(1+z_{-2}), \tag{3.46}$$

where we obtained the constant value, -3.01 ± 0.08, in the last relation (eq. 3.46) by fitting the halo mass history model (eq. 3.44) to the simulation data.

We have investigated how cosmology affects the semi-analytic model. We found that as long as a suitable $c - M$ relation and the value for the best-fitting parameter in the $\langle\rho\rangle(< r_{-2}) - \rho_{\rm crit}(z_{-2})$ relation are assumed for the cosmology being considered, the semi-analytic models describes the MAHs with high accuracy. In addition, we investigated how different mass definitions change the halo mass histories and we found that as long as we use a $c - M$ relation that is consistent with the adopted halo mass definition, the semi-analytic model accurately reproduces the halo mass history.

In addition, we have compared the analytic model from Chapter 2 with the semi-analytic model presented in this chapter and found very good agreement in the mass range $10^9 - 10^{14}{\rm M}_{\odot}$. However, we found that the analytic model predicts larger masses at high redshift for halos with final masses $> 10^{14}{\rm M}_{\odot}$, whereas the semi-analytic model overpredicts the mass history of low-mass halos (halos with final masses $< 10^9{\rm M}_{\odot}$). This is expected because the semi-analytic model depends on the adopted $c - M$ relation, which deviates from the assumed power-law at low masses. The reader may find a step-by-step guide on how to implement the semi-analytic model in Appendix A, as well as

numerical routines online[iv].

Interestingly, by combining these two models (semi-analytic and analytic) we established the physical link between a halo concentration and the initial density perturbation field, which explains the correlation between concentration and *rms* fluctuation of the primordial density field, σ (Fig. 3.13).

Putting the pieces together, we have addressed the question of how the structure of halos depends on the primordial density perturbation field. We have found that concentration is the link between the halo mass profile and the halo mass history (and that one can be determined from the other). We have also found that the 'shape' of the halo mass history is given by the linear growth factor and linear power spectrum of density fluctuations. Therefore, we concluded that halo concentrations are directly connected to the initial density perturbation field.

In the next chapter we combine the analytic and semi-analytic models to predict the $c - M$ relation. We investigate its evolution and show that extrapolations to low masses of power-law fits to simulation results are highly inadequate, and investigate whether linear $\langle\rho\rangle(< r_{-2}) - \rho_{\rm crit}(z_{-2})$ relation holds at redshifts other than 0.

[iv] Available at *https://bitbucket.org/astroduff/commah*.

4

A physical model for the concentration-mass relation

This chapter presents the physical relation between the dark matter halo concentration and the mass accretion history.

It is generally believed that the concentration-mass relation (throughout this thesis $c-M$ relation) relies on the fact that concentrations depend on the evolutionary stage of halos when they were formed, and thus on their mass accretion histories (throughout this thesis MAH). In this chapter we explore the relation between the halo MAH and its concentration. We derive a semi-analytic, physically motivated model for dark matter halo concentration as a function of halo mass and redshift. The semi-analytic model combines an analytic model for the halo MAH derived in Chapter 2, with the empirical relation between concentration and formation time obtained in Chapter 3. The model predicts a change of slope in the $z \sim 0$ $c-M$ relation at a mass scale of $10^{11}\,\mathrm{M}_{\odot}$. We find that this is due to the change in the functional form of the halo MAH, which goes from being dominated by an exponential (for high-mass halos) to a power-law (for low-mass halos). During the latter phase, the core radius remains approximately constant, and the concentration grows due to the drop of the background density. We also analyse how the $c-M$ relation predicted by this work affects the power produced by dark matter annihilation, finding that at $z = 0$ the power is two orders of magnitude lower than that obtained from extrapolating best-fitting $c-M$ relations. Finally, we provide fitting formulas for the $c-M$ relations, a step-by-step description on how to implement the semi-analytic $c-M$ model in Appendix A, as well as numerical routines online[i].

[i] Available at http://astro.physics.unimelb.edu.au/Research/Public-Data-Releases/COMMAH

4.1 Introduction

Over the past few years large cosmological simulations have been performed to determine the properties of dark matter halos, including density profiles, shapes and accretion histories (see e.g. Bryan et al. 2013; Klypin et al. 2011; Springel et al. 2005). These properties are of particular interest, as forming galaxies depend on the structural properties of the halos in which they are embedded.

During hierarchical growth, halos acquire a density profile with a near universal shape, that can be described by the NFW profile (Navarro et al. 1996, 1997). As discussed in §1.2.3 and in §3.3.1, the NFW density profile is described by just two parameters, halo mass, M, and concentration, c. A halo's concentration is defined as the ratio of the virial radius, r_{200}, and the scale radius, r_{-2}, which is defined as the radius where the logarithmic density slope is -2. Thus, given the NFW profile, only a relation between concentration and halo mass is needed to fully specify halo structure at fixed mass. Therefore, numerous studies have been undertaken to improve the $c - M$ calibration.

Despite its importance, there is still no solid agreement on the dependence of halo concentration on halo mass and redshift. A small change in the adopted cosmology can have important effects on the structure of dark matter halos (Macciò et al. 2008), and on their mass histories (Zhao et al. 2009, but also see 2.3 and 3.4.1.1). For example, the mean concentrations of dwarf-scale dark matter halos change by a factor of 1.5 between the various Wilkinson Microwave Anisotropy Probe (WMAP) cosmologies (Spergel et al. 2003, 2007). The Planck cosmology (Planck Collaboration et al. 2014) has higher matter density, $\Omega_{\mathrm{m},0}$, and higher power spectrum normalization, σ_8, compared to the cosmological parameters of the year 5 data release of WMAP (WMAP5; Komatsu et al. 2009). The Planck cosmology therefore suggests that halos assemble earlier and are more concentrated (c.f. $c - M$ relations from Dutton & Macciò 2014 and Duffy et al. 2008).

However, cosmology may not be the primary reason for the differences in the $c - M$ relations found by various authors. Recent works that adopt the same cosmology still find different $c - M$ relations (compare for example Dutton & Macciò 2014 and Diemer & Kravtsov 2015, or Klypin et al. 2011 and Prada et al. 2012). Dutton & Macciò (2014), found that the $c-M$ relation is well described by a power-law, but flattens at high redshift and exhibits a positive slope at $z > 4$. In contrast, Diemer & Kravtsov (2015) found a strong upturn in the high-mass end of the $c - M$ relation at all redshifts. The disparity between these studies could be due to the dynamical state of the selected dark matter halos. For example, Ludlow et al. (2012) showed that massive halos that are substantially out of equilibrium are more likely to be found at a transient stage of high concentration, thus explaining the puzzling upturn in the high-mass end of the $c - M$ relation. Indeed, they reported that the upturn disappears when only dynamically-relaxed systems are

considered. However, Klypin et al. (2014) argued that the virial criterion used by Ludlow et al. (2012) to select relaxed systems is incorrect, as it needs to include effects of the surface pressure and external forces. Klypin et al. (2014) modified the virial criterion and ended up selecting massive halos that had previously been considered as unrelaxed. As a result, Klypin et al. (2014) obtained an upturn in the $c - M$ relation of their relaxed halo sample and concluded that the upturn is a real feature of the $c - M$ relation. They explained that as extremely massive halos have more radial infall velocities, infalling mass penetrates deeper within the inner halo, thus increasing the concentration and producing the upturn.

The main goal of this chapter is to derive a physically motivated model for the $c - M$ relation of relaxed halos based on the dark matter halo accretion history. We extend the analysis done in Chapter 3 by deriving a halo MAH model (based on the analytic model of Chapter 2) suitable to the describe the halo MAH at any starting redshift. By doing that, we are able to explore the $c - M$ relation at any redshift (not only redshift zero) and its evolution. By relating the concentration to the halo accretion history, we find that the $c - M$ relation does not show any upturn or strong flattening. We then study the $c - M$ relation in detail using simulations and selecting relaxed halos without using the virial criterion, and investigate whether recently accreted particles are able to reach the inner parts of the halo and thus increase the concentration.

Our $c-M$ model relies on the fact that concentrations depend on the evolutionary stage of halos when they were formed. Several works have suggested that halo formation can be described as an inside out process, where a bound core (of a certain fraction of the halo mass today) collapses, followed by the gradual addition of material at the cosmological accretion rate (Manrique et al. 2003; Wang & Abel 2007; Dalal et al. 2010; Salvador-Solé et al. 2012, see also §3.3.2). In this framework, the halo concentration should depend on the epoch at which a certain fraction of the halo mass was assembled. As a result, various authors (Bullock et al. 2001; Wechsler et al. 2002; Zhao et al. 2003; Ludlow et al. 2014) have provided models that relate c to the halo MAH. For instance, Zhao et al. (2003) showed that when the mass accretion rate of a halo slows down at low redshift, its scale radius, r_{-2}, remains approximately constant, and hence that concentration scales with the virial radius. On the other hand, in the regime of a high mass accretion rate (at high redshift), the scale radius scales approximately as the virial radius and thus c remains constant.

As we have seen the previous chapter, the connection between a halo's MAH and its concentration, c, is obtained through its 'formation' time. The halo formation (or assembly) time is traditionally defined as the point in time when the halo mass reached a fraction of the total mass today. Low-mass halos typically assemble earlier, when the Universe was denser, than high-mass halos do. As a result, low-mass halos are more

concentrated. Clearly, if concentration correlates with formation time, and formation time depends on the mass variance, σ (because σ describes the halo MAH, see the analytic model for the MAH from Chapter 2), then it is expected that c correlates with σ and hence with the peak height, ν, defined as $\nu = 1.686/\sigma$. This is indeed what several works have found (e.g. Zhao et al. 2009; Prada et al. 2012; Ludlow et al. 2014; Dutton & Macciò 2014). Chapter 3 shows that the physical origin of the $c - \sigma$ (or $c - \nu$) relation is the halo MAH.

Chapters 2 and 3 present two models for the MAH of halos, an analytic model and a semi-analytic model, respectively. The semi-analytic model uses a functional form for the MAH, that is motivated by the EPS theory, and links the MAH to halo structure through two empirical relations obtained from simulations. The analytic model is based on the EPS formalism and thus does not require calibration against any simulation data.

In the analytic model, the halo MAH is described in terms of the *rms* of the density perturbation field, σ, as $M(z) = M_0(1+z)^{af(M_0)}e^{-f(M_0)z}$, where M_0 refers to the present halo mass, a depends on cosmology, and $f(M_0) \sim 1/\sigma(M_0)$. This expression illustrates that as σ decreases with halo mass, the function $f(M_0)$ increases, causing the exponential in $M(z)$ to dominate. As a result, high-mass halos accrete faster than low-mass ones, due to their low value of σ. As low σ implies large peak height, the EPS formalism predicts that density perturbations with large ν experience an accelerated collapse phase relative to the average, and grow faster in time.

This chapter presents a semi-analytic, physically motivated model for dark matter halo concentration as a function of halo mass, redshift and cosmology. The semi-analytic model, which builds on that of Ludlow et al. (2014), uses the analytic model for the halo MAH derived in Chapter 2 as well as an extension of the empirical relation between concentration and formation time obtained in Chapter 3. As a result, the semi-analytic model for halo concentrations shows how the $c - M$ relation is expected to evolve based on the hierarchical growth of halos.

This chapter is organized as follows. We begin in §4.2 with a short description of the analytic MAH model and extend it to make it suitable to describe the halo MAH at any starting redshift z_i and not just $z = 0$. We refer to this model as the *extended analytic model*. In §4.3, we define halo formation time and build an empirical relation between formation time and concentration through fits to simulation data. Next, we describe the semi-analytic model for halo concentrations that combines the extended analytic model for the MAH and the empirical relation described previously. We analyse the evolution of concentration that predicts the semi-analytic model in §4.5. In §4.6 we discuss the impact of the results of our semi-analytic model for halo concentration on the signal from dark matter annihilation. In §4.7 we discuss the main assumptions the semi-analytic model relies on. Finally, we summarize and conclude in §4.8.

Throughout this chapter we compare our analytic results to the output from numerical simulations. We use a set of cosmological dark matter only (DMONLY) simulations from the OWLS project (Schaye et al. 2010). For a detailed description of this simulation series see 3.2. We remind the reader that the simulation names contain strings of the form LxxxNyyy, where xxx is the simulation box size (ranging from 25 to 400 comoving h^{-1}Mpc) and yyy is the cube root of the number of particles (ranging from 128^3 to 512^3). Our DMONLY simulations assume the WMAP5 cosmology. However, to investigate the dependence on the adopted cosmology, we use an extra set of five dark matter only simulations ($100\,h^{-1}$Mpc box size and 512^3 dark matter particles) which assume values for the cosmological parameters derived from different releases of the WMAP and the Planck missions. See the table 4.2 for the sets of cosmological parameters adopted in the different simulations.

4.2 Halo mass accretion history

We begin this section by briefly reviewing the analytic model for the MAH derived in Chapter 2, and showing how the MAH depends on cosmology and on the initial peak of the primordial density field. Next, we extend it to estimate the halo MAH tracked from an arbitrary redshift. Readers only interested in the concentration−mass relation model can skip directly to §4.3.

4.2.1 Analytic model for the halo mass history

In Chapter 2, we used simple analytic arguments based on the EPS formalism and the analytic formulation of Neistein et al. (2006), to show that the 'shape' of the MAH is determined by the growth factor of the initial density pertubations. The halo MAH is well described by an exponential in the high-redshift regime, but it slows to a power law at low redshift, because the growth of density perturbations is halted in the dark energy dominated era due to the accelerated expansion of the Universe. Therefore, we showed that the expression

$$M(z)_{\Lambda\mathrm{CDM}} = M_0(1+z)^{\alpha}e^{\beta z}, \tag{4.1}$$

is able to capture the median halo MAH, where M_0 refers to halo mass today, and α and β are parameters that depend on M_0, cosmology and the linear power spectrum. In the case of an Einstein de Sitter (EdS) cosmology ($\Omega_{\Lambda,0} = 0$ and $\Omega_{\mathrm{m},0} = 1$) or an open universe ($\Omega_{\Lambda,0} = 0$ and $\Omega_{\mathrm{m},0} < 1$), there is no acceleration in the expansion of the Universe at low redshift. Then the halo mass history is simply described by an exponential as $M(z)_{\mathrm{EdS}} = M_0 e^{\beta z}$, where $\beta = -1.686(2/\pi)^{1/2} f(M_0)$. For a complete description of the model see Chapter 2.

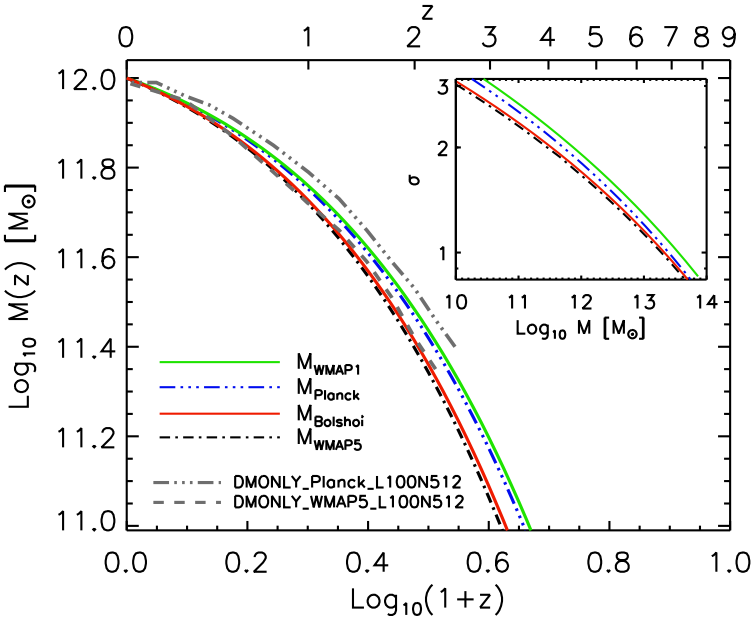

Figure 4.1: Halo MAH of a $10^{12}\,M_\odot$ halo (coloured lines) obtained from the model given by eqs. (4.2)-(4.8), and by assuming various cosmologies as indicated in the legend. The grey lines correspond to MAH obtained from DMONLY simulations that assume the Planck and WMAP5 cosmologies. In the top right corner, we plot σ versus halo mass, to show that the change in σ under different cosmologies drives the change in the MAH.

We find that the MAH model can be used to calculate halo mass histories in cosmologies other than WMAP5, and that the differences are mainly driven by the changes in σ_8 and $\Omega_{\rm m}$. We show this in Fig. 4.1, where the halo MAH of a $10^{12}\,M_\odot$ halo (coloured lines) was estimated for the various cosmologies, as indicated in the legend. In the top right corner of Fig. 4.1, we plot σ versus halo mass, to show how the change in σ drives the change in the MAH. The exception is the Planck cosmology, which has a relatively low σ_8 but a large $\Omega_{\rm m,0} = 0.317$, which raises $M(z)$ close to the WMAP1 $M(z)$.

The overplotted grey lines in Fig. 4.1 correspond to the MAH obtained from DMONLY simulations that assume the Planck and WMAP5 cosmologies. In this case, we compute the MAH of the main subhalo (that is not embedded inside a larger halo) of Friends-of-Friends (FoF) groups (Davis et al. 1985), by tracking the virial mass of the main progenitor at each prior output redshift. Halo virial masses and radii were determined using a spherical overdensity routine within the SUBFIND algorithm (Springel et al. 2001) centred on the main subhalo of FoF halos. Throughout this work we define the halo mass as the total mass within the radius r_{200} for which the mean internal density is 200 times the critical density. For a more detailed description of the method used to create merger trees, see Chapter 3.

4.2.2 Analytic model for the MAH: high redshift prediction

The model presented in Chapter 2 is suitable for estimating halo MAHs that are tracked from $z = 0$. In this section we extend this analytic model to estimate MAHs of halos of the same halo mass that are tracked from arbitrary redshifts z_i. This is shown in Fig. 4.2, where the MAHs of $10^{11}\,\mathrm{M}_\odot$ halos are obtained from DMONLY simulations (coloured curves). The curves show the mean MAH of halos of the same mass ($10^{11}\,\mathrm{M}_\odot$ in this case) that begin at $z_i = 0$ (blue curve), 1 (dark green curve), 2 (green curve), 3 (orange curve) and 4 (red curve). High-redshift MAHs are dominated by large accretion rates and characterized by a pure exponential.

The reason to extend the MAH model to an arbitrary starting redshift z_i is to simplify the calculations of z_i halo concentrations in the following section, where we show that halo concentrations are related to formation times through the extended MAH model (eq. 4.18).

We generalize the analytic model so that it describes the MAHs from any z_i redshift. Expression (4.1) can be rewritten as

$$\tilde{M}(z, M(z_i), z_i) = M(z_i)(1 + z - z_i)^{\tilde{\alpha}} e^{\tilde{\beta}(z - z_i)}, \tag{4.2}$$

where $\tilde{M}(z, z_i)$ denotes the MAH of a halo with mass $M(z_i)$ at redshift z_i. In the above expression, $z > z_i$ and the parameters $\tilde{\alpha}$ and $\tilde{\beta}$ depend on $M(z_i)$ and redshift z_i

$$\begin{aligned}
\tilde{\alpha} &= \left[\frac{1.686(2/\pi)^{1/2}}{D(z_i)^2}\frac{\mathrm{d}D}{\mathrm{d}z}|_{z=z_i} + 1\right] f(M(z_i)), && (4.3)\\
\tilde{\beta} &= -f(M(z_i)), && (4.4)\\
f(M(z_i)) &= [\sigma^2(M(z_i)/q) - \sigma^2(M(z_i))]^{-1/2}, && (4.5)\\
\sigma^2(R) &= \frac{1}{2\pi^2}\int_0^\infty P(k)\hat{W}^2(k;R)k^2\mathrm{d}k, && (4.6)\\
q &= 4.137 \times z_\mathrm{f}^{-0.9476}, && (4.7)\\
z_\mathrm{f} &= -0.0064(\log_{10} M_0)^2 + 0.0237(\log_{10} M_0) && (4.8)\\
&\quad +1.8837,
\end{aligned}$$

where $D(z)$ is the linear growth factor, $P(k)$ the linear power spectrum, $\hat{W}(k;R)$ the Fourier transform of a top hat window function and R defines σ in a sphere of mass $M = (4\pi/3)\rho_{\mathrm{m},0}R^3$, where $\rho_{\mathrm{m},0}$ is the mean background density today. We use the approximation of Eisenstein & Hu (1998) to compute $P(k)$, normalized such that $\sigma(8h^{-1}\mathrm{Mpc}) = \sigma_8$. As a result, $f(M_0)$ depends on the power spectrum and halo mass. It can be seen from eqs. (4.3-4.4) that at large z_i, $\tilde{\alpha} \to 0$ due to $D(z_i) \propto 1.686(2/\pi)^{1/2}/(1+z_i)$

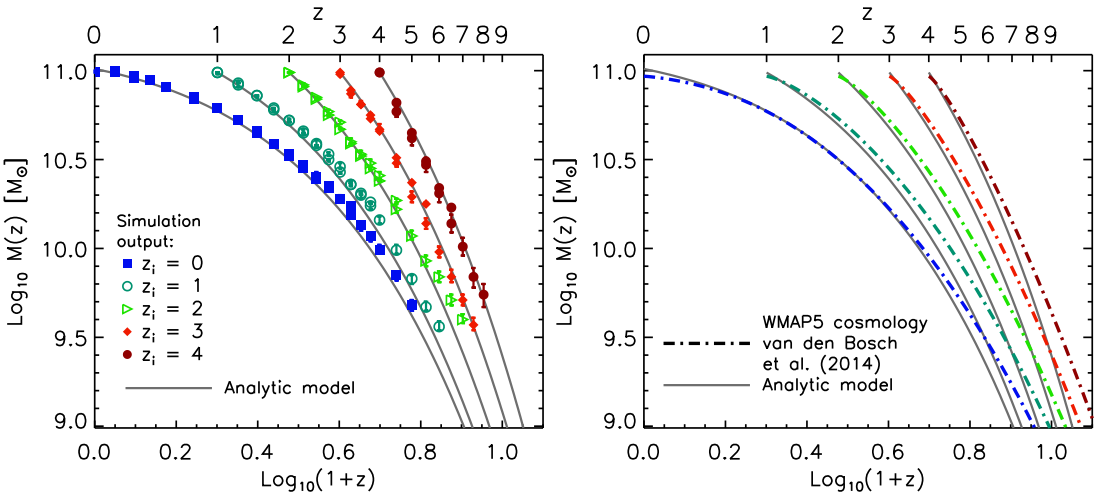

Figure 4.2: Median MAHs for halos of $10^{11}\,\mathrm{M}_\odot$ starting from various redshifts. In both panels the grey solid lines correspond to the analytic model described in §4.2.2. The coloured curves in the left panel are the MAHs obtained from the DMONLY simulations WMAP5_L025N512 and WMAP5_L050N512. The mass histories are computed by calculating the median value and the 1σ error bars are determined by bootstrap resampling the halos from the merger tree at a given output redshift. The coloured dot dashed curves in the right panel are the MAHs obtained from the van den Bosch et al. (2014) model.

for $z_i \gg 1$, indicating that the MAH is mainly described by an exponential. Table 4.1 provides a summary of the nomenclature adopted throughout this chapter. The above equations introduce an extended analytic halo MAH model based on EPS theory that does not require calibration against any simulation data (see Chapter 2 for more details). The numerical values given in eqs. (4.7) and (4.8) were determined by assuming the WMAP5 cosmology ($\Omega_{\mathrm{m},0} = 0.258, \Omega_{\Lambda,0} = 0.742, h = 0.72, n_s = 0.963, \sigma_8 = 0.796$).

In the left panel of Fig. 4.2, we compare the model given by eqs. (4.3-4.8) to various MAHs obtained from a set of DMONLY simulations. Our analytic model is shown by grey solid lines, where we have taken $M(z_i) = 10^{11}\,\mathrm{M}_\odot$. The coloured curves in the left panel correspond to the MAHs obtained from the DMONLY simulations WMAP5_L025N512 and WMAP5_L050N512. We find very good agreement between the simulation outputs and the analytic model at all redshifts. The simulation outputs from the boxes $L = 25\,h^{-1}$Mpc and $L = 50\,h^{-1}$Mpc converge up to $z = 5$. At higher z, the outputs from the $L = 25\,h^{-1}$Mpc simulation underestimate $M(z)$ because the box size limits the maximum sizes of the structures that can form at each redshift.

In the right panel of Fig. 4.2, we compare our extended analytic model with the van den Bosch et al. (2014) model. van den Bosch et al. (2014) extracted halo mass histories from the Bolshoi simulations (Klypin et al. 2011) and extended them below the numerical resolution limit using EPS merger trees. Once they had obtained the MAH curves for a large range of redshifts and halo masses, they made use of a semi-analytic model to

transform the (average or median) MAHs, based on the Bolshoi cosmology, to other cosmologies. Using their publicly available code, we calculate the mass history curves for the WMAP5 cosmology for comparison with our results. We find that there is some discrepancy at high-redshift for all the curves. The van den Bosch et al. (2014) MAH model seems to over predict the halo mass at $z > 5$, most likely as a consequence of the different halo definitions, and subtle differences in the definition of the main progenitor (van den Bosch, private communication). Overall, there is very good agreement between the most recent accretion history study in the literature and our model, as well as with the simulation outputs. In §4.3 we will make use of our analytic MAH model to calculate concentrations.

Using the extended MAH model for high redshift, we can calculate the accretion rate of a halo at redshift z. We differentiate eq. (4.2) with respect to time and replace $\mathrm{d}z/\mathrm{d}t$ by $-H_0[\Omega_{\mathrm{m},0}(1+z)^5 + \Omega_{\Lambda,0}(1+z)^2]^{1/2}$, to obtain

$$\begin{aligned}\frac{\mathrm{d}\tilde{M}(z, M(z_i), z_i)}{\mathrm{d}t} &= 71.6\ \mathrm{M}_\odot \mathrm{yr}^{-1} \left(\frac{\tilde{M}(z, M(z_i), z_i)}{10^{12}\mathrm{M}_\odot}\right) \left(\frac{h}{0.7}\right) [-\tilde{\alpha}/(1+z-zi) - \tilde{\beta}] \\ &\times (1+z)[\Omega_{\mathrm{m},0}(1+z)^3 + \Omega_{\Lambda,0}]^{1/2}, \end{aligned} \tag{4.9}$$

where $\tilde{\alpha}$ and $\tilde{\beta}$ are given by eqs. (4.3) and (4.4), respectively. Note that the above formula will give the accretion rate at redshift z of a halo that has mass $M(z_i)$ at redshift z_i, and mass $\tilde{M}(z, M(z_i), z_i)$ at redshift z.

4.3 Concentration– mass relation

A theoretical understanding of the physical connection between concentration (the parameter that characterizes the internal structure of NFW dark matter halos) and the initial conditions of the density field, is essential for the physical interpretation of relations like $c - \nu$ (concentration−peak height) or $c - M$, that have been calibrated using cosmological simulations (e.g. Bullock et al. 2001; Neto et al. 2007; Gao et al. 2005; Macciò et al. 2007; Duffy et al. 2008; Ludlow et al. 2013; Dutton & Macciò 2014; Diemer & Kravtsov 2015).

It has previously been shown that concentration is determined by the halo MAH, and that the MAH depends on the power spectrum and the adopted cosmological parameters (Wechsler et al. 2002; Zhao et al. 2003; Ludlow et al. 2013, 2014). In this section we show, through analytic and numerical modelling, how the concentration of dark matter halos depends on cosmology and the power spectrum of density perturbations. Our results imply that the halo MAH is the physical link between concentration and peak height.

4.3.1 Formation redshift

As discussed in 4.1, halo MAHs can be used to estimate halo concentrations. Halo concentrations reflect the mean density of the Universe at the formation redshift (Navarro et al. 1997; Wechsler et al. 2002; Zhao et al. 2003, 2009; Ludlow et al. 2013). Therefore, the essential link between a halo's MAH and its internal structure is the formation redshift. For a halo with mass $M(z_i)$ at redshift z_i, we define the formation redshift to be z_{-2}, the redshift at which the mass of the main progenitor equals the mass enclosed within the scale radius at $z = z_i$,

$$z_{-2} = z[\tilde{M}(z_{-2}, M(z_i), z_i) = M_r(r_{-2}, z_i)], \tag{4.10}$$

(Ludlow et al. 2013). Here $\tilde{M}(z_{-2}, M(z_i), z_i)$ is the mass at z_{-2} of a halo with mass $M(z_i)$ at z_i, and we denote the mass enclosed within r, $M(< r)$, as M_r. For an NFW profile the internal mass $M_r(r_{-2}, z_i)$ is related to the total halo mass as

$$M_r(r_{-2}, z_i) = M(z_i)\frac{Y(1)}{Y(c[M(z_i), z_i])}, \tag{4.11}$$

where $Y(u) = \ln(1+u) - u/(1+u)$, $c[M(z_i), z_i]$ is the concentration at z_i and $M(z_i)$ is the total halo mass at z_i. In cases where we identify halos at $z_i = 0$ and track their mass histories, we calculate z_{-2} by setting $M(z_{-2})$ equal to the mass enclosed within r_{-2} today. In cases where we identify halos at $z_i > 0$, we first calculate r_{-2} and $M_r(r_{-2}, z_i)$ at the particular redshift z_i, and then find z_{-2} by tracking the MAH (for $z > z_i$) and equating $\tilde{M}(z_{-2}, M(z_i), z_i)$ to $M_r(r_{-2}, z_i)$. See Table 4.1 for a summary of the nomenclature.

Ludlow et al. (2013, 2014) and Chapter 3 showed that z_{-2} correlates strongly with c, and §3.4.0.1 demonstrated that the scatter in z_{-2} and in the halo MAH predicts the scatter in c. In this section we explore how the formation time − concentration relation varies for halos identified at various redshifts.

We computed density profiles and MAHs for halos identified at redshifts $z_i = 0, 1, 2, 3$ and 4. The density profiles were computed by fitting the NFW density profile,

$$\rho(r, z_i) = \frac{\rho_{\rm crit}(z_i)\delta_c}{(cr/r_{200})[1 + (cr/r_{200})]^2}, \tag{4.12}$$

for each individual halo. In the above equation $\rho_{\rm crit}(z_i) = 3H^2(z_i)/8\pi G$ is the critical density of the universe, δ_c is a dimensionless parameter related to the concentration $c = r_{200}/r_{-2}$ by $\delta_c = \frac{200}{3}\frac{c^3}{Y(c)}$ and r_{200} is the virial radius.

We begin by fitting NFW profiles to all halos at z_i that contain at least 10^4 dark matter particles within the virial radius. Throughout this work we define the virial radius as r_{200}, the radius for which the mean internal density is 200 times the critical density.

Table 4.1: Notation reference.

Notation	Definition
$M(z_i)$	Total halo mass at z_i, defined as M_{200}
r_{200} or $r_{200}[M(z_i), z_i]$	Virial radius at z_i of a halo of total mass $M(z_i)$
r_{-2} or $r_{-2}[M(z_i), z_i]$	NFW scale radius at z_i
c or $c[M(z_i), z_i]$	NFW concentration at z_i
$M_r(r, z_i)$	$M(< r)$, mass enclosed within r at z_i of a halo of total mass $M(z_i)$
$M_r(r_{-2}, z_i)$	Mass enclosed within r_{-2} at z_i
$\tilde{M}(z, M(z_i), z_i)$	Mass at z of a halo with mass $M(z_i)$ at z_i
z_{-2}	Formation redshift, when equating $\tilde{M}(z_{-2}, M(z_i), z_i)$ to $M_r(r_{-2}, z_i)$
$\langle\rho\rangle(< r_{-2}, z_i)$	Mean density within r_{-2} at z_i
$\rho_{\rm crit,0}$	Critical density today
$\rho_{\rm crit}(z_i)$	Critical density at z_i

Then, for each halo, all particles in the range $-1.25 \leq \log_{10}(r/r_{200}) \leq 0$ are binned radially in equally spaced logarithmic bins of size $\Delta \log_{10} r = -0.078$. The density profile is then fitted to these bins by performing a least square minimization of the difference between the logarithmic densities of the model and the data, assuming equal weighting. The corresponding mean enclosed mass, $M_r(r_{-2}, z_i)$, and mean inner density at r_{-2}, $\langle\rho\rangle(< r_{-2}, z_i)$, are found by interpolating along the cumulative mass and density profiles from $r = 0$ to $r_{-2} = r_{200}/c$, where c is the concentration from the fit of the NFW halo. Then we generate merger trees for these halos and by interpolation we determine the redshift z_{-2} at which $\tilde{M}(z_{-2}, z_i) = M_r(r_{-2}, z_i)$.

In order to obtain robust estimates and to test whether the $c - M$ relation includes an upturn in the median concentrations of massive halos (Prada et al. 2012; Dutton & Macciò 2014; Diemer & Kravtsov 2015), we only consider 'relaxed' halos. We define relaxed halos as those halos for which the separation between the most bound particle and the centre of mass of the Friends-of-Friends halos is smaller than $0.07R_{\rm vir}$ (following Macciò et al. 2007, Neto et al. 2007 and Duffy et al. 2008), where $R_{\rm vir}$ is the radius within which the mean density is Δ, as given by Bryan & Norman 1998, times the critical density. Our relaxed sample contains 2425 halos at $z = 0$, 726 halos at $z = 1$, 226 halos at $z = 2$ and 78 and 20 halos at $z = 3$ and $z = 4$, respectively.

The left panel of Fig. 4.3 shows the mean density within the NFW scale radius, r_{-2}, at redshift z_i. The median values of $\langle\rho\rangle(< r_{-2}, z_i)$ follow the best-fitting relation

$$\langle\rho\rangle(< r_{-2}, z_i) = 200 \frac{c[M(z_i), z_i]^3 Y(1)}{Y(c[M(z_i), z_i])} \rho_{\rm crit}(z_i), \tag{4.13}$$

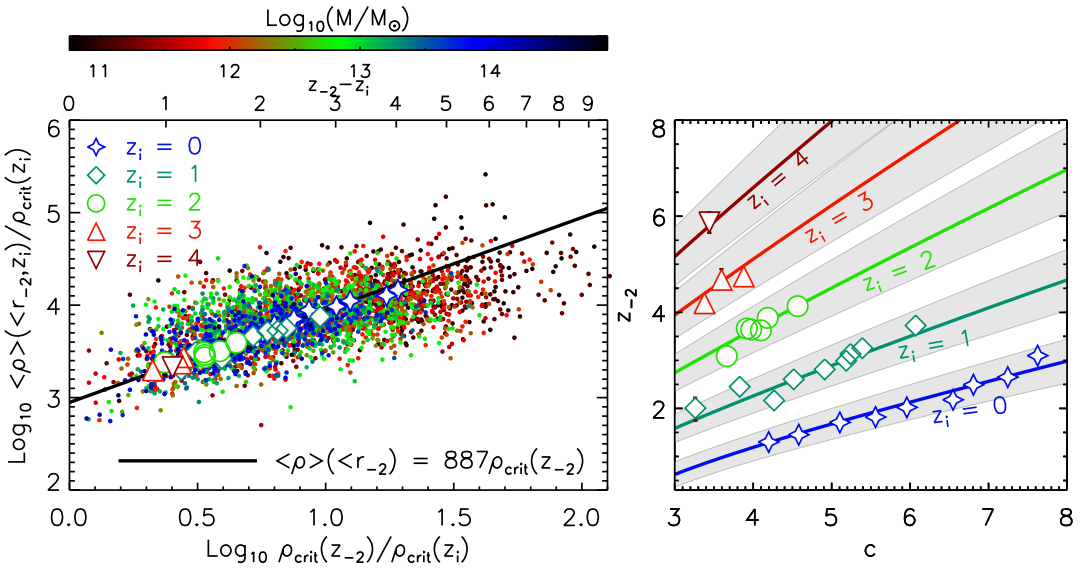

Figure 4.3: *Left panel:* mean density within the NFW scaled radius, $\langle\rho\rangle(< r_{-2})$, at z_i against the critical density of the universe at the formation time, $\rho_{\rm crit}(z_{-2})$. Each dot in the panel corresponds to an individual relaxed halo identified at z_i and coloured by mass according to the colour bar at the top of the plot. The star symbols show the median values of the sample at z_i as indicated by the legend in logarithmic mass bins of width $\delta \log_{10} M = 0.4$. The solid line shows the best linear fit to the $\rho_{\rm crit}(z_{-2}) - \langle\rho\rangle(< r_{-2})$ relation. *Right panel:* formation redshift against concentration. The solid lines show the $c - z_{-2}$ relations given by equation (4.16) for various z_i as indicated in the legend of the left panel. The star symbols correspond to the median values of the samples in logarithmic mass bins of width $\delta \log_{10} M = 0.4$ and are colour coded by z_i. The grey areas show the scatter in z_{-2}.

expressed as a function of the critical density of the Universe at z_{-2},

$$\rho_{\rm crit}(z_{-2}) = \rho_{\rm crit,0}[\Omega_{\rm m,0}(1+z_{-2})^3 + \Omega_{\Lambda,0}], \tag{4.14}$$

where $\rho_{\rm crit,0} = 3H^2(z=0)/8\pi G$. Note that densities along both the $x-$ and $y-$axes are expressed in units of the critical density at z_i. Each dot in the panel corresponds to an individual relaxed halo identified at z_i and coloured by mass according to the colour bar at the top of the plot. The star symbols show the median value of the sample in logarithmic mass bins of width $\delta \log_{10} M = 0.4$ and are coloured by z_i as indicated in the legend[ii].

At each redshift z_i, the $\rho_{\rm crit}(z_{-2}) - \langle\rho\rangle(< r_{-2}, z_i)$ correlation clearly shows that halos which collapsed earlier have denser cores.

We perform a least-square minimization of the quantity $\Delta^2 = \frac{1}{N}\sum_{j=1}^{N}[\langle\rho_j\rangle(< r_{-2}, z_i) - F(\rho_{\rm crit,j}(z_{-2}), A)]$, where j goes from 1 to the number of dark matter halos, N, at z_i and $F(\rho_{\rm crit,j}(z_{-2}), A) = A \times \rho_{\rm crit,j}(z_{-2})$, to obtain the constant of proportionality, A. The

[ii]Note that it is possible for individual halos to appear multiple times in Fig. 4.3 (left panel). For example a $10^{13}\,{\rm M}_\odot$ halo at $z=0$, has a total mass of $\sim 10^{12.2}\,{\rm M}_\odot$ at $z=2$, therefore the halo will be included in the $\rho_{\rm crit}(z_{-2}) - \langle\rho\rangle(< r_{-2}, z_i)$ relation at $z_i = 0$ but also at $z_i = 2$.

solid line corresponds to the best-fit to the $\rho_{\rm crit}(z_{-2}) - \langle\rho\rangle(< r_{-2}, z_i)$ relation, and we find (in agreement with Ludlow et al. 2014) that the average relation

$$\frac{\langle\rho\rangle(< r_{-2}, z_i)}{\rho_{\rm crit}(z_i)} = A \times \frac{\rho_{\rm crit}(z_{-2})}{\rho_{\rm crit}(z_i)} \tag{4.15}$$

is maintained through time with $A = 887 \pm 36$, where the 1σ error was obtained from the least squares fit.

Using eqs. (4.13) and (4.14) we can rewrite this relation as

$$\frac{c[M(z_i), z_i]^3 Y(1)}{Y(c[M(z_i), z_i])} = \frac{A}{200} \frac{[\Omega_{\rm m}(1+z_{-2})^3 + \Omega_\Lambda]}{[\Omega_{\rm m}(1+z_i)^3 + \Omega_\Lambda]}, \tag{4.16}$$

The right panel of Fig. 4.3 shows the $c - z_{-2}$ relation (solid lines) given by eq. (4.16) for various z_i. The star symbols correspond to the median values of the sample in logarithmic mass bins of width $\delta \log_{10} M = 0.4$. The grey areas show the scatter in z_{-2}.

4.4 Semi-analytic model for halo concentration

In this section we describe the semi-analytic model for halo concentration as a function of halo mass and redshift. This model combines the analytic model for the halo MAH given by eqs. (4.2-4.8) and the empirical relation between z_{-2} and c given by eq. (4.16).

We begin by calculating $\tilde{M}(z_{-2}, M(z_i), z_i)$ from eq. (4.2), and use the equality

$$\frac{\tilde{M}(z_{-2}, M(z_i), z_i)}{M(z_i)} = \frac{M_r(r_{-2}, z_i)}{M(z_i)} = \frac{Y(1)}{Y(c[M(z_i), z_i])}, \tag{4.17}$$

which follows from eqs. (4.10) and (4.11) and is valid under the assumption that the halo density profile follows the NFW profile, to obtain

$$\frac{Y(1)}{Y(c[M(z_i), z_i])} = (1 + z_{-2} - z_i)^{\tilde{\alpha}} e^{\tilde{\beta}(z_{-2} - z_i)}, \tag{4.18}$$

where $\tilde{\alpha}$ and $\tilde{\beta}$ are given by eqs. (4.3) and (4.4), respectively. Next, we combine eqs. (4.16) and (4.18) to obtain the concentration, $c[M(z_i), z_i]$, of a halo of total mass $M(z_i)$ at z_i. We remind the reader that throughout this work the adopted halo mass definition is M_{200}, and the concentrations are therefore defined as $c = c_{200}$.

Fig. 4.4 shows the concentration−mass relation at $z = 0$ (left panel), at $z = 1$ (middle panel), and at $z = 2$ (right panel). The dots in the panels correspond to individual relaxed halos identified in the simulations at $z_i = 0, 1$ and 2, whereas the star symbols correspond to the median values in logarithmic mass bins of width $\delta \log_{10} M = 0.4$. The solid line shows the $c - M$ relation that results from the semi-analytic model described above. We find excellent agreement between the median values from the simulations and

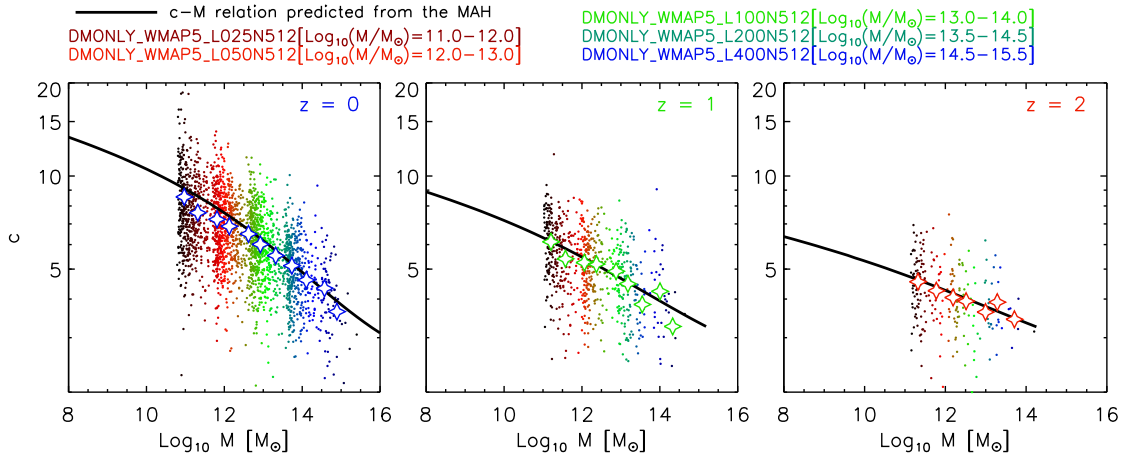

Figure 4.4: Concentration−mass relations at $z = 0$ (left panel), $z = 1$ (middle panel) and $z = 2$ (right panel). The dots in the panels correspond to individual, relaxed halos illustrating the scatter in the relation. The simulations assume the WMAP5 cosmological parameters and have box sizes of 400, 200, 100, 50 and 25 h^{-1}Mpc, as indicated. Because of resolution limits only halos in the mass ranges indicated in the top legend were used from a particular simulation. The star symbols show the median $c - M$ values in logarithmic mass bins of width $\delta \log_{10} M = 0.4$. The solid line shows the prediction of the $c - M$ model obtained from the halo MAH as described in §4.3.

the $c - M$ relation predicted by the semi-analytic model at all redshifts.

So far we have adopted the WMAP5 cosmology. In the following subsection we discuss the dependence of our concentration-mass relation model on cosmology and extend it to make it suitable for any values of the cosmological parameters.

4.4.1 Cosmology dependence

The adopted cosmological parameters affect the halo MAH so that the larger σ_8 or $\Omega_{\rm m,0}$, the earlier halos assemble. As the formation time increases with increasing σ_8 or $\Omega_{\rm m,0}$ (see §2.3 and §3.4.1.1), so does concentration. Therefore, in this section, we analyse how the change in cosmology affects our concentration-mass relation model.

Our $c-M$ model relies on the halo MAH model, which we showed in §4.1 to be suitable for any cosmology. However, our semi-analytic model for halo concentration also relies on the formation redshift through the best-fitting relation given by eq. (4.15),

$$\frac{\langle\rho\rangle(< r_{-2}, z_i)}{\rho_{\rm crit}(z_i)} = A \times \frac{\rho_{\rm crit}(z_{-2})}{\rho_{\rm crit}(z_i)},$$

where A depends on cosmology ($A = 887$ for WMAP5).

We investigate the cosmology dependence of A by following the analysis done in §4.3.1 and using the simulations with different cosmologies listed in Table 4.2. We calculate the best-fitting $\langle\rho\rangle(< r_{-2}, z_i) - \rho_{\rm crit}(z_{-2}, z_i)$ relation to obtain the parameter $A_{\rm cosmo}$, where

Table 4.2: Cosmological parameters.

Simulation	Ω_m	Ω_Λ	h	σ_8	n_s
DMONLY_WMAP1	0.25	0.75	0.73	0.90	1.000
DMONLY_WMAP3	0.238	0.762	0.73	0.74	0.951
DMONLY_WMAP5	0.258	0.742	0.72	0.796	0.963
DMONLY_WMAP9	0.282	0.718	0.70	0.817	0.964
DMONLY_Planck1	0.317	0.683	0.67	0.834	0.962

cosmo is WMAP1, WMAP3, WMAP9 or Planck. We found that if we keep $A = 887$ fixed when computing the $c-M$ relations for cosmologies other than WMAP5, we obtain relations that are in very good agreement with the various relations in the literature. However, we obtain even better agreement with the simulations when we let A vary slightly with cosmology. We found that $A_{\rm WMAP1} = 853$, $A_{\rm WMAP3} = 850$, $A_{\rm WMAP9} = 950$ and $A_{\rm Planck} = 880$, reproduce the $c - M$ relations best. For a calculation of $c - M$ relations in cosmologies other than the ones listed above, we recommend the reader to set $A = 887$ fixed.

It is important to note that if the A parameter is in fact cosmology dependent then halos which formed at different formation times (e.g. $z_{-2,\rm cosmo1}$ and $z_{-2,\rm cosmo2}$), but that correspond to the same background density ($\rho_{\rm crit}(z_{-2,\rm cosmo1}) = \rho_{\rm crit}(z_{-2,\rm cosmo2})$), will have different concentrations ($c_{\rm cosmo1} \neq c_{\rm cosmo2}$). This implies that other factors affect the dark matter halo density profiles, and that the halo MAH alone is not sufficient for predicting concentrations.

4.4.2 Impact of relaxedness on the $c - M$ relation

Several recent studies (Klypin et al. 2011; Prada et al. 2012; Dutton & Macciò 2014; Diemer & Kravtsov 2015) have found that the $c - M$ relation flattens at high redshift and exhibits an 'upturn' at the high-mass end, meaning that the concentration increases with halo mass for the most massive halos. In this section we investigate whether this interesting behavior is seen in our semi-analytic model or in the simulation outputs.

Our model does not predict an upturn. The model relates c to the MAH via the formation redshift, z_{-2} (see Fig. 4.3, right panel), which decreases with halo mass, meaning that more massive halos are less concentrated because they formed more recently. If c were to increase with halo mass, then high-mass halos would have to form earlier than low-mass ones, at a point when the Universe was denser. This behavior is neither seen in our simulations (see Fig. 4.1, coloured lines), as we only consider relaxed systems, nor predicted by EPS theory, because it would be antihierarchical for such systems.

To investigate further, we use the simulation outputs to calculate concentrations by fitting NFW profiles to halos that are resolved with at least 10^4 particles within the virial

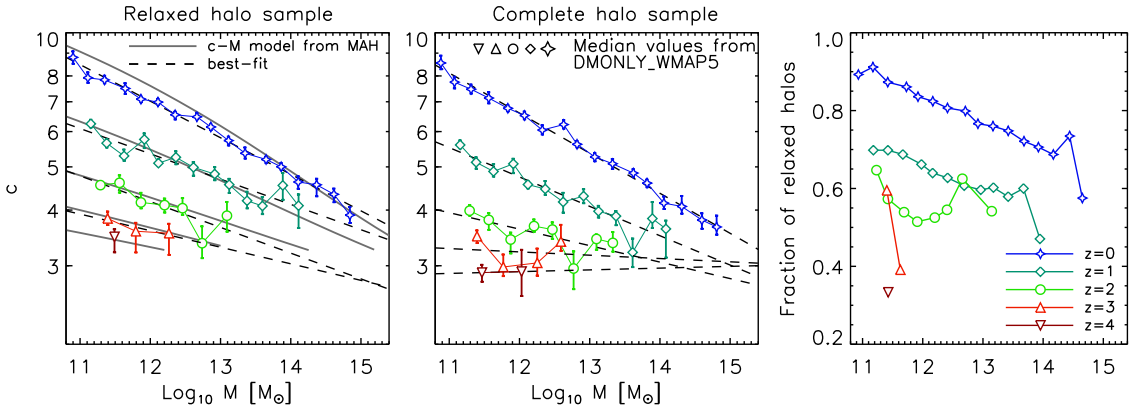

Figure 4.5: Concentration−mass relation at $z = 0, 1, 2, 3$ and 4 under the WMAP5 cosmology for the relaxed halo sample (left panel) and the full sample (middle panel). The star symbols indicate the median concentrations in logarithmic mass bins of width $\delta \log_{10} M = 0.25$ at $z = 0$ and $z = 1$, and $\delta \log_{10} M = 0.30$, 0.40 and 0.50 at $z = 2$, 3 and 4, respectively. Only bins containing at least 10 halos are shown. The error bars show the 1σ confidence limits. The dashed lines correspond to the best-fitting power-laws to the star symbols. In the left panel, the solid grey line shows the $c-M$ relation predicted by the semi-analytic model. The right panel shows the fraction of relaxed halos, with respect to the complete sample, for each mass bin and redshift. The inclusion of unrelaxed halos results in a flattening of, or even an upturn in, the $c - M$ relation at high redshift.

radius, and for which the convergence radius[iii] (Power et al. 2003) is smaller than the minimum fit radius of 0.05 times the virial radius. In addition, we consider two halo samples. A relaxed halo sample[iv] and a full halo sample. When considering only relaxed halos, as we have done so far, we find that we restrict our halo sample to around 80% of the total at $z = 0$, 65% at $z = 1$, 55% at $z = 2$, 50% at $z = 3$ and 43% at $z = 4$.

Fig. 4.5 shows the concentration-mass relation (at various z) of the relaxed sample (left panel) and the full sample (middle panel). These panels show the median value of the concentration (star symbols) in logarithmic mass bins of width $\delta \log_{10} M = 0.25$ at $z = 0$ and 1, and $\delta \log_{10} M = 0.30$, 0.40 and 0.50 at $z = 2$, 3 and 4, respectively. We increase the bin size with redshift so that each bin at a fixed mass contains on average approximately the same number of halos. For each bin the 1σ error bars were determined by bootstrap resampling the halos. Only bins containing at least 10 halos are shown. The dashed lines correspond to the best-fitting power-laws to the star symbols. In addition, the left panel, shows the $c - M$ relations predicted by the semi-analytic model in the solid grey lines. The middle panel shows a strong flattening and upturn in the $c - M$ relation at high z, in agreement with Muñoz-Cuartas et al. (2011) and Prada et al. (2012). However, this

[iii] The convergence radius is defined such that the two−body dynamical relaxation time-scale of the particles is similar to the age of the universe. For more details see Power et al. (2003) or Duffy et al. (2008).

[iv] As proposed by Neto et al. (2007), relaxed halos are defined as those halos for which the separation between the most bound particle and the centre of mass of the Friends-of-Friends halo is smaller than 0.07 times the virial radius.

upturn is not seen for the relaxed sample. Thus, we conclude that the previously seen upturn results from the inclusion of unrelaxed halos, in agreement with Ludlow et al. (2012). We show the fraction of relaxed halos (with respect to the total sample) for each mass bin and redshift in the right panel of Fig. 4.5. We find that the relaxed fraction tends to decrease towards high mass and redshift.

Our results suggest that the dynamical state of dark matter halos should be considered when analysing the parameters that describe the halo internal structure, because the density profiles of unrelaxed halos are poorly captured by the NFW fitting formula (e.g. Neto et al. 2007). Because halo concentrations are clearly affected by transient departures from equilibrium, we only consider relaxed halos in the remainder of this work.

4.4.3 Comparison with previous studies

In this section we compare the $c-M$ relations of the most recent studies on dark matter halo concentrations, van den Bosch et al. (2014) (hereafter, vdB14), Diemer & Kravtsov (2015) (hereafter, DK14), Dutton & Macciò (2014) (hereafter, DM14) and Ludlow et al. (2014) (hereafter, L14), with the model presented in this work.

vdB14 used the $c-M$ relation of Zhao et al. (2009) (obtained from fits of a full halo sample from numerical simulations) and adjusted the parameters by fitting it to the $c-M$ relation of the full halo sample from the Bolshoi simulations. vdB14 assumed the Bolshoi cosmology (consistent with WMAP7, Komatsu et al. 2011), but they made use of a semi-analytic model to scale their model to any cosmology. We assume the Planck cosmology and use the publicly available code of vdB14 to calculate their $c-M$ relation. DK14 obtained a concentration model given by a best-fit seven parameter function of peak height (ν) and slope of the linear power spectrum. They considered their full halo sample and extended their model to make it suitable for any cosmology. Finally, DM14 followed the evolution of the concentration of relaxed dark matter halos from a series of N-body simulations that assumed the Planck cosmology. DM14 fitted a power-law to the $c-M$ relation and restricted their analysis to relaxed halos only.

The left panel of Fig. 4.6 shows a comparison of our $c-M$ model (solid lines) to the model of vdB14. To compare with vdB14, we predicted the concentrations using the analytic expression for the MAH assuming the Planck cosmology (shown in Fig. 4.1) and a $z_{-2}-c$ relation with a constant of proportionality of 850 instead of the value 887 used for the WMAP5 cosmology (see §4.4.1 for a discussion of the cosmology dependence of our model). We find broad agreement with the relation of vdB14 only at $z=1$ and 2. In their work, van den Bosch et al. (2014) used the Zhao et al. (2009) model which assumes that c never drops below 4 at high redshift.

The middle-panel of Fig. 4.6 shows the DK14 $c-M$ relation calculated assuming the Planck cosmology. As they included their entire sample of halos for their $c-\nu$ relations,

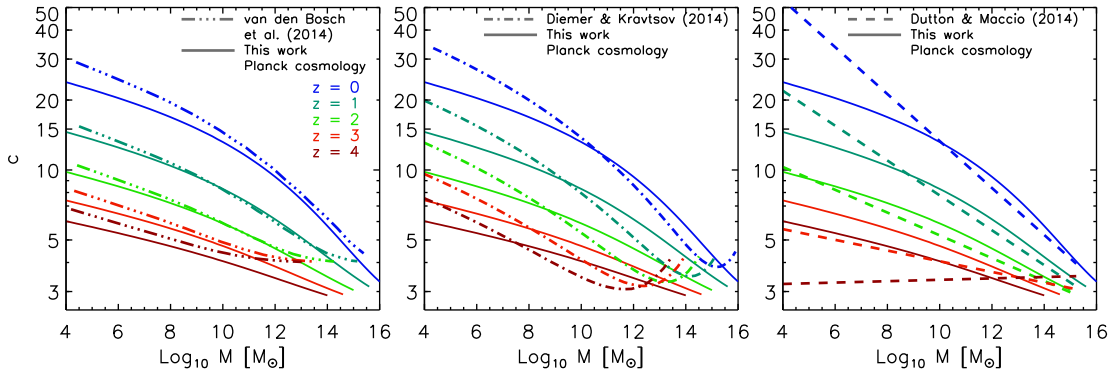

Figure 4.6: Comparison of the $c - M$ relation predicted by our model (solid lines) with the relations of van den Bosch et al. (2014) (left-panel), Diemer & Kravtsov (2015) (middle-panel) and Dutton & Macciò (2014) (right-panel). Note that Dutton & Macciò (2014) consider only relaxed halos for their best-fitting model and fit their model in the halo mass range $10^{10} - 10^{15}\,\mathrm{M}_{\odot}$, whereas Diemer & Kravtsov (2015) and van den Bosch et al. (2014) use their full halo sample and fit their model in halo mass range $10^{10} - 10^{15}\,\mathrm{M}_{\odot}$ and $10^{11} - 10^{15}\,\mathrm{M}_{\odot}$, respectively.

they obtained an upturn at the high-mass end at all redshifts. We find that our model predicts concentrations that are a factor of 1.2 larger just before the high-mass upturn. Finally, the right-panel of Fig. 4.6 shows reasonable agreement between our model and the Dutton & Macciò (2014) $c - M$ relation for $z = 0, 1, 2$ and 3 although the results diverge at low masses. In their work, DM14 fitted a power-law, $c \propto M^{\alpha}$, to the $c - M$ relation at all redshifts, and found that the slope, α, increases from -0.1 at $z = 0$, to 0.03 at $z = 5$. As they restricted their halo sample to relaxed halos, they did not obtain a significant upturn at the high-mass end of the $c - M$ relation.

Fig. 4.6 shows that the physically motivated model presented in this work yields $c - M$ relations that are generally in agreement with previous results. However, the important improvement with respect to previous works is that we are presenting a physical analytic model that can then be extrapolated to very low-masses, and is suitable for any cosmology.

The model for dark matter halo concentrations presented in this work strongly relies on the relation $\langle\rho(r_{-2})\rangle - \rho_{\rm crit}(z_{-2})$, which supports the idea that halos grow inside-out. This relation was introduced in Ludlow et al. (2013) and explored in L14, who recently presented a related model for the concentration-mass relation. In their work, L14 used the average MAHs from van den Bosch (2002a) and Zhao et al. (2009) that begin at $z_i = 0$[v]. They fitted the halo MAHs, written as $M(\rho_{\rm crit})$, with the NFW profile expressed in terms of the enclosed density. They looked for a correlation between the concentration parameter $c_{\rm MAH}$, that results from an NFW fit to the halo MAH, and the concentration

[v]L14 $c - M$ model used MAHs from van den Bosch (2002a) and Zhao et al. (2009) to show specific examples on how to construct a $c(M, z)$ relation for a given MAH, but any MAH model can be used.

parameter of the halos density profile, $c_{\rm NFW}$, and used the best-fitting relation to predict $c_{\rm NFW}$ from $c_{\rm MAH}$. L14 and this work use the same formation redshift definition to connect concentrations with halo MAHs. L14 used the $\langle\rho(r_{-2})\rangle - \rho_{\rm crit}(z_{-2})$ relation to find the $c_{\rm MAH} - c_{\rm NFW}$ relation, whereas in this work we used the analytic MAH model to define formation redshifts and used the $\langle\rho(r_{-2})\rangle - \rho_{\rm crit}(z_{-2})$ relation to predict concentrations. Although there is good agreement between L14 and our $c - M$ relation at $z = 0$, there are differences in the relations at high$-z$, e.g. a factor of 1.2 difference between the concentrations of a $10^{10}h^{-1}{\rm M}_{\odot}$ halo at $z = 2$ ($c \sim 5.25$ versus $c_{\rm L14} \sim 6.3$), and a factor of 1.58 for a $10^{5}h^{-1}{\rm M}_{\odot}$ halo at $z = 2$ ($c \sim 7.95$ versus. $c_{\rm L14} \sim 12.58$), for the WMAP5 cosmology. Those differences are mainly due to the different MAH models. Since the $\langle\rho(r_{-2})\rangle - \rho_{\rm crit}(z_{-2})$ relation is essentially equivalent to the $c_{\rm MAH} - c_{\rm NFW}$ relation, we expect L14 and our semi-analytic model to give consistent results if the same MAH model is used. We believe however that we have improved upon the L14 $c - M$ model by combining the $\langle\rho(r_{-2}, z_i)\rangle - \rho_{\rm crit}(z_{-2}, z_i)$ relation with an analytical MAH model, $M(z, z_i)$, that begins at any redshift z_i, and allows a detailed analysis of the redshift dependence of the $c(M, z)$ relation for relaxed halos. Another important difference is the tentative evidence for a cosmology dependence in the $\langle\rho(r_{-2}, z_i)\rangle - \rho_{\rm crit}(z_{-2}, z_i)$ relation (for a discussion see §4.4.1).

4.4.4 Extrapolation to low halo masses and high redshifts

Because our semi-analytic model for halo concentration is physical, rather than a purely empirical fit to the simulation results, we can use it to extrapolate beyond the mass and redshift ranges spanned by our simulations, assuming that the $z_{-2} - c$ relation given by eq. (4.16) holds. Fig. 4.7 shows the predicted concentration-mass relation for a wide range of halo masses ($\log_{10} M/\,{\rm M}_{\odot} = [-2, 16]$) and redshifts ($z = 0 - 20$). The dashed lines correspond to the high-mass power-law $c - M$ relations at low redshift. These are included to aid the comparison of the slopes of the $c - M$ relation in the high- and low-mass regimes. There is a clear 'break' in the $z = 0$ $c - M$ relation. For $M > 10^{12}\,{\rm M}_{\odot}$ concentration scales as $c \propto M^{-0.083}$, whereas at $M < 10^{9}\,{\rm M}_{\odot}$ it scales as $c \propto M^{-0.036}$. The change of slope around these halo masses is substantial up to $z = 3 - 4$. However, at $z > 4$ there is no 'break' in the $c - M$ relation. In §4.5 we provide a tentative explanation for the physical origin of the break in the $c - M$ relation.

We provide fitting functions for the $c - M$ relation in the high-z and low-z regimes. The following expression is suitable for the low-redshift regime ($z \leq 4$) and at all halo masses,

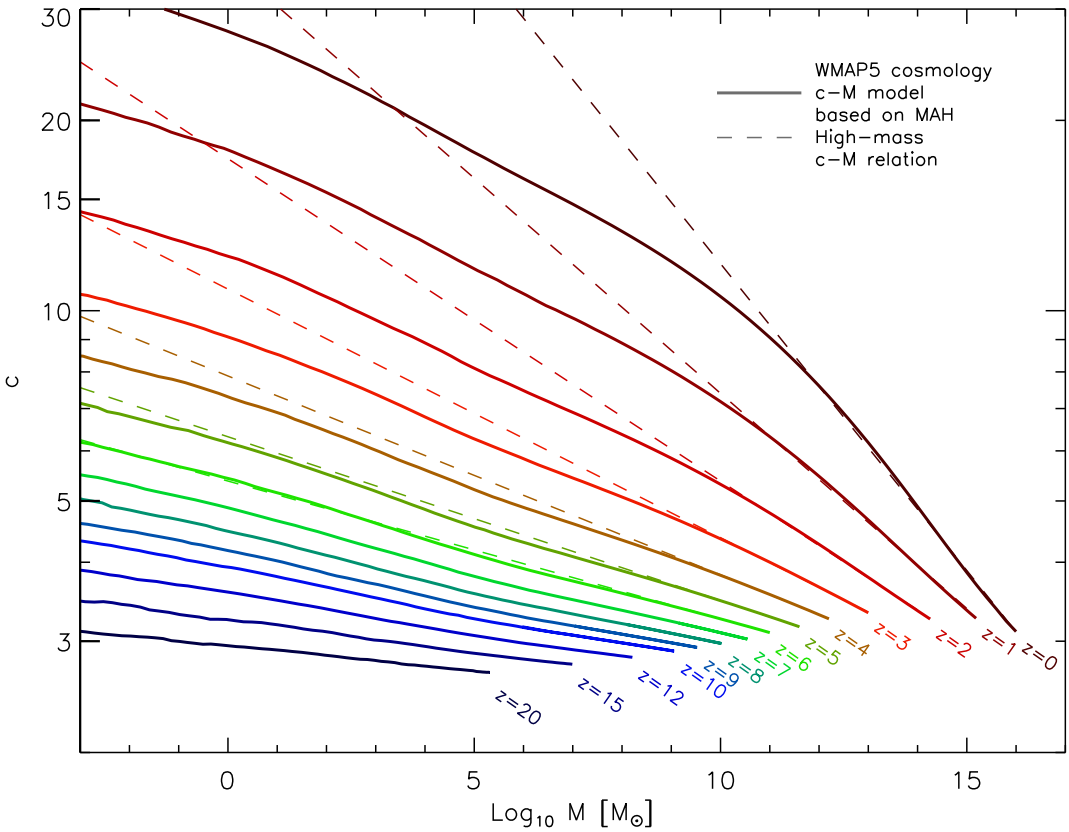

Figure 4.7: Predicted concentration − mass relation for the WMAP5 cosmology over a wide range of halo masses ($\log_{10} M/\,\mathrm{M}_\odot = [-2, 16]$) and redshifts ($z = 0 - 20$). The solid lines correspond to our $c - M$ model obtained from the halo MAH as described in §4.3. The lines are coloured as a function of redshift as indicated. The dashed lines correspond to power-law fits to the high-mass $c - M$ relation.

$$\begin{aligned} \log_{10} c &= \alpha + \beta \log_{10}(M/\,\mathrm{M}_\odot)[1 + \gamma(\log_{10} M/\,\mathrm{M}_\odot)^2], \\ \alpha &= 1.62774 - 0.2458(1+z) + 0.01716(1+z)^2, \\ \beta &= 1.66079 + 0.00359(1+z) - 1.6901(1+z)^{0.00417}, \\ \gamma &= -0.02049 + 0.0253(1+z)^{-0.1044}. \end{aligned} \tag{4.19}$$

In the high-redshift regime the $c - M$ relation can be fitted using only two parameters. The following expression is suitable for $z > 4$ and at all halo masses,

$$\begin{aligned} \log_{10} c &= \alpha + \beta \log_{10}(M/\,\mathrm{M}_\odot), \\ \alpha &= 1.226 - 0.1009(1+z) + 0.00378(1+z)^2, \\ \beta &= 0.008634 - 0.08814(1+z)^{-0.58816}. \end{aligned} \tag{4.20}$$

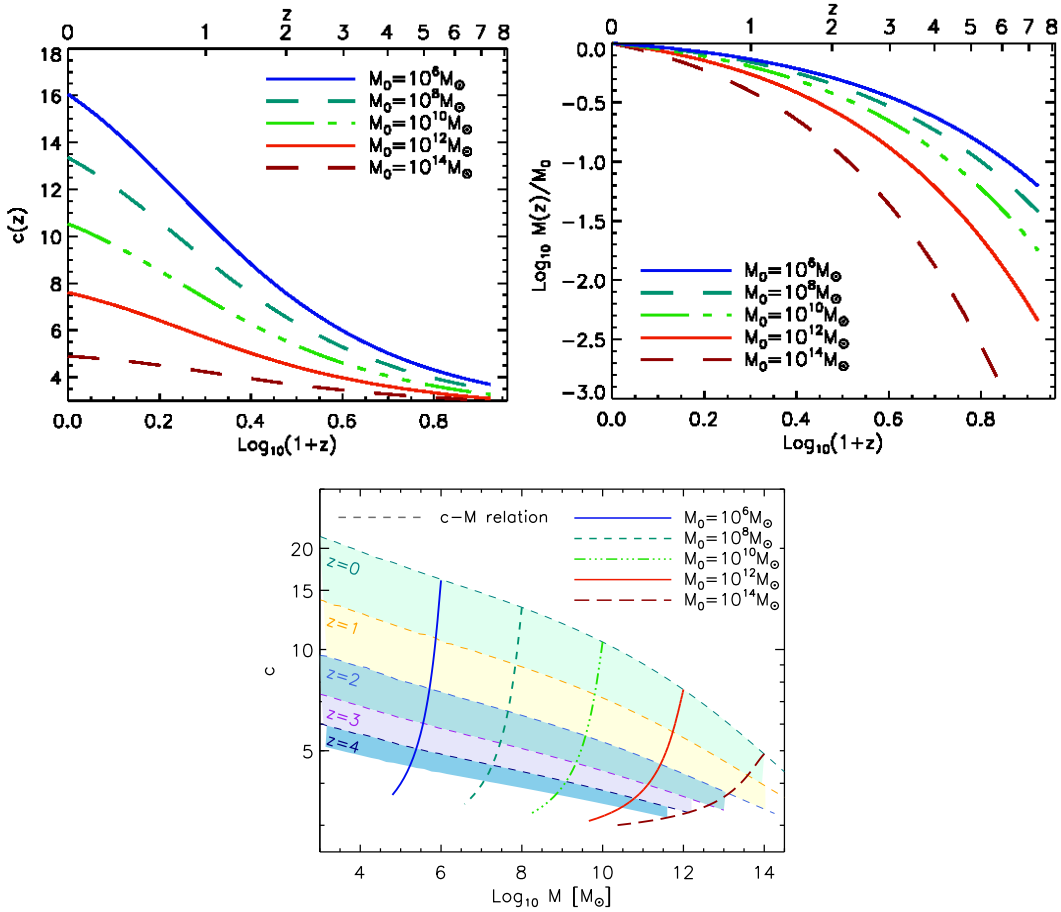

Figure 4.8: *Top left panel*: evolution of the concentrations of halos that at $z = 0$ have masses of $M_0 = 10^6, 10^8, 10^{10}, 10^{12}$ and $10^{14}\,\mathrm{M}_\odot$, as indicated in the legends. *Top right panel*: MAHs of halos of the same masses as in the left panel. *Bottom panel*: $c - M$ evolution (solid lines) of halos whose $c(z)$ and $M(z)$ are shown in the left and middle panels, respectively. The dashed curves show the concentration−mass relation at various redshifts z.

The above fitting functions have been calculated assuming the WMAP5 cosmology. Appendix A provides a series of best-fitting relations for the Planck cosmology, as well as a short discussion of the cosmology dependence of the $c - M$ relation presented in this work. In addition, Appendix A provides a description of a simple code (available for download in IDL and Python) that computes concentrations, MAHs and accretion rates as a function of redshift for any cosmology.

The $c - M$ model presented in this work predicts a concentration of $c = 3$ for microhalos of $10^{-7}\,\mathrm{M}_{\odot}$ at $z = 31$, in agreement with simulations of microhalo formation from Anderhalden & Diemand (2013) and Ishiyama (2014). In their work, Anderhalden & Diemand (2013) compared the empirical $c - M$ relations from Bullock et al. (2001) and Macciò et al. (2008) to their simulation outputs, and concluded that extrapolating simple power-law approximations to typical microhalo scales results in an overestimation of c by up to a factor of 10 at low$-z$. We also find large differences between extrapolations of the high-mass power-law fits to low-masses and the predictions of our physical model, as can be seen by comparing the dashed and solid lines in Fig. 4.7. This impacts calculations of the dark matter (DM) annihilation signal boost (see e.g. Sánchez-Conde & Prada 2014) and the power from DM annihilation (see e.g. Mack 2014), which make extensive use of $c - M$ relations at various redshifts. In §4.6 we analyse this issue in more detail by calculating the power from DM annihilation, assuming either the Duffy et al. (2008) $c - M$ relation (an empirical power-law fit for high halo masses) or the $c - M$ relation from this work.

4.5 Evolution of the concentration

In this section we use our semi-analytic model to investigate the evolution of concentration and the effects that determine the slope of the $c - M$ relation. The top left panel of Fig. 4.8 shows the evolution of the concentration of halos that have masses of $M_0 = 10^6, 10^8, 10^{10}, 10^{12}$ and $10^{14}\,\mathrm{M}_{\odot}$ at $z = 0$. The middle panel shows the corresponding halo MAHs normalized to the final halo mass at $z = 0$ (M_0). We computed $c(z)$ and $M(z)$ following the models described in §4.3 and §4.2.2, respectively.

In Chapter 3 we used EPS theory to show that the MAH of all halos can be described by the expression $M(z) = M_0(1 + z)^{\alpha} e^{\beta z}$, where the exponential is due to the fast growth at high$-z$ and the power-law due to the slow growth at low$-z$. In addition, the parameters α and β depend on halo mass. As a result, MAHs of halos larger than $10^{11}\,\mathrm{M}_{\odot}$ are mainly characterized by an exponential growth, whereas lower-mass halos exhibit a MAH closer to a power-law, as can be seen in the top right panel of Fig. 4.8.

Comparing the coloured curves in the top left and right panels of Fig. 4.8, we see an interesting relation between the evolution of c and the corresponding MAH. Dark matter halos with a small growth rate are *appear* to contract, and so their concentrations

grow rapidly. This can be understood as follows. At low redshift, during the dark energy dominated epoch, $M(z)$ of low-mass halos is characterized by a power-law (see Chapter 2). During this epoch, there is a drop in the accretion and merger rates of small halos, and the halo mass increases due to the evolution of the reference density used in the spherical overdensity definition of the halo ($\rho_{\rm crit}(z)$ in this case). This so-called *pseudo-evolution* of the halo mass is thus driven by the halo mass definition rather than the accretion of new material (see Diemer et al. 2013 and references therein). The pseudo-evolution of the halo mass gives the impression that concentrations are increasing because of contraction of the bound cores (Tasitsiomi et al. 2004; Zhao et al. 2003; Lu et al. 2006; Li et al. 2008; van den Bosch et al. 2014), when in fact the core radius remain constant. Indeed, the evolution of the $c-M$ relation has been shown to be sensitive to the definition of halo mass (e.g. Duffy et al. 2008). If we assume that r_{-2} is constant in the redshift range $z=0-1$, then the increase in r_{200} due to the drop in $\rho_{\rm crit}$ gives the approximate increase in the concentration values. We find $\frac{c(z=0)}{c(z=1)} = \frac{r_{200}(z=0)}{r_{200}(z=1)} = \left(\frac{\rho_{\rm crit}(z=1)}{\rho_{\rm crit}(z=0)}\right)^{1/3} \sim 1.4$, in agreement with the increase in concentration of a $M_0 = 10^6\,{\rm M}_\odot$ halo.

In the high-redshift regime ($z \gg 1$, matter-dominated epoch), the halo MAH is mainly characterized by exponential growth. During this time, concentrations grow by a factor of 2 (from $z=8$ to $z=2$) for a $M_0 = 10^6\,{\rm M}_\odot$ halo, decreasing to a factor of 1.08 (from $z=8$ to $z=2$) for a $M_0 = 10^{14}\,{\rm M}_\odot$ halo. The pseudo-evolution of the halo mass is negligible in comparison with the high accretion rates, and the core radius increases simultaneously with the virial radius, hence the concentration hardly grows.

In the case where the halo mass history is characterized by exponential growth at all z, representing the situation of a universe with no dark energy but $\Omega_{\rm m} \leq 1$, we find that concentrations do not reach such large values at $z=0$. We thus conclude that the evolution of the concentration is indirectly affected by the accelerated expansion of the Universe through the MAH and the halo mass definition.

Next, we analyse how the evolution of the concentration determines the change in slope of the $c-M$ relation. The bottom panel of Fig. 4.8 shows $c-M$ relations at various redshifts (dashed lines), and the $c-M$ evolution of halos with $M_0 = 10^6, 10^8, 10^{10}, 10^{12}$ and $10^{14}\,{\rm M}_\odot$ (solid lines). From this figure we see that the 'break' in the low-redshift $c-M$ relation that occurs at $M \sim 10^{11}\,{\rm M}_\odot$ is produced by the change in the halo MAH.

As mentioned, $M(z)$ changes from being dominated by exponential growth for high-mass halos, to power-law growth for low-mass halos. It is natural to ask why the break in $M(z)$ (and consequently in $c-M$) occurs at $\sim 10^{11}\,{\rm M}_\odot$. The answer is given by the rms of the linear theory density perturbation field, σ, that determines at which halo mass $M(z)$ changes from power-law dominated to exponential dominated. Since $\sigma \gg 1$ at low masses ($\ll 10^{11}\,{\rm M}_\odot$) and $\sigma \ll 1$ at high masses ($\gg 10^{11}\,{\rm M}_\odot$), the low values of σ at high masses increase the value of the β parameter in the exponential function of

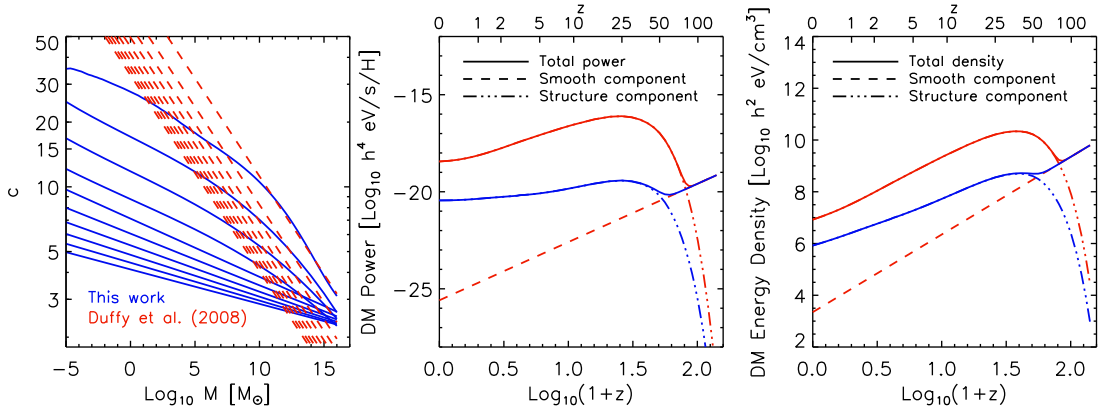

Figure 4.9: *Left panel:* Concentration-mass relation at various z ($z = 0 - 10$, top to bottom) from this work (blue solid lines) and from Duffy et al. (2008) (red dashed lines). At $z = 10$ and at a mass-scale of $1\,\mathrm{M}_\odot$ concentrations of Duffy et al. (2008) are a factor of 10 larger than concentrations predicted by this work, and a factor of 40 for a $10^{-9}\,\mathrm{M}_\odot$ halo. *Middle panel:* DM annihilation power per hydrogen nucleus as a function of redshift. The dashed line corresponds to the smooth component of the power and the dot-dashed lines to the structure component. The solid lines show the sum of the two components (structure+smooth). The red lines correspond to the power assuming the Duffy et al. (2008) $c - M$ relation, whereas the blue lines correspond to the power assuming the $c - M$ relation from this work. *Right panel:* as the middle panel, but showing the effective DM energy density as a function of redshift.

the $M(z)$ model, and thus $M(z)$ is mostly dominated by the exponential growth. As a result, higher mass halos increase their mass faster, their inner cores increase with the virial radius, and their concentrations do not grow as rapidly. The different growth rate of the concentrations produced by the change in the halos MAH, creates the 'break' in the $c - M$ relation.

Therefore, the break can be understood as being produced by the varying power in the density perturbations through the halo MAH, where the MAH of low-mass halos at $z < 1$ is mostly driven by pseudo-evolution. The break is less prominent at $z > 1$, because at higher redshifts $M(z)$ is mostly exponential for all halo masses (see eq. 4.3, $\tilde{\alpha} \to 0$ for $z_i > 0$ due to the growth factor and Fig. 4.2).

4.6 Implications for the dark matter annihilation signal

Dark matter (DM) particles are predicted to self-annihilate into Standard Model particles, thus injecting energy into the surrounding medium (e.g. Furlanetto et al. 2006). In this section we calculate the DM annihilation rate per unit volume produced by a smooth density field of DM (dominant before structure formation) and by cosmic structures (halos and microhalos). We separate DM into a smooth and structure component because the spatial distribution of mass is almost completely smooth at very early cosmic times. Later gravitational instability causes overdensities to grow, until micro DM halos form.

We follow Cirelli et al. (2009) and Mack (2014) in this calculation, and obtain the DM energy density and mean power from DM annihilation, assuming the physical $c - M$ relation from this work and from extrapolations of the fits to simulations from Duffy et al. (2008). Below we briefly describe the calculation of the DM annihilation rate produced by cosmic structures.

The DM annihilation rate per unit volume results from the sum of two parts, a structure contribution and a smooth contribution. The smooth contribution, dominant before structure formation, $z \gtrsim 100$, can be written as

$$R^{\rm smooth}(z) = \frac{\langle \sigma\nu \rangle}{2m_\chi^2}\rho_{\rm DM,0}^2(1+z)^6.$$

Where m_χ is the mass of the DM particle, $\langle \sigma\nu \rangle$ the self-annihilation cross section, and $\rho_{\rm DM,0}$ the smooth DM density today, $\rho_{\rm DM,0} = \Omega_{\rm DM,0}\rho_{\rm crit,0}$.

The DM annihilation rate per unit volume due to halos, R, is given by

$$R(z) = \frac{\langle \sigma v \rangle}{2m_\chi^2}\int {\rm d}M \frac{{\rm d}n}{{\rm d}M}(z,M)(1+z)^3 \int {\rm d}r 4\pi r^2 \rho^2(r,M). \tag{4.21}$$

Here m_χ is the mass of the dark matter particle and $\langle \sigma v \rangle$ is the average annihilation cross section, which we assume to be 100 GeV and $10^{-26}{\rm cm}^3{\rm s}^{-1}$, respectively (e.g. Aprile & et al. 2012). For the halo mass function, $\frac{{\rm d}n}{{\rm d}M}(z,M)$, we adopt the expression from Reed et al. (2007). For $\rho(r,M)$ we use the NFW density profile. We use M_{200} as the halo mass definition.

Next, we calculate the effective DM density from structure formation, defined as

$$\rho_{\rm DM}^{\rm eff}(z) \equiv \rho_{\rm DM,0}(1+z)^3 R_i(z), \tag{4.22}$$

$$R_i(z) \equiv \left(\frac{2m_\chi^2}{\langle \sigma v \rangle}R(z)\right)^{1/2}, \tag{4.23}$$

where $\rho_{\rm DM,0}$ is the average DM density today, $\rho_{\rm DM,0} = \Omega_{\rm DM,0}\rho_{\rm crit,0}$, with $\Omega_{\rm DM,0}h^2 = 0.11$. In this calculation we assume the WMAP5 cosmology in order to facilitate a comparison with models using the extrapolation of the Duffy et al. (2008) power-law fit to the $c-M$ relation predicted by WMAP5 N-body simulations.

Similarly, we calculate the averaged volume power, per hydrogen nucleus, produced from DM annihilation events as

$$P(z) = 2m_\chi c^2 \frac{R(z)}{n_{\rm H}(z)}, \tag{4.24}$$

with $n_{\rm H}(z) = \Omega_{\rm b,0}\rho_{\rm crit,0}(1-Y_{\rm p})(1+z)^3/m_{\rm H}$,[vi] the number density of hydrogen.

4.6.1 Implications

Several of the models that have been used to predict the DM annihilation signal (see e.g. Pieri et al. 2008; Lavalle et al. 2008; Pinzke et al. 2011) have extrapolated $c-M$ relations, obtained from power-law fits to simulation results, to mass far below the resolution limit of the simulations. These power-law extrapolations assign huge concentrations to the smallest halos, thus increasing the DM annihilation power. In this section we explore how our physically motivated $c-M$ relation, which flattens towards low-masses at low-redshift, affects the DM annihilation power when comparing it to the power calculated using an extrapolation of the Duffy et al. (2008) power-law $c-M$ relation (the results are similar for other published power-law fits to the $c-M$ relation from simulations).

The left panel of Fig. 4.9 shows a comparison between the concentration-mass relations at various redshifts ($z=0-10$) from this work (in blue solid lines) and of Duffy et al. (2008) (in red dashed lines). For $z=0$ there is good agreement at the high-mass end between both relations. However, at $z=10$ and at a mass-scale of $1\,{\rm M}_\odot$, the concentrations of Duffy et al. (2008) are a factor of 10 larger than the concentrations predicted by this work. For mass-scales of $10^{-9}\,{\rm M}_\odot$ the difference is a factor of 40. In the middle and right panels of Fig. 4.9 we investigate the effects of these different $c-M$ relations, showing the DM annihilation power per hydrogen nucleus and the effective DM energy density, respectively, as a function of redshift. In the middle panel, the dashed line corresponds to the smooth DM component of the power whereas the dot-dashed lines correspond to the structure component. The solid line shows the sum of the two components (structure+smooth). In each case the red lines correspond to the power assuming the Duffy et al. (2008) $c-M$ relation, whereas the blue lines correspond to the power assuming the $c-M$ relation from this work. The change in $c-M$ affects the normalization of the power as well as the redshift at which structures begin to dominate. Lower concentrations result in lower central densities. Since the annihilation rate per unit volume, R, scales as ρ^2, it is clear that R should decrease accordingly. At $z=0$, the DM annihilation power that assumes the $c-M$ relation predicted by this work is 2 orders of magnitude lower than the power obtained by extrapolating the Duffy et al. (2008) $c-M$ relation. In addition, the higher concentrations predicted by the Duffy et al. (2008) $c-M$ relation imply that halos dominate the power over the smooth DM density component at higher redshifts. Adopting the $c-M$ relation from this work results in the power from structures starting to dominate at $z\approx 50$ rather than at $z\approx 85$ (in agreement with Mack 2014; Ng et al. 2014). This lower redshift of structure formation dominating over the smooth component

[vi] $\Omega_{\rm b,0}$ is the present day baryon density parameter, $Y_{\rm p}=0.24$ the primordial mass fraction of helium and $m_{\rm H}$ the proton mass.

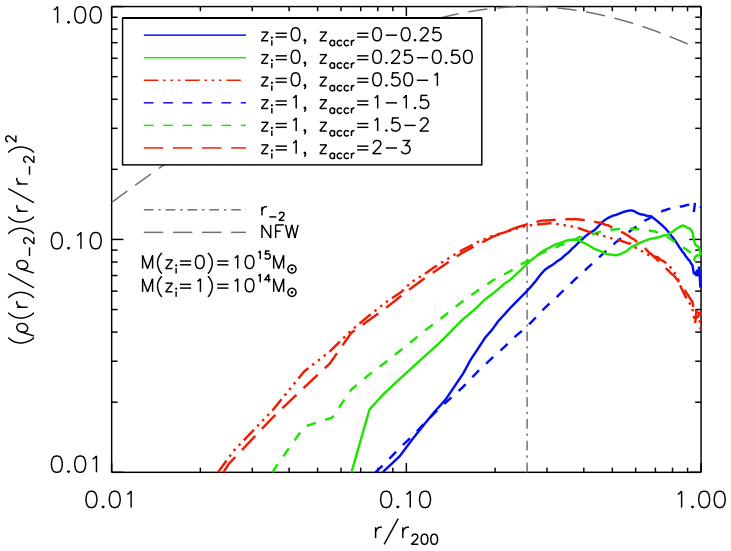

Figure 4.10: Distribution of particles within r_{200}. We show the particle distribution of two different halo samples, the first sample contains halos of $10^{15}\,M_\odot$ identified at $z_i = 0$ (solid lines) and the second sample contains halos of $10^{14}\,M_\odot$ identified at $z_i = 1$ (dashed lines). The solid grey line corresponds to a NFW density profile with concentration $c = 4$ and the vertical dashed line to the corresponding r_{-2} radius. The different colours indicate the redshift ($z_{\rm accr}$) during which the particles were accreted onto the halos (note that the same colour corresponds to different redshift ranges for different z_i).

could have important implications for searches of the 'Dark Ages' by radio telescopes (e.g. Pritchard & Loeb 2012).

4.7 Discussion

Dark matter halo concentrations have recently been the subject of extensive analysis due to the controversial reports of an upturn at the high-mass end of the relation (Prada et al. 2012; Muñoz-Cuartas et al. 2011; Diemer & Kravtsov 2015; Klypin et al. 2014). However, the semi-analytic model for dark matter halo concentrations presented in this work does not predict such an upturn. In this section we review the main assumptions that the model relies on and discuss the plausibility of the existence of the upturn.

First, the model assumes that the halo density profile is described by the NFW profile at all times. Although it is known that the Einasto (Einasto 1965) profile is more accurate than the NFW profile (Gao et al. 2008), it has an extra 'shape' parameter that complicates the fitting procedure and affects the concentration. Also, the residuals from the systematic deviations from the NFW shape are generally smaller than 10% and the NFW concentrations only differ by $10 - 20\%$ from Einasto fit and the velocity profile fit (as recently discussed by Dutton & Macciò 2014 and Klypin et al. 2014). We thus conclude that using the NFW profile to predict densities is not a major determinant in

the model.

Secondly, the model depends on the calibration of the $\rho_{\rm crit}(z_{-2}) - \langle\rho\rangle(< r_{-2})$ relation, which implies that halo formation is an inside out process, where the central part of a dark matter halo (contained within r_{-2}) forms first, and later accretion and mergers increase the mass and size of the halo without adding much material to its inner regions (Huss et al. 1999; Wang & Abel 2007). We test the assumption of 'halo formation' of our model. We analyze the distribution of particles within r_{200}, and differentiate the particles according to the period of time during which they were accreted. Fig. 4.10 shows the radial distribution of particles of two different halo samples. The first sample contains halos of $10^{15}\,{\rm M}_{\odot}$ identified at $z_i = 0$ (which are formed at $z_{-2} \approx 1$) and the second sample contains halos of $10^{14}\,{\rm M}_{\odot}$ identified at $z_i = 1$ (formed at $z_{-2} \approx 2$). We analysed halos of different masses but focused on massive halos, because their large radial velocities makes them more likely to contain recently accreted particles in their inner regions, and they are located in the upturn in the $c - M$ relation.

Fig. 4.10 shows the NFW density profile (in grey solid line) and the r_{-2} radius (in vertical dashed line) for a concentration of $c = 4$. The figure also shows the distribution of particles at $z_i = 0$ (solid coloured lines) and at $z_i = 1$ (dashed coloured lines). The different colours indicate the redshift ($z_{\rm accr}$) during which the particles were accreted onto the halos. The blue lines show that recently accreted particles are distributed around r_{200} and that only a tiny fraction ($< 2\%$ of the total, in the two cases), reside in the inner parts of the halo. In the case of the distribution of particles at $z_i = 0$, 2.5% of the total particles are in regions within r_{-2} after being accreted during $z_{\rm accr} = 0.25 - 0.5$, and 4.5% during $z_{\rm accr} = 0.5 - 1$. The same behavior is observed in halos of different masses identified at higher redshifts. We find that 8% of all particles accreted after the halo has formed are in the center, not enough to significantly alter the mass within r_{-2} so as to increase concentration. We then find the halo formation assumption that the model relies on to be valid.

Finally, in the calibration of the $\rho_{\rm crit}(z_{-2}) - \langle\rho\rangle(< r_{-2})$ relation, we only consider relaxed halos. The selection conditions generally used to differentiate relaxed halos from unrelaxed (Macciò et al. 2007; Neto et al. 2007) have recently been revisited by Klypin et al. (2014). These conditions include the virial parameters ($2K/|W| - 1$, where K and W are the kinetic and potential energies), the offset parameter $X_{\rm off}$ (distance between the potential minimum and the center of mass), and the spin parameter. In their work, Klypin et al. (2014) argued that the virial equilibrium condition is too simplistic and needs to include the effects of the surface pressure and external forces. They applied these corrections to the virial parameters and selected halos that had previously been rejected. As a result, they obtained an upturn in the high-mass end of the $c - M$ relation and claimed that the large concentration of massive halos is due to their infall velocities,

which are more radial and result in deeper penetration of infalling mass into the halo that reaches the inner parts. In this work we selected relaxed halos using only the condition that $X_{\rm off} < 0.07$ following Duffy et al. (2008) and Neto et al. (2007), who found that this simple criterion resulted in the removal of the vast majority of unrelaxed halos. We did not use any additional criteria and did not find any upturn at high halo masses, but concluded that the strong flattening of the $c - M$ relation at high redshift is due to unrelaxed halos (Fig. 4.5). We cannot say we disagree with Klypin et al. (2014) regarding the relaxation conditions, because our simulations do not have sufficiently large box sizes to model a large sample of the massive highly unrelaxed halos that likely 'shape' the upturn.

4.8 Conclusion

In this chapter we have linked the concentration of a halo to its MAH. We extended the analytic framework presented in Chapter 2 to show that the halo mass history $\tilde{M}(z, M(z_i), z_i)$ of a halo with mass $M(z_i)$ at z_i can be described by

$$\tilde{M}(z, M(z_i), z_i) = M(z_i)(1 + z - z_i)^{\tilde{\alpha}} e^{\tilde{\beta}(z - z_i)},$$

where $\tilde{\alpha}$ and $\tilde{\beta}$ are parameters that depend on $M(z_i)$ and cosmology. We have compared the above formula to simulation outputs and the most recent empirical mass history model from the literature (van den Bosch et al. 2014) and found generally reasonable agreement.

Building on the work by Ludlow et al. (2014), we presented a semi-analytic model for halo concentration as a function of halo mass and redshift. The resulting $c - M$ relations were tested using N-body simulations, and compared to the most recent empirical $c - M$ relations from the literature (van den Bosch et al. 2014; Diemer & Kravtsov 2015; Dutton & Macciò 2014). The 'upturn' at high masses seen by some studies (Diemer & Kravtsov 2015; Klypin et al. 2011; Prada et al. 2012; Dutton & Macciò 2014) is not reproduced by our physically derived model which, however, only applies to relaxed halos. We analysed the $c - M$ relations obtained from the numerical simulations, where we differentiated between relaxed and unrelaxed halos. We found that the upturn is due to the inclusion of unrelaxed halos, supporting the previous claim of Ludlow et al. (2012).

Our model predicts a change in the slope of the $c - M$ relation at $z = 0 - 3$ and a 'break' in the $z \sim 0$ $c - M$ relation at a mass of $\sim 10^{11}\,{\rm M}_{\odot}$. We analysed the evolution of concentration and found that it increases more rapidly during the dark energy era, when the accretion rates of dark matter halos decrease due to the accelerated expansion of the Universe. We found that the break at a halo mass $\sim 10^{11}\,{\rm M}_{\odot}$ results from the change of the functional form of $M(z)$, that goes from being dominated by a power-law (for

low-mass halos) to an exponential (for high-mass halos). This change in $M(z)$ is driven by the rms of the linear density perturbation field. Halos with mass $M \gg 10^{11}\,\mathrm{M}_{\odot}$, have $\sigma \ll 1$, are characterized by an exponential growth, and have lower concentrations as a result. Whereas halos with mass $M \ll 10^{11}\,\mathrm{M}_{\odot}$, have large σ, are characterized by a power-law growth. In this last case, there is a pseudo-evolution in the halo masses (i.e. mass growth due to the definition of the halo in terms of a overdensity criterion, Diemer et al. 2013) and the core radius remains approximately constant, causing the concentrations to grow. The different growth rate of the concentrations at low and high mass produces the break in the $z \sim 0$ $c - M$ relation. This break is not so evident for $z > 1$, because at higher redshifts $M(z)$ is mostly exponential for all halo masses ($\tilde{\alpha} \to 0$ for $z_i > 0$ due to the growth factor), causing all concentrations to grow at approximately the same rate (as seen in Fig. 4.8).

Finally, we addressed the impact of the $c - M$ relation presented in this work on predictions for the dark matter annihilation signal. We calculated the DM annihilation rate from cosmic structures and compared the results obtained by extrapolating the Duffy et al. (2008) power-law fit (which is similar to other published fits to the results of simulations) to the rate obtained by using the $c-M$ relation predicted by our model. We found that the power from DM annihilation at $z = 0$ is 2 orders of magnitude lower than the power obtained by extrapolating the Duffy et al. (2008) $c-M$ relation (in agreement with Mack 2014; Ng et al. 2014).

5

On the hot halo formation

This chapter discusses the physical mechanisms that drive the formation of the hot hydrostatic halo.

In the previous chapters we studied the formation and growth of dark matter halos, that are essential for the condensation of gas and formation of galaxies. The latter part of this thesis is devoted to investigating the physical state of gaseous halos and their connection to the evolution of galaxies. Gas, unlike dark matter, is affected by the presence of additional physical processes, such as hydrodynamical forces and radiative cooling. Most of the cosmological gas that falls into the potential well of a dark matter halo is deviated from its path towards the inner galaxy. When it crosses the virial radius it encounters other gas, it shocks and is heated, or it is expelled out of the halo and eventually re-accreted, depending on the physical state of the gaseous halo. Understanding then the structure of the hot hydrostatic halo atmosphere, its origin and subsequent evolution, is essential for any comprehensive theory of galaxy formation. In this chapter we use a suite of hydrodynamical cosmological simulations to investigate the thermal properties of gas accreting onto halos, and the hot halo formation. We analyze how the presence of energy sources like stellar and AGN feedback impact on the evolution of the hot halo. We then develop a semi-analytic approach to calculate a critical mass-scale above which the hot halo forms. The model depends on the amount of hot gas in the halo as well as on the fraction of gas that experiences a shock when crossing the virial radius. Readers unfamiliar with this topic are encouraged to first read §1.3 for a brief description on galaxy formation theory.

5.1 Introduction

One of the major goals of modern galaxy formation theory is to understand the physical mechanisms that halt the star formation process, by either removing, heating or preventing the infall of cold gas onto the galactic disc. X-ray observations suggest that for halos hosting massive galaxies the majority of baryonic matter resides not in the galaxies, but in the halo in the form of virialized hot gas (e.g. Lin et al. 2003; Crain et al. 2010; Anderson & Bregman 2011). This work is devoted to investigate the formation of the hot gaseous corona (also refereed to as 'hot halo' or 'hot atmosphere') around galaxies, that may help to prevent the infall of gas onto galaxies, and has been suggested to explain the observed galaxy bimodality (Dekel & Birnboim 2006).

The hot gaseous corona is produced as a result of an important heating process, that was initially discussed by Rees & Ostriker (1977), Silk & Rees (1998), White & Rees (1978) and White & Frenk (1991), as an attempt to explain the reduced efficiency of star formation within massive halos. They proposed that while a dark matter halo relaxes to virial equilibrium, gas falling into it would experience a shock depending on the cooling time of gas at the virial radius. As long as the cooling time is smaller than the dynamical time (or Hubble time), the infalling gas cools (typically inside a current 'cooling radius') and settles into the galaxy. If, on the other hand, the cooling time exceeds the dynamical time, the gas is not able to radiate away the thermal energy that supports it. It therefore adjusts its density and temperature quasi statically, forming a hot hydrostatic halo atmosphere, pressure supported against gravitational collapse. If the gas accretes supersonically (as it will do if the halo virial temperature exceeds the temperature of the accreting gas, see Binney 1977), it will experience a shock and heat to the virial temperature of the halo. Over the past decade, the works of Birnboim & Dekel (2003) and Dekel & Birnboim (2006, hereafter DB06) investigated the stability of accretion shocks around galaxies, and confirmed that a hot atmosphere forms when the compression time of shocked gas is larger than its cooling time, occuring when halos reach a mass scale of $6 \times 10^{11}\,\mathrm{M}_{\odot}$.

Numerical simulations showed that cold gas accreting through filaments does not necessarily experience a shock when crossing the virial radius, even if the spherically averaged cooling radius is smaller than the virial radius. Simulation-based works then concluded that there are two modes of gas accretion, named as hot and cold accretion, that are able to coexist in high-mass halos at high redshift (Kereš et al. 2005; Dekel & Birnboim 2006; Ocvirk et al. 2008; Dekel et al. 2009; van de Voort et al. 2011; Faucher-Giguère et al. 2011; Nelson et al. 2013). The hot mode of accretion refers to the accreted gas that shock-heats to the halo virial temperature. The cold mode refers to gas that flows along dark matter filaments and is accreted onto the central galaxy without being shock

heated near the virial radius. It has been found that the cold streams end up being the dominant mode of accretion in halos at high redshift (Dekel et al. 2009). However, it has also been found that most of cold gas from filaments does experience significant heating at the moment of accretion onto the galaxy (Nelson et al. 2013).

Numerical deficiencies inherent from different simulations may modify the relative contributions of the hot and cold modes of accretion. In this work we discuss the differences in the performance of gas mixing in the moving mesh code AREPO (Springel 2010), in the standard SPH code GADGET (Springel 2005) and in the most recent formulation of SPH named 'Anarchy' (Dalla Vecchia 2016 in prep.), and also compare different criteria to select hot mode accretion onto halos.

Besides the rates of gas accretion, the hot halo is susceptible to feedback mechanisms, that can suppress cooling from the hot halo, modify the distribution of hot gas in the halo (van de Voort & Schaye 2012) and (to a limited degree) reduce the accretion rates onto halos (van de Voort et al. 2011). In this work we investigate the impact of feedback mechanisms on the hot halo in detail and analyze whether feedback is able to modify the mass scale of hot halo formation.

We use the suite of cosmological hydrodynamical simulations from the EAGLE project to investigate the physical properties of the hot gas in the halo, and its dependence on energy sources like stellar feedback and AGN feedback. The main goal of this work is to study the thermal properties of gas accreting onto halos and the gas mass that remains hot in the halo ($M_{\rm hot}$). We will make use of $M_{\rm hot}$ and the fraction of shock-heated gas in the derivation of a semi-analytic approach, to calculate the heating rates of gas in the halo and the mass scale of hot halo formation. In a companion work, Correa et al. (2016, hereafter Paper II), we compare gas cooling rates implemented in semi-analytic models with those obtained with the EAGLE simulations. Having determined the mass scale above which a hot halo forms, we derive a physically motivated model for gas accretion onto galaxies that depends on the hot/cold modes of accretion onto halos, and on the rate of gas cooling from the hot halo.

The outline of this chapter is as follows. First, we describe the EAGLE simulations series used in this study and analysis methodology in §5.2. We present our main results concerning the physical properties of hot and cold gas in the halo in §5.3 and on the modes of gas accretion in §5.4. In §5.5 we develop a semi-analytic approach to calculate a 'critical mass scale', $M_{\rm crit}$, for hot halo formation, and compare with our numerical results and previous works. Finally, in §5.6 we summarize our conclusions.

Table 5.1: List of simulations. From left-to-right the columns show: simulation identifier; comoving box size; number of dark matter particles (there are equally many baryonic particles); initial baryonic particle mass; dark matter particle mass; comoving (Plummer-equivalent) gravitational softening; maximum physical softening.

Simulation	L (cMpc)	N	$m_{\rm b}$ ($\rm M_\odot$)	$m_{\rm dm}$ ($\rm M_\odot$)	$\varepsilon_{\rm com}$ (ckpc)	$\varepsilon_{\rm prop}$ (proper kpc)
L025N0376	25	376^3	1.81×10^6	9.70×10^6	2.66	0.70
L025N0752	25	752^3	2.26×10^5	1.21×10^6	1.33	0.35
L050N0752	50	752^3	1.81×10^6	9.70×10^6	2.66	0.70
L100N1504	100	1504^3	1.81×10^6	9.70×10^6	2.66	0.70

5.2 Simulations

To investigate the formation and evolution of the hot halos surrounding galaxies, we use cosmological, hydrodynamical simulations from the Evolution and Assembly of GaLaxies and their Environments project (EAGLE; Schaye et al. 2015; Crain et al. 2015). The EAGLE simulations were run using a modified version of GADGET 3 (Springel 2005), a N-Body Tree-PM smoothed particle hydrodynamics (SPH) code. The EAGLE version contains a new formulation of SPH, new time stepping and new subgrid physics. Below we present a summary of the EAGLE models. For a more complete description see Schaye et al. (2015).

The EAGLE simulations assume a ΛCDM cosmology with the parameters derived from *Planck-1* data (Planck Collaboration et al. 2014), $\Omega_{\rm m} = 1 - \Omega_\Lambda = 0.307$, $\Omega_{\rm b} = 0.04825$, $h = 0.6777$, $\sigma_8 = 0.8288$, $n_s = 0.9611$. The primordial mass fractions of hydrogen and helium are $X = 0.752$ and $Y = 0.248$, respectively.

Table 5.1 lists the box sizes and resolutions of the simulations used in this work. We use the notation Lxxx$N$yyyy, where xxx indicates box size (ranging from 25 to 100 comoving Mpc) and yyyy indicates the cube root of the number of particles per species (ranging from 376^3 to 1504^3, with the number of baryonic particles initially equal to the number of dark mater particles). The gravitational softening was kept fixed in comoving units down to $z = 2.8$ and in proper units thereafter. We will refer to simulations with the mass and spatial resolution of L025N0376 as intermediate-resolution runs, and to simulations with the resolution of L025N0752 as high-resolution runs.

5.2.1 Baryonic physics

Radiative cooling and photo-heating are included as in Wiersma et al. (2009). The element-by-element radiative rates are computed in the presence of the cosmic microwave background (CMB), and the Haardt & Madau (2001) model for UV and X-ray background radiation from quasars and galaxies.

Star formation is modelled following the recipe of Schaye & Dalla Vecchia (2008). Star formation is stochastic above a density threshold, $n_{\rm H,0}$, that depends on metallicity (in the model of Schaye 2004, $n_{\rm H,0}$ is the density of the warm, atomic phase just before it becomes multiphase with a cold, molecular component), with the probability of forming stars dependent on pressure, which is limited to values above a polytropic equation of state $P \propto \rho_{\rm gas}^{4/3}$. The implementation of stellar evolution and mass loss follows the work of Wiersma et al. (2009). Star particles are treated as simple stellar populations with a Chabrier (2003) initial mass function, spanning the range $0.1 - 100\,{\rm M}_\odot$. Feedback from star formation and supernovae events follows the stochastic thermal feedback scheme of Dalla Vecchia & Schaye (2012). Rather than heating all neighbouring gas particles within the SPH kernel, they are selected stochastically based on the available energy, and then heated by a fixed temperature difference of $\Delta T = 10^{7.5}$K. The probability that a neighbouring SPH particle is heated is determined by the fraction of the energy budget that is available for feedback, $f_{\rm th}$, defined as

$$f_{\rm th} = f_{\rm th,min} + \frac{f_{\rm th,max} - f_{\rm th,min}}{1 + \left(\frac{Z}{0.1Z_\odot}\right)^{n_Z} \left(\frac{n_{\rm H,birth}}{n_{\rm H,0}}\right)^{-n_n}}, \tag{5.1}$$

which depends on maximum and minimum threshold values ($f_{\rm th,max}$ and $f_{\rm th,min}$, respectively), on density ($n_{\rm H,0}$ refers to hydrogen number density and $n_{\rm H,birth}$ to the density inherited by the star particle) and metallicity (Z) of the gas particle. If ΔT is sufficiently high to ensure that radiative losses are initially small, the physical efficiency of feedback can be controlled by adjusting $f_{\rm th}$. By convention $f_{\rm th} = 1$ corresponds to the expected value of injected energy being $E_{\rm SN} = 1.736 \times 10^{49}$ erg ${\rm M}_\odot^{-1}$ of stellar mass formed.

For AGN feedback, black hole seeds (of $\approx 1.4 \times 10^5\,{\rm M}_\odot$) are included in the most bound gas particle in halos of mass greater than $\approx 1.4 \times 10^{10}\,{\rm M}_\odot$ (Springel et al. 2005). Black holes can grow through mergers and accretion. The accretion events follow a modified Bondi-Hoyle formula that accounts for the angular momentum of the accreting gas (Rosas-Guevara et al. 2013; Schaye et al. 2015), and a free parameter that is related to disk viscosity. AGN feedback follows the accretion of mass onto the black hole, where a fraction (0.015) of the accreted rest mass energy is released as thermal energy into the surrounding gas, and is implemented stochastically, as per the supernova feedback scheme, with a fixed free parameter heating temperature, $\Delta T_{\rm AGN}$.

The reference simulations (hereafter REF) use $f_{\rm th,max} = 3$, $f_{\rm th,min} = 0.3$, $n_{\rm H,0} = 0.67$ cm^{-3} and $\Delta T_{\rm AGN} = 10^{8.5}$ K. The values were chosen to obtain very good agreement with the present-day galaxy stellar mass function and disk galaxy sizes (Schaye et al. 2015). When the resolution is increased, the parameters may need to be (re-)calibrated to match the observales. The high-resolution simulation with recalibrated parameters is called RECAL. In addition to REF and RECAL, we also use simulations with different

Table 5.2: List of feedback parameters that are varied in the simulations. From left-to-right the columns show: simulation identifier (prefix), asymptotic maximum and minimum values of the efficiency of star formation feedback ($f_{\rm th}$), density term denominator ($n_{\rm H,0}$) and exponents ($n_{\rm n}$ and $n_{\rm Z}$) from eq. (5.1), and temperature increment of stochastic AGN heating ($\Delta T_{\rm AGN}$).

Simulation	$f_{\rm th,(max,min)}$	$n_{\rm H,0}$ ($\rm cm^{-3}$)	$n_{\rm n}(=n_{\rm Z})$ ($\rm cm^{-3}$)	$\Delta T_{\rm AGN}$ (K)
REF	$3.0, 0.30$	0.67	$2/\ln(10)$	$10^{8.5}$
WeakFB	$1.5, 0.15$	0.67	$2/\ln(10)$	$10^{8.5}$
StrongFB	$6.0, 0.60$	0.67	$2/\ln(10)$	$10^{8.5}$
NoAGN	$3.0, 0.30$	0.67	$2/\ln(10)$	–
AGNdT9	$3.0, 0.30$	0.67	$2/\ln(10)$	$10^{9.5}$

feedback implementations to test the impact of feedback on the formation of the hot halo. Table 5.2 lists the values of the feedback parameters adopted in each simulation. Additional information regarding the performance of the EAGLE simulations, including an analysis of subgrid parameter variations, a study of the evolution of galaxy masses and of star formation rates can be found in Crain et al. (2015), Furlong et al. (2014) and Schaye et al. (2015).

5.2.2 Hydrodynamics

There has been a lot of debate regarding the utility of SPH modelling of fluid mixing and of gas heating and cooling. For instance, three-dimensional hydrodynamical simulations (Kay et al. 2000; Fardal et al. 2001; Kereš et al. 2005; Kereš et al. 2009; van de Voort et al. 2011) have suggested that the majority of the gas entering galaxies has never been shock-heated. On the other hand, it has been shown by Thacker et al. (2000), Agertz et al. (2007) and Creasey et al. (2011) that SPH simulations may not adequately resolve shocks of accreted gas. Since shocks are generally spread over several SPH kernel lengths, the heating rate is smoothed over time, making it easier for radiative cooling to become important. In addition, if radiative cooling is able to limit the maximum temperature reached by the gas particle, the radiative loses are enhanced.

Differently from SPH, numerical simulations using grids do not widely smooth out the shocks, and are then better at identifying shock temperatures spikes. Recently, Nelson et al. (2013) compared the moving mesh code AREPO (Springel 2010) with the standard SPH code GADGET, and found that most of the cold gas from filaments experiences significant heating at the moment of accretion, implying that the numerical deficiencies inherent in different simulations may modify the relative contributions of hot and cold modes of accretion. Similarly, Vogelsberger et al. (2012) compared both codes and discussed the two main reasons for the differences in the cooling rates. First, gas mixing is largely suppressed in GADGET, especially at density phase boundaries. Second, the

presence of turbulent energy drives differences in dissipative heating in halos. The same conclusion was reached by Schaller et al. (2015), who compared GADGET with a more recent formulation of SPH named 'Anarchy' (Dalla Vecchia 2016 in prep., see Appendix A of Schaye et al. 2015 and Section 2.2.2 of Schaller et al. 2015), and found that unlike GADGET, Anarchy is able to mix phases in contact discontinuity allowing dense clumps to dissolve into the hot halo.

The EAGLE simulations include Anarchy, which has proven to solve the problems identified by Vogelsberger et al. (2012), and greatly improves the performance on standard hydrodynamical tests, when compared to the original SPH implementation in GADGET (Dalla Vecchia 2016 in prep. but see Hu et al. 2014 for similar results). Anarchy makes use of the pressure-entropy formulation derived in Hopkins (2013), allowing it to avoid spurious jumps at contact discontinuities. It also uses an artificial viscosity switch as in Cullen & Dehnen (2010), that allows the viscosity limiter to be stronger when shocks and shear flows are present. In addition, Anarchy includes an artificial conduction switch (similar to that of Price 2008), the C^2 Wendland (1995) kernel and the time step limiters of Durier & Dalla Vecchia (2012), which ensure that ambient particles do not remain inactive when a shock is approaching. These substantial improvements of the SPH formulation in the EAGLE simulations motivate a detailed description of the resulting predictions for hot halo formation and of hot/cold mode accretion.

Besides numerical performances, some differences in the contribution of hot and cold modes of accretion onto galaxies and halos are due to the method employed to select shock-heated gas. Previous works (e.g. Kereš et al. 2005, 2009; Faucher-Giguère et al. 2011; van de Voort et al. 2011; Nelson et al. 2013, among others) followed the gas thermal history and applied a fixed temperature cut on the distribution of the gas maximum temperature ($T_{\rm max}$), to separate shock-heated from cold gas. However, we believe that at high redshift $T_{\rm max}$ may not be suitable for identifying cold flows, if it occurs that gas goes through a shock but immediately cools afterwards (due to in-shock cooling, e.g. Hutchings & Thomas 2000). In this case, if a filament is mostly cold except at a point in space and for a short period of time, numerical studies would label it as hot mode accretion but observations would call it a cold flow. Using the EAGLE simulations and the $T_{\rm max}$ criteria to select hot mode accretion (with $T_{\rm max,cut} = 10^{5.5}$ K), we analyse in-shock cooling. We find that 80% (90%) of the gas particles labeled as shock-heated accretion onto $10^{12}\,{\rm M}_\odot$ ($10^{13}\,{\rm M}_\odot$) halos in the redshift interval 2.01-2.24, remain hot after crossing the virial radius (have temperatures larger than 10^5 K at $z = 2$). But the remaining 20% (10%) that goes through a shock and is heated, rapidly cools afterwards (have temperatures lower than 10^5 K at $z = 2$). Then, to avoid counting gas particles as hot when they are actually undergoing in-shock cooling, we analyse an alternative method to identify shock-heated particles in §5.4, based on post-shock temperature and

entropy values.

5.2.3 Identifying halos and galaxies

Throughout this work we select the largest subhalo in each Friends-of-Friends (FoF) group (Davis et al. 1985), and use the SUBFIND algorithm (Springel et al. 2001; Dolag et al. 2009) to identify the substructures (subhalos) within it. The FoF algorithm adopts a dimensionless linking length of 0.2, and the SUBFIND algorithm calculates halo virial masses and radii via a spherical overdensity routine that centers the main subhalo from the FoF group on the minimum of the gravitational potential. We define halo masses, M_{200}, as all matter within the radius r_{200} for which the mean internal density is 200 times the critical density.

Once we have identified the largest halos, we build merger trees across the simulation snapshots as follows. First, at each output redshift (snapshot) we select 'resolved' halos which contain more than 1000 dark matter particles, corresponding to a minimum halo mass of $M_{200} = 10^{9.818}\,\mathrm{M}_\odot$ ($10^{8.835}\,\mathrm{M}_\odot$) in the intermediate- (high-) resolution simulations. This limit on the number of dark mater particles results from a convergence analysis that we present in Chapter 6, where we find that in smaller halos the accretion onto galaxies does not converge, indicating that the inner galaxies are not well resolved. We refer to the resolved halos as 'descendants', and then link each descendant with a unique 'progenitor' at the previous output redshift. This is nontrivial due to halo fragmentation, in which subhalos of a progenitor halo may have descendants that reside in more than one halo. Such fragmentation can be either spurious or due to a physical unbinding event. To correct this, we link the descendant to the progenitor that contains the majority of the descendant's 25 most bound dark matter particles (see 3 for an analysis of halo mass history convergence using the mentioned criteria to connect halos between snapshots).

To select the central galaxies embedded in each resolved halo, we identify the gravitationally bound cold and dense gas within r_{200} that is star-forming and/or has a hydrogen number density, $n_\mathrm{H} > 0.01\mathrm{cm}^{-3}$, and temperature $T < 10^5\mathrm{K}$ (atomic ISM). We also require that all particles should be contained within a sphere of radius $0.15 \times r_{200}$, in order not to confuse infalling cold flows (that would be included by the $T - n_\mathrm{H}$ cuts but are at large radii) as part of the galaxy.

5.2.4 Measuring gas accretion

In this chapter (as well as in Chapter 6), we distinguish between gas accreted onto a halo from gas accreted onto a galaxy. To select gas particles accreted onto halos we first build merger trees across the simulation snapshots. For each descendant halo at z_i and its

linked progenitor at z_j ($z_j > z_i$), we identify the particles that are in the descendant but not in its progenitor by performing particle ID matching. We then select particles that are new in the system and are within the virial radius, as particles accreted in the redshift range $z_i \leq z < z_j$. To calculate gas accretion onto galaxies we follow the methodology described above for calculating accreted particles onto halos, but now we select the new particles within the radius $0.15 \times r_{200}$ as particles accreted onto the galaxies in the redshift range $z_i \leq z < z_j$ (see Chapter 6 for a discussion on methods for calculating gas accretion onto galaxies).

5.3 Hot halo formation

The standard model of galaxy formation (e.g. Rees & Ostriker 1977 and White & Rees 1978) assumes that as long as the cooling time, $t_{\rm cool}$, is shorter than the dynamical time, $t_{\rm dyn}$, the infalling gas cools (typically inside a 'cooling radius', White & Frenk 1991) and settles into the galaxy. Otherwise, the gas is unable to radiate away its thermal energy and forms a hot hydrostatic atmosphere, which is pressure supported against gravitational collapse. In this section we investigate when the hot halo forms in the EAGLE simulations, by analyzing the interplay between the cooling and dynamical times of the gas particles in the inner halo. Throughout this work we define hot gas as all gas particles that have $t_{\rm cool} > t_{\rm dyn}$, and that do not form part of the galaxy, i.e. $r > 0.15 r_{200}$.

We calculate $t_{\rm dyn}$ as a function of the radial position of the gas particle as

$$t_{\rm dyn} = r/V_{\rm c}(r), \tag{5.2}$$

where $V_{\rm c}(r) = [GM(< r)/r]^{1/2}$ is the circular velocity and $M(< r)$ is the mass in the halo enclosed within r. We calculate $t_{\rm cool}$ as

$$t_{\rm cool} = \frac{3nk_{\rm B}T}{2\Lambda}, \tag{5.3}$$

where n is the number density of the gas particle ($n = \rho_{\rm gas}/\mu m_{\rm p}$, $\mu = 0.59$ for a fully ionized gas and $m_{\rm p}$ is the proton mass), $k_{\rm B}$ is the Boltzmann constant, T is the gas temperature and Λ is the cooling rate per unit volume with units of erg cm^{-3}s^{-1}. To calculate Λ, we use the tabulated cooling function for gas exposed to the evolving UV/X-ray background from Haardt & Madau (2001) given by Wiersma et al. (2009), which was also used in the EAGLE simulations.

Fig. 5.1 shows temperature profiles (left panels), logarithmic ratio between cooling times and dynamical times (middle panels) and the respective mass-weighted probability density function (PDF) of $\log_{10} t_{\rm cool}/t_{\rm dyn}$ (right panels) of gas particles from halos in the mass range $10^{11.9} - 10^{12.1}\,{\rm M}_\odot$ (top panels), $10^{11.4} - 10^{11.6}\,{\rm M}_\odot$ (middle panels) and

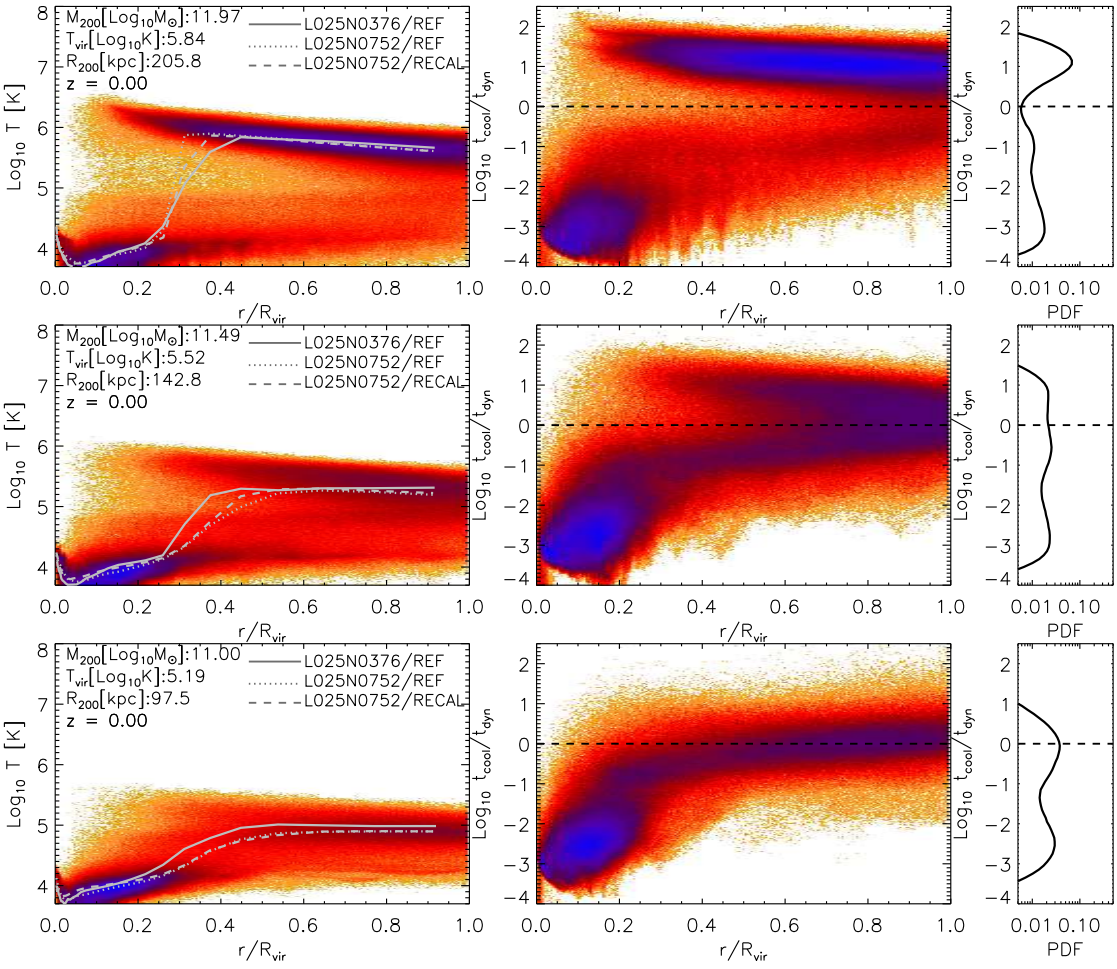

Figure 5.1: Temperature profile (left panels), logarithmic ratio between cooling times and dynamical times (middle panels) and the respective mass-weighted probability density function (PDF, right panels) of $\log_{10} t_{\rm cool}/t_{\rm dyn}$ of gas particles from halos in the mass range $10^{11.9} - 10^{12.1}\,{\rm M}_{\odot}$ (top panels), $10^{11.4} - 10^{11.6}\,{\rm M}_{\odot}$ (middle panels) and $10^{10.9} - 10^{11.1}\,{\rm M}_{\odot}$ (bottom panels) at $z = 0$ taken from the L025N0752/REF simulation. The number of particles in a pixel is used for colour coding. The solid, dotted and dashed lines in the left panels correspond to the median temperature per radial bin for different simulations.

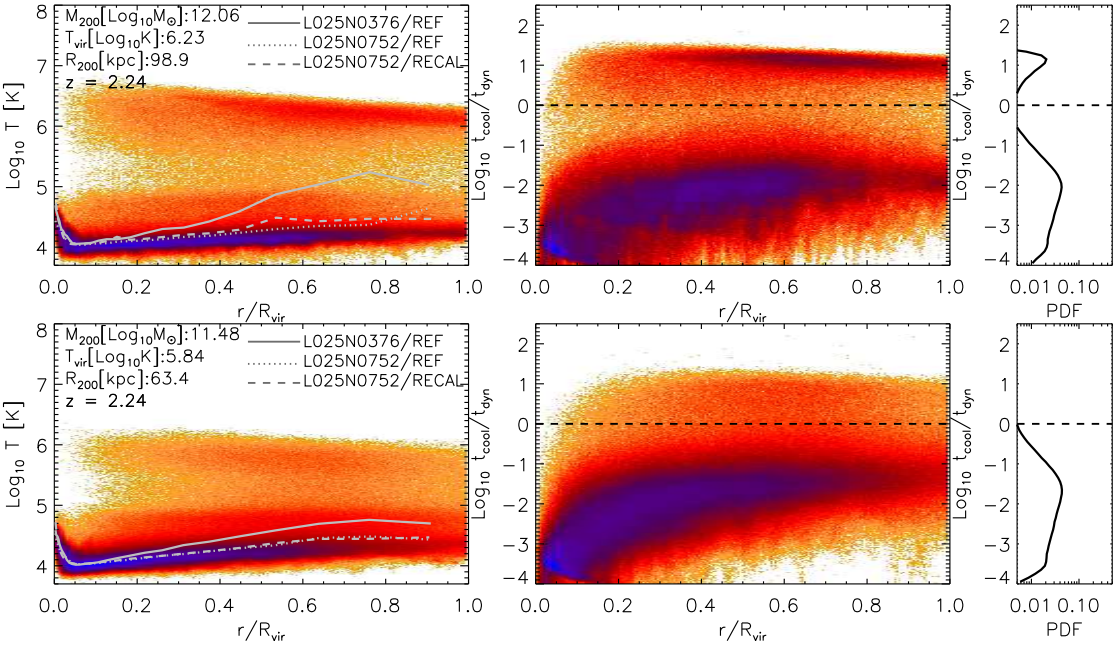

Figure 5.2: Same as Fig. 5.1 but for halos at $z = 2.24$.

$10^{10.9} - 10^{11.1}\,\mathrm{M}_\odot$ (bottom panels) at $z = 0$, taken from the L025N0752/REF simulation. In the right panels and throughout this work, the PDFs are calculated by stacking halos in the selected mass range and distributing the gas particles in logarithmic bins of size 0.1. We then sum the mass of the gas particles in each bin and normalize the distribution by the total gas mass. In the left panels, we include the median values of the mass, virial temperature and virial radius of halos selected in each mass bin. The left panels also show in solid, dotted and dashed lines the median temperature per radial bin of gas from halos taken from the simulations L025N0376/REF, L025N0752/REF and L025N0752/RECAL, respectively.

The left panels of Fig. 5.1 show that while there is very good agreement in the median temperature profiles at low ($r/r_{200} < 0.2$) and high ($r/r_{200} > 0.4$) radii, at intermediate radii the median temperatures from the intermediate-resolution run (L025N0376/REF) are slightly larger (up to 0.3 dex) with respect to the high-resolution runs (L025N0752). However, overall we find the median temperature profiles mostly converge when decreasing the resolution. This is in agreement with the convergence analysis done by Nelson et al. (2015), who concluded that the physics (different models of stellar winds or AGN feedback) further modifies $T(r)$ rather than resolution (van de Voort & Schaye 2012; Nelson et al. 2015; Suresh et al. 2015). We also find, that in the radial range $0.2-0.4\times r/r_{200}$, the median temperatures drop to $T_{\rm gas} \sim 10^4$ K (in agreement with Nelson et al. 2015, $r_{\rm drop} = 0.25 r_{200}$ and van de Voort & Schaye (2012), $r_{\rm drop} = 0.2 r_{200}$), because of the high densities, that rapidly decrease the gas cooling times, making it able to radiate away its thermal energy and join the ISM.

The top and middle left panels of Fig. 5.1 show a deficit of $T \sim 10^{5.5}$ K gas particles

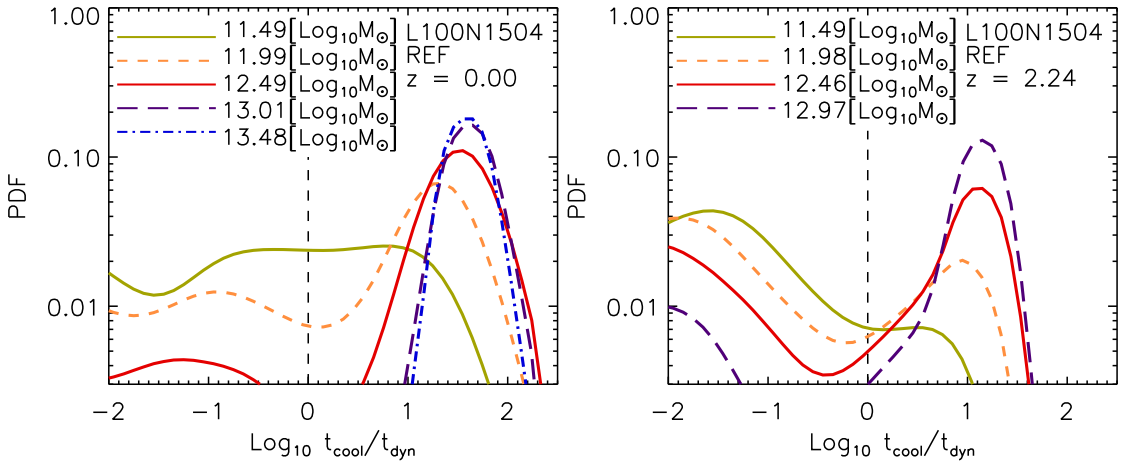

Figure 5.3: Probability density function of the logarithmic ratio between cooling times and dynamical times of gas from halos in the mass range $10^{11.4} - 10^{11.6}\,\mathrm{M}_\odot$, $10^{11.9} - 10^{12.1}\,\mathrm{M}_\odot$, $10^{12.4} - 10^{12.6}\,\mathrm{M}_\odot$, $10^{12.9} - 10^{13.1}\,\mathrm{M}_\odot$, and $10^{13.4} - 10^{13.6}\,\mathrm{M}_\odot$ at $z = 0$ (left panel) and $z = 2.24$ (right panel).

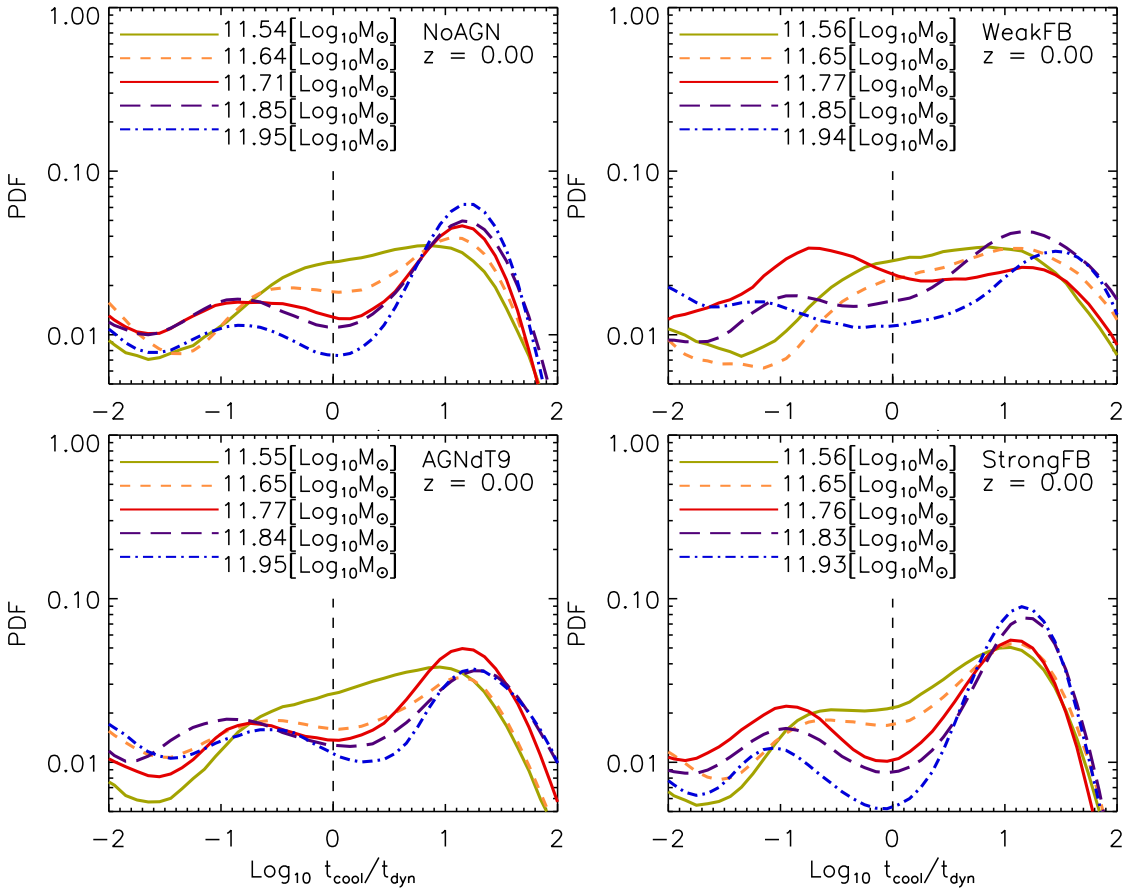

Figure 5.4: Probability density function of the logarithmic ratio between cooling times and dynamical times of gas from halos in the mass range $10^{11.5} - 10^{11.6}\,\mathrm{M}_\odot$, $10^{11.6} - 10^{11.7}\,\mathrm{M}_\odot$, $10^{11.7} - 10^{11.8}\,\mathrm{M}_\odot$, $10^{11.8} - 10^{11.9}\,\mathrm{M}_\odot$ and $10^{11.9} - 10^{12}\,\mathrm{M}_\odot$ at $z = 0$. The legends show the median mass of the halos in each mass bin. The different panels show simulations with different feedback prescriptions: no AGN (top left), weak stellar feedback (top right), strong AGN (bottom left) and strong stellar feedback (bottom right).

at small radii, reflecting the drop in their cooling times as they infall into the galaxy. For a better understanding of the cooling flows as a function of halo mass, we next analyse the middle and right panels. The bottom middle panel shows that in halos with masses between $10^{10.9} - 10^{11.1}\,\mathrm{M}_{\odot}$, most of the gas follows the cooling flow towards the inner galaxy, despite the small fraction of gas with large $t_{\rm cool}$. At larger halo masses, the cooling flow decreases as the hot halo forms. In this case, the gas particles above the black dashed line are not able to cool and therefore form the hot halo. The middle panel shows that halos between $10^{11.4} - 10^{11.6}\,\mathrm{M}_{\odot}$ are in the intermediate stage between developing a hot stable atmosphere or continuing to fuel the galaxy through cooling flows. The top middle panel clearly shows remnants of the cooling flow and a stable hot halo. In these panels there is no evidence of cold flows from filaments.

Fig. 5.2 shows results corresponding to those in Fig. 5.1, but for halos in the mass range $10^{11.9} - 10^{12.1}\,\mathrm{M}_{\odot}$ (top panels), $10^{11.4} - 10^{11.6}\,\mathrm{M}_{\odot}$ (bottom panels) halos at $z = 2.24$. The top middle panel shows that $10^{12}\,\mathrm{M}_{\odot}$ halos are able to develop a hot atmosphere, despite the significant fraction of cold gas at large radii that is accreted onto the inner halo. This cold gas forms part of the cold flows from filaments, that cross the virial radius, and are directly accreted onto the inner galaxy. The presence of cold flows produces gaseous halos with an isothermal temperature profile of $T_{\rm gas} \sim 10^4$ K at all radii. Rather than analyzing the cooling time profiles, Nelson et al. (2015) and van de Voort & Schaye (2012) analysed the entropy profiles of halos at $z = 2$, and concluded the that while entropy of the cold-mode gas decreases smoothly and strongly towards the center, the entropy of the hot-mode gas decreases slightly down to $0.2r_{200}$, after which it drops steeply. We find that the cooling time profiles of the hot ($t_{\rm cool} > t_{\rm dyn}$) and cold ($t_{\rm cool} < t_{\rm dyn}$) modes follow that of entropy.

Figs. 5.1 and 5.2 not only indicate that the stable hot halo forms between the halo mass range $10^{11.5}\,\mathrm{M}_{\odot}$ and $10^{12}\,\mathrm{M}_{\odot}$ with a weak dependence on redshift, but also that a halo with a hot atmosphere should present a bimodal $t_{\rm cool}/t_{\rm dyn}$ PDF. This bimodality will have a local maximum at $t_{\rm cool} > t_{\rm dyn}$ followed by a local minimum at $t_{\rm cool} < t_{\rm dyn}$ (see top right panel). It is important to note that the amount of hot gas at large radii depends not only on accretion shocks that occur close to r_{200}, but also on the energy produced by stars (energy expelled through stellar winds, radiation and supernovae) and AGN. We investigate this further in the following subsection.

5.3.1 Impact of feedback

Feedback can affect the formation of the hot halo around galaxies. For example, strong SN activity generates large outflows and strong winds, that shock against the gaseous halo. As a result, the winds fill the halo with gas expelled from the galaxy, increasing the amount of hot gas at large radii. In this subsection we compare the $t_{\rm cool}/t_{\rm dyn}$

mass-weighted PDF at fixed halo mass obtained from simulations with different feedback implementations (see Table 5.2 for reference and §5.2.1 for a brief description), and determine by visual inspection the mass range where the hot halo is forming by following the analysis from the previous section.

Fig. 5.3 shows the mass-weighted PDF of $t_{\rm cool}/t_{\rm dyn}$ of gas from halos in the mass range $10^{11.4} - 10^{11.6}\,{\rm M}_{\odot}$, $10^{11.9} - 10^{12.1}\,{\rm M}_{\odot}$, $10^{12.4} - 10^{12.6}\,{\rm M}_{\odot}$, $10^{12.9} - 10^{13.1}\,{\rm M}_{\odot}$, and $10^{13.4} - 10^{13.6}\,{\rm M}_{\odot}$ at $z = 0$ (left panel) and $z = 2.24$ (right panel). In the figures, the labels show the median mass of halos in each mass bin. In this case the $t_{\rm cool}/t_{\rm dyn}$ PDFs were calculated from the L100N1504/REF simulation. The region where $t_{\rm cool} > t_{\rm dyn}$ corresponds to hot gas close to r_{200}.

As the halo mass increases so does the amount of hot gas, and the $t_{\rm cool}/t_{\rm dyn}$ PDF of gas in $10^{12}\,{\rm M}_{\odot}$ halos at $z = 0$ shows a bimodal shape, that turns to be mostly unimodal in larger halos ($> 10^{13}\,{\rm M}_{\odot}$). At $z = 2.24$, the $t_{\rm cool}/t_{\rm dyn}$ PDF bimodality is still present in $10^{12}\,{\rm M}_{\odot}$ halos, and remains in larger halos due to the contribution of cold flows that also increase the peak at $t_{\rm cool} < t_{\rm dyn}$. We find that the presence of the bimodality in the $t_{\rm cool}/t_{\rm dyn}$ PDF indicates the increasing amount of hot gas at large radii and the eventual formation of the hot halo. Then, from visual inspection, we determine that the hot atmosphere is forming in halos with masses between $10^{11.5}$ and $10^{12}\,{\rm M}_{\odot}$ at $z = 0$ and $z = 2.24$.

The panels in Fig. 5.4 repeat the analysis shown in the left panel of Fig. 5.3, but instead show $t_{\rm cool}/t_{\rm dyn}$ mass-weighted PDFs from the L025N0376 simulations with different feedback prescriptions. In this case, the PDFs correspond to gas from halos in the mass range $10^{11.5} - 10^{11.6}\,{\rm M}_{\odot}$, $10^{11.6} - 10^{11.7}\,{\rm M}_{\odot}$, $10^{11.7} - 10^{11.8}\,{\rm M}_{\odot}$, $10^{11.8} - 10^{11.9}\,{\rm M}_{\odot}$ and $10^{11.9} - 10^{12}\,{\rm M}_{\odot}$.

In the top left panel of Fig. 5.4, the simulation does not have AGN feedback but includes the same feedback from star formation as in REF. It can be seen that neither the bimodality of the $t_{\rm cool}/t_{\rm dyn}$ PDF nor the amount of hot gas are strongly affected. The same conclusion is found for the strong AGN feedback case (bottom left panel), meaning that in halos with masses between $10^{11.5} - 10^{11.9}\,{\rm M}_{\odot}$, AGN feedback does not play a major roll in determining the amount of hot gas in the inner halo, nor in regulating the formation of the hot halo. In larger halos ($\geq 10^{12}\,{\rm M}_{\odot}$), AGN feedback is able to reduce the mass fraction of cold-dense gas (Suresh et al. 2015) and decrease the hot gas fraction (van de Voort et al. 2011; van de Voort & Schaye 2012). This last can be seen by comparing the blue dot-dashed curves ($10^{12}\,{\rm M}_{\odot}$ halos) from the top and bottom panels, where the amount of gas with $t_{\rm cool} > t_{\rm dyn}$ decreases in halos with stronger AGN feedback.

The right panels show the $t_{\rm cool}/t_{\rm dyn}$ PDFs in the weak (top panel) and strong stellar feedback (bottom) scenarios (but including the same AGN feedback as in the REF model).

For these halo masses, stellar feedback has a stronger impact on the $t_{\rm cool}/t_{\rm dyn}$ PDFs than AGN feedback. By comparing the weak (top right panel), fiducial (top left panel) and strong (bottom right panel) stellar feedback scenarios, we find that stellar feedback increases the fraction of hot gas in low-mass halos ($< 10^{12}\,{\rm M}_{\odot}$), and thus limits the build-up of cold-mode gas in the halo centre (i.e. by shock heating, in agreement with van de Voort & Schaye 2012).

We investigate this behavior further in §5.5 by deriving an analytic model to determine the formation of a stable hot hydrostatic atmosphere. The model depends on the amount of hot gas within the halo, which we calculate in the next subsection, and also on the fraction of accreted gas that shock-heats to the halo virial temperature (§5.4).

5.3.2 Hot halo mass

In this section we look for a correlation between $M_{\rm hot}$, i.e. the mass of gas with $t_{\rm cool} > t_{\rm dyn}$ and $r > 0.15 r_{200}$, and the total halo mass as a function of redshift. Fig. 5.5 shows the median ratio of $M_{\rm hot}/(\Omega_{\rm b,0}/\Omega_{\rm m,0})M_{200}$ (with $\Omega_{\rm b,0}/\Omega_{\rm m,0} = 0.146$ the universal baryon fraction) at $z = 0$ taken from a range of simulations (as indicated in the legends) at $z = 0$ (top panel) and at $z = 2.24$ (middle panel). In these panels the error bars show the 1σ scatter of the relation. The median ratio of $M_{\rm hot}/(\Omega_{\rm b,0}/\Omega_{\rm m,0})M_{200}$ is also shown in the bottom panel, but in this case the values are taken from the L100N1504/REF simulation and at various output redshifts.

The top panel of Fig. 5.5 does not show good agreement between the intermediate-resolution and the high-resolution simulations. A better agreement is achieved at $z = 2.24$ (middle panel). Although only weak convergence is achieved at $z = 0$, we find that the box-size test between the intermediate-resolution simulations is in excellent agreement at all redshifts. The intermediate-resolution runs show that the hot gas represents $< 10\%$ of the total halo gas mass for $M_{200} < 10^{11.7}\,{\rm M}_{\odot}$ at $z = 0$. The hot gas mass fraction reaches $80 - 90\%$ in $10^{13.5}\,{\rm M}_{\odot}$ halos and remains roughly constant for higher masses. In smaller halos ($M_{200} < 10^{10.5}\,{\rm M}_{\odot}$), the hot gas mass fraction remains roughly constant ($M_{\rm hot}/(\Omega_{\rm m,0}/\Omega_{\rm b,0})M_{200} \sim 0.02 - 0.03$). In these halos cold accretion dominates, therefore the only heating mechanism that maintains $M_{\rm hot}$ is the UV background (since Fig. 5.6 shows that $M_{\rm hot}$ in low-mass halos is feedback invariant).

The bottom panel of Fig. 5.5 shows the redshift evolution of the hot gas in halos. We find that in halos larger than $10^{11.5}\,{\rm M}_{\odot}$, $M_{\rm hot}/(\Omega_{\rm b,0}/\Omega_{\rm m,0})M_{200}$ remains constant in the redshift range 3 to 6 and at low redshift it increases with time. In smaller halos ($M_{200} < 10^{11.5}\,{\rm M}_{\odot}$), $M_{\rm hot}/(\Omega_{\rm b,0}/\Omega_{\rm m,0})M_{200}$ increases with time until $z = 1$. At $z < 1$ it decreases due to to drop in the accretion rates onto small halos produced by the accelerated expansion of the Universe (Chapter 2). Due to the decrease in the amount of gas accreted hot, the hot gas already in the halo is not re-heated, it then cools and $M_{\rm hot}$

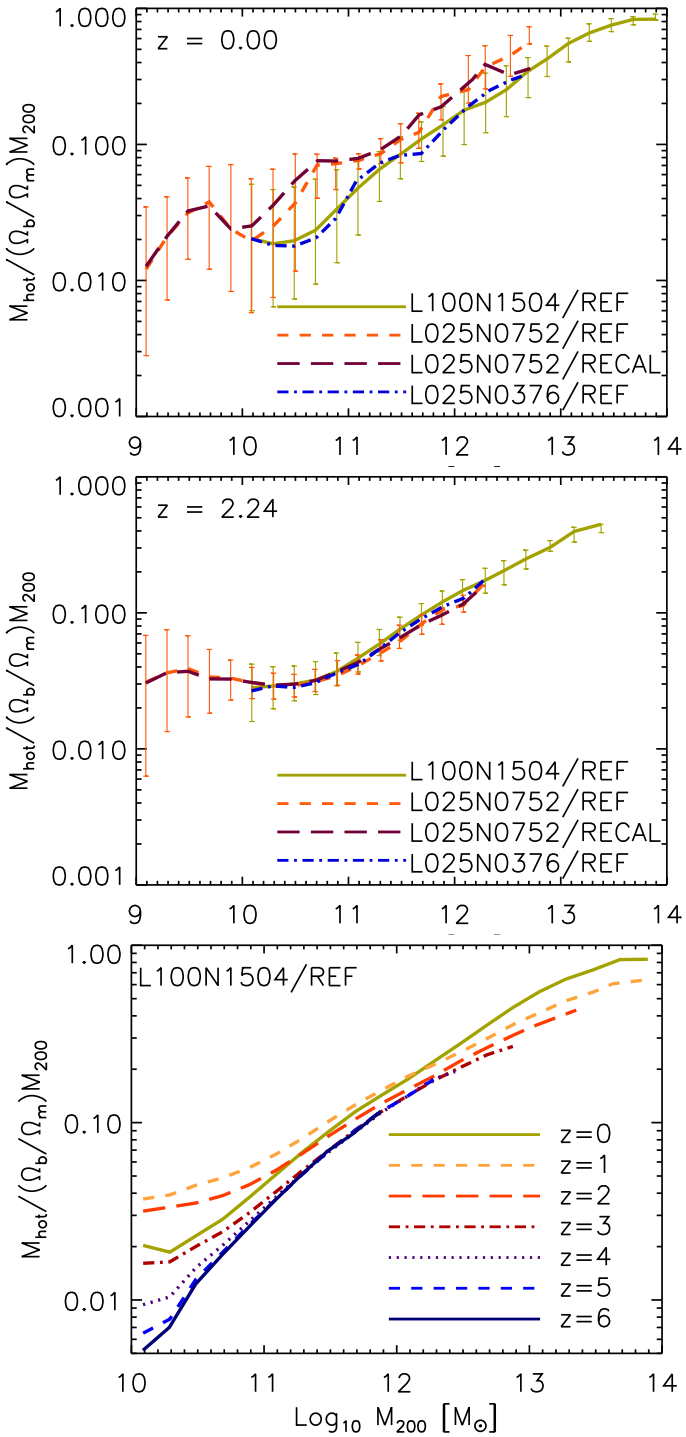

Figure 5.5: Fraction of hot gas mass with respect to the total halo mass, M_{200} (normalized by the universal baryon fraction), as a function of M_{200} from different simulations at $z = 0$ (top panel), at $z = 2.24$ (middle panel), and for REF-L100N1504 at various redshifts (from $z = 0$ to $z = 6$, bottom panel). The error bars in the top and middle panels show the 1σ scatter of the relation. Each bin contains at least 5 halos.

decreases. In the case of high-mass halos we do not find that $M_{\rm hot}$ decreases at $z < 1$, despite the fact that the halo accretion rates also decrease. This is because the stronger feedback mechanisms in large halos (like AGN feedback) expel material out of the galaxy, that shocks and re-heats the hot gas already in the halo.

We next perform a least-square minimization to look for the best-fit relation $M_{\rm hot} - (\Omega_{\rm b,0}/\Omega_{\rm m,0})M_{200}$ as a function of redshift. We apply equal weighting for each mass bin from the L100N1504/REF simulation (which we use to cover a large halo mass range) and minimize the quantity $\Delta_j = \frac{1}{N}\sum_{i=1}^{N} Y_i^2$, where

$$Y_i = \log_{10}\left[\frac{M_{\rm hot}}{(\frac{\Omega_{\rm b,0}}{\Omega_{\rm m,0}})M_{200}}\right]_i - F[M_{200,i}, \alpha(z_j), \beta(z_j), \gamma(z_j)], \tag{5.4}$$

N is the number of bins at each output redhisft z_j, and F is

$$F = \alpha(z_j) + \beta(z_j)x_i + \gamma(z_j)x_i^2, \tag{5.5}$$

$$x_i = \log_{10}(M_{200,i}/10^{12}\,{\rm M}_\odot). \tag{5.6}$$

We obtain the best-fitting values for α, β and γ at each redshift z_j, and following the same methodology we look for the best-fit expression of these parameters as functions of redshift.

We find that the following expression best reproduces the relation in the halo mass range $M_{200} = 10^{11} - 10^{14}\,{\rm M}_\odot$,

$$\log_{10}\left(\frac{M_{\rm hot}}{f_{\rm b}M_{200}}\right) = \alpha(z) + \beta(z)x + \gamma(z)x^2, \tag{5.7}$$

$$x = \log_{10}(M_{200}/10^{12}\,{\rm M}_\odot), \tag{5.8}$$

where $f_{\rm b} = \Omega_{\rm b,0}/\Omega_{\rm m,0}$ is the universal baryon fraction and α, β and γ are functions of z given by

$$\text{if } z \le 2 \begin{cases} \alpha(z) = -0.792 + 0.315\tilde{z} - 0.958\tilde{z}^2, \\ \beta(z) = 0.519 - 0.574\tilde{z} + 0.852\tilde{z}^2, \\ \gamma(z) = -0.055 + 0.003\tilde{z}, \end{cases} \tag{5.9}$$

$$\text{if } z > 2 \begin{cases} \alpha(z) = -0.384 - 1.556\tilde{z} + 1.167\tilde{z}^2, \\ \beta(z) = 0.117 + 0.938\tilde{z} - 0.552\tilde{z}^2, \\ \gamma(z) = -0.049, \end{cases} \tag{5.10}$$

where $\tilde{z} = \log_{10}(1+z)$.

Next, we investigate how the presence of different feedback mechanisms affect the amount of hot gas in the halo. Fig. 5.6 shows the $M_{\rm hot} - (\Omega_{\rm b,0}/\Omega_{\rm m,0})M_{200}$ relation for halos in the mass range $10^{10} - 10^{13}\,{\rm M}_{\odot}$ at $z = 0$ from the L025N0376 simulations. The different coloured lines correspond to simulations with different feedback prescriptions. As concluded from the previous section, stellar feedback has a larger impact on the amount of hot gas than AGN feedback. Strong stellar feedback increases the hot gas mass fraction by a factor of 1.67 in $10^{12}\,{\rm M}_{\odot}$ halos relative to the REF model, whereas weak stellar feedback decreases the hot gas mass fraction by a factor of 2.29. Similarly, no (strong) AGN activity results in an increase (decrease) by a factor of 1.41 in the hot mass fraction. While strong stellar feedback increases the hot gas mass in the halo, stronger AGN feedback decreases it. We find that although stellar and AGN feedback use a similar thermal implementation (Dalla Vecchia & Schaye 2012), *a strong AGN mainly ejects gas mass out of the halo, or prevents it from falling into the halo, whereas strong stellar feedback ejects gas mass out of the galaxy into the inner halo.*

In this section, gas particles with long cooling times ($t_{\rm cool} > t_{\rm dyn}$) are considered to be hot and counted in the calculation of $M_{\rm hot}$. Different from this work, van de Voort & Schaye (2012) separated hot gas from cold by performing a $T_{\rm max}$ cut, and found that the hot fraction as a function of radius decreases not only when AGN feedback is switched on, but also when stellar winds are enhanced. The reason for this is the way stellar feedback is implemented. In the OWLS simulations (Schaye et al. 2010) used by van de Voort & Schaye (2012), the winds velocity scales with the local sound speed, so it largely overcomes the pressure of the ISM, blowing the gas out of the galaxy and halo (Dalla Vecchia & Schaye 2008), thus decreasing the amount of hot gas. In this work, the efficiency of stellar feedback is regulated by the fraction of the energy budget available ($f_{\rm th}$), and not to a temperature increase, that would drive larger outflow velocities (Dalla Vecchia & Schaye 2012).

So far we have analysed the behavior of the hot gas mass in the halo. In the next section we investigate the fraction of gas that is accreted via hot and cold modes as a function of halo mass and redshift.

5.4 Hot and cold modes of accretion

Over the last decade, numerical simulations have shown that gas accretion onto halos occurs in two different modes, either gas shock-heats to the halo virial temperature when crossing the virial radius (the hot accretion mode), or crosses the virial radius unperturbed (the cold accretion mode). Several works have found that cold accretion mostly dominates in low-mass halos ($M_{200} < 10^{11}\,{\rm M}_{\odot}$) at $z < 2$ (e.g. Katz et al. 2003; Kereš et al. 2005, 2009; Ocvirk et al. 2008; van de Voort et al. 2011; van de Voort & Schaye 2012) and in all halos at $z > 2$. Both modes appear to coexist at high redshift in massive

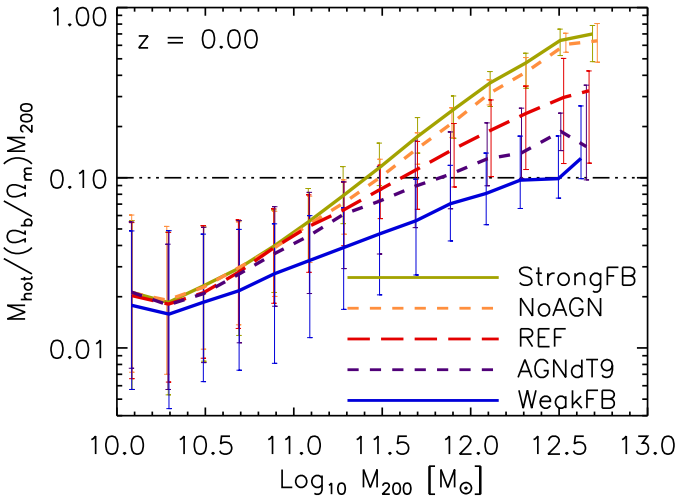

Figure 5.6: Fraction of hot gas mass with respect to the total halo mass, M_{200} (normalized by the universal baryon fraction), as a function of M_{200} at $z = 0$. The different lines correspond to the L025N0376 simulations with different feedback prescriptions (see Table 5.2 and/or §5.2).

halos, which develop a hot hydrostatic atmosphere despite experiencing significant cold accretion from filaments. The cold accreted gas, that forms part of filaments, is generally referred to as a 'cold flow' (Kereš et al. 2005; Dekel et al. 2009). Cold flows are essential to galaxy formation, because despite experiencing significant heating when crossing the hot atmosphere (Nelson et al. 2013), they are responsible for delivering cold, star-forming, gas deep within the halo (e.g. Dekel et al. 2009).

The contributions from the different modes of accretion can be calculated from the temperature history of the accreted gas. In the simulations, the evolution of each gas particle is traced and the maximum temperature, $T_{\rm max}$, ever reached by the particle (at redshift $z_{\rm max}$) is stored in a separate variable. $T_{\rm max}$ is updated whenever the gas particle reaches a higher temperature. However, if the gas particle is star-forming, $T_{\rm max}$ is not updated, and so any possible shock it experiences is ignored. As in van de Voort et al. (2011), ignoring such shocks is not an inconvenient in our calculations, because we are interested in the $T_{\rm max}$ the particle reached *before* entering the galaxy and becoming star-forming.

Kereš et al. (2005) found a clear bimodality in the distribution of $T_{\rm max}$ of accreted particles. They proposed a threshold value, $T_{\rm max} = 2.5 \times 10^5$ K, given by the minimum in the distribution of $T_{\rm max}$ values, to determine whether gas is accreted hot ($T_{\rm max} \geq 2.5 \times 10^5$ K) or cold ($T_{\rm max} < 2.5 \times 10^5$ K). This is an often used method but other approaches have also been taken. For example, Brooks et al. (2009) identified hot gas accretion based on an entropy jump criterion, and concluded that their method led to a distinction of hot/cold mode in very good agreement with the selection of hot/cold gas based on the use of a constant temperature threshold. In the following section we utilize different

methods to distinguish between the hot/cold modes of accretion, based on entropy jumps and maximum temperatures.

5.4.1 Shock definition

Following the method described in §5.2.4, we first look for gas particles that crossed the virial radius between two consecutive snapshots. Next, we aim to identify all gas particles that experienced a shock when crossing the virial radius, but do not cool immediately after (due to in-shock cooling or heating rate smoothing). To this end, we first analyse the mass-weighted PDF of $T_{\rm max}$, $T_{\rm gas}$ and $S_{\rm gas}$ of accreted gas particles. Then, we compare the maximum temperature criterion with a more physically motivated method based on the post-shock gas temperature and entropy ($T_{\rm post-shock}$ and $S_{\rm post-shock}$, respectively), and conclude that $T_{\rm post-shock}+S_{\rm post-shock}$ is a better method for selecting hot gas accretion.

The top panels of Fig. 5.7 show the mass-weighted PDF of $T_{\rm max}$ in the redshift interval $0.0 < z \leq 0.1$ (top left panel) and $2.0 < z \leq 2.2$ (top right panel). The curves are colored according to the color bars at the top of the figure, which indicate the halo mass (and its virial temperature) that particles are accreted onto. It can be seen that the $T_{\rm max}$ PDF varies according to M_{200}, being unimodal in low-mass halos and bimodal in high-mass halos. The minimum of the bimodality also changes with M_{200}, going from $T_{\rm max,min} = 10^{5.5}$ K in $10^{12}\,{\rm M}_\odot$ halos to $T_{\rm max,min} = 10^{6}$ K in $10^{14}\,{\rm M}_\odot$ halos. Besides this local minimum, there is a local maximum at $10^{7.5}$ K for all halo masses. This peak is produced by stellar feedback instead of accretion shocks. We find that gas particles that were ejected out of the halo due to stellar feedback, are eventually re-accreted. However, since they did not reach a temperature larger than $10^{7.5}$ K when crossing r_{200}, $T_{\rm max}$ is not updated, and they are then always considered as hot mode accretion by the maximum temperature criterion. When applying this criterion, rather than calculating a $T_{\rm max,min}$ threshold value that changes with M_{200}, we follow previous works from the literature (e.g. van de Voort et al. 2011; Nelson et al. 2013) and use $T_{\rm max} = 10^{5.5}$ K to separate hot from cold accretion.

We next separate hot from cold accretion using the post-shock gas thermal properties. In this case, it is well known that a shock front compresses the gas and raises its temperature abruptly, generating large entropy values. The compression and heating push the gas out of thermal equilibrium. To reach a new equilibrium configuration the gas cools in a 'radiative relaxation layer', which is generally larger than the shock front due to the collisions required to cool the gas. Within this layer, the post-shock temperature drops (generally to a fraction of the halo virial temperature, $T_{\rm post-shock} \approx (\gamma-1)T_{\rm vir}$, with $\gamma = 5/3$ for an ideal gas, see e.g. Tozzi & Norman 2001), the gas is further compressed and moves subsonically. However, if the shock-heated gas has a long cooling time, after crossing the radiative layer its temperature will be somewhat higher, therefore rather

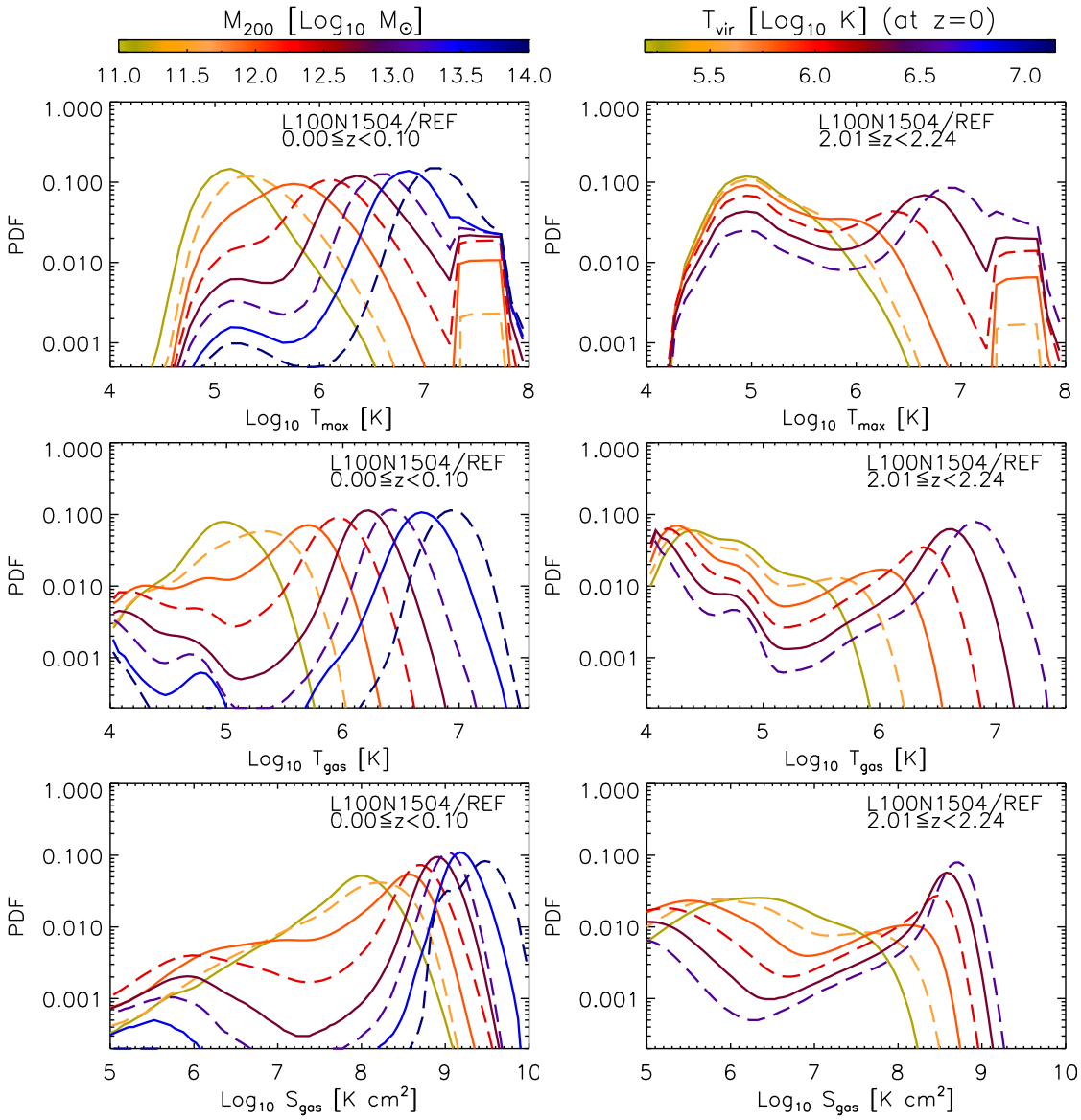

Figure 5.7: Probability density function of maximum temperature (top panels), temperature (middle panels) and entropy (bottom panels) of gas accreted on to halos in the redshift ranges $z = 0 - 0.1$ (left panels) and $z = 2.0 - 2.2$ (right panels). The curves are colored according to the colorbar at the top of the figure, which indicates the halo mass and virial temperature.

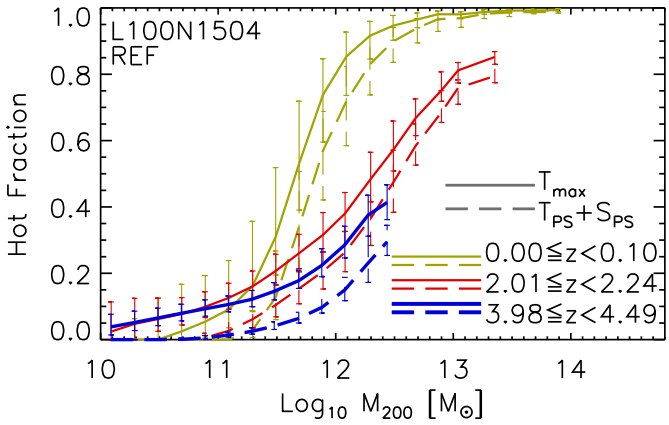

Figure 5.8: Fraction of gas accreted hot during the redshift ranges $0 \leq z < 0.1$ (green lines), $2.0 \leq z < 2.2$ (red lines) and $4.0 \leq z < 4.49$ (thick blue lines), against halo mass. The solid curves correspond to the hot fraction calculated using the $T_{\rm max}$ method, whereas the dashed curves correspond to $T_{\rm post-shock}+S_{\rm post-shock}$ method. The error bars show the 1σ scatter of the fractions.

than infalling onto the galaxy, the gas remains hot forming part of the hot hydrostatic halo.

To identify the gas particles that do not cool immediately after the shock, we analyse the post-shock gas temperature and entropy. We select the gas particles that were accreted during the redshift interval $z_i - z_j$ ($z_i < z_j$), and shocked when crossing r_{200} using a temperature and entropy threshold value. We calculate the gas temperature and entropy mass-weighted PDFs at redshift z_i. As per $T_{\rm max}$, the middle and bottom panels of Fig. 5.7 show that the $T_{\rm gas}$ and $S_{\rm gas}$ PDFs have a bimodal shape. We use the local minimum of the bimodalities as the threshold values ($T_{\rm post-shock} = 10^{5.5}$ K and $S_{\rm post-shock} = 10^{7.2}$ K cm^2), and label a gas particle as 'shocked' when both its entropy and temperature after accretion are larger than the entropy and temperature thresholds. We find that large entropy values alone do not correctly indicate whether a particle experienced an accretion shock, because sometimes occurs that $S_{\rm gas} \propto T_{\rm gas}/\rho_{\rm gas}^{2/3} \geq S_{\rm post-shock}$, due to the fact that $\rho_{\rm gas}$ is small. Therefore, in addition to the entropy condition, we also use the temperature $T_{\rm post-shock}$ condition. We also note that the temperature of the particles alone is not enough to define shocked gas, due to additional heating from the UV background, that mostly impacts on gas accreting onto low-mass halos.

Fig. 5.8 shows a comparison between the fraction of hot mode gas accretion, $f_{\rm hot}$, calculated using $T_{\rm max}$ (solid lines) and $T_{\rm post-shock} + S_{\rm post-shock}$ (dashed lines) at $z = 0$ (green lines), $z = 2$ (red lines) and $z = 4$ (thick blue lines). It can be seen that the fraction of shock-heated gas particles given by $T_{\rm post-shock} + S_{\rm post-shock}$ is a factor 1.25 lower than $f_{\rm hot}$ given by $T_{\rm max}$ in 10^{12} M$_\odot$ halos at $z = 0$, a factor of 1.6 at $z = 2$ and a factor of 2 at $z = 4$. Although changing the threshold values $T_{\rm post-shock}$ and $S_{\rm post-shock}$ (as well as changing $T_{\rm max}$) can bring the $f_{\rm hot}$ curves into better agreement, the current disagreement is expected because of numerical deficiencies, such as in-shock cooling or

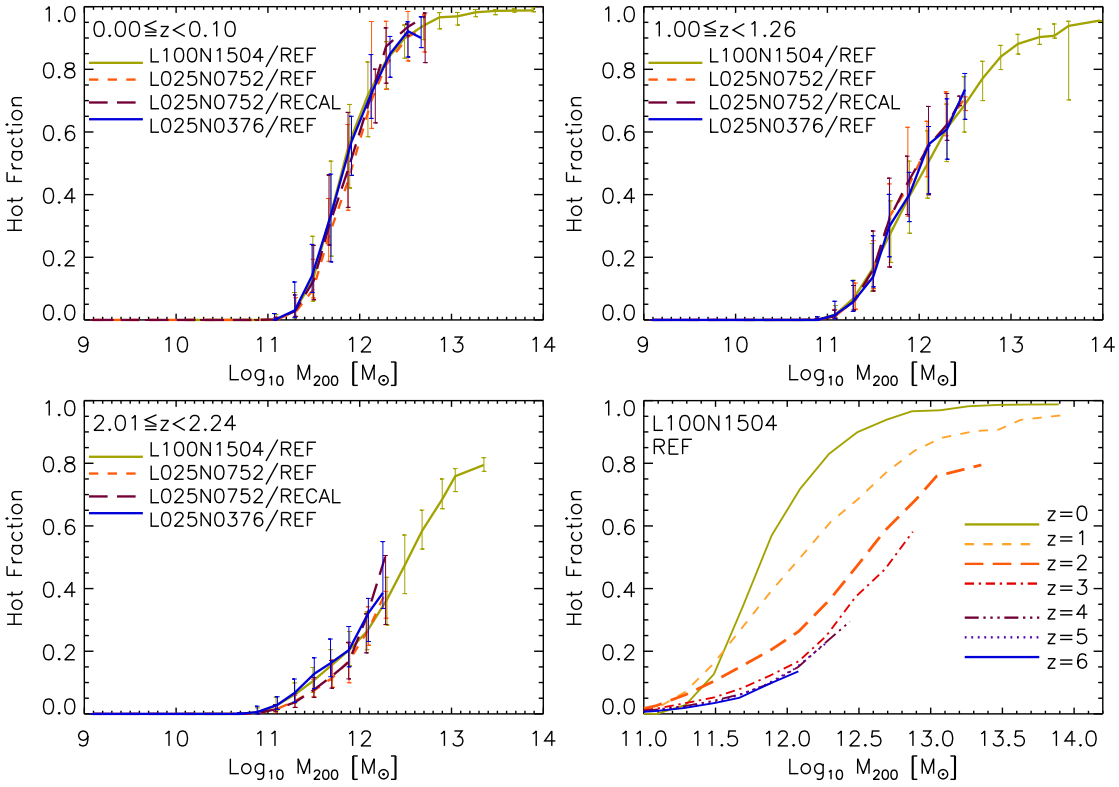

Figure 5.9: Fraction of hot mode gas accretion during $0 \leq z < 0.1$ (top left panel), $1.0 \leq z < 1.26$ (top right panel), $2.0 \leq z < 2.24$ (bottom left panel) against halo mass. In these panels, the different lines correspond to different simulations and the error bars show the 1σ scatter of the hot fractions. The bottom right panel shows fraction of hot mode gas accretion in various redshift ranges.

heating rate smoothing, that enhance the radiative looses of gas undergoing shocks (see §5.2.2 for a discussion). We believe that $T_{\rm post-shock} + S_{\rm post-shock}$ is a better method to select hot gas accretion, because it does not include gas particles that go through a shock but immediately cool afterwards (or are not even shock-heated but counted as hot accretion, as occurs when $T_{\rm max}$ is affected by stellar feedback), and therefore do not contribute to the hot halo formation process.

5.4.1.1 Gadget vs. Anarchy

In this section we extend the discussion presented in §5.2.2, and analyse the differences in the hot/cold modes of accretion onto halos when the formulation of the hydrodynamics scheme is varied. We compare two L025N0376 simulations that use the same subgrid models but no feedback, one employs the standard SPH code GADGET, while the other the Anarchy formulation of SPH used in the fiducial EAGLE runs. Fig. 5.10 shows the same as Fig. 5.8 for $z = 0$ (top panel) and $z = 2$ (bottom panel), but the lines correspond to the GADGET (blue lines) and Anarchy (orange lines) simulations output.

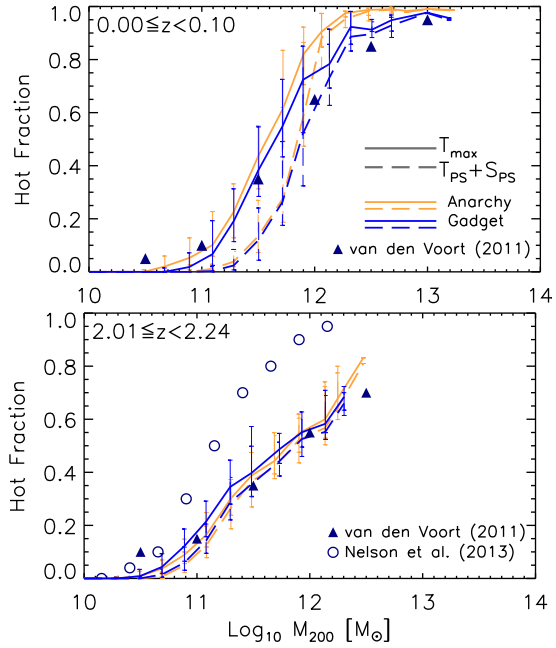

Figure 5.10: Fraction of gas accreted hot during the redshift ranges $0 \leq z < 0.1$ (top) and $2.0 \leq z < 2.2$ (bottom) against halo mass. The panels show the same as Fig. 5.8, but in this case the curves correspond to the hot fraction calculated from the L025N0376/NoFeedback Anarchy (orange lines) and GADGET (blue lines) simulations. The error bars show the 1σ scatter of the fractions. The symbols correspond to the hot fraction estimates of van de Voort et al (2011, blue triangles) and Nelson et al. (2013, open circles).

In addition, the panels show the hot fractions estimates from van de Voort et al. (2011) in filled triangles and from Nelson et al. (2015) in open circles. The top panel shows excellent agreement between the $f_{\rm hot}$ values in halos smaller than $10^{12}\,{\rm M}_{\odot}$, and interesting differences in larger halos. The Anarchy simulation exhibits a larger fraction of hot accretion onto large halos (in both, $T_{\rm max}$ and $T_{\rm post-shock} + S_{\rm post-shock}$, methods), than its GADGET counterpart. This is expected, since the spurious surface tension appearing in the GADGET formulation of SPH prevents the cold dense clumps of gas from being disrupted, mixed and heated when crossing R_{200}. We then find that in $z = 0$ $10^{12} - 10^{12.5}\,{\rm M}_{\odot}$ halos, the difference in $f_{\rm hot}$ between GADGET and Anarchy can be as large as 0.2 dex. At $z = 2$ the $f_{\rm hot}$ values are not only in very good agreement between the different simulations (along the halo mass range analysed, differences can appear in larger halos), but also between the different methods ($T_{\rm max}$ vs. $T_{\rm post-shock} + S_{\rm post-shock}$) employed.

In addition, the top panel of Fig. 5.10 shows that the $T_{\rm max}$ hot fractions taken from the GADGET simulation are in very good agreement with the hot fractions from van de Voort et al. (2011). The fact that van de Voort et al. (2011) obtained lower $f_{\rm hot}$ values in halos $> 10^{12}\,{\rm M}_{\odot}$ is expected, since they used the OWLS simulation series (Schaye et al. 2010) with stellar feedback. When comparing with the top panel with Fig. 5.8, we find that when feedback is switched on, $f_{\rm hot}$ decreases (on average) by 0.1 dex at

fixed halo mass. The bottom panel also shows very good agreement with van de Voort et al. (2011), but large differences with Nelson et al. (2013). While van de Voort et al. (2011) used the GADGET formulation of SPH in their simulations, Nelson et al. (2013) analysed a simulation series that employ the moving mesh code AREPO (Springel 2010). Nelson et al. (2013) traced the evolution of the gas properties using a Monte Carlo tracer particle technique that allow them to compute $T_{\rm max}$. In their work, they did not find large differences between GADGET and AREPO in the cold mode of accretion onto halos, and concluded that the cold fraction onto halos mainly depends on the manner (either with $T_{\rm max}$ or other cut-off temperature) in which it is measured.

5.4.2 Hot/Cold fraction

The final ingredient for our model of hot halo formation (§5.5) is the fraction of hot and cold mode of gas accretion onto halos. The fraction of hot mode gas accretion, $f_{\rm hot}(M,z)$, can be considered as an indirect measure of the presence of hot gas in the halo, since large values of $f_{\rm hot}$ imply large values of $M_{\rm hot}/M_{200}$. Fig. 5.9 shows $f_{\rm hot}(M,z)$ at $z=0-0.1$ (top left panel), $z=1.0-1.26$ (top right panel) and $z=2.0-2.24$ (bottom left panel). At each redshift range we find excellent agreement between the $f_{\rm hot}(M,z)$ curves taken from simulations with different resolution and box size. We find that $f_{\rm hot}(M,z)$ increases smoothly with halo mass and decreasing redshift.

We look for the best-fit expression of $f_{\rm hot}(M_{\rm halo},z)$ by performing a least-square minimization. We follow the method described in §5.3.2, we apply equal weighting for each mass bin from the L100N1504/REF simulation and minimize the quantity $\Delta_j = \frac{1}{N}\sum_i^N [f_{\rm hot}(M_i,z_j) - F(M_{200,i}, a(z_j), M_{1/2}(z_j))]^2$, where N is the number of mass bins at each output redshift z_j, and F is

$$F = [\exp(a(z_j)[x - \log_{10} M_{1/2}(z_j)]) + 1]^{-1}, \quad (5.11)$$

$$x = \log_{10}(M_{200,i}/10^{12}\,{\rm M}_\odot). \quad (5.12)$$

We calculate the best-fitting values of a and $M_{1/2}$ at each redshift $0 \le z_j < 6$ and in the halo mass range $10^{10} \le M_{200} < 10^{14}\,{\rm M}_\odot$. We then look for the best-fitting expressions of a and $M_{1/2}$ as a function of redshift. We find that the relations

$$f_{\rm hot}(x,z) = [\exp(a(z)[x - \log_{10} M_{1/2}(z)]) + 1]^{-1}, \quad (5.13)$$

$$x = \log_{10}(M_{200}/10^{12}\,{\rm M}_\odot), \quad (5.14)$$

$$a(z) = \begin{cases} -4.301 \times 10^{-1.269\tilde{z}+1.288\tilde{z}^2} & \text{if } 0 \leq z < 2, \\ -1.080 \times 10^{0.810\tilde{z}-0.423\tilde{z}^2} & \text{if } 2 \leq z < 4, \\ -2.471 & \text{if } z \geq 4, \end{cases} \tag{5.15}$$

$$\tilde{z} = \log_{10}(1+z), \tag{5.16}$$

$$M_{1/2}(z) = \begin{cases} -0.149 + 0.217z + 0.067z^2 & \text{if } 0 \leq z < 2, \\ -0.248 + 0.534z - 0.069z^2 & \text{if } 2 \leq z < 4, \\ 0.724 + 0.015z & \text{if } z \geq 4, \end{cases} \tag{5.17}$$

best reproduce the fraction of hot mode accretion as a function of halo mass and redshift. To cover a large range in halo mass we calculated the best-fitting relations using the fractions of hot accretion from the L100N1504/REF simulation. The bottom right panel of Fig. 5.9 shows the fraction of hot accretion in various redshift ranges ($0 \leq z < 6$) taken the L100N1504/REF simulation. We find that the redshift evolution of $f_{\rm hot}$ is similar to that of $M_{\rm hot}/(\Omega_{\rm b,0}/\Omega_{\rm m,0})M_{200}$ (shown in the bottom panel Fig. 5.5). For a given halo mass, $f_{\rm hot}$ increases with time until $z = 1$. At $z < 1$ $f_{\rm hot}$ increases in high-mass halos ($M_{200} > 10^{11.5}\,{\rm M}_\odot$) but decreases in low-mass halos ($M_{200} < 10^{11.5}\,{\rm M}_\odot$). This is in agreement with van de Voort et al. (2011), who calculated $f_{\rm hot}$ using the $T_{\rm max}$ criterion.

We also investigate how $f_{\rm hot}(M, z)$ is affected when we vary the feedback mechanisms. We find that despite the total gas accretion onto the halo remaining unchanged under varying feedback mechanisms (in agreement with van de Voort et al. 2011), $f_{\rm hot}(M, z)$ increases at fixed halo mass for strong stellar feedback and no AGN feedback scenarios. There is a larger impact from stellar feedback, i.e. strong stellar feedback increases $f_{\rm hot}(M, z)$ by a factor of 1.2 in $10^{12}\,{\rm M}_\odot$ halos, whereas weak stellar feedback decreases it by a factor of 1.26. Strong AGN feedback decreases $f_{\rm hot}(M, z)$ but only in high-mass halos and by up to a factor of 1.1. As in van de Voort et al. (2011), we find that the impact of feedback mechanisms on the fraction of hot mode gas accretion is small, and can be treated as negligible.

In the next section we derive a semi-analytic model for hot halo formation by making use of the fraction of hot mode gas accretion calculated in this section, and on the amount of hot gas mass in the halo calculated in §5.3.2.

5.5 Toy model

It is known that shock-heated gas can develop sufficient pressure to balance the gravitational attraction towards the halo centre (e.g. Birnboim & Dekel 2003), remain hot and form part of the halo hot hydrostatic atmosphere. In this section we present a semi-

analytic model that describes the formation of a stable hot halo. We begin by analyzing the evolution of the specific energy of the post-shock gas in the halo. Here, we consider that the gas after going through an accretion shock, remains hot and close to r_{200}. We then express the variation of the gas specific energy, $\mathscr{E}$, due to compression and radiative loses as

$$\dot{\mathscr{E}} = -P\dot{v} - q/N, \tag{5.18}$$

where P is the pressure, $v = V/N$ is the specific volume, N is the number of hot gas particles, q is the radiative cooling rate and the upper dots denote derivatives with respect to time. The variation in time of post-shock gas specific volume is driven by an increase in the number of shock-heated gas particles, that produce a compression, and not because of a decrease in the volume the gas is occupying. Then, $\dot{v} = -V\dot{N}/N^2$, and under the assumption of an ideal gas eq. (5.18) can be rewritten as

$$\dot{\mathscr{E}} = k_{\rm B}T\frac{\dot{N}}{N} - \frac{q}{N}, \tag{5.19}$$

$$\dot{\mathscr{E}} = k_{\rm B}T_{\rm vir}\frac{\dot{M}_{\rm hot}}{M_{\rm hot}} - \Gamma_{\rm cool}, \tag{5.20}$$

where T is the mean gas temperature, which we assume to be $T = T_{\rm vir}$, and $M_{\rm hot} = \mu m_{\rm p} N$ (assuming μ invariant). In eq. (5.20), $\Gamma_{\rm cool} = q/N$ refers to the cooling rate per particle and $\Gamma_{\rm heat} = k_{\rm B}T_{\rm vir}\dot{M}_{\rm hot}/M_{\rm hot}$ refers to the heating rate per particle. As a result, eq. (5.20) yields

$$\dot{\mathscr{E}} = \Gamma_{\rm heat} - \Gamma_{\rm cool}, \tag{5.21}$$

and sets the *energy condition* of the post-shock gas under which a halo develops a stable hot hydrostatic atmosphere. When

$$\Gamma_{\rm heat} > \Gamma_{\rm cool}, \tag{5.22}$$

the accumulative shock-heated gas at the virial radius gains the necessary pressure through external shock heating to balance the energy loss from radiative cooling. We follow Dekel & Birnboim (2006) and define a critical mass, $M_{\rm crit}$, above which halos develop a hot atmosphere. We define $M_{\rm crit}$ as the halo mass at which the cooling rate, $\Gamma_{\rm cool}$, of gas at the virial radius equals the heating rate, $\Gamma_{\rm heat}$, produced by the accretion shocks. In the following subsections we present the calculations for the halo mass at which heating through accretion shocks balances cooling of gas.

5.5.1 Virial heating rate and accretion history

In a ΛCDM cosmology, halos grow through mergers and smooth accretion. Rapid mass accretion and mergers dynamically heat the gas when halos form, with virialisation continually transforming gravitational potential energy into kinetic energy of baryons and dark matter. For the gaseous component, kinetic turbulent energy is transformed into thermal energy through shocks and viscous dissipation. The increase in the halo mass through mergers and smooth accretion therefore leads to a heating rate that depends on the virial temperature, the accretion rate and the hot gas mass as follows

$$\Gamma_{\rm heat} \;=\; k_{\rm B} T_{\rm vir} f_{\rm hot} (\Omega_{\rm b,0}/\Omega_{\rm m,0}) \frac{\dot{M}_{200}}{M_{\rm hot}}, \tag{5.23}$$

where we have replaced $\dot{M}_{\rm hot} = f_{\rm hot}(\Omega_{\rm b,0}/\Omega_{\rm m,0})\dot{M}_{200}$ in eq. (5.19), $f_{\rm hot}$ is given by eqs. (5.13-5.17), and $M_{\rm hot}$ by eqs. (5.7-5.10).

The virial temperature of a halo formed at redshift z is related to the total mass $M_{\rm halo}$ as

$$T_{\rm vir} = 10^{5.3}\,{\rm K}\,(M_{200}/10^{12}\,{\rm M}_\odot)^{2/3}(1+z), \tag{5.24}$$

where we assumed that the halo encloses a characteristic virial overdensity $\Delta_c = 200$ relative to the critical density at redshift z, $\rho_{\rm crit}(z) = \left(\frac{3H_0^2}{8\pi G}\right)[\Omega_{\rm m,0}(1+z)^3 + \Omega_{\Lambda,0}]$.

To calculate the halo accretion rate, we use the analytic derivation from Chapter 2

$$\frac{{\rm d}M(z)}{{\rm d}t} = 71.6\,{\rm M}_\odot{\rm yr}^{-1} \left(\frac{M(z)}{10^{12}{\rm M}_\odot}\right)\left(\frac{h}{0.7}\right) f(M_0)[(1+z)-a][\Omega_{\rm m,0}(1+z)^3+\Omega_{\Lambda,0}]^{1/2}, \tag{5.25}$$

where $f(M_0)$ and a depend on halo mass and the linear power spectrum. This formula gives the accretion rate at redshift z. For more details on the accretion rate model see the §2.2.2. Note that in this Chapter (as well as in Chapter 6) we are assuming Planck cosmology and not WMAP5 as we did in the previous chapters.

5.5.2 Cooling rate

To find halos for which the infalling gas is shock-heated and prevented from cooling onto the inner halo, we compare the heating rate in eq. (5.23) to the gas cooling rate per particle $\Gamma_{\rm cool}$ [erg/s],

$$\Gamma_{\rm cool} = \Lambda(T,Z)/n_{\rm gas}(r), \tag{5.26}$$

where $\Lambda(T, Z)$ [erg $\times$ cm^{-3}s^{-1}] is the cooling rate per unit volume and $n_{\rm gas}$ is the gas particle number density.

If both gas ($\rho_{\rm gas}$) and dark matter ($\rho_{\rm dm}$) are in static equilibrium within the same potential well, we can assume that at $r = r_{200}$ the density of gas is a fraction of the dark matter density $\rho_{\rm gas} = (\Omega_{\rm b,0}/\Omega_{\rm m,0})\rho_{\rm dm}$. Assuming that dark matter follows an NFW profile (Navarro et al. 1997), then

$$\rho_{\rm gas}(r_{200}) = (\Omega_{\rm b,0}/\Omega_{\rm m,0})\rho_{\rm s}/[c(1+c)^2], \tag{5.27}$$

where $\rho_{\rm s} = \frac{c^3 M}{4\pi m(c) r_{200}^3}$, $m(c) = \ln(1+c) - c/(1+c)$, and c is the concentration calculated from the relation derived in Chapter 4 for halos in virial equilibrium. The gas number density evaluated at the virial radius is $n_{\rm gas}(r_{200}) = \rho_{\rm gas}(r_{200})/\mu m_{\rm p}$.

Lastly, we need to calculate the mean metallicity Z (in solar units) as a function of redshift, to include in the cooling rate. We use the best-fitting expression from Ma et al. (2015), who studied the galaxy mass-metallicity relation from $z = 0 - 6$ using high-resolution cosmological zoom-in simulations from the Feedback in Realistic Environment project. Their best-fitting relation,

$$\log_{10}(Z/Z_\odot) \quad = \quad 0.35\log_{10}(M_*/10^{10}\,{\rm M}_\odot) + 0.93e^{0.43z} - 1.05, \tag{5.28}$$

depends on redshift and stellar mass (M_*), and has proven to be in excellent agreement with observed data from Tremonti et al. (2004), Erb et al. (2006), Mannucci et al. (2009), Zahid et al. (2011), Steidel et al. (2014) and Sanders et al. (2015) at multiple redshifts. We use eq. (5.28) and assume that $M_* = 0.1 f_{\rm b} M_{200}$ (10% of gas is locked in stars).

5.5.3 Critical halo mass

In this subsection we use the energy condition of post-shock gas given by eq. (5.21) and calculate the halo mass, $M_{\rm crit}$, for which the heating rate, $\Gamma_{\rm heat}$ (given by eq. 5.23), equals the cooling rate, $\Gamma_{\rm cool}$ (given by eq. 5.26). $M_{\rm crit}$ is a critical halo mass that represents the halo mass above which the heating rate exceeds the cooling rate behind the shock, and as a result the halo develops a stable hot hydrostatic atmosphere. To calculate $M_{\rm crit}$, we use the toy model derived in the previous subsections, that makes use of analytic derivations as well as best-fitting relations, such as $M_{\rm hot}(M_{200}, z)$ (given by eqs. 5.7-5.10) and $f_{\rm hot}(M_{200}, z)$ (given by eqs. 5.13-5.17).

The top panel of Fig. 5.11 shows $M_{\rm crit}$ (red solid line) and the transition mass, $M_{\rm half}$ (blue dashed line), as a function of redshift. $M_{\rm half}$, as referred to by previous works (Ocvirk et al. 2008; Faucher-Giguère et al. 2011; van de Voort et al. 2011, among oth-

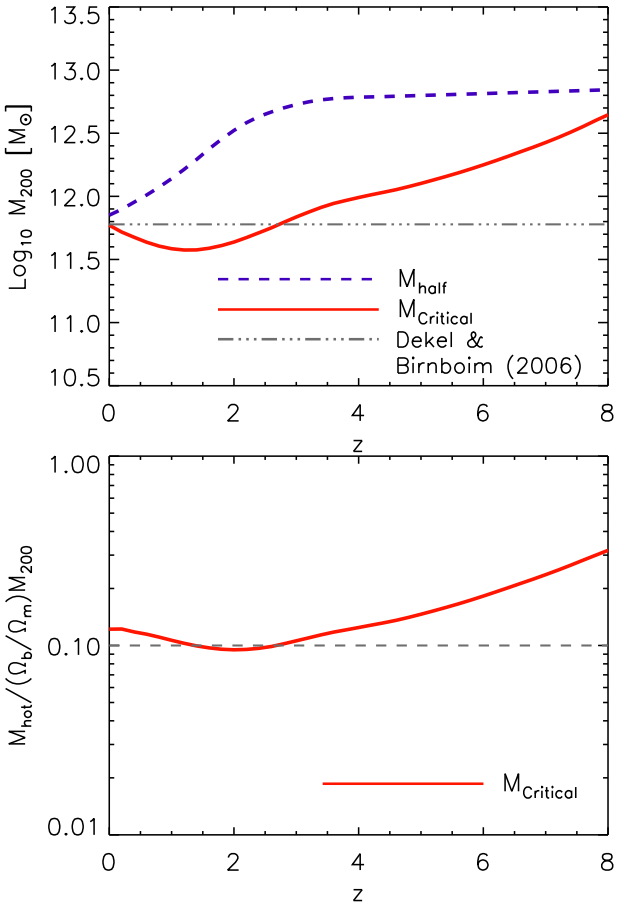

Figure 5.11: Top panel: Critical halo mass, $M_{\rm crit}$ (red solid line), halo mass where the hot and cold modes of accretion contribute equally ($f_{\rm hot}(M_{\rm half}(z), z) = 1/2$, blue dashed line) and critical mass obtained by the work of Dekel & Birnboim (2006) (grey dot-dashed line) as function of redshift. Bottom panel: Fraction of hot mass in halos with $M_{\rm crit}$ masses as a function of redshift

ers), is the halo mass at which the hot and cold modes of accretion contribute equally ($f_{\rm hot}(M_{\rm half}(z), z) = 1/2$ as given by eq. 5.17). The bottom panel of Fig. 5.11 shows the hot gas mass (normalized to the halo mass times the baryon fraction), in halos with masses equal to $M_{\rm crit}$.

There are a few things we can conclude from this simple calculation. First, we find that $M_{\rm crit}$ agrees with $M_{\rm half}$ at $z = 0$, but both halo masses increase towards high redshift at different rates with $M_{\rm crit}$ always greater than $M_{\rm half}$. It is not possible for $M_{\rm half} < M_{\rm crit}$, because a lack of a hot atmosphere would imply little to no hot accretion. Besides, $M_{\rm crit}$ is not related to $M_{\rm half}$ *because equal hot/cold modes of accretion do not imply the existence of a hot atmosphere or lack thereof.* The opposite situation, $M_{\rm half} > M_{\rm crit}$, is expected at high redshift because massive halos are able to develop a hot atmosphere (and hence virial shocks), despite having a large fraction of accreted gas in the cold mode due to the large contribution from cold filaments. We caution the reader that although $M_{\rm half}$ has been calculated with high accuracy in the redshift ranges 0 to 4, at higher redshifts

($z = 4 - 6$) $M_{\rm half}$ was calculated assuming the parameter a fixed and at $z = 6 - 8$ $M_{\rm half}$ corresponds to the best-fit extrapolation.

Second, the bottom panel of Fig. 5.11 shows that in the redshift range $z = 0 - 4$, $M_{\rm hot}(M_{\rm crit})/[\frac{\Omega_{\rm b,0}}{\Omega_{\rm m,0}} M_{\rm crit}] \sim 0.1$. This indicates that when the hot halo becomes stable, the hot gas mass reaches $\sim 10\%$ of the total baryonic mass. We therefore define a *mass condition* for a halo to develop a stable hot atmosphere as

$$\frac{M_{\rm hot}}{\left(\frac{\Omega_{\rm b,0}}{\Omega_{\rm m,0}}\right) M_{\rm halo}} \geq 0.1, \tag{5.29}$$

and test this condition for hot halo formation in the presence of feedback variations.

The toy model presented in this section assumes that the formation of the hot halo is only driven by the heating from gravitational accretion shocks. However, in the presence of other energy sources, like stellar or AGN, the heating rate should increase, and therefore extra terms (like $\Gamma_{\rm stellar}$ or $\Gamma_{\rm AGN}$) should be added. In this case we do not compute extra heating sources for the presence of feedback, but we still find very good agreement between the analytical results and the numerical analysis (see §5.5.4). We next test how $M_{\rm crit}$ is affected by the presence different feedback implementations. To do it, we go back to Fig. 5.6, which shows $M_{\rm hot}/(\frac{\Omega_{\rm b,0}}{\Omega_{\rm m,0}} M_{\rm crit})$ as a function of halo mass for different feedback scenarios, and we calculate the halo mass at which $M_{\rm hot}/(\frac{\Omega_{\rm b,0}}{\Omega_{\rm m,0}} M_{\rm crit}) = 0.1$. From the figure we conclude that in the weak stellar feedback scenario $M_{\rm crit} \sim 10^{12.2}\,{\rm M}_\odot$ at $z = 0$, in the strong AGN $M_{\rm crit} \sim 10^{11.8}\,{\rm M}_\odot$, in the no AGN (but moderate) $M_{\rm crit} \sim 10^{11.5}\,{\rm M}_\odot$, and in the strong stellar $M_{\rm crit} \sim 10^{11.4}\,{\rm M}_\odot$. In the case of SN feedback, the larger the heating rate, the larger the amount of hot gas in the halo, and so the lower $M_{\rm crit}$. This is in agreement with the analysis in §5.3.1. On the other hand, when the heating rate from AGN feedback is large, gas is expelled from the halo, thus reducing the amount of hot gas and increasing $M_{\rm crit}$. We find good agreement between the estimated hot halo formation obtained from Fig. 5.6 and eq. (5.29), and the analysis in §5.2.1, where we found that in the scenarios of strong SN and no AGN feedback, $M_{\rm crit}$ was lower than in scenarios of weak SN and strong AGN.

Interestingly, our calculations for the critical halo mass, $M_{\rm crit}$, is in very good agreement with the calculations from Dekel & Birnboim (2006) at $z = 0$. In §5.5.5 we investigate why this is the case.

5.5.4 Comparison with numerical results

In this subsection we compare our semi-analytic predictions for $M_{\rm crit}$ presented in the previous section, with results of our simulations. To do this, we investigate whether halos with masses equal to $M_{\rm crit}$ present a bimodal cooling time PDF, indicating that the large heating rate from accretion shocks prevents gas from cooling (see §5.3 for a discussion of

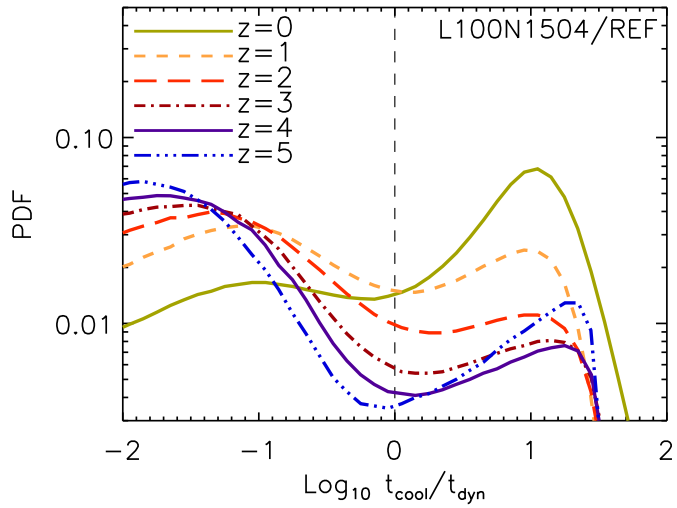

Figure 5.12: Cooling time mass-weighted PDF of gas particles from halos with masses in the logarithmic mass range $\log_{10}(M_{\rm crit}) \pm 0.1$ at $z = 0$, 1, 2, 3, 4 and 5.

cooling time PDF).

Fig. 5.12 shows the PDF of $\log_{10}(t_{\rm cool}/t_{\rm dyn})$ for halos with masses equal to $M_{\rm crit}$ from $z = 0 - 5$. We find that all curves have a bimodal shape and a local minimum in the range $-1 < \log_{10}(t_{\rm cool}/t_{\rm dyn}) < 1$. We therefore conclude that the hot atmosphere has been formed in these halos at each redshift, despite the increasing contribution of cold gas from filaments.

5.5.5 Comparison with Dekel & Birnboim (2006) model

Dekel & Birnboim (2006) derived a post-shock stability criterion based on the interplay between the cooling time and the compression time. In their derivation, Dekel & Birnboim began by defining the adiabatic index

$$\gamma_{\rm eff} = \gamma - \rho q/(\dot{\rho}\mathscr{E}), \tag{5.30}$$

which they rewrote in terms of the compression time, defined as $t_{\rm comp} = \Gamma\rho/\dot{\rho}$, with Γ an arbitrary constant and $\rho = N/V$, and the cooling time, $t_{\rm cool} = \mathscr{E}N/q$, as follows

$$\gamma_{\rm eff} = \gamma - \Gamma^{-1} t_{\rm comp}/t_{\rm cool}. \tag{5.31}$$

They found that the shock is stable if $\gamma_{\rm eff} > \gamma_{\rm crit} = 2\gamma/(\gamma + 2/3)$, which is equivalent to $t_{\rm cool} > t_{\rm comp}$. Once the cooling time is larger, the pressure gained by compression can balance the loss by radiative cooling, and thus support the shock. In their derivation, the factor $\Gamma = (3\gamma + 2)/[\gamma(3\gamma - 4)]$ was introduced to simplify the final expression in equation (5.31).

We compare our hot halo formation condition analysis with that of Dekel & Birnboim

(2006). We begin by writing equation (5.18) in terms of $t_{\rm cool}$ and $t_{\rm comp}$.

$$\dot{\mathscr{E}} = -P\dot{v} - q/N, \tag{5.32}$$
$$\frac{\dot{\mathscr{E}}}{\mathscr{E}} = \frac{P\dot{\rho}}{\mathscr{E}\rho^2} - \frac{q}{N\mathscr{E}}, \tag{5.33}$$
$$\frac{\dot{\mathscr{E}}}{\mathscr{E}} = t_{\rm comp}^{-1} - t_{\rm cool}^{-1}. \tag{5.34}$$
$$\tag{5.35}$$

In the second step we substituted $\dot{v} = -V\dot{N}/N^2 = -\dot{\rho}/\rho^2$ and divided by $\mathscr{E}$, and in the last step we substituted $P = (\gamma - 1)\mathscr{E}\rho$ and defined compression time as $t_{\rm comp} = (\gamma - 1)^{-1}\rho/\dot{\rho}$.

We conclude that our model is equivalent to Dekel & Birnboim (2006), and thus should yield to the same results at $z = 0$. At $z > 0$ we do not expect to obtain the same results as Dekel & Birnboim (2006) because of the different redshift dependence. In our model $\Gamma_{\rm heat} \propto \dot{M}_{\rm halo}$, whereas in Dekel & Birnboim (2006) $t_{\rm comp} \propto$ constant. Thus $M_{\rm critical,Dekel} \sim 6 \times 10^{11}\,{\rm M}_\odot$ for all redshifts. We believe we have improved upon the Dekel & Birnboim (2006) model by introducing not only a redshift dependence in the definition of $\Gamma_{\rm heat}$, which is seen in the numerical simulations, but also a dependence on the amount of shock-heated gas, which we find to decrease with increasing redshift at fixed halo mass due to the presence of cold filaments (see panels in Fig. 5.8).

5.6 Conclusions

We have studied the hot hydrostatic halo formation, its dependence on feedback mechanisms, hot gas mass in the halo and fraction of hot gas accretion using the EAGLE suite of hydrodynamical simulations as well as analytic calculations.

We have analysed the PDF of cooling time of gas in the halo and found that when the hot halo is formed, it produces a bimodality in the PDF. The bimodal shape indicates that the hot halo reduces the cooling flows, and thus increases the hot gas mass, $M_{\rm hot}$, at large radii. By inspection of cooling time PDFs, we have found that the mass scale for hot halo formation is $10^{11.7}\,{\rm M}_\odot$ at $z = 0$, as originally proposed by Dekel & Birnboim (2006).

However, the hot hydrostatic atmosphere forms in smaller (larger) halos in scenarios of strong (weak) stellar feedback. In the case of AGN feedback, we have found that the cooling time PDF is almost unchanged between scenarios with strong AGN and no AGN feedback. However, the PDFs do change at higher halo masses ($> 10^{12}\,{\rm M}_\odot$).

In addition to the hot gas in the halo, we have calculated the fraction of hot mode

gas accretion, $f_{\rm hot}$. Rather that using the maximum temperature to select shock-heated gas particles, we have used the gas temperature and entropy after accretion and obtain lower $f_{\rm hot}$ values. We believe $T_{\rm post-shock} + S_{\rm post-shock}$ is a better method to select hot gas accretion, because it does not include gas particles that go through a shock but immediately cool afterwards (i.e. due to in-shock cooling or heating rate smoothing) or are not even shock-heated but counted as hot accretion (as occurs when $T_{\rm max}$ is affected by stellar feedback), and therefore do not contribute to the hot halo formation process.

Finally, we have derived an semi-analytic model of hot halo formation that depends on hot gas mass in the halo, as well as accretion rates and the fraction of hot gas accretion. We have assumed energy conservation in the presence of radiative loses and ideal gas, and found that the change in the internal energy of the gas depends on the cooling rate and the heating rate. When the heating rate is larger than the cooling rate, the hot gas in the halo gains the necessary pressure through external shock heating to balance the energy loss by radiative cooling, and forms the hot halo.

We followed Dekel & Birnboim (2006) and defined a critical mass, $M_{\rm crit}$, above which the halo develops a hot atmosphere because the gas has larger heating than cooling rate. We have obtained $M_{\rm crit} = 10^{11.7}\,{\rm M}_{\odot}$ at $z = 0$. At higher redshift $M_{\rm crit}$ increases and reaches $10^{12.66}\,{\rm M}_{\odot}$ at $z = 8$. We have compared the values of $M_{\rm crit}$ with those of Dekel & Birnboim (2006) and found very good excellent agreement in the redshift range $z = 0-3$. At $z = 0$ this is expected because we showed that our stability condition expression is equivalent to that of Dekel & Birnboim (2006). At $z > 0$ we have a different redshift dependence introduced through the accretion rate, fraction of hot accretion and hot gas mass.

The formation of a hot stable atmosphere can be considered as a preventive feedback mechanism that decreases the gas accretion rate onto central galaxies, and thus reduces the amount of gas available to form stars. This has been seen in hydrodynamical simulations (see e.g. Faucher-Giguère et al. 2011; van de Voort et al. 2011; Nelson et al. 2013), however, due to the complexity in the interaction between the hot halo and AGN or stellar feedback, that modify the manner in which galaxies accrete gas, a physical model of galaxy gas accretion is still missing. In the following chapter we make use of the analytic calculations presented in this chapter and derive a model for gas accretion onto galaxies that depends on the hot/cold modes of gas accretion onto halos and on the rate of gas cooling from the hot halo.

6

On the hot halo cooling flow

This chapter investigates the physics that drives the gas accretion rate onto galaxies at the center of dark matter halos.

The manner gas falls into galaxies through cosmic time is a topic of open debate, due to the complexity in the interaction of multiple physical mechanisms that prevent gas in the halo from cooling. In this chapter we address this topic in detail. Using a suite of hydrodynamical cosmological simulations, we analyse the gas accretion rate onto the interstellar medium (ISM) and onto the galaxy. We find that the accretion rate onto the ISM remains roughly constant in halos larger than $10^{11.7}\,\mathrm{M}_{\odot}$, whereas the accretion rate onto the galaxy increases with increasing halo mass and flattens in the halo mass range $10^{11.7} - 10^{12.7}\,\mathrm{M}_{\odot}$, and at redshifts $z \leq 2$. The flattening is produced by the presence of the hot halo atmosphere that acts as a preventive feedback mechanism, and can be explained by comparing the cooling time of shock-heated gas accreted onto halos and the time that has passed since halos developed the hot atmosphere. We derive a physically motivated model of gas accretion onto galaxies, that depends on the rate of gas cooling from the hot halo, on the fraction of shock-heated gas, and on the rate of cold gas accretion. Finally, we show the model is equally successful in scenarios with and without AGN feedback. Readers unfamiliar with this topic are encouraged to first read §1.3 for a brief description on galaxy formation theory, and the previous chapter (Chapter 5) for a detailed analysis of gas accretion onto halos and hot halo formation.

6.1 Introduction

As discussed in chapters 1 and 2, dark matter halos form at the peaks of the primordial density field, and grow in mass through mergers and smooth accretion of dark matter and gas. Although there are recent claims that the dark matter and gas accretion rates onto halos are tightly coupled (Wetzel & Nagai 2015), gas, unlike dark matter, follows a more complicated physics. In the previous chapter we learned about the physical properties of gas in halos and the impact of feedback on the evolution of the gaseous halo. In this chapter we continue this analysis, and focus on the manner gas falls into galaxies.

There are several mechanisms that affect the way gas crosses the virial radius and falls into galaxies. The most important are accretion shocks and feedback from stars and black holes. Accretion shocks occur as a result of collisions between gas from the intergalactic medium falling into the halo and the stationary hot gas already in the halo. When accretion shocks occur, the gravitational energy of infall of gas is converted into thermal energy. Accretion shocks are then an important heating process, that were initially discussed by Rees & Ostriker (1977), Silk & Rees (1998) and White & Rees (1978). These works concluded that gas in the halo will infall into the galaxy only if the cooling radius is smaller than the virial radius. Otherwise, a hot hydrostatic halo is formed.

When gas crosses the hot halo and cools, feedback from stars and black holes reheats it and prevents it from falling into the galaxy. Stars and SN events produce large outflows in the form of winds that expel gas out of the galaxy into the inner halo, and thus produce a sort of recycling galactic fountain that acts as an extra mode of accretion onto galaxies (see e.g. Oppenheimer et al. 2010; Übler et al. 2014). Black holes, located in the center of the AGN, generate large radio jets that expand in the form of bubbles on scales > 30kpc, and are then able to heat the gas from the surrounding halo (e.g. Voit & Donahue 2005; Fabian et al. 2006; De Young 2010). This is generally referred to as "radio mode" feedback (Bower et al. 2006; Hopkins et al. 2007), that quenches the diffuse accretion rates onto galaxies (Croton et al. 2006; Sijacki et al. 2007; Martizzi et al. 2012; Dubois et al. 2012, 2013). Due to the complexity in the interaction of all the possible mechanisms that modify the manner in which galaxies accrete gas, a physical model of galaxy gas accretion is still missing. In this work, however, we make an attempt in modelling the gas accretion rates onto galaxies.

To understand the manner gas falls into galaxies, we first investigated the physical state of the gaseous halo, and the modes of gas accretion onto halos. In Chapter 5 we derive a new criteria to determine when the halo develops a hot hydrostatic atmosphere, based on the different modes of gas accretion onto halos. Namely, hot accretion, characterized by gas that shock-heats to the halo virial temperature, and cold accretion, that tends

to be filamentary, clumpy, of higher density than the hot mode, and strongly correlated with the dark matter filaments that feed halos (e.g. Kereš et al. 2005; Ocvirk et al. 2008; Dekel et al. 2009; van de Voort et al. 2011; Faucher-Giguère et al. 2011; Nelson et al. 2013; Woods et al. 2014). We calculate a heating rate produced by accretion shocks and compare it to the gas cooling rate, and find that dark matter halos that are above a critical mass threshold of $10^{11.7}\,\mathrm{M}_{\odot}$, are able to develop a hot stable atmosphere, in agreement with previous works (Birnboim & Dekel 2003; Dekel & Birnboim 2006).

The hot halo formation and the distinction between two cooling regimes have been implemented in semi-analytic models of galaxy formation (SAMs) since the work of White & Frenk (1991), who modelled the transition between rapid and slow cooling regimes depending on the cooling radius. The cooling radius ($r_{\rm cool}$) is defined as a radial scale below which all gas in the halo is able to cool, and it is obtained by finding where the cooling time (that depends on $r_{\rm cool}$ through the gas density) is equal to the dynamical time. If $r_{\rm cool}$ is smaller than the virial radius (r_{200}), then a hot atmosphere is formed, and gas accretion onto galaxies goes from being in the rapid cooling regime, to the slow cooling regime. Hydrodynamical simulations however, have shown that there are multiple overlapping gas components in the halo as a function of radius. These components are crudely described as quasi-static and inflowing material (see Nelson et al. 2015 for latest analysis and references therein). The hot/cold modes of accretion are in fact able to coexist in massive halos at high redshift (Dekel et al. 2009, see Chapter 5 for a description) and feed the galaxy at the same time. The co-evolution between the different modes of accretion has not been implemented in SAMs until recently. Cousin et al. (2015) included a two phase smooth baryonic accretion, with the hot and cold component built over the smooth dark matter accretion, whereas Lu et al. (2015) modelled a circum-halo medium, assumed to be preheated up to a certain entropy level, to reduce the baryonic accretion.

In this chapter, we aim to derive a physically motivated model of gas accretion onto galaxies, that is in perfect agreement with numerical simulations, depends on feedback and hot/cold modes of accretion, and can potentially be implemented in SAMs. To do it we begin by considering that the distinction from hot to cold accretion is not sharp. In Chapter 5 we showed that the fraction of hot accretion onto halos is a smooth function that goes from being 0 in low-mass halos ($< 10^{11}\,\mathrm{M}_{\odot}$) to 1 in high-mass halos ($> 10^{11}\,\mathrm{M}_{\odot}$), since halos that develop a stable hot atmosphere still accrete unshocked gas. We also take into account feedback that, as we showed in Chapter 5, affects the mass-scale of hot halo formation and therefore impacts on the distribution of gas in the halo. Feedback will then be included through the gas density profile, as an indicator of the distribution hot gas cooling in the halo.

This chapter is organized as follows. In §6.2 we briefly describe the numerical simulations used to study the gas accretion rates onto galaxies (for a more detailed description

Table 6.1: List of simulations. From left-to-right the columns show: simulation identifier; comoving box size; number of dark matter particles (there are equally many baryonic particles); initial baryonic particle mass; dark matter particle mass; comoving (Plummer-equivalent) gravitational softening; maximum physical softening.

Simulation	L (cMpc)	N	$m_{\rm b}$ ($\rm M_\odot$)	$m_{\rm dm}$ ($\rm M_\odot$)	$\varepsilon_{\rm com}$ (ckpc)	$\varepsilon_{\rm prop}$ (pkpc)
L100N1504/REF	100	1504^3	1.81×10^6	9.70×10^6	2.66	0.70
L100N0752/REF	100	752^3	1.44×10^7	7.76×10^7	5.32	1.40
L050N0752/REF	50	752^3	1.81×10^6	9.70×10^6	2.66	0.70
L050N0376/REF	50	376^3	1.44×10^7	7.76×10^7	5.32	1.40
L025N0752/REF	25	752^3	2.26×10^5	1.21×10^6	1.33	0.35
L025N0376/REF	25	376^3	1.81×10^6	9.70×10^6	2.66	0.70
L025N0376/No Feedback	25	376^3	1.81×10^6	9.70×10^6	2.66	0.70
L050N0752/No AGN	25	376^3	1.81×10^6	9.70×10^6	2.66	0.70
L050N0752/Strong AGN	25	376^3	1.81×10^6	9.70×10^6	2.66	0.70

see §5.2), and the method followed to measure the accretion rates. In §6.3 we analyse the total gas accretion rates onto galaxies from the EAGLE simulations as a function of halo mass and redshift, as well as the hot and cold modes of accretion. In §6.4 we investigate the density profile of gas in halos and derive a best-fitting model for the gas density profile. Next, we derive a physically motivated model of gas accretion onto galaxies in §6.5, that accurately reproduces the gas accretion rates from the EAGLE simulations. We analyze the role of AGN in the rates of gas cooling from the hot halo in §6.6, and show that the model from §6.5 is equally successful in scenarios with and without AGN feedback. Finally, we summarize and conclude in §6.7.

Throughout this chapter (as well as in Chapter 5) we define the halo mass, M_{200}, as all matter contained within r_{200}, radius where the mean density is 200 times the critical background density. We denote derivatives with respect to time as upper dots, therefore $\dot{M}_{\rm gas,galaxy}$ denotes gas accretion rate onto galaxies and $\dot{M}_{\rm gas,halos}$ onto halos.

6.2 Simulations

In this work we study gas accretion onto galaxies using a set of cosmological, hydrodynamical simulations from the Evolution and Assembly of GaLaxies and their Environments project (EAGLE; Schaye et al. 2015). EAGLE simulations were run using a modified version of GADGET 3 (Springel 2005), a N-Body Tree-PM smoothed particle hydrodynamics (SPH) code. In order to assess the numerical convergence we use simulations with different box sizes (ranging from 25 to 100 comoving Mpc) and particle numbers (ranging from 376^3 to 1504^3). The simulation names contain strings of the form Lxxx$N$yyyy, where xxx is the simulation box size in comoving Mpc and yyyy is the cube root of the number of particles per species (where the number of baryonic particles is equal to the number of dark mater particles). The simulations assume a ΛCDM cosmology with the parame-

ters given by *Planck-1* data (Planck Collaboration et al. 2014), $\Omega_{\rm m,0} = 1 - \Omega_\Lambda = 0.307$, $\Omega_{\rm b,0} = 0.04825$, $h = 0.6777$, $\sigma_8 = 0.8288$, $n_s = 0.9611$. The starting and final redshift of all simulations is $z = 127$ and $z = 0$, respectively.

In the previous chapter (§5.2) we provide a more complete description of the modeling of EAGLE simulations, but see Table 6.1 for a summary of the simulations used. Throughout this work we use the reference simulations (hereafter REF), that are in very good agreement with observables, e.g. the galaxy stellar mass function (Schaye et al. 2015; Crain et al. 2015). For the purpose of convergence analysis, we will refer to simulations with the mass and spatial resolution of L050N0376 as low-resolution, with the same resolution of L025N0376 as intermediate-resolution runs, and with the resolution of L025N0752 as high-resolution runs.

6.2.1 Methodology

We follow the methodology described in Chapter 5 to identify resolved halos and build merger trees. We use these merger trees to link halos through the snapshots and calculate the gas accretion onto halos and their central galaxies. We select gas particles accreted onto halos by performing an ID matching between particles within linked halos from consecutive snapshots. Therefore particles that are new to the system, and are within the virial radius are labeled as accreted particles in the redshift range $z_i < z < z_j$.

Different methods have been employed to determine gas accretion onto galaxies. For example, Faucher-Giguère et al. (2011) measured accretion rates through shells of prescribed radii. In order to differentiate outflows from inflowing material, they added the particles that intersect a given shell and defined the net accretion as $\dot{M} \propto \sum_p M_p \mathbf{v}_p / \Delta r_p$ (with M_p particle mass, $\mathbf{v_p}$ velocity vector and Δr_p thickness of shell). They classified the net accretion rates as inward or outward according to the direction of the velocity vector. A different approach was carried by van de Voort et al. (2011) who, in order to distinguish the galaxy from the halo, used a cut in the hydrogen number density ($n_{\rm H} > 0.1\ {\rm cm}^{-3}$) to define the interstellar medium (ISM), and considered particles that are part of the ISM or stellar mass at z_i, but which were gaseous and not part of the ISM at z_j to have been accreted onto a galaxy at $z_i < z < z_j$. Similarly, Nelson et al. (2013) made use of a density-temperature ($\rho - T$) cut criterion ($\log_{10}(T/{\rm K}) - 0.25 \log_{10}(\rho/\rho_{{\rm crit},z=0}) < 4.11$, with $\rho_{{\rm crit},z=0}$ critical density today), along with a radial cut ($< 0.15 \times r_{200}$). They considered a gas element to have accreted onto a galaxy if it belonged to that galaxy at z_j, and either crossed the phase space cut in $\rho - T$ or the radial cut during $z_i < z < z_j$.

In this work we are interested in investigating whether the hot halo impacts on the rate of inflowing gas onto galaxies. We follow the method of van de Voort et al. (2011) and consider the ISM to be formed by all particles within a sphere of radius $0.15 \times r_{200}$ (centered in the minimum gravitational potential) that are star-forming or that have

$n_{\rm H} > 0.01\,{\rm cm}^{-3}$ and $T < 10^5\,{\rm K}$ (atomic ISM). We next calculate two rates of gas accretion, gas accretion in the *vicinity* of the galaxy, $\dot{M}_{0.15r_{200}}$ and gas accretion onto the ISM, $\dot{M}_{\rm ISM}$. $\dot{M}_{0.15r_{200}}$ considers gas that cools from the gaseous halo and crosses the radial boundary $0.15 \times r_{200}$ during $z_i < z < z_j$, whereas $\dot{M}_{\rm ISM}$ considers gas that crosses the radial boundary and is star-forming or crosses the phase space cut $n_{\rm H} - T$ during $z_i < z < z_j$.

The top panel of Fig. 6.1 shows $\dot{M}_{0.15{\rm r}_{200}}$ (solid lines) and $\dot{M}_{\rm ISM}$ (dashed lines) as a function of halo mass, calculated from the L100N1504/REF simulation. For a comparison, the figure also includes the gas accretion of star-forming particles, $\dot{M}_{\rm SFR>0}$ (dot-dashed lines), which is (on average) a factor of 2 lower than $\dot{M}_{\rm ISM}$. In this case, $\dot{M}_{\rm SFR>0}$ considers gas that crosses the radial boundary and is star-forming during $z_i < z < z_j$. It can be seen that in large halos ($> 10^{12.5}\,{\rm M}_\odot$), $\dot{M}_{0.15{\rm r}_{200}}$ increases with halo mass, therefore it is dominated by gas cooling from the hot halo. However, $\dot{M}_{\rm ISM}$ and $\dot{M}_{\rm SFR>0}$ remain *roughly constant* with increasing halo mass, and only increase by ~ 0.5dex in the halo mass range $10^{12} - 10^{14}\,{\rm M}_\odot$. The bottom panel of Fig. 6.1 shows the specific accretion rate of the vicinity of the galaxy, ISM and star-forming particles. The specific accretion onto the ISM is calculated by taking the ratio between $\dot{M}_{\rm ISM}$ and the total mass of gas from the halo that forms part of the ISM. The specific accretion onto the $r < 0.15 \times r_{200}$ region is calculated by taking the ratio between $\dot{M}_{0.15{\rm r}_{200}}$ and the total gas mass from the halo contained within $0.15 \times r_{200}$. Similarly, the specific accretion rate of star-forming particles is calculated by taking the ratio between $\dot{M}_{\rm SFR>0}$ and the total mass of star-forming particles within $0.15 \times r_{200}$. The panel shows that the specific accretion rates of the ISM, galaxy region and star-forming particles are roughly the same, with a maximum factor of 1.6 difference between $\dot{M}_{\rm ISM}/M_{\rm ISM}$ and $\dot{M}_{0.15{\rm r}_{200}}/M_{0.15{\rm r}_{200}}$ in $10^{10}\,{\rm M}_\odot$ halos and 2.6 between $\dot{M}_{\rm SFR>0}/M_{\rm SFR>0}$ and $\dot{M}_{0.15{\rm r}_{200}}/M_{0.15{\rm r}_{200}}$ in $10^{11.5}\,{\rm M}_\odot$ halos.

We find that there is a median factor of 1.3 difference between the specific accretion rates of the ISM and galaxy region, we then assume that there is an accretion rate function, κ, that relates $\dot{M}_{0.15{\rm r}_{200}}$ and $\dot{M}_{\rm ISM}$ as

$$\kappa = \frac{\dot{M}_{\rm ISM}}{\dot{M}_{0.15{\rm r}_{200}}}, \tag{6.1}$$

$$= \frac{1}{1.3}\frac{M_{\rm ISM}}{M_{0.15{\rm r}_{200}}}, \tag{6.2}$$

$$= \frac{1}{1.3}\frac{\langle\rho_{\rm ISM}\rangle_{0.15r_{200}}}{\langle\rho_{\rm gas}\rangle_{0.15r_{200}}}, \tag{6.3}$$

where in eq. (6.2) we use the fact that $1.3\dot{M}_{\rm ISM}/M_{\rm ISM} = \dot{M}_{0.15{\rm r}_{200}}/M_{0.15{\rm r}_{200}}$. To derive expression (6.3), we assume that all gas from the ISM and the galaxy region is contained within $0.15 \times r_{200}$, so that the ratio between the masses is equal to the ratio between

their average densities. Therefore, $\langle\rho_{\rm ISM}\rangle_{0.15r_{200}}$ is the mean density of the ISM and $\langle\rho_{\rm gas}\rangle_{0.15r_{200}}$ is the mean enclosed gas density within a sphere of radius $r = 0.15 \times r_{200}$. Clearly $\dot{M}_{\rm ISM}$ strongly depends on $\dot{M}_{0.15{\rm r}_{200}}$. In this work we first focus on modelling and analyzing how the gas cooling from the hot halo impacts on $\dot{M}_{0.15{\rm r}_{200}}$ (§6.5.2), then we show that we can estimate $\dot{M}_{\rm ISM}$ from $\dot{M}_{0.15{\rm r}_{200}}$ using eq. (6.3) as follows

$$\dot{M}_{\rm ISM} = \frac{1}{1.3}\frac{\langle\rho_{\rm ISM}\rangle_{0.15r_{200}}}{\langle\rho_{\rm gas}\rangle_{0.15r_{200}}}\dot{M}_{0.15{\rm r}_{200}} \tag{6.4}$$

(§6.5.3).

In numerical simulations it is challenging to separate the galaxy from the surrounding halo. We define the atomic ISM through radial and $n_{\rm H}-T$ cuts, but the galaxy can extend beyond the ISM because it also contains gas heated by SN events or expelled by the central AGN. Therefore, we assume that the gas accretion rate onto a galaxy is the same as the accretion rate measured in the vicinity of the galaxy ($\dot{M}_{\rm gas,galaxy} = \dot{M}_{0.15{\rm r}_{200}}$). To distinguish between gas that accreted onto the halo and galaxy, we denote $\dot{M}_{\rm gas,galaxy}$ to gas particles that have crossed the radius $0.15 \times r_{200}$ during the redshift range $z_i < z < z_j$, whereas $\dot{M}_{\rm gas,halo}$ refers to gas particles that have crossed r_{200} during the redshift range $z_i < z < z_j$.

When calculating gas accretion onto galaxies and halos, the hot and cold modes of accretion are generally estimated by following the temperature history of the accreted gas, see e.g. Faucher-Giguère et al. (2011) and van de Voort et al. (2011). However, in Chapter 5 we concluded that selecting gas particles according to their temperature and entropy ($T_{\rm post-shock}$ and $S_{\rm post-shock}$, respectively) after accretion was a better method to determine the fraction of hot/cold accretion. This is because it does not include gas particles that go through a shock but immediately cool afterwards (i.e. due to in-shock cooling or heating rate smoothing, for a discussion the reader is encourage to read §5.2.2 and §5.4.1). Then, throughout this work, we select hot accreted gas particles as those that, after being accreted, have temperatures and entropies larger than $T_{\rm post-shock} = 10^{5.5}$ K and $S_{\rm post-shock} = 10^{7.2}$ K cm^2, respectively.

6.3 Gas accretion rates

In this section we calculate the rates of gas accretion onto halos and galaxies from the EAGLE simulations, and follow the methodology described in §6.2.1. We first analyse numerical convergence. We find excellent agreement between the accretion rates onto halos and galaxies from simulations with the same resolution and different box size, but not between simulations with different numerical resolution and same box size. In the latter case we find that $\dot{M}_{\rm gas,galaxy}$ increases by up to a factor of 10 if the mass resolution is increased by a factor of 64. For a detailed analysis of numerical convergence see following

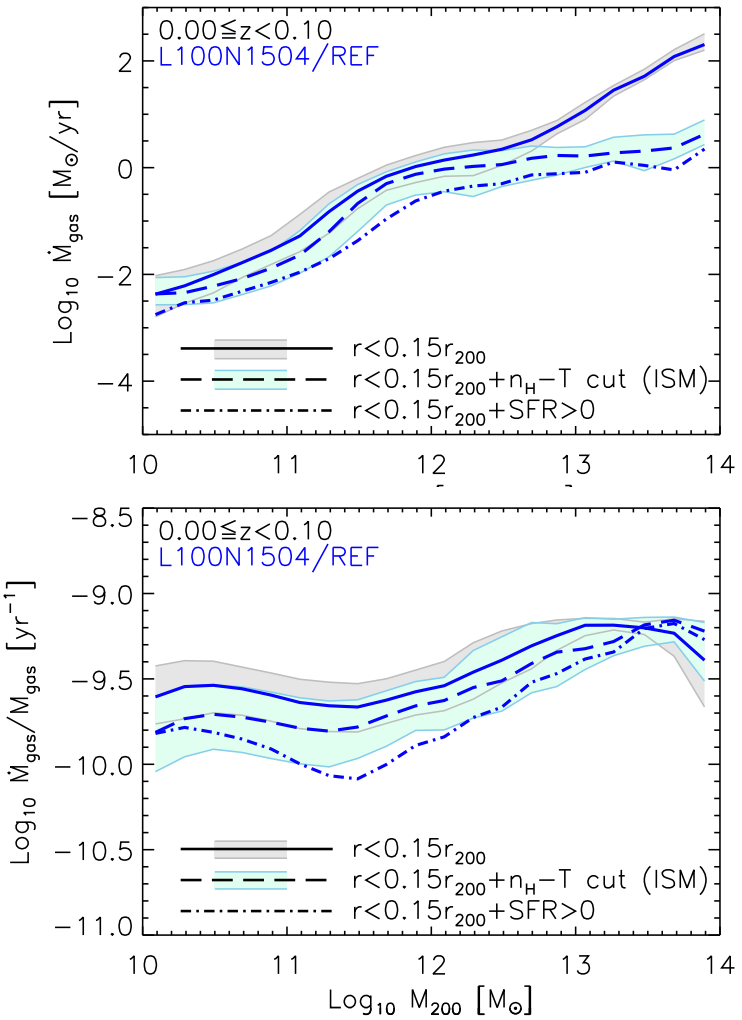

Figure 6.1: Top panel: accretion rate of gas onto the central galaxies of dark matter halos as a function of halo mass in the redshift range $0 \leq z < 0.1$. The solid line corresponds to gas accretion calculated by only counting gas particles that crossed $0.15 \times r_{200}$ during the consecutive snapshots, whereas the dashed line and dot-dashed line correspond to gas accretion onto the ISM and onto the $0.15 \times r_{200}$ regions of star-forming particles. Bottom panel: growth rate of gas forming part of the central galaxies (solid line), the ISM (dashed line) and star-forming (dot-dashed line). In the panels, the grey and cyan shade regions enclosing the median values of $\dot{M}_{\rm gas}$ and $\dot{M}_{\rm gas}/M_{\rm gas}$ correspond to the 1σ scatter (16-84th percentiles) onto the $0.15 \times r_{200}$ region and ISM, respectively. The 1σ scatter of $\dot{M}_{\rm SFR>0}$(and $\dot{M}_{\rm SFR>0}/M_{\rm SFR>0}$), not included in the figure, is (on average) 0.3 dex.

subsection. Throughout this work we use the intermediate-resolution simulations, which were carried out for different box sizes (from 25 to 100 comoving Mpc), and cover a large range in halo mass. In §6.3.2, we calculate the accretion rates onto halos and galaxies, covering four order of magnitude in halo mass (from 10^{10} to $10^{14}\,\mathrm{M}_{\odot}$) and the redshift ranges from 0 to 9. In §6.3.3 we analyse the hot and cold modes of accretion of gas onto galaxies.

6.3.1 Numerical convergence

In this section we investigate how numerical resolution impacts on the rates of gas accretion in the EAGLE simulations. Fig. 6.2 shows the total gas accretion onto halos (top panel) and their central galaxies (bottom panel) in the redshift range $0 \leq z < 0.1$. Both panels show that the accretion rates increase with increasing halo mass, and that numerical convergence is achieved in the process, but only between same-resolution simulations (between L0100N1504 and L0025N0376 and between L0100N0752 and L0050N0376). Numerical resolution is directly related to the efficiency of feedback mechanisms, the larger the resolution in the simulation the more efficient the implemented feedback, which gives raise to the need for (re-)calibration (see Schaye et al. 2015 for a discussion). We then do not expect strong convergence (between different-resolution simulations) in the gas accretion rates onto galaxies that, due to recycling winds from SN and AGN outflows, is feedback dependent. However, we find interesting that we do not have strong convergence in the accretion rates onto halos, which were found to be invariant to feedback (van de Voort et al. 2011). There are a few reasons that can explain this and that are not related to feedback. One is accretion shocks, it is possible that the low-resolution simulations (shown as purple curves in the panels) do not resolve the shocks properly (Creasey et al. 2011, or see §5.2.2 for a discussion). Hot accreted gas tends to cross the virial radius multiple times before settling onto the hot halo, thus producing an increase in the rate of gas accretion. If the shocks are not well resolved in regions where gas particles do not have long cooling times, hot accreted gas will cool rapidly, particularly around low-mass halos ($< 10^{12}\,\mathrm{M}_{\odot}$). However, the overcooling is not significant in high-mass halos ($> 10^{12}\,\mathrm{M}_{\odot}$) because the cooling time of the gas particles is too long, as a result there is better convergence between the low- and the intermediate-resolution simulations (yellow curves) in the high-mass end. Another possible explanation is the method used in this work to calculate accretion rates. Rather than following the entire mass growth of the halos and dividing it by the time step (as done in Chapter 3), individual particles that cross the virial radius are counted. Therefore increasing resolution leads to an increasing inflow of particles.

It is important to note that the top panel from Fig. 6.2 shows an abrupt drop in the accretion rates from the intermediate-resolution simulations (yellow curves) in halos

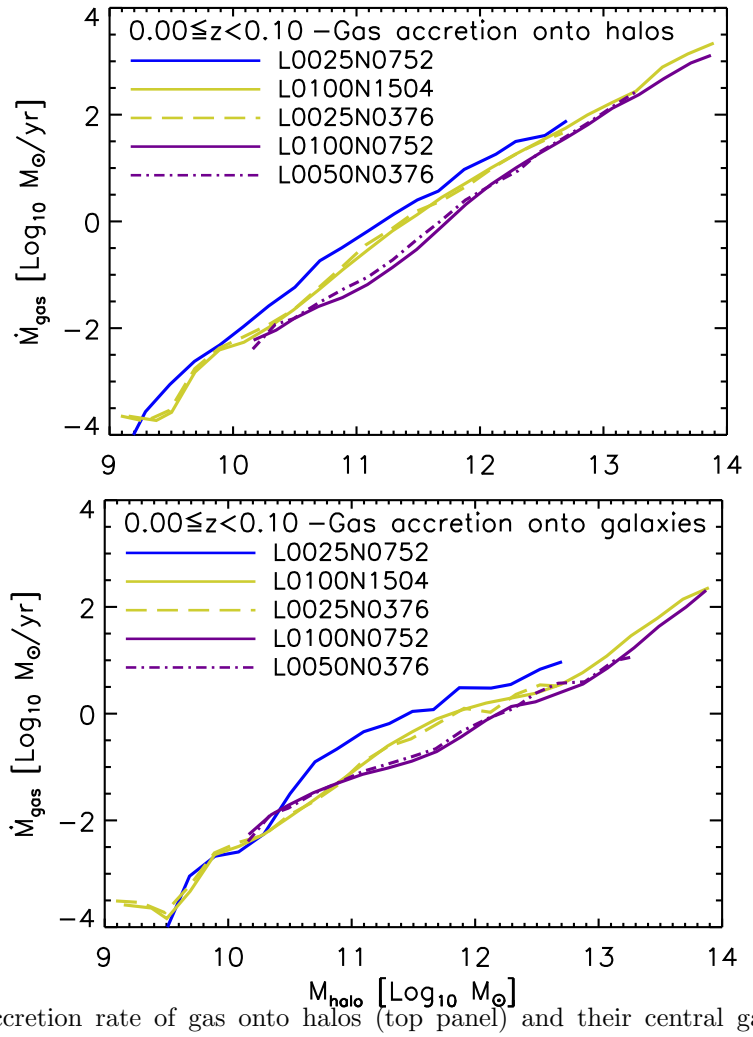

Figure 6.2: Accretion rate of gas onto halos (top panel) and their central galaxies (bottom panel) as a function of halo mass in the redshift range $0 \leq z < 0.1$. The curves show the median values of the total accretion rates of halos in logarithmic mass bins of 0.2, each mass bin contains at least 10 halos. To analyze numerical convergence, we compare accretion rates from simulations with different box sizes and number of particles and therefore different resolution. We classify the simulations as high-resolution (blue curves), intermediate-resolution (yellow ruves) and low-resolution (purple curves). We are able to find numerical convergence between same-resolution simulations.

smaller than $10^{10}\,\mathrm{M}_\odot$. This can be a numerical artifact because such drop is not seen in the accretion rates from the large-resolution simulation (blue curve). We therefore set the minimum halo mass for accretion onto halos (and their inner galaxies) to correspond to 1000 dark matter particles ($\sim 10^{10}\,\mathrm{M}_\odot$ halo mass for the intermediate-resolution simulations). The galaxy accretion rates (shown in the bottom panel of Fig. 6.2) increase by up to a factor of 10 ($\dot{M}_{\mathrm{gas,galaxy}} = 1\,\mathrm{M}_\odot/\mathrm{yr}$ from L0025N0752 with respect to $\dot{M}_{\mathrm{gas,galaxy}} = 0.1\,\mathrm{M}_\odot/\mathrm{yr}$ from L0050N0376 at $\sim 10^{11.5}\,\mathrm{M}_\odot$) if the mass resolution is increased by a factor of 64. This is opposite to van de Voort et al. (2011) who found a decrease, but also measured accretion through a density-cut, rather than only a radial cut.

Throughout this work we use the intermediate-resolution simulations, since those were carried out for different box sizes (from 25 to 100 comoving Mpc), they are more suitable to cover a large range in halo mass.

6.3.2 Accretion rates onto galaxies and halos

In this section we investigate the gas accretion rates onto halos and galaxies in more detail. Fig. 6.3 shows the total gas accretion rate onto halos (bottom-left panel) and onto galaxies (bottom-right panel) over many redshift ranges. The solid lines correspond to the median gas accretion rates from the L100N1504/REF simulation. In this case we calculated the accretion rates by adding the mass of all the accreted particles onto individual halos and dividing by the time interval between the snapshots. The figure shows the median accretion rates of stack of halos separated in logarithmic mass bins of 0.2. The dashed lines correspond to the extended analytic accretion rates times the baryon fraction (f_b) derived in Chapter 4. In this case, we are not using the universal baryon fraction ($f_b^{\mathrm{univ}} = \Omega_{\mathrm{b},0}/\Omega_{\mathrm{m},0} = 0.157$), instead, we find that in order to obtain a good agreement between the curves at high redshift, f_b must be $f_\mathrm{b} = 0.1$. This is in agreement with Schaller et al. (2015), who calculated the mass fractions of baryons within r_{200} and found that the baryon fractions are much lower than the universal value for all halos smaller than $10^{14}\,\mathrm{M}_\odot$, i.e. $f_\mathrm{b} \approx 0.05$ for $10^{12}\,\mathrm{M}_\odot$ halos and $f_\mathrm{b} \approx 0.1$ for $10^{13}\,\mathrm{M}_\odot$ halos. In the figure, all the curves are coloured according to the redshift interval, as indicated in the legends. The top panels show the 1σ scatter of $\dot{M}_{\mathrm{gas,halo}}$ (top-left) and $\dot{M}_{\mathrm{gas,galaxy}}$ (top-right) for each mass bin.

We find that the low-redshift accretion rates onto halos deviate from the analytic prediction of Chapter 4. This is due to feedback mechanisms that change the halo population. We find that while the $\dot{M}_{\mathrm{gas,halo}}$ curves taken from simulations with different feedback implementations disagree with the model of Chapter 4 (but are in very good agreement with each other, as also shown by van de Voort et al. 2011), $\dot{M}_{\mathrm{gas,halo}}$ median values from the no feedback simulations are in perfect agreement with the model. At high

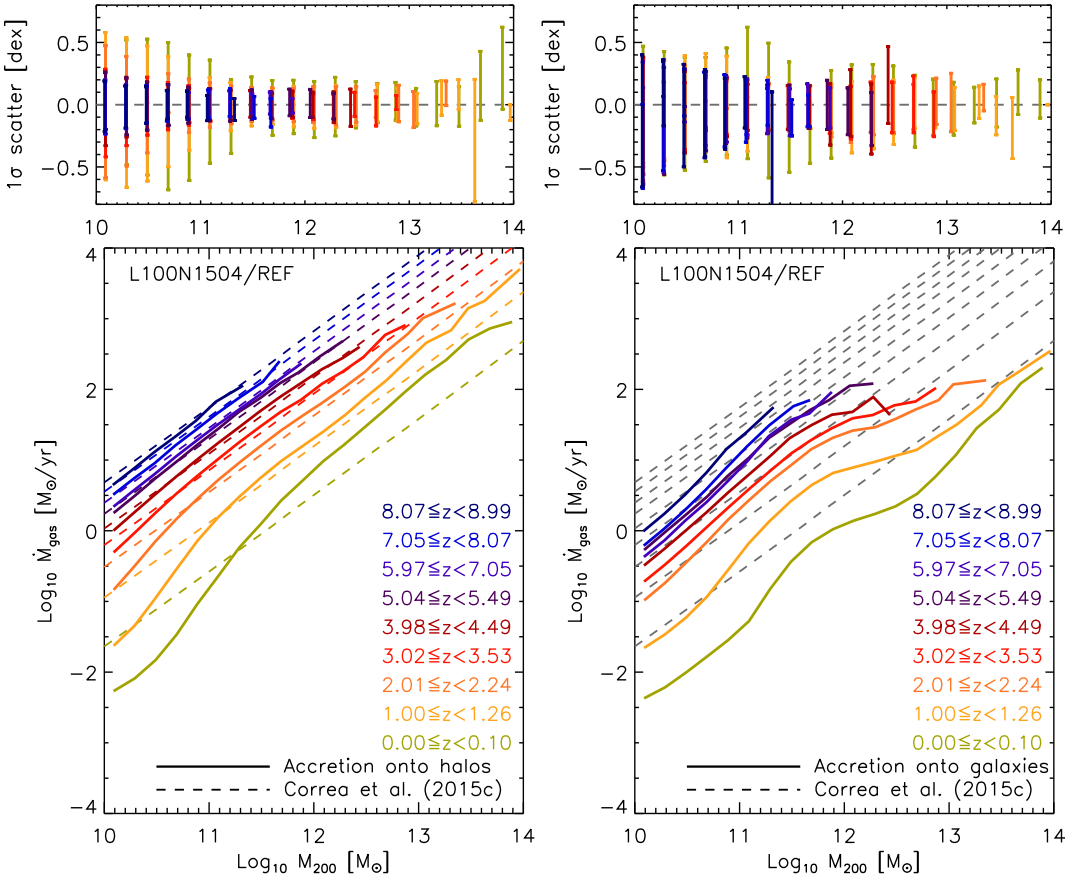

Figure 6.3: Accretion rates onto halos (bottom-left panel) and galaxies (bottom-right panel) as a function of halo mass for a large range of redshift. The curves are colored matching the redshift interval indicated in the legends at which they were calculated. The solid curves correspond to the accretion rates taken from the L100N1504/REF simulation, whereas the dashed curves correspond to the extended analytic model derived in Chapter 4 for halo accretion rates. The 1σ scatter (16-84th percentiles) of the median accretion rates onto halos and galaxies are shown in the top-left and top-right panel, respectively.

halo masses, a possible explanation for this discrepancy is that AGN feedback expels most of the gas from the halo, so that the gas remains hot and crosses the virial radius multiple times generating a recycling effect that increases the accretion rate in large halos. In small halos the fact that the accretion rates are lower than the analytic prediction is less easily understood, because at these halo masses AGN is not thought to have a large impact, and stellar feedback is not a sufficient strong mechanism to lower the halo accretion rates. The signature of low accretion onto low-mass halos and high-accretion onto high mass halos is also seen in the redshift range 1.0 to 1.26 and 2.01 to 2.24. As expected, at higher redshifts the accretion curves are in much better quantitative agreement with the analytic model.

We look for the best-fit expression that reproduces the halo gas accretion rates in the presence of feedback from the REF model. We find it to be

$$\log_{10}\dot{M}_{\rm gas,halo} = a_{z\leq4}(z) + b_{z\leq4}(z)x + c_{z\leq4}(z)x^2, \quad (6.5)$$
$$a_{z\leq4}(z) = 0.830 + 0.553z - 0.0523z^2, \quad (6.6)$$
$$b_{z\leq4}(z) = 1.436 - 0.149z + 0.007z^2, \quad (6.7)$$
$$c_{z\leq4}(z) = -0.134 + 0.099z - 0.023z^2, \quad (6.8)$$
$$x = \log_{10}(M_{200}/10^{12}\,{\rm M}_\odot), \quad (6.9)$$

if $0 \leq z \leq 4$ and

$$\log_{10}\dot{M}_{\rm gas,halo} = a_{z>4}(z) + b_{z>4}(z)x, \quad (6.10)$$
$$a_{z>4}(z) = 3.287 - 0.401z + 0.045z^2, \quad (6.11)$$
$$b_{z>4}(z) = 1.016 + 0.003z + 0.002z^2. \quad (6.12)$$

if $z > 4$.

The bottom-right panel of Fig. 6.3 shows that the gas accretion rate onto galaxies is quite different from those onto halos. Although it initially increases with halo mass, it flattens in the halo mass range $10^{11.7} - 10^{12.7}\,{\rm M}_\odot$, particularly at $z \leq 2$. The flattening is produced by the presence of the hot halo atmosphere, which forms in $\sim 10^{11.7}\,{\rm M}_\odot$ halos at $z = 0 - 4$ (Chapter 5) and thus prevents gas from cooling and falling into the galaxy region. Our galaxy accretion rates are in close agreement with other simulations (Kereš et al. 2005; Ocvirk et al. 2008; Faucher-Giguère et al. 2011; van de Voort et al. 2011; Nelson et al. 2013).

We aim to provide a physical understanding of gas accretion onto galaxies. To do so, in the following subsection we investigate the impact of feedback mechanisms on galaxy gas accretion as well as the hot and cold contributions to the total gas accretion rates onto galaxies. In §6.5.2 we derive a semi-analytic, physically motivated model that reproduces the solid curves shown in the right panel of Fig. 6.3.

6.3.2.1 Impact of feedback and hydrodynamics

It has been shown that the inflow rate of gas onto galaxies not only depends sensitively on definition (as discussed in Section 6.2.1), but also on feedback physics (e.g. Oppenheimer et al. 2010; van de Voort et al. 2011; Faucher-Giguère et al. 2011; Nelson et al. 2015; Übler et al. 2014). Recently, Nelson et al. (2015) compared two simulations run with the AREPO code, while one included energetic feedback from star formation driven winds

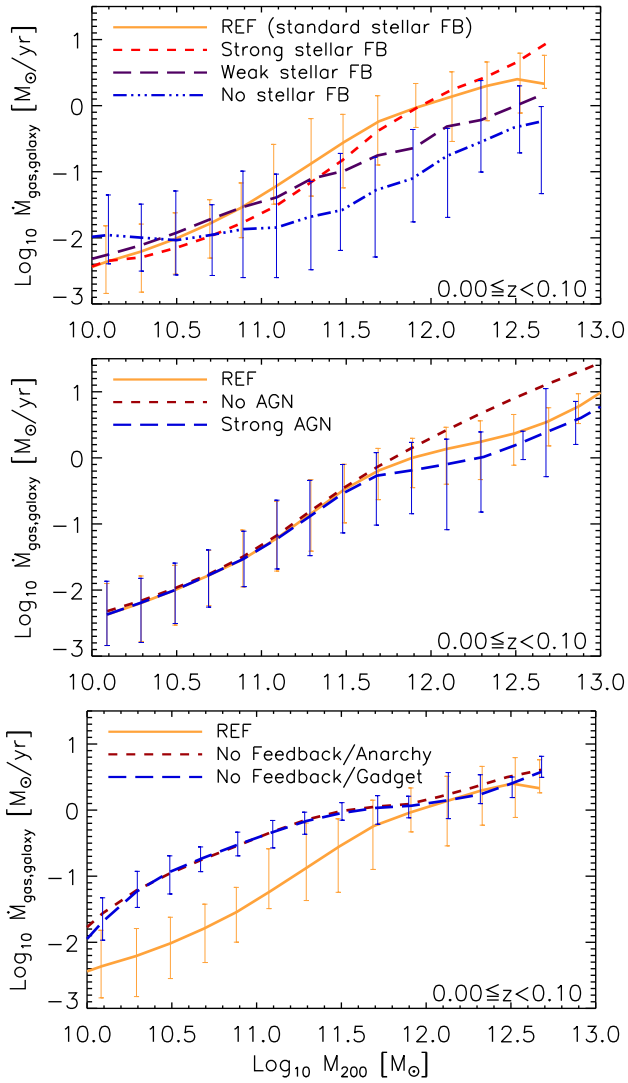

Figure 6.4: Gas accretion rate onto central galaxies as a function of halo mass in the redshift range $0 \leq z < 0.1$. The top panel compares accretion rates from same-resolution simulations (L025N0376 box) but with standard stellar feedback (REF, solid orange line), strong stellar feedback (red short-dashed line), weak stellar feedback (purple long-dashed line) and no stellar feedback (blue dot-dashed line). The middle panel compares the accretion rates calculated from the L050N0752 simulations that include standard AGN feedback (REF, solid orange line), no AGN feedback (purple short-dashed line) and strong AGN feedback (blue long-dashed line). The bottom panel shows the same as the middle and top panel, but in this case the curves correspond to the accretion rates calculated from the L025N0376/REF (orange solid line), L025N0376/NoFeedback Anarchy (purple short-dashed line) and L025N0376/NoFeedback Gadget (blue long dashed line) simulations. In the panels the error bars show the 16-84th percentiles.

as well as supermassive black holes, the other did not include any treatment of metal line cooling, stellar or associated black hole feedback. They found that feedback strongly suppresses the net accretion rate onto central galaxies (counted as the number of gas tracers crossing the radius $0.15r_{200}$) by a factor of $\sim$3 at $z = 5$, and a factor of $\sim$10 at $z = 1$. A similar conclusion was reached by van de Voort et al. (2011), who showed that the effects of stellar feedback and metal-line cooling are much stronger for accretion onto galaxies than for accretion onto halos, and can result in differences of an order of magnitude.

In scenarios of strong stellar feedback, the galaxy accretion rates are higher due to 'recycling accretion'. Stellar driven winds blow gas out of the galaxy, but not out of the halo, as a result the same gas elements are accreted onto the galaxy multiple times (Oppenheimer et al. 2010). Übler et al. (2014) implemented a hybrid thermal/kinetic stellar feedback scheme, and calculated the gas accretion histories onto discs as a function of cosmic time. They found that the re-accreted gas can be as large as a factor of 10 in the strong feedback models with respect to weak feedback, and tends to dominate the net accretion at $z < 1$. To investigate the effect of stellar feedback on the galaxies accretion rate from the EAGLE simulations, we compare the reference model with same resolution simulations (the L025N0376 case) that include strong and weak stellar feedback (StrongFB and WeakFB, respectively). The REF, StrongFB and WeakFB simulations employ the same feedback prescription and choice of parameters for AGN feedback, but the energy budget expelled by the stellar feedback is varied. In the REF model the probability that a neighbouring SPH particle is heated is determined by the fraction of the energy, which depends on the maximum ($f_{\rm th,max} = 3.0$) and minimum ($f_{\rm th,min} = 0.3$) threshold values. In the StrongFB and WeakFB models the thresholds change as $f_{\rm th,max} = 6.0$ and $f_{\rm th,min} = 0.6$ for the StrongFB case, and $f_{\rm th,max} = 1.5$ and $f_{\rm th,min} = 0.15$ for the WeakFB case (for more details see Schaye et al. 2015).

Fig. 6.4 shows the accretion rate of gas onto the central galaxies of dark matter halos as a function of halo mass in the redshift range $0 \leq z < 0.1$. The top panel compares the accretion rates between the REF model (orange solid line), StrongFB model (red short-dashed line), WeakFB model (purple long-dashed line) and No stellar FB model (blue dot-dashed line, where stellar feedback is switched off). The panel shows that while there is no strong difference in $\dot{M}_{\rm gas,galaxy}$ between the REF and StrongFB models (on average the difference is less than 0.3 dex). In halos larger than $10^{11}\,{\rm M}_\odot$ the accretion rate decreases when stellar feedback is weak (by up to 0.6 dex) or switched off (by up to 1.5 dex). As discussed in the previous paragraph, the main reason for these differences is the decrease in the recycling accretion due to stellar winds, that dominates $\dot{M}_{\rm gas,galaxy}$ at low redshift.

We next investigate the effect of AGN feedback on the gas accretion onto central

galaxies. It is well known that the central supermassive black holes observed in many massive galaxies expel large amounts of gas in the form of jets (radio mode feedback). The jets heat the gas in the surrounding circumgalactic medium and prevent it from cooling and falling into the central disc (e.g. Dubois et al. 2012). To understand how AGN feedback alters $\dot{M}_{\rm gas,galaxy}$ in massive halos, we compare simulations that include the same stellar feedback scheme but different AGN feedback, varying from no feedback, standard feedback (REF model), to strong AGN feedback. In the EAGLE simulations, the main difference between REF and Strong AGN simulations is the temperature increment of stochastic AGN heating ($\Delta T_{\rm AGN}$), which is $\Delta T_{\rm AGN} = 10^{8.5}$ K in the REF model and $\Delta T_{\rm AGN} = 10^{9.5}$ K in the Strong AGN model. The middle panel of Fig. 6.4 shows $\dot{M}_{\rm gas,galaxy}$ from the REF model (orange solid line), from the no AGN feedback model (purple short-dashed line) and from the strong AGN feedback model (blue long-dashed line). As expected, AGN feedback impacts on $\dot{M}_{\rm gas,galaxy}$ in massive halos ($> 10^{11.5}\,{\rm M}_{\odot}$) by decreasing the rate of inflow by up to 0.6 dex for the standard AGN feedback, and up to 0.8 dex in the strong AGN feedback in $10^{12.5}\,{\rm M}_{\odot}$ halos, with respect to the galaxy accretion rate from the no AGN simulation. We investigate the impact of AGN feedback on $\dot{M}_{\rm gas,galaxy}$ in more detail in §6.6, where we analyse the relation between AGN feedback and the hot halo cooling flow.

Finally, we compare simulations with different hydrodynamics schemes. In Chapter 5 we discuss the differences between the standard SPH code GADGET and a more recent formulation of SPH included in the EALGE simulations named Anarchy (Dalla Vecchia 2016 in prep.). We find that while gas mixing is largely suppressed in GADGET, Anarchy is able to mix phases in contact discontinuity allowing dense clumps to dissolve into the hot halo. As a result the fraction of hot gas accretion onto halos is lower (by up to 0.2 dex) in the GADGET simulation with respect to its Anarchy counterpart. In the bottom panel of Fig. 6.4 we compare the gas accretion rates onto galaxies calculated from the REF (orange solid line), the NoFeedback/Anarchy (purple short-dashed line) and NoFeedback/GADGET (blue long-dashed line) simulations. The panel shows that in the absence of feedback the gas accretion rates onto galaxies is larger (by up to an order of magnitude) in halos smaller than $10^{11.5}\,{\rm M}_{\odot}$. In larger halos we find very good agreement between accretion rates. In this last case we caution the reader that we are comparing same-resolution simulations run in the L025N0376 box, as a result the number of halos above $10^{12}\,{\rm M}_{\odot}$ is $\sim$10 in each mass bin and therefore it does not represent a complete sample.

In the following subsection we investigate the contributions of hot and cold modes in the galaxy accretion rates, and further analyse how these galaxy hot/cold rates change with feedback and hydrodynamics.

6.3.3 Hot and cold modes of accretion

When gas crosses the virial radius it can either experience a shock and be heated to the halo virial temperature or infall into the halo unperturbed. In Chapter 5 we calculate the fractions of hot and cold accretion modes using the EAGLE simulations, and find the best-fit expression for the fractions as a function of halo mass and redshift to be

$$f_{\rm hot}(x,z) = [\exp(a(z)[x-\log_{10} M_{1/2}(z)])+1]^{-1}, \tag{6.13}$$

$$x = \log_{10}(M_{200}/10^{12}\,{\rm M}_\odot), \tag{6.14}$$

$$a(z) = \begin{cases} -4.301\times10^{-1.269\tilde{z}+1.288\tilde{z}^2} & \text{if } 0\le z<2, \\ -1.080\times10^{0.810\tilde{z}-0.423\tilde{z}^2} & \text{if } 2\le z<4, \\ -2.471 & \text{if } z\ge 4, \end{cases} \tag{6.15}$$

$$\tilde{z} = \log_{10}(1+z), \tag{6.16}$$

$$M_{1/2}(z) = \begin{cases} -0.149+0.217z+0.067z^2 & \text{if } 0\le z<2, \\ -0.248+0.534z-0.069z^2 & \text{if } 2\le z<4, \\ 0.724+0.015z & \text{if } z\ge 4, \end{cases} \tag{6.17}$$

In this section we extend this analysis by focusing on the modes of accretion onto galaxies. We select gas particles using the radial cut ($0.15\times r_{200}$) and separate the gas accretion rates into the two modes by following the thermal properties of the particles (see §6.2.1 for a description on how we calculate hot/cold gas accretion). We then obtain a cold mode of gas accretion onto the galaxy that directly contributes to the SFR. As well as a hot mode of gas accretion, that it is formed by the gas cooling from the hot halo, hereafter 'hot halo cooling flow'.

Fig. 6.5 shows the total accretion rate onto galaxies (black solid lines), the hot mode of gas accretion (short-dashed red lines) and the cold mode of gas accretion (long-dashed blue lines) for different redshift ranges $0\le z<0.1$ (top left panel), $1.0\le z<1.26$ (top right panel), $2.01\le z<2.24$ (bottom left panel) and $3.02\le z<3.53$ (bottom right panel). We find that when $\dot{M}_{\rm gas,galaxy}$ flattens, it changes from being cold-mode dominated to hot-mode dominated. As a result, in $>10^{12.7}\,{\rm M}_\odot$ halos, $\dot{M}_{\rm gas,galaxy}$ increases with increasing halo mass while being hot dominated, meaning that there is a halo mass scale above which cooling flows from the hot halo are able to develop.

The fact that gas cooling from the hot halo raises $\dot{M}_{\rm gas,galaxy}$ can be explained by comparing the typical cooling time of shock-heated gas, with the time that has passed

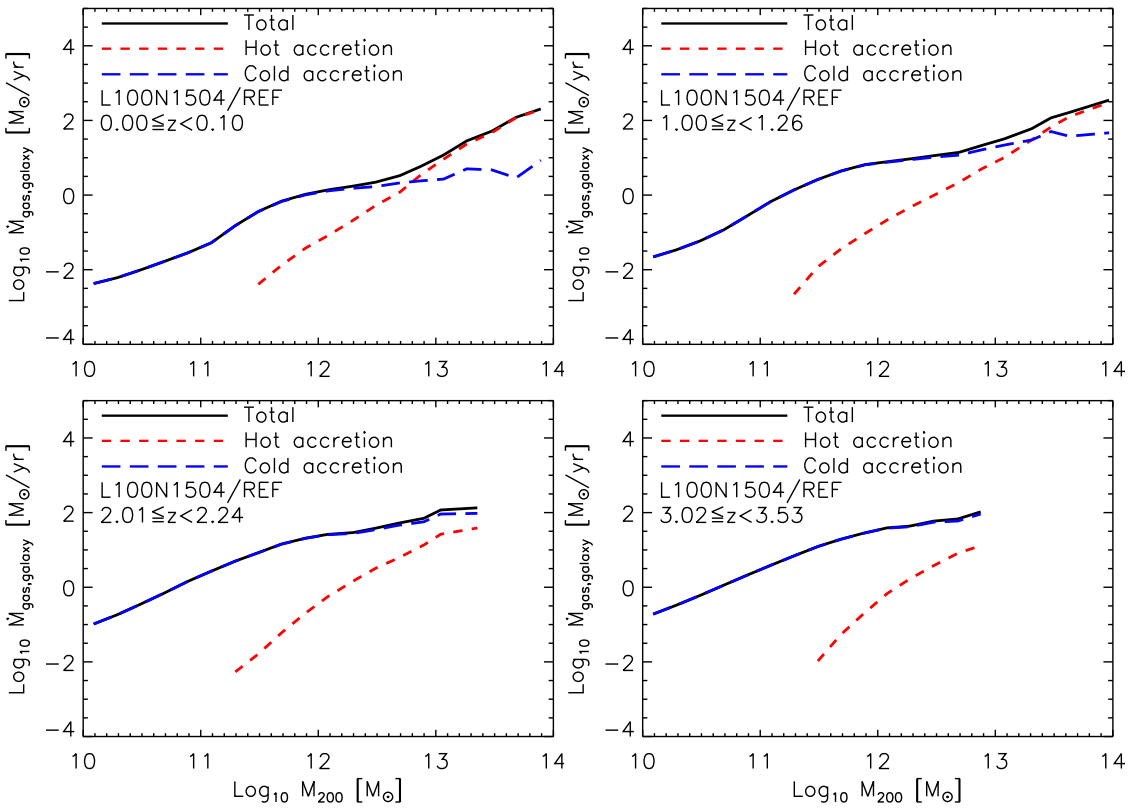

Figure 6.5: Gas accretion rates onto galaxies as a function of halo mass in the redshift ranges $0 \leq z < 0.1$ (top left panel), $1 \leq z < 1.26$ (top right panel), $2 \leq z < 2.24$ (bottom left panel) and $3 \leq z < 3.53$ (bottom right panel). The black solid curves correspond to the total gas accretion rates (both hot and cold gas are included), whereas the red short dashed lines and blue long dashed line correspond to the hot and cold modes of gas accretion, respectively. As can be seen from the panels, cold accretion always dominates in small halos (e.g. $< 10^{11.5}\,\mathrm{M}_{\odot}$ at $z = 0$), whereas hot accretion dominates in large halos at late times. The accretion rates were calculated averaging the rates from halos separated in logarithmic mass bins of 0.2, that contained at least 10 halos.

since halos developed the hot atmosphere. For instance, a $10^{12.0}\,M_\odot$ halo at $z = 0$ had a mass of $10^{11.7}\,M_\odot$ at $z \approx 1.16$ (according to the analytic model of halo MAH from Chapter 2). Since $10^{11.7}\,M_\odot$ is the mass scale of hot halo formation, we conclude that a $10^{12}\,M_\odot$ halo formed its hot atmosphere at $z = 1.16$, when most of the shock-heated gas had a cooling time of ≈ 10Gyr (see §5.3). Since only 8.53Gyr passed between the redshift range 0 to 1.16, not all the hot gas in the halo has been able to cool. This produces a flattening in the gas accretion rates onto galaxies from halos with masses between $10^{11.7}$ and $10^{12.7}\,M_\odot$. Larger halos ($\gg 10^{12}\,M_\odot$) on the other hand, that formed their hot atmospheres earlier (more than 10 Gyr ago), contain gas that is able to cool, therefore $\dot{M}_{\rm gas,galaxy}$ increases with increasing halo mass.

At $z = 0$ there are no cold filaments penetrating the hot halo and delivering cold gas within galaxies, but these are present at $z = 2$ (see §5.3). We therefore expect the amount of cold accretion to increase towards high redshift at fixed halo mass. In Chapter 5 we compare two different methods to select particles accreted hot or cold based on the maximum temperature ($T_{\rm max}$) ever reached by the gas particle and the temperature and entropy ($T_{\rm post-shock} + S_{\rm post-shock}$) of the gas particle after being accreted. By applying the $T_{\rm max}$ method, which has been the most commonly used (e.g. Kereš et al. 2005, 2009; Faucher-Giguère et al. 2011; van de Voort et al. 2011; Nelson et al. 2013, among others), we find that the fraction of hot accretion onto halos is in very good agreement with van de Voort et al. (2011), as it decreases with increasing redshift at fixed halo mass.

However, the hot/cold modes of accretion onto galaxies calculated in this work largely deviate from previously published works, that have claimed that there are no cold accretion onto galaxies at $z = 2$. For example, Nelson et al. (2015) (as well as Kereš et al. 2009) found that at $z = 2$ cold accretion of external diffuse gas accounts for only 10% of the total accretion onto central galaxies of $10^{12}\,M_\odot$ halos. Nelson et al. (2015) used simulations run with the AREPO code (Springel 2010), and defined hot accretion if the maximum past temperature of the gas particles was larger than the virial temperature of the host halo at the accretion time (time of the most recent radial crossing). In Paper I as well as throughout this work, we apply the $T_{\rm post-shock} + S_{\rm post-shock}$ method, based on the current temperature and entropy of the gas particle, to calculate the hot/cold modes of gas accretion. As a result, we find that cold accretion onto galaxies in $10^{12}\,M_\odot$ halos accounts for 50% (70%) of the total at $z = 0$ ($z = 2$) using the $T_{\rm max}$ criteria, but it accounts for 90% (95%) using the $T_{\rm post-shock} + S_{\rm post-shock}$ criteria.

The different method we employ to calculate the modes of accretion explains the large differences with respect to previous works. We believe that $T_{\rm max}$ is not suitable for identifying cold flows for the following reasons. First, it occurs that gas goes through a shock but immediately cools afterwards (due to in-shock cooling, e.g Hutchings & Thomas 2000). In this case if gas is mostly cold except at a point in space and for a short period

of time, numerical studies would label it as hot accretion but observations would call it a cold flow. Secondly, it also occurs that SN outflows heat the surrounding gas particles, that reach large temperature values ($\sim 10^{7.5}$K) while being expelled out the galaxy. After that, the particles eventually cool and are re-acreted onto the galaxy. However, since they did not reach a temperature larger than $10^{7.5}$K when crossing $0.15 \times R_{200}$, $T_{\rm max}$ is not updated and they are considered as hot mode accretion by the $T_{\rm max}$ criterion (for more details see Chapter 5).

We next analyse how feedback impacts on hot gas accretion onto galaxies. In the previous subsection we found that the total rate of gas accretion onto galaxies changes with feedback, by decreasing in scenarios of weak and no stellar feedback, and increasing when there is no AGN feedback. We investigate how the fraction of hot gas accretion onto galaxies ($f_{\rm hot,galaxy}$, ratio of hot gas accretion with respect to the total) changes with feedback. We compare simulations with strong, standard and weak stellar feedback and find that stellar feedback does not significantly alter $f_{\rm hot,galaxy}$. Similarly, we compare simulations with strong, standard and no AGN feedback and find that while $f_{\rm hot,galaxy}$ from standard and strong AGN feedback are in very good agreement, $f_{\rm hot,galaxy}$ from the no AGN feedback simulation increases by $\sim$0.2 dex at fixed halo mass (in halos larger than $10^{12}\,{\rm M}_{\odot}$). This is very encouraging, since it indicates that $T_{\rm post-shock} + S_{\rm post-shock}$ method is not as feedback dependent as the $T_{\rm max}$ method (Nelson et al. 2015). Also it proves that the galaxy hot gas accretion is connected with the hot halo cooling flow, able to develop earlier when there is no AGN feedback. We further analyse the cooling flow-AGN feedback connection in §6.6.

Finally, we analyze how $f_{\rm hot,galaxy}$ changes in simulations with no feedback and different hydrodynamic scheme. We compare $f_{\rm hot,galaxy}$ from the NoFeedback/Anarchy simulation with the NoFeedback/Gadget simulation, and find that in halos larger than $10^{11.5}\,{\rm M}_{\odot}$ the fraction of hot gas accretion onto galaxies is larger in Anarchy, by up to 0.4 dex, with respect to Gadget. This is expected, since Anarchy is able to mix phases in contact discontinuity, dense cold clumps dissolve while crossing the hot halo (Schaller et al. 2015), and the amount of gas accreted hot increases.

6.4 Density profile of gaseous halos

In this section we investigate how the gas density profile evolves due to the continued infall, reheating and cooling of gas in the halo. During hierarchical growth, dark matter halos in equilibrium are able to acquire a density profile with a near universal shape. The functional form of the universal shape is generally refereed to as 'NFW' profile (Navarro et al. 1997), which depends on halo mass and concentration[i]. In Chapter 4 we presented

[i] A halo's concentration is defined as the ratio of the virial radius and the scale radius, which is defined as the radius where the logarithmic density slope is -2. Thus, given the NFW profile, only a relation

a semi-analytic, physically motivated model for dark matter halo concentration as a function of halo mass and redshift. The model combines an analytic description of the halo mass accretion history (MAH) based on extended Press Schechter (EPS) theory (see Chapter 2), with an empirical relation between concentration and formation time obtained through fits to the results of numerical simulations (see Chapter 3). Because the model is based on EPS theory, it can be applied to a wide range of mass, redshift and cosmology. In gaseous halos however, baryons not only produce more concentrated density profiles (if radiative cooling is efficient and feedback is weak, Duffy et al. 2010), but also produce cuspier profiles (Schaller et al. 2015). In fact, neither the NFW nor other profiles (like Einasto, Einasto 1965) are able to reproduce the density profiles of gas (as recently shown by Schaller et al. 2015).

Therefore, in this section we analyse the gas density profile, $\rho_{\rm gas}(r)$, of halos from the EAGLE simulations and investigate whether $\rho_{\rm gas}(r)$ deviates from the often assumed isothermal shape. Rather than following our methodology from Chapter 4 and only considering relaxed halos[ii], we work with all halos from the L100N1504/REF simulation and separate them in mass bins of $\Delta \log_{10}(M_{200}) = 0.2$ width. To calculate $\rho_{\rm gas}(r)$, we define a set of concentric spherical shells of width $\Delta \log_{10}(r) = 0.078$ (with the outermost bin touching the virial radius), we add the mass of the particles within each shell and divided by the volume. As we are only interested in analysing the density profile of gas from the inner regions of halos (not within galaxies), we restrict the analysis of $\rho_{\rm gas}(r)$ to the radial range 0.15 to $1 \times r_{200}$.

Fig. 6.6 shows the median gas density profile at $z = 0$ (left panel) and $z = 2$ (right panel) of stacks of halos in the mass range $\log_{10}(M_{200}/\,{\rm M}_\odot) \pm 0.1$, with $\log_{10}(M_{200}/\,{\rm M}_\odot)$ varying from 11.5 to 13.7, as indicated in the legends. The figure shows that $\rho_{\rm gas}(r)$ largely deviates from the isothermal shape at large halo masses. If we define γ as the logarithmic density slope ($\mathrm{d}\ln\rho_{\rm gas}/\mathrm{d}\ln r = \gamma$), we obtain that γ increases from -1.86 in $10^{12}\,{\rm M}_\odot$ halos to -0.95 in $10^{12.7}\,{\rm M}_\odot$ halos, and then decreases again towards larger halo masses. In smaller halos, $\rho_{\rm gas}(r)$ is steeper inside the galaxy region and $\gamma \sim -2$.

The change in the slope of $\rho_{\rm gas}(r)$ shows how the distribution of the hot gas in the halo evolves, and can be explained as follows. Since a stable hot halo forms in the mass range $10^{11} - 10^{12}\,{\rm M}_\odot$, gas crossing r_{200} remains hot. As a result the gas density in the range $0.5 - 1r_{200}$ increases and the density profile flattens. In halos larger than $10^{13}\,{\rm M}_\odot$ the hot gas begins to cool and infall into the galaxy. Thus the amount of hot gas in the range $0.5 - 1r_{200}$ slowly decreases, steepening the density profile.

We assume that the functional form of $\rho_{\rm gas}(r)$ is given by the following expression

between concentration and halo mass is needed to fully specify halo structure at fixed mass.

[ii] Relaxed halos are those where the separation between the centre of the potential and the centre of the mass is less than $0.07r_{200}$ (Macciò et al. 2007; Neto et al. 2007).

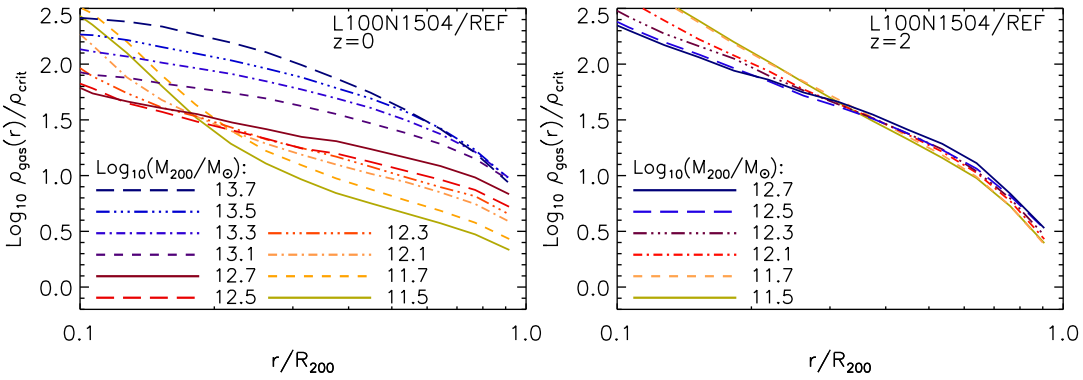

Figure 6.6: Median gas density profile of gas at $z = 0$ (left panel) and $z = 2$ (right panel) of stack of halos in the mass range $\log_{10}(M_{200}/\,\mathrm{M}_\odot) \pm 0.1$, with $\log_{10}(M_{200}/\,\mathrm{M}_\odot)$ varying from 11.5 to 13.7, as indicated in the legends.

$$\rho_{\rm gas}(r) \;=\; \rho_{\rm norm}\left(\frac{r}{r_{200}}\right)^{\gamma} 10^{\beta[\log_{10}(r/r_{200})]^2}, \tag{6.18}$$

where γ and β are free parameters and $\rho_{\rm norm}$ is the normalization. We obtain γ and β by performing a least-square minimization of the quantity $\Delta_{j,k} = \frac{1}{N}\sum_i^N Y_i^2$, with

$$\begin{aligned} Y_i \;&=\; \log_{10}[\rho_{\rm gas}(r_i, M_{200,j}, z_k)/\rho_{\rm crit}(z_k)] \\ &\quad -F[M_{200,j}, \gamma(M_{200,j}, z_k), \beta(M_{200,j}, z_k)], \end{aligned} \tag{6.19}$$

where F is the functional form given by eq. (6.18) and N is the number of radial bins for a given halo mass $M_{200,j}$ and output redshift z_k. In the case of $\rho_{\rm norm}$, we calculate it by imposing that $M_{\rm gas,halo} = f_{\rm b} M_{200} = \int_0^{r_{200}} 4\pi\rho_{\rm gas}(r) r^2 {\rm d}r$, with $f_{\rm b} = \Omega_{\rm b,0}/\Omega_{\rm m,0}$ the baryon fraction.

We find the best-fit expressions for γ and β, as a function of halo mass and redshift, are

$$\gamma(M_{200}, z) \;=\; \gamma_1(z) + \gamma_2(z)x + \gamma_3(z)x^2, \tag{6.20}$$

$$\beta(M_{200}, z) \;=\; \beta_1(z) + \beta_2(z)x + \beta_3(z)x^2, \tag{6.21}$$

$$x \;=\; \log_{10}(M_{200}/10^{12}\,\mathrm{M}_\odot), \tag{6.22}$$

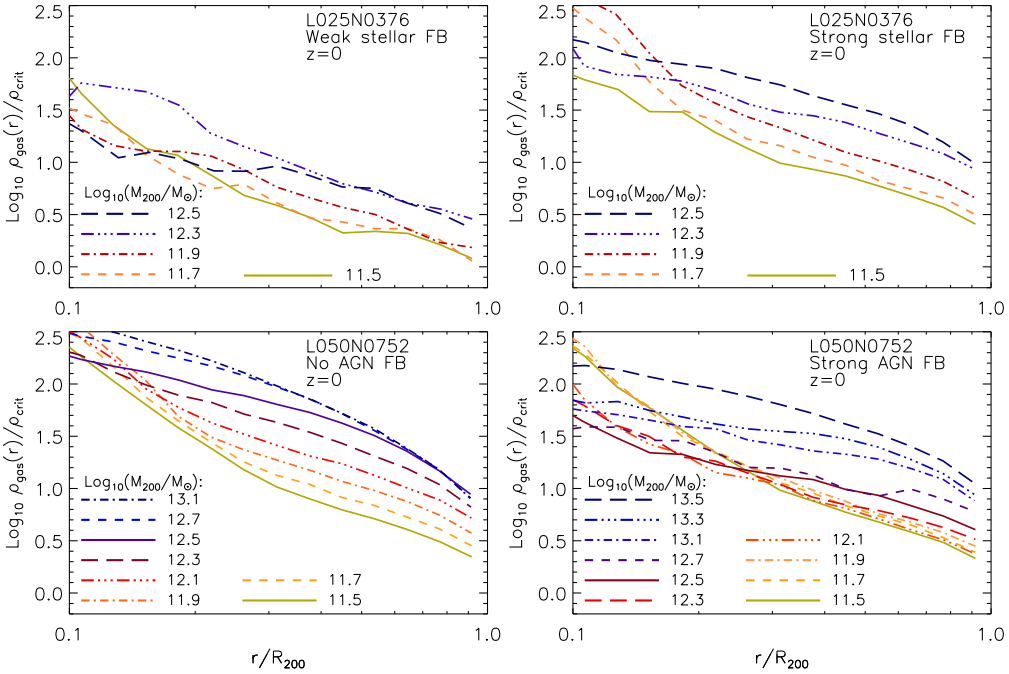

Figure 6.7: Same as left panel from Fig. 5 from simulations with weak stellar feedback (top left panel), strong stellar feedback (top right panel), no AGN feedback (bottom left panel) and strong AGN feedback (bottom right panel).

$$\text{if } z \leq 2 \begin{cases} \gamma_1(z) = -0.842 - 1.588z + 0.297z^2, \\ \gamma_2(z) = -0.629 + 0.523z - 0.114z^2, \\ \gamma_3(z) = -0.282 - 0.481z + 0.361z^2, \\ \beta_1(z) = +0.323 - 0.819z + 0.148z^2, \\ \beta_2(z) = -1.035 + 0.472z - 0.119z^2, \\ \beta_3(z) = +0.052 - 0.724z + 0.388z^2, \end{cases} \tag{6.23}$$

$$\text{if } z > 2 \begin{cases} \gamma_1(z) = -2.83, \\ \gamma_2(z) = -0.039, \\ \gamma_3(z) = +0.2, \\ \beta_1(z) = -0.723, \\ \beta_2(z) = -0.567, \\ \beta_3(z) = +0.156. \end{cases} \tag{6.24}$$

6.4.1 Impact of feedback

In this section we investigate the dependence of the gas density profile of halos on feedback model. We calculate the median gas density profile at $z = 0$ of stacks of halos in the mass range $\log_{10}(M_{200}/\,\mathrm{M}_\odot) \pm 0.1$, with $\log_{10}(M_{200}/\,\mathrm{M}_\odot)$ varying from 11.5 to 12.5 (in L025N0376 simulations, top panels from Fig. 6.7) and from 11.5 to 13.5 (in L050N0752

simulations, bottom panels from Fig. 6.7). We use simulations with weak and strong stellar feedback, as well as strong and no AGN feedback. Fig. 6.7 shows a comparison between the gas density profiles. The top panels show that when stellar feedback is weak, the number of gas particles per radial bin decreases, on the contrary, when stellar feedback is strong, the number of gas particles increases. This is expected since SN outflows expel gas particles from the galaxy into the halo, thus raising the gas density. Besides the normalization, we find that in both scenarios (weak and strong stellar feedback), $\rho_{\rm gas}(r)$ deviates from the isothermal shape, and as the halo mass increases, the density profile flattens.

The bottom panels of Fig. 6.7 show the same as the top panels, but the density profiles are taken from simulations with no AGN feedback (bottom left panel) and strong AGN feedback (bottom right panel). In this case we also note a change in the normalization of $\rho_{\rm gas}(r)$, which increases in the no AGN feedback scenario and decreases when AGN feedback is strong. In addition, we also find that the shape of $\rho_{\rm gas}(r)$ changes with halo mass. In the strong AGN feedback model $\rho_{\rm gas}(r)$ evolves as in the standard AGN model (left panel from Fig. 6.6), in the halo mass range $10^{11.5} - 10^{12.5}\,{\rm M}_{\odot}$ the gas density in the range $(0.5 - 1)R_{200}$ increases, indicating that hot gas is being accumulated, the stable hot halo is forming (for a more detail description of hot halo formation see §5.3), and the density profile flattens. In the no AGN case, $\rho_{\rm gas}(r)$ also changes with halo mass but it does not show a strong flattening. The slope of $\rho_{\rm gas}(r)$ reaches -1.4 in $10^{12.7}\,{\rm M}_{\odot}$ halos, whereas in the standard AGN feedback case $\gamma = -0.95$ and in the strong AGN feedback case $\gamma = -0.82$. We believe that $\rho_{\rm gas}(r)$ does not flattens because in the absence of AGN feedback the cooling flows from the hot halo are able to develop. We investigate this further in §6.6.

6.5 Modelling gas accretion onto galaxies

In this section we derive a physically motivated model for gas accretion onto galaxies, that is based on the original model of radiative cooling from White & Frenk (1991), and includes an evolving density profile. We begin with a brief description of the simplest cooling model from SAMs in §6.5.1 and derive the model of gas accretion in §6.5.2.

6.5.1 Radiative cooling model in SAMs

To date, only a few SAMs have implemented the co-existence of the hot and cold modes of accretion onto central galaxies. SAMs instead assume that recently accreted gas is instantaneously redistributed within the halo, and is only able to cool and fall into the galaxy if it is within the cooling radius. The lack of distinction between hot and cold modes of accretion is not very important at redshift zero, because there are no cold

filaments penetrating the hot halo, and most of the gas accreted is hot in halos larger than $10^{11.7}\,\mathrm{M}_{\odot}$ (more than 50%, see Chapter 5). SAMs assume that cooling is an inside-out process, and that for a given halo mass the gas is distributed following an isothermal density profile,

$$\rho_{\rm gas}(r) = \frac{m_{\rm gas}}{4\pi r_{200} r^2}, \tag{6.25}$$

where $m_{\rm gas} = 0.9(\Omega_{\rm b,0}/\Omega_{\rm m,0})M_{200}$ is the hot gas mass contained within the halo (it is usually assumed that 10% of the gas mass is locked in stars). If the cooling radius, obtained by equalling the cooling time with dynamical time, is smaller than the virial radius, the cooling is said to be 'slow' or under a 'static hot halo regime'. In the case the cooling radius is larger than the virial radius, the cooling is said to be 'rapid' and the cooling rate is equal to the halo accretion rate. The dynamical and cooling times are calculated as in §5.3 following eqs. (5.2) and (5.3).

6.5.2 Semi-analytic model of gas accretion onto galaxies

In §6.3.3 we showed that the total gas accretion onto galaxies is the result of two different modes of accretion, hot and cold. We consider these two different modes in our model of gas accretion and calculate $\dot{M}_{\rm gas,galaxy}$ in terms of the rate of gas cooling from the hot halo, $\dot{M}_{\rm cool}$, and the rate of cold gas accretion onto halos in the form of filaments, $f_{\rm cold}\dot{M}_{\rm gas,halo}$, as

$$\dot{M}_{\rm gas,galaxy} \quad \propto \quad \dot{M}_{\rm cool} + f_{\rm cold}\dot{M}_{\rm gas,halo}. \tag{6.26}$$

Here $\dot{M}_{\rm gas,halo}$ is the gas accretion rate onto halos in the presence of feedback, given by eqs. (6.5-6.12).

We define $M_{\rm cool}$ as the gas mass from the hot halo contained within $r_{\rm cool}$. We calculate $M_{\rm cool}$ as $M_{\rm cool} = \int_0^{r_{\rm cool}} 4\pi\rho_{\rm hot\,gas}(r)r^2{\rm d}r = 4\pi r_{200}^3\rho_{\rm norm}\left(\frac{r_{\rm cool}}{r_{200}}\right)$, where we assumed (for simplicity) that the density profile of hot gas is $\rho_{\rm hot\,gas} = \rho_{\rm norm}r^{-2}$. We determine $\rho_{\rm norm}$ by requiring that $\int_0^{r_{200}} 4\pi\rho_{\rm hot\,gas}(r)r^2{\rm d}r$ is equal to the total hot gas mass in the halo, $M_{\rm hot}$. Then $M_{\rm cool}$ results

$$M_{\rm cool} = M_{\rm hot}\frac{r_{\rm cool}}{r_{200}}. \tag{6.27}$$

Next, by assuming that $r_{\rm cool}/r_{200}$ remains roughly constant during a short time step, we obtain

$$\dot{M}_{\rm cool} \approx \dot{M}_{\rm hot}\frac{r_{\rm cool}}{r_{200}}, \tag{6.28}$$

$$\dot{M}_{\rm cool} \approx f_{\rm hot}\dot{M}_{\rm gas,halo}\frac{r_{\rm cool}}{r_{200}}, \tag{6.29}$$

where in eq. (6.29) we assumed that the variation of hot gas in the halo, $\dot{M}_{\rm hot}$, is driven by the hot mode of accretion, $\dot{M}_{\rm hot} = f_{\rm hot}\dot{M}_{\rm gas,halo}$. As a result, eq. (6.29) gives the cooling radius a new physical meaning. Rather than being the radius below which all gas is able to cool, it is now the fraction of shock-heated gas that cools ($\frac{r_{\rm cool}}{r_{200}} = \frac{\dot{M}_{\rm cool}}{f_{\rm hot}\dot{M}_{\rm gas,halo}}$). In other words, it is the rate of the hot halo cooling flow. By substituting eq. (6.29) into eq (6.26) the accretion rate onto galaxies results

$$\dot{M}_{\rm gas,galaxy} = \varepsilon_{\rm eff}(f_{\rm hot}r_{\rm cool}/r_{200} + f_{\rm cold})\dot{M}_{\rm gas,halo}, \tag{6.30}$$

where we include the free parameter $\varepsilon_{\rm eff}$, defined as the efficiency for the rate of gas cooling. We use $\varepsilon_{\rm eff}$ to control the normalization of $\dot{M}_{\rm gas,galaxy}$ and fit the simulation result to the model.

To determine $\dot{M}_{\rm gas,galaxy}$, we need to calculate $r_{\rm cool}$ as a function of halo mass. We do it by following two different methods. We first apply the classical model described in §6.5.1. Secondly, we apply a 'modified' model based on equaling the following heating and cooling rates

$$\Gamma_{\rm heat} = k_B T_{\rm vir} f_{\rm hot}(\Omega_{\rm b,0}/\Omega_{\rm m,0})\frac{\dot{M}_{\rm gas,halo}}{M_{\rm hot}}, \tag{6.31}$$

$$\Gamma_{\rm cool} = \Lambda(T,Z)/n_{\rm gas}(r). \tag{6.32}$$

(see Chapter 5 for details). In both cases, we calculate $r_{\rm cool}$ by assuming an isothermal density profile from eq. (6.25) and the density profile with an evolving slope calculated in §6.4.

The top panel of Fig. 6.8 shows a comparison between the model of galaxy gas accretion given by eq. (6.30), calculated using the 'modified' model for the cooling radius with an isothermal density profile (dot-dashed blue line) and the modified model with the density profile derived in §6.4 (yellow solid line). In addition, we include in the panel the gas accretion rate onto galaxies taken from the L100N1504/REF simulation (red diamond symbols) and the best-fit of the galaxy gas accretion from low-mass halos (grey dashed line). It can be seen that while the blue dot-dashed curve does not seem to correctly capture the rate of galaxy gas accretion from the simulations, the yellow solid curve is in

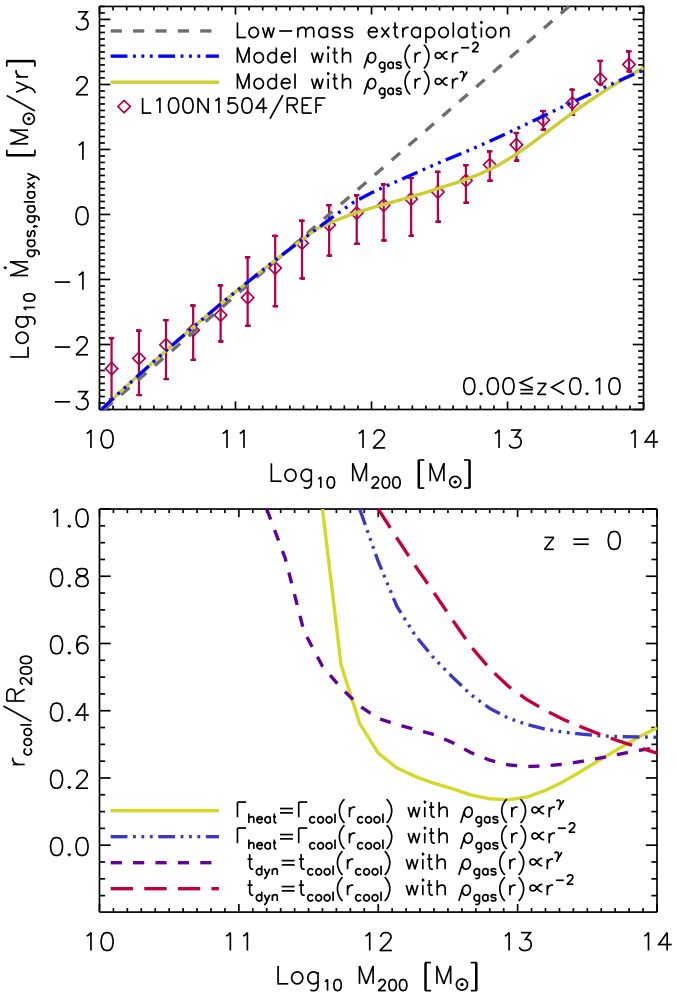

Figure 6.8: Top panel: gas accretion rates onto galaxies as a function of halo mass in the redshift range $0 \leq z < 0.1$. The red symbols correspond to the galaxy gas accretion rate taken from the L100N1504/REF simulation and the error bars correspond to the 1σ scatter. The yellow solid line corresponds to the gas accretion model, which we calculated using the heating and cooling rates from Chapter 5 and the density profile from §6.4. Similarly, the blue dot-dashed line corresponds to the same model but an isothermal density profile. For comparison, the dashed grey line corresponds the galaxy gas accretion rate from low-mass halos extrapolated to higher halo masses. Bottom panel: analytic estimations of the cooling radius as a function of halo mass at $z = 0$ from the same models shown in the top panel (yellow solid and dot-dashed blue lines), and from the classical model using an isothermal density profile (red dashed line) as well as the density profile estimated in §6.4 (purple dashed line).

excellent agreement. We find that because the cooling radius is smaller than the virial radius when $M_{200} > 10^{11.6}\,\mathrm{M}_{\odot}$, the accretion rate decreases towards higher halo masses with respect to the grey dashed line. However, the cooling radius does not continuously decrease towards high halo masses as generally thought, when we apply an evolving density profile with halo mass, the cooling radius describes an upturn. It decreases with increasing halo mass until $10^{12.7}\,\mathrm{M}_{\odot}$ halos and then increases.

The evolution of the cooling radius is explored in more detail in the bottom panel of Fig. 6.8. This panel shows the cooling radius as a function of halo mass for the different models considered. The dot-dashed blue line corresponds to the modified model with an isothermal density profile whereas the yellow solid line corresponds to the same method, but with an evolving density profile. The red and purple dashed lines are calculated using the classical method with an isothermal and evolving density profile, respectively.

We find that the density profile with changing slope is able to produce (in both models, modified and classical) a cooling radius that initially decreases for masses up to $10^{13}\,\mathrm{M}_{\odot}$, and then increases. However, we find that using r_{cool} from the modified model in the calculation of the galaxy gas accretion gives a much better agreement to the simulation data than r_{cool} from the classical model.

The upturn in the $r_{\mathrm{cool}}-M_{200}$ relation can be explained by analyzing the evolving radial slope of the gas density profile. When we calculate r_{cool} by equalising the relations (6.31) and (6.32), we obtain that $\Lambda/\Gamma_{\mathrm{heat}} = n_{\mathrm{gas}}(r_{\mathrm{cool}})$. If we assume that $\Lambda/\Gamma_{\mathrm{heat}}$ is roughly constant and independent of the density profile used, we then find that $(r_{\mathrm{cool},-2}/r_{200})^{-2} = (r_{\mathrm{cool},\gamma}/r_{200})^{\gamma}$. Since γ increases with respect to -2 in the halo mass range $10^{12}-10^{13}\,\mathrm{M}_{\odot}$, reaches a maximum value and then decreases, $r_{\mathrm{cool},\gamma}/r_{200}$ follows the same but inverse behavior, and as a result the relation with $r_{\mathrm{cool},-2}/r_{200}$ is maintained.

In addition, since the ratio $r_{\mathrm{cool}}/r_{200}$ gives the fraction of shock-heated gas that cools, the upturn can also be understood in terms of the hot halo cooling flow. When the halo develops a stable hot atmosphere, the infalling gas heated by accretion-shocks remains hot and close to r_{200}. The gas is able to cool after a cooling time which is approximately 10Gyr (Chapter 5). As a result, halos that develop a hot atmosphere within the past 10Gyr will not have a continuous flow of gas cooling from the hot halo and r_{cool} will decrease and be smaller than r_{200}. Only larger halos ($> 10^{13}\,\mathrm{M}_{\odot}$) are able to have a hot halo cooling flow. For that reason, r_{cool} increases in halos larger than $10^{13}\,\mathrm{M}_{\odot}$.

When we analyse the evolution of r_{cool} with halo mass and redshift, we find that r_{cool} describes an upturn only at $z \leq 2$, at higher redshifts r_{cool} decreases with increasing halo mass. We next investigate whether the analytic estimations of r_{cool} for different redshifts produce galaxy gas accretion rates in agreement with the simulation data. The panels from Fig. 6.9 show a comparison between the semi-analytic model for $\dot{M}_{\mathrm{gas,galaxy}}$ (solid lines) and the gas accretion rates onto galaxies taken from the L100N1504/REF

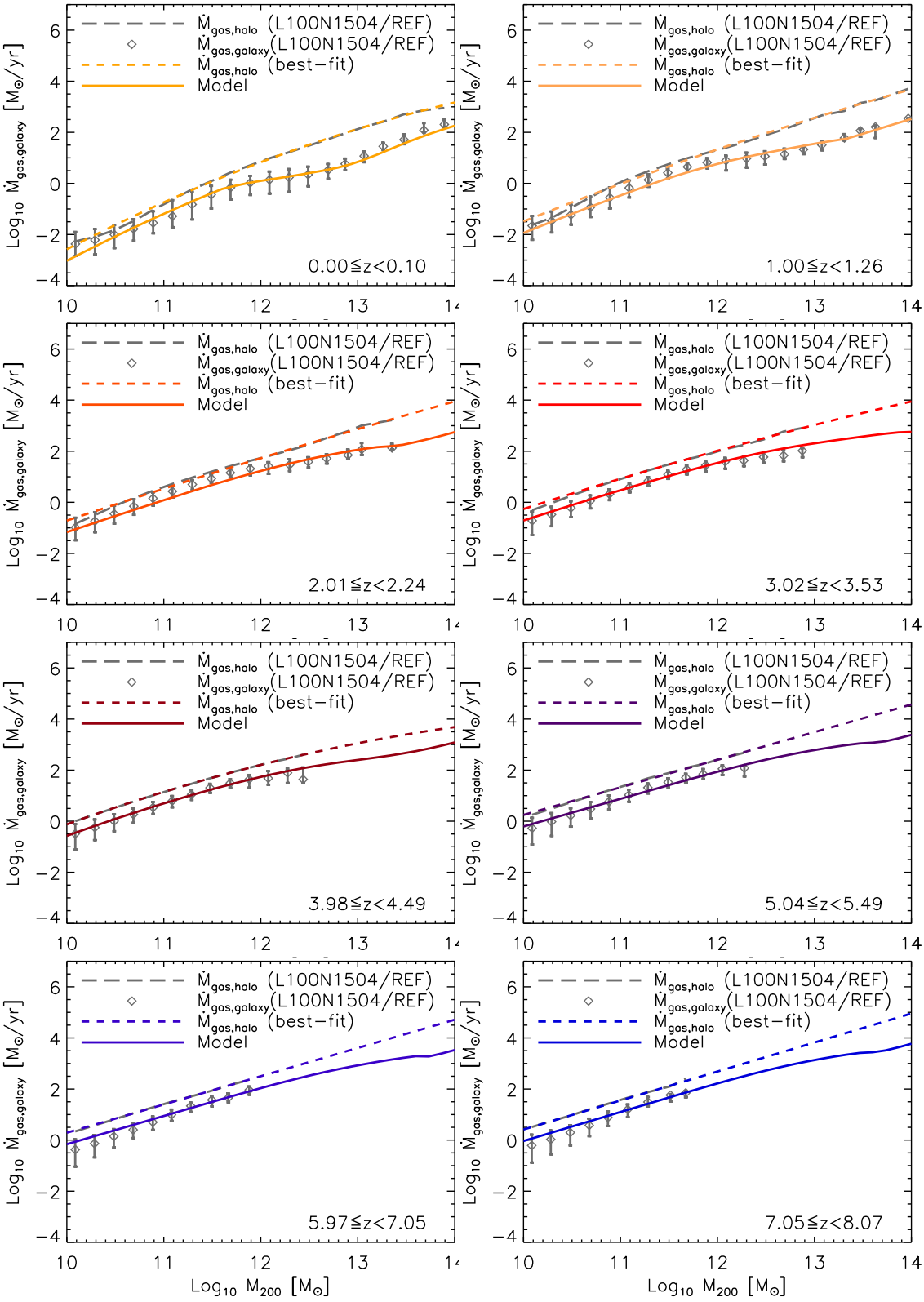

Figure 6.9: Gas accretion rates onto galaxies as a function of halo mass in various redshift ranges as indicated in the legends. Each panel shows the gas accretion rates onto galaxies taken from the L100N1504/REF simulation (diamond symbols, with the error bars the 1σ scatter) and predicted by the theoretical model (solid lines). For comparison, the panels show the gas accretion onto halos (grey long-dashed lines) and the best-fitting relations from eqs. (6.5-6.12) (colored short-dashed lines).

simulation (diamond symbols). In addition, the panels show the median gas accretion rates onto halos from the L100N1504/REF simulation (grey long-dashed line) and the best-fitting relations given by eqs. (6.5-6.12) (short dashed color lines). To achieve good agreement between the model with the simulation data we calculated the best-fitting value of the free parameter $\varepsilon_{\rm eff}$ in eq. (6.30) and found $\varepsilon_{\rm eff} = 0.35$. Overall Fig. 6.9 shows an excellent agreement with the simulated data at all redshifts.

6.5.3 Accretion rate onto the ISM

In the previous subsection we derive a semi-analytic model for gas accretion onto galaxies that reproduces the median accretion rates obtained from the simulations. The next step is however, to analyse whether we are able to relate the accretion rates onto galaxies with the accretion rates onto the ISM. In §6.2.1 we have found that since the growth rate of the galaxy and ISM is roughly the same, the accretion rates are related by the ratio between the total masses. However, given that all the gas from the ISM and galaxy is contained within $0.15 \times r_{200}$, the ratio between the masses is equal to the ratio between the mean enclosed densities.

To calculate the mean ISM density we consider that the typical hydrogen number density for the ISM is $n_{\rm H} = 0.1$ cm^{-3}, which corresponds to a density $\rho_{\rm ISM} = \mu m_{\rm p} n_{\rm H} = 10^{-25}$ gr cm^{-3} $= 10^4 \rho_{\rm crit}$ (with $\rho_{\rm crit} = 1.879\,10^{-29} h^2$ gr cm^{-3} the critical density today). We then assume $\langle \rho_{\rm ISM} \rangle_{0.15 r_{200}} = 10^4 \rho_{\rm crit}$. To calculate the mean enclosed gas density within $0.15 \times r_{200}$, we perform the integral $M(< 0.15 \times r_{200}) = \int_0^{0.15 r_{200}} 4\pi r^2 \rho_{\rm gas}(r) {\rm d}r$ and obtain $\langle \rho_{\rm gas} \rangle_{0.15 {\rm r}_{200}} = M(< 0.15 \times r_{200}) / [4\pi/(0.15 r_{200})^3/3]$.

We calculate $\dot{M}_{\rm ISM}$ by assuming that all cold gas accreted onto the galaxy falls into the ISM, but that only a fraction $\tilde{\kappa}$ of hot gas is able to cool and fall into the ISM. Here, $\tilde{\kappa} = \tau_{\rm delay} \kappa$, where $\kappa = \frac{1}{1.3} \frac{\langle \rho_{\rm ISM} \rangle_{0.15 r_{200}}}{\langle \rho_{\rm gas} \rangle_{0.15 r_{200}}}$ and $\tau_{\rm delay} = 1.25 \times 10^{-3}$ is a delay factor that represents the efficiency of hot gas cooling and falling into the ISM. $\tau_{\rm delay}$ is calculated by performing a least-square minimization between the curves of Fig. 6.10 and looking for the best-fit normalization. We then find that the accretion rate onto the ISM can be calculated using the following relation

$$\dot{M}_{\rm ISM} = \varepsilon_{\rm eff} [f_{\rm hot} (r_{\rm cool}/r_{200}) \tilde{\kappa} + f_{\rm cold}] \dot{M}_{\rm gas,halo}. \tag{6.33}$$

Fig. 6.10 shows the gas accretion rates onto galaxies and ISM. The semi-analytic model is plotted in yellow lines while the simulation output in purple symbols and lines, as indicated in the legend. We find that $\dot{M}_{\rm ISM}$ obtained from eq. (6.33) is in very good agreement with the simulation output for halos larger than $10^{11.5}$ M$_\odot$. In smaller halos, the model overpredicts the rates by up to 0.5 dex.

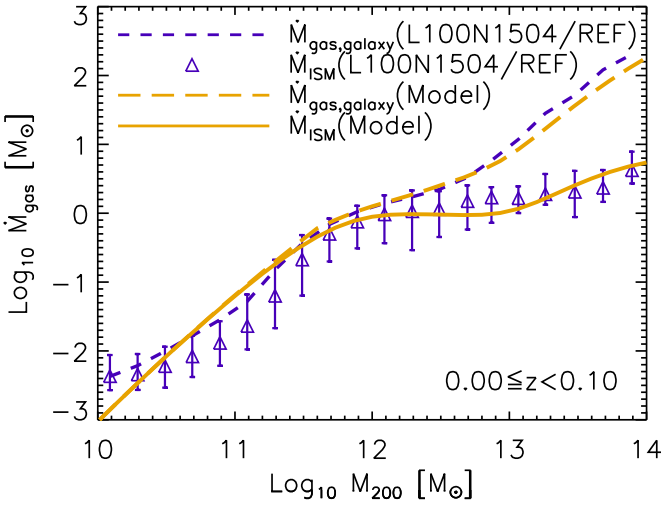

Figure 6.10: Gas accretion rate onto central galaxies and ISM in the redshift range 0 to 0.1. The purple dashed line and diamond symbols show the respective accretion rate onto galaxies and ISM calculated from the L100N1504/REF simulation. The yellow long-dashed curve shows the accretion rate onto galaxies obtained by the model described in §6.5.2 and the yellow solid curve shows an analytic estimation of the accretion rate onto the ISM obtained by multiplying the semi-analytic model of gas accretion with the ratio between densities (eq. 6.33).

6.6 AGN feedback and hot halo cooling

The model of gas accretion onto galaxies derived in §6.5 accurately describes the accretion rates from the simulations. However, there are various mechanisms that can alter $\dot{M}_{\rm gas,galaxy}$. At high halo masses ($> 10^{12}\,{\rm M}_\odot$), the most important is AGN feedback. The central supermassive black holes observed in many massive galaxies expel large amounts of gas in the form of jets (radio mode feedback). In Chapter 5 we investigated how the hot gas mass in the halo, $M_{\rm hot}$, changes with feedback, and found that the presence of AGN feedback decreases $M_{\rm hot}$ at fixed halo mass with respect to the same halos with no AGN by up to a factor of 2.

In the previous chapter we also showed that a halo with no central AGN is able to form a stable hot atmosphere when it reaches a mass of $10^{11.5}\,{\rm M}_\odot$, whereas the same halo with AGN feedback forms the hot atmosphere when it reaches $10^{11.7}\,{\rm M}_\odot$. Thus there is a connection between hot halo formation and AGN feedback. In this section we investigate the difference between gas accretion onto galaxies with and without AGN feedback, and show that the model presented in this work is able to reproduce both scenarios.

The left panel of Fig. 6.11 shows the gas accretion rate onto galaxies with no AGN feedback (blue solid line), with standard AGN feedback (blue dashed line), and with strong AGN feedback (blue dot-dashed line) in the redshift range $0 \leq z < 0.1$ (left panel) and $2 \leq z < 2.24$ (right panel). The 1σ scatter of $\dot{M}_{\rm gas,galaxy}$ without AGN feedback and strong AGN feedback are shown in the grey and cyan shade regions, respectively.

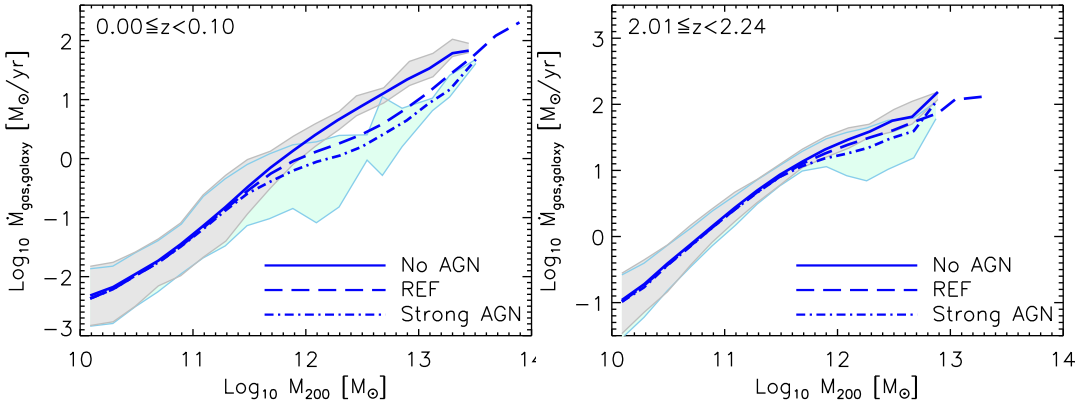

Figure 6.11: Gas accretion rate onto galaxies with no AGN feedback (blue solid line), with standard AGN feedback (blue dashed line) and with strong AGN feedback (blue dot-dashed line) in the redshift range $0 \leq z < 0.1$ (left panel) and $2 \leq z < 2.24$ (right panel). The panels show the 1σ scatter of the median values of $\dot{M}_{\rm gas,galaxy}$ per mass bin in grey shade area (for $\dot{M}_{\rm gas,galaxy}$ without AGN feedback) and in cyan shade area (for $\dot{M}_{\rm gas,galaxy}$ with strong AGN feedback).

There is a significant change in the dependence of $\dot{M}_{\rm gas,galaxy}$ on halo mass when there is no AGN feedback. We find $\dot{M}_{\rm gas,galaxy}$ monotonically increases with halo mass, whereas in the scenario with strong AGN feedback $\dot{M}_{\rm gas,galaxy}$ follows the same shape as in the case of standard AGN feedback (but with a 0.2 dex lower normalization). The difference of $\dot{M}_{\rm gas,galaxy}$ in the case of no AGN feedback seems to indicate that there is no hot halo impact on galaxy gas accretion, however this does not always seem to be the case. The right panel of Fig. 6.11 shows the same as the left panel, but in the redshift range $2 \leq z < 2.24$. As can be seen there is good agreement (less than 0.1 dex difference) between $\dot{M}_{\rm gas,galaxy}$ from the different AGN prescriptions. This prompts us to ask what causes the disagreement at $z = 0$?

To understand how $\dot{M}_{\rm gas,galaxy}$ changes with and without AGN feedback we refer to our model of gas accretion. As outlined in this chapter, the model includes hot and cold contributions to the total gas accretion rate onto halos. It also includes the hot gas mass in the halo, $M_{\rm hot}$, as well as the evolution of the density profile, $\rho_{\rm gas}(r)$, with halo mass. We investigate how each at these inputs change in the No AGN simulation case with respect to the REF model:

- $\dot{M}_{\rm gas,halo}$: we compare the gas accretion rates onto halos from the REF and No AGN simulation and find no significant difference in $\dot{M}_{\rm gas,halo}$ (in agreement with van de Voort et al. 2011). We then use the eqs. (6.5-6.12) to calculate $\dot{M}_{\rm gas,halo}$.
- $f_{\rm hot}$: we find that $f_{\rm hot,NoAGN}$ is slightly larger than $f_{\rm hot,REF}$ in the halo mass range $10^{12} - 10^{13}\,{\rm M}_{\odot}$, i.e. by a maximum factor of 1.03 in $10^{12.4}\,{\rm M}_{\odot}$ halos. We then assume that $f_{\rm hot}$ is feedback invariant and use the best-fitting expressions given by the eqs. (6.13-6.17).

- $M_{\rm hot}$: In Chapter 5 we find that $M_{\rm hot,NoAGN}$ is larger than $M_{\rm hot,REF}$ in the halo mass range $10^{11.7} - 10^{14}\,{\rm M}_\odot$, i. e. by a factor of 1.41 in $10^{12}\,{\rm M}_\odot$ halos. We then calculate the best-fit expression for the $M_{\rm hot} - M_{200}$ relation and find $\log_{10}(M_{\rm hot}/\frac{\Omega_{\rm b,0}}{\Omega_{\rm m,0}} M_{200}) = -0.659 + 0.729x$, with $x = \log_{10}(M_{200}/10^{12}\,{\rm M}_\odot)$.
- $\rho_{\rm gas}(r)$: we analyse how the distribution of gas in the halo changes in the absence of AGN. We find that as the hot halo is forming, the amount of hot gas at large radii increases. As a result, $\rho_{\rm gas}(r)$ flattens, but not as much as in the presence of AGN, for which ($\rho_{\rm gas,NoAGN}(r)$ reaches a maximum slope of -1.14 in $10^{12.8}\,{\rm M}_\odot$ halos (which should be compared to the maximum -0.9 reached by $\rho_{\rm gas,REF}(r)$)). This means that the hot gas in halos with no AGN begins to cool before hot gas in halos with AGN. The best-fit parameters at $z = 0$ for the density profile given by eq. (6.18) are $\gamma = -1.727 - 1.379x - 0.135x^2$ and $\beta = -0.381 - 1.464x + 0.085x^2$, with $x = \log_{10}(M_{200}/10^{12}\,{\rm M}_\odot)$.

In Fig. 6.12 we show the results of our model of gas accretion after including these differences. The top panel shows the gas accretion rate onto galaxies predicted by our model with no AGN feedback (yellow solid line) and with AGN feedback (yellow dashed line). The blue symbols correspond to the gas accretion rates from the L050N0752/NoAGN simulation, whereas the blue dashed line corresponds to the L100N1504/REF simulation. The middle panel of Fig. 6.12 shows the cooling radius as a function of halo mass from the model with no AGN feedback (blue solid line) and with AGN (yellow dashed line). There is an important difference in the evolution of $r_{\rm cool}$ with halo mass. In the case of no AGN, $r_{\rm cool}$ decreases with halo mass in the mass range $10^{11.5} - 10^{12.1}\,{\rm M}_\odot$, but it does not reach the same minimum value as in the case with AGN (minimum value of $r_{\rm cool,NoAGN}$ is 0.56 compared with 0.13 from $r_{\rm cool,AGN}$). This means that the rate of gas cooling from the hot halo is always larger in the absence of AGN activity.

Going back to the top panel of Fig. 6.12, we find that the model of gas accretion faithfully reproduces the accretion rates from the No AGN simulation. Mathematically, $\dot{M}_{\rm gas,galaxy}$ monotonically increases because the rate of gas cooling from the hot halo $\dot{M}_{\rm cool} = (r_{\rm cool}/r_{200}) f_{\rm hot} \sim 1$ remains roughly constant with increasing halo mass ($f_{\rm hot}$ increases with halo mass at the same rate $r_{\rm cool}$ decreases). Physically, this means that the effect on gas accretion can no longer be seen since $10^{12}\,{\rm M}_\odot$ and even larger halos have already undergone cooling from a hot halo in the absence of AGN.

This can be understood better by analyzing the bottom panel of Fig. 6.12, which shows the growth in halo mass of 10^{12} (yellow solid line), $10^{12.5}$ (blue dot-dashed line) and $10^{13}\,{\rm M}_\odot$ (red dashed line) halos against redshift (bottom x-axis) and the age of the universe (top x-axis). Here, we used the extended model of halo mass growth from Chapter 4 and assumed the same cosmological parameters as the EAGLE simulations. In the figure we also show the threshold values in halo mass above which halos are

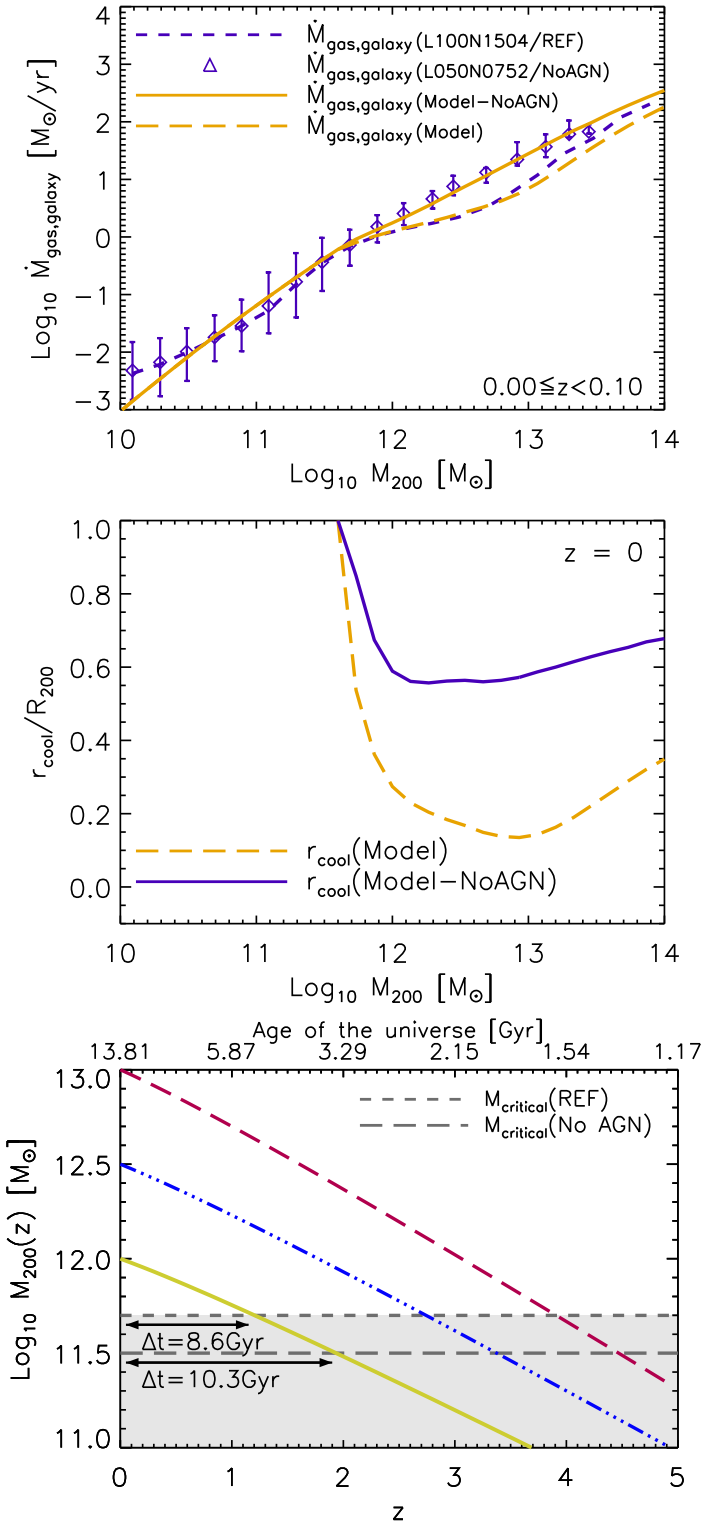

Figure 6.12: Top panel: Gas accretion rate onto galaxies predicted by our model with No AGN (yellow solid line), with AGN (yellow long-dashed line) and from the simulations L050N0752/NoAGN (blue diamond symbols) and L100N1504/REF (blue short-dashed line) in the redshift range $0.0 \leq z < 0.1$. Middle panel: cooling radius obtained by equaling heating and cooling rates using the no AGN best-fits for $\rho_{\rm gas}$, $M_{\rm hot}$ and $f_{\rm hot}$ (blue solid line) and the standard AGN best-fits (yellow dashed line). Bottom panel: mass growth of 10^{12}, $10^{12.5}$ and 10^{13} $M_\odot$ halos as predicted by the model of Chapter 4. They grey short- and long-dashed lines correspond to the threshold values of hot halo formation in the case of AGN feedback and no AGN feedback, respectively.

expected to develop a hot stable atmosphere. The threshold is $10^{11.7}\,M_\odot$ for halos with AGN feedback and $10^{11.5}\,M_\odot$ for halos without AGN feedback (Chapter 5). Finally, we highlight in the figure the time that has passed since a $10^{12}\,M_\odot$ halo formed a hot atmosphere. The main difference between the two scenarios is the time intervals of 8.6Gyr (for halos with AGN feedback) and 10.3Gyr (for halos without AGN feedback). Given that a typical cooling time of hot gas in the halo is $t_{\rm cool} = 10{\rm Gyr}$[iii], the bottom panel of Fig. 6.12 shows that only halos with No AGN activity would have had the time to develop a hot halo cooling.

6.7 Conclusion

In this work we have investigated the evolution of the gas accretion rates onto the galaxy and ISM with halo mass and redshift. We have found that, although the specific accretion rates onto the galaxy and ISM are roughly the same, the accretion rate onto the ISM increases with halo mass but remains constant in halos larger than $10^{12}\,M_\odot$. Whereas the gas accretion rate onto galaxies increases with halo mass and only flattens in the halo mass range $10^{11.7} - 10^{12.7}\,M_\odot$. In order to understand this behavior, we have developed a semi-analytic model of galaxy gas accretion. The model considers that two modes of accretion, cold and hot, contribute to the total gas accretion rate. Cold gas accretion onto galaxies is driven by the rate of cold accretion onto halos, whereas hot gas accretion is driven by the rate of gas cooling from the hot halo, that depends on the fraction of shock-heated gas accreting onto the halo and on the cooling radius.

To calculate the cooling radius, we have equalled the heating rate produced by accretion shocks (derived in Chapter 5) with the cooling rate. However, in the calculation of the cooling rate we have used a new functional form for the density profile. We have found that the density profile, $\rho_{\rm gas}(r)$, of halos from the EAGLE simulations deviates from the isothermal shape. The logarithmic density slope increases with halo mass, it reaches a maximum of -0.91 in $10^{13}\,M_\odot$ halos and then decreases. The change in the slope of the density profile shows how the distribution of the hot gas changes as the halo evolves due to continued infall, reheating and cooling. Because the logarithmic density slope evolves with halo mass, when we calculated the cooling radius we obtained that it does not decrease with halo mass, instead it describes an upturn. It is smaller than r_{200} and decreases in the halo mass range $10^{11.6} - 10^{13}\,M_\odot$ and increases towards larger halos.

This evolution of the cooling radius is not only able to produce a rate of gas accretion onto galaxies in excellent agreement with the simulation data, but also reveals interesting physics. When the halo develops the hot atmosphere, the infalling gas which is heated by accretion shocks remains hot and forms part of the hot halo. The gas is only able to

[iii] $t_{\rm cool}$ can be calculated from eq. (5.3) assuming a virial temperature of 10^6K, a net cooling rate of $\Lambda = 10^{-22}$erg cm^3 s^{-1} and gas density of $\rho_{\rm gas} = 10^{-30}$gr cm^{-3}.

cool after a cooling time (which we found in Chapter 5 to be approximately 10Gyr), and as a result, the gaseous halos that developed the hot atmosphere less than 10Gyr ago do not have a continuous flow of gas from the hot halo that is now cooling. Only larger halos ($> 10^{13}\,\mathrm{M}_{\odot}$), are able to have a large rate of hot gas cooling. For that reason, r_{cool} begins to increase halos larger than $10^{13}\,\mathrm{M}_{\odot}$.

The formation of the hot halo not only explains the flattening in the accretion rates onto galaxies, but also the gas accretion rates onto galaxies that do not have AGN activity, due to the fact that the rate of gas cooling from the hot halo is larger in the absence of AGN activity. We have compared our semi-analytic model of gas accretion with the galaxy accretion rates calculated from the simulation in various redshift ranges and have found excellent agreement.

Finally, we have related the galaxy gas accretion with the rate of gas accretion onto the ISM using our density profile model, and have found very good agreement with the accretion rates onto the ISM from high-mass halos obtained from the simulation output. This last step is very important because in high-mass halos the star formation rate is directly proportional to $\dot{M}_{\mathrm{ISM}}$, and since $\dot{M}_{\mathrm{ISM}}$ is related to $\dot{M}_{\mathrm{gas,halo}}$, we are then able to predict how the star formation of the central galaxy in the halo is dependent on the amount of gas that enters the halo.

7

Conclusion

This chapter summarizes the main findings of this thesis and presents ideas for future work.

Our understanding of structure formation in the universe, outlined in the standard model of cosmology, has greatly improved over the last few decades. Throughout this thesis we have contributed to this understanding by studying three main topics: the physics that drives the accretion history of dark matter halos, its relation with the halos internal structure, and the impact of halos accretion history on galaxy evolution. We summarize the analysis and conclusions of this thesis in §7.1, and discuss the implications of this study for the future of the field in §7.2.

7.1 Summary of findings

The first questions addressed in this thesis are: what drives the halo mass accretion history? and what is the physical origin of the function that describes its shape? In order to answer these questions, in Chapter 2 we derived an analytic model for the halo MAH using the EPS formalism. We concluded that the halo MAH is determined by the initial power spectrum of density fluctuations and the growth factor. We showed that the halo MAH can be well described by an exponential function ($M(z) \sim e^{\beta z}$) in the high-redshift

regime but not in the low-redshift regime. At low redshift, in the dark energy dominated era, the growth of density perturbations is halted due to the accelerated expansion of the Universe, as a result the halo mass growth slows down and the halo MAH can be described by a power law function ($M(z) \sim (1+z)^{\alpha}$). However, the parameters in the function depend on the power spectrum, that determines when the structures are formed. We showed that the larger the power spectrum index, the more(less) power there is at small(large) scales, and as a result low-(high-)mass halos are formed earlier(later).

Throughout the last decade, several works attempted to quantify halo MAHs using numerical simulations and analytic calculations (e.g van den Bosch 2002a; Wechsler et al. 2002; McBride et al. 2009; Fakhouri et al. 2010; Behroozi et al. 2013), but despite these efforts a clear physical explanation of the universality of the halo accretion history was still missing. In Chapter 2 we explored the origin of the 'shape' of the halo MAH and derived an analytic model that is in very good agreement with simulation-based works.

The following question we explored is what is the connection between the halo density profile, the halo accretion history and the power spectrum. In Chapter 3 we used a series of cosmological high-resolution simulations from the OWLS project to address this question. We examined the density profiles and mass histories of all resolved halos and their progenitors. We separated them into a 'relaxed' sample, and a 'complete' sample (that included both relaxed and unrelaxed halos). We calculated the mass, M_{-2}, enclosed within the NFW scale radius r_{-2} of each halo, and the redshift, z_{-2}, when the mass of the main progenitor equals M_{-2}. We confirmed the finding of Ludlow et al. (2013), that for relaxed halos the mean enclosed density within r_{-2}, $\langle\rho\rangle(< r_{-2})$, is directly proportional to the critical density of the Universe at the formation redshift, z_{-2}. Concluding that $\langle\rho\rangle(< r_{-2})$, and so a halo's concentration, depends on the evolutionary stage of the halo when it is formed. Since low-mass halos assemble earlier, when the Universe was denser, than high-mass halos, low-mass halos have higher inner densities and are then more concentrated. Using the relation $\langle\rho\rangle(< r_{-2}) = 900\rho_{\rm crit}(z_{-2})$, we derived a halo concentration-formation time relation.

We first analysed concentrations and found that, on average, halo concentrations differ by a factor of 1.16 between the relaxed and complete samples. The lower individual concentrations of unrelaxed halos (due to spurious subhalos or ongoing mergers that do not result in an accurate fit for an NFW density profile) produce incorrect enclosed halo masses and therefore lower formation times (by a factor of 1.1). However, on average, the formation time-concentration relation does not change, indicating that the halo mass history is not affected by the fact that a halo is out of equilibrium at a particular redshift. We then analysed formation times and found that z_{-2} decreases with increasing mass (at a non-linear rate), meaning that high-mass halos are still accreting mass rapidly in the present epoch, while low-mass halos accreted their mass early.

The formation time−concentration relation provides the physical link between the halo mass history and internal structure. This result led us to provide a semi-analytic model for the halo mass history, that adopts the same functional form as the analytic model from Chapter 2, but the parameters in the model depend on the halo concentration through the relation $\langle\rho\rangle(< r_{-2}) = 900\rho_{\rm crit}(z_{-2})$, that was obtained from fits to simulation results.

Finally, we compared the semi-analytic MAH model presented in Chapter 3 with the analytic MAH model from Chapter 2. We found very good agreement in the mass range $10^9 - 10^{14}{\rm M}_\odot$ between the models. However, we found that the analytic model predicts larger masses at high redshift for halos with final masses $> 10^{14}{\rm M}_\odot$, whereas the semi-analytic model overpredicts the mass history of low-mass halos (halos with final masses $< 10^9{\rm M}_\odot$). This last is expected because the semi-analytic model depends on the adopted concentration-mass relation, which deviates from the assumed power law at low masses.

By combining the analytic and semi-analytic halo MAH models we showed that the power spectrum can be directly related to the halo internal structure. Power spectrum determines the halo accretion history, and the halo MAH determines the halo mass profile through the formation time-concentration relation. We then showed that the correlation between concentration and *rms* fluctuation of the primordial density field found by previous works (e.g. Prada et al. 2012; Diemer & Kravtsov 2015) is driven by the halo accretion history.

Moving to Chapter 4, the question that motivated the study presented is: what is the physical relation between the dark matter halo concentration and the mass accretion history? This question was partially addressed in the previous chapter through the analysis of the formation time-concentration relation at $z = 0$. In Chapter 4 we extended the analysis to high redshift. We began by extending the analytic framework presented in Chapter 2, and derived a model to the describe the halo MAH at any starting redshift z_i. Next, using OWLS simulations, we analysed whether the relation $\langle\rho\rangle(< r_{-2}, z_i) = 900\rho_{\rm crit}(z_{-2}, z_i)$ changes at high-redshift. We found that the average relation is maintained through time. Then, building on the work by Ludlow et al. (2014), we derived a semi-analytic model for halo concentration as a function of halo mass and redshift. The model uses the extended analytic MAH model and the concentration-formation time relation.

The resulting $c - M$ relations were tested using N-body simulations, and compared to the most recent empirical $c - M$ relations from the literature (van den Bosch et al. 2014; Dutton & Macciò 2014; Diemer & Kravtsov 2015). The 'upturn' at high masses seen by some studies (Klypin et al. 2011; Prada et al. 2012; Dutton & Macciò 2014; Diemer & Kravtsov 2015) is not reproduced by our physically derived model which, however, only applies to relaxed halos.

We next analysed the physical relation between halo concentration and accretion history, and concluded that the halo MAH strongly impacts on halo concentration. Halos

have small or large concentrations depending on how fast or slow was their mass growth rate. At high-redshift, halos generally have low concentrations. This is because at early times halos growth rate is characterized by an exponential growth, as a result their core radius, r_{-2}, increase with the virial radius, and concentrations remain roughly constant. At low redshift the situation is different, low-mass halos have large concentrations in comparison to high-mass halos. We found that at low redshift, during the dark energy dominated epoch, there is a drop in the accretion and merger rates of small halos, and the halo mass increases due to the evolution of the reference density used in the spherical overdensity definition of the halo ($\rho_{\rm crit}(z)$ in this case). This is known as pseudo-evolution of the halo mass, that is thus driven by the halo mass definition rather than the accretion of new material. The pseudo-evolution of the halo mass gives the impression that concentrations are increasing because of contraction of the bound cores, when in fact the core radius remain constant. We then showed that when assuming r_{-2} constant in the redshift range $z = 0-1$, the increase in r_{200} due to the drop in $\rho_{\rm crit}$ gives the approximate increase in the concentration values.

Interestingly, the different growth rates of the concentrations produced by the change in the halo MAHs, creates a 'break' in the $c-M$ relation. The break is produced by the halo MAH, that goes from being dominated by a power-law (for low-mass halos, thus high concentrations) to an exponential (for high-mass halos, thus low concentrations).

The latter part of this thesis focussed on the impact of halo accretion history on galaxy evolution. Chapter 5 studied the formation of the hot hydrostatic halo, its dependence on feedback mechanisms as well as on the modes of gas accretion. The question we addressed is: what physical mechanisms drive the formation of the hot hydrostatic halo? To do so we made use of the EAGLE suite of hydrodynamical simulations as well as analytic calculations.

We analysed the probability density function (PDF) of cooling time of gas in the halo and found that when the hot halo is formed, it produces a bimodality in the PDF. The bimodal shape indicates that the hot halo reduces the cooling flows, and thus increases the hot gas mass, $M_{\rm hot}$, at large radii. By inspection of cooling time PDFs we found that the mass scale for hot halo formation is $10^{11.7}\,{\rm M}_\odot$ at $z = 0$, as originally proposed by Dekel & Birnboim (2006). However, stellar and AGN feedback modify the mass scale for hot halo formation.

In the case of stellar feedback, outflows from SN events expel gas out of the galaxy into the halo and generate recycling winds. This changes the distribution of the hot gas in the halo because the gas expelled from the galaxy produces shocks, heats the surrounding gas and increases $M_{\rm hot}$. We found that in strong stellar feedback scenarios the hot gas mass in the halo is larger than in the REF model that contains moderate stellar and AGN feedback (i.e. by a factor of 1.67 in $10^{12}\,{\rm M}_\odot$ halos, with $M_{\rm hot,REF} = 10^{10.44}\,{\rm M}_\odot$),

and as a result the hot atmosphere is potentially forming in $10^{11.45}\,\mathrm{M}_\odot$ halos. In weak stellar feedback scenarios the situation is different. The amount of hot gas decreases with respect to the REF model (i.e. by a factor of 2.29 in $10^{12}\,\mathrm{M}_\odot$ halos), and the hot atmosphere is able to form when the halo reaches a mass of $\sim 10^{12}\,\mathrm{M}_\odot$.

In the case of AGN feedback, we found that the cooling time PDF is almost unchanged between scenarios with strong AGN and no AGN feedback. However, the PDFs do change at higher halo masses ($> 10^{12}\,\mathrm{M}_\odot$). We showed that in the no AGN feedback scenario, the hot gas mass in the halo slightly increases, and the hot atmosphere is able to form in $10^{11.6}\,\mathrm{M}_\odot$ halos. On the contrary, in strong AGN activity scenarios, $M_{\rm hot}$ decreases by up to a factor of 1.5 with respect to the REF model, and the hot halo is formed in $10^{11.8}\,\mathrm{M}_\odot$ halos.

We then analysed the hot and cold mode of accretion onto halos and calculated the fraction of hot mode gas accretion, $f_{\rm hot}$. In this work we used the gas temperature and entropy, $T_{\rm post-shock}$ and $S_{\rm post-shock}$ respectively, after accretion as parameters to select shock-heated gas, rather than the commonly used maximum temperature, $T_{\rm max}$, ever reached by the gas particles. We found that $T_{\rm post-shock} + S_{\rm post-shock}$ is a better method to select hot gas accretion, because it does not include gas particles that go through a shock but immediately cool afterwards (due to in-shock cooling or heating rate smoothing, or are not even shock-heated but counted as hot accretion, as occurs when $T_{\rm max}$ is affected by stellar feedback), and therefore do not contribute to the hot halo formation process. The resulting fraction of hot accretion found increases in time at fixed halo mass.

Finally, we derived a semi-analytic model of hot halo formation that depends on hot gas mass in the halo, as well as accretion rates and the fraction of hot gas accretion. We assumed energy conservation in the presence of radiative losses and ideal gas, and found that the change in the internal energy of the gas depends on the cooling rate and the heating rate. When the external shock heating overcomes radiative cooling, the gas pressure and temperature increase, forming the hot halo.

Following the seminal work of Dekel & Birnboim (2006), we defined a critical mass, $M_{\rm crit}$, above which the halo develops a hot atmosphere because the gas has larger heating than cooling rate. We obtained $M_{\rm crit} = 10^{11.7}\,\mathrm{M}_\odot$ at $z = 0$. At higher redshift $M_{\rm crit}$ increases and reaches $10^{12.66}\,\mathrm{M}_\odot$ at $z = 8$. We compared the values of $M_{\rm crit}$ with those of Dekel & Birnboim (2006) and found very good excellent agreement in the redshift range $z = 0 - 3$. At $z = 0$ this is expected because we showed that our stability condition expression is equivalent to that of Dekel & Birnboim (2006). At $z > 0$ we have a different redshift dependence introduced through the accretion rate, fraction of hot accretion and hot gas mass. We then concluded that not only AGN and SN feedback affect the mass scale of hot halo formation, but also the accretion history and the presence of filaments. Larger accretion rates, but unchanged fraction of hot accretion, would decrease $M_{\rm crit}$

and halos would form their hot atmospheres earlier. While a larger fraction of cold gas accretion, but unchanged accretion rates, would increase $M_{\rm crit}$ and halos would form their hot atmosphere later.

The final question we addressed in this thesis is: what drives the gas accretion rate onto galaxies at the center of dark matter halos? This is a very challenging question to answer because of the complex physical mechanisms, such as gas dynamics, star formation, stellar and AGN feedback and heating from the hot halo, that govern the evolution of galaxies. However, we made an attempt to answer this question and using the EAGLE simulations we investigated the evolution of the rates of gas accretion onto the central galaxies and ISM. We found that, although the specific accretion rates onto the galaxy and ISM are roughly the same, the accretion rate onto the ISM increases with halo mass but remains constant in halos larger than $10^{12}\,{\rm M}_{\odot}$. Whereas the gas accretion rate onto galaxies increases with halo mass and only flattens in the halo mass range $10^{11.7} - 10^{12.7}\,{\rm M}_{\odot}$.

In order to better understand the dependence of the galaxy gas accretion rate with halo mass and redshift, we developed a simple semi-analytic model of galaxy gas accretion. In the model, we first assumed that two modes of gas accretion, hot and cold, add to the total gas accretion rate. We assumed that cold accretion is driven by the rate of cold accretion onto halos, whereas hot gas accretion is driven by the rate of gas cooling from the hot halo, which in the model depends on the fraction of shock-heated gas accreting onto the halo and on the cooling radius, $r_{\rm cool}$.

To calculate the cooling radius, we equaled the heating rate produced by accretion shocks with the cooling rate. However, in the calculation of the cooling rate we used a new functional form for the density profile. We analysed the gas density profile of halos in the simulations and found that high-mass halos largely deviate from the commonly assumed isothermal density profile. The logarithmic density slope changes with halo mass, it increases with halo mass and reaches a maximum in $10^{13}\,{\rm M}_{\odot}$ halos and then decreases. The change in the slope of the density profile shows how the distribution of the hot gas evolves due to continued infall, reheating and cooling. Because the logarithmic density slope changes with halo mass, when we calculated the cooling radius, we obtained that it does not decrease with increasing halo mass, instead it describes an upturn. It decreases in the halo mass range $10^{11.6} - 10^{13}\,{\rm M}_{\odot}$ and increases towards larger halos.

The evolution of the cooling radius is included in the rate of gas cooling from the hot halo and as a result, it not only predicts rates of gas accretion onto galaxies that are in excellent agreement with the simulation data, but also reveals interesting physics. When the halo develops the hot atmosphere, the infalling gas which is heated by accretion shocks remains hot and forms part of the hot halo. The gas is only able to cool after a cooling time (which is approximately 10Gyr), and as a result, the gaseous halos that developed the hot atmosphere less than 10Gyr ago do not have a continuously flow of gas

from the hot halo that is now cooling. Only larger halos ($> 10^{13}\,\mathrm{M}_{\odot}$), are able to have a large rate of hot gas cooling. For that reason, r_{cool} begins to increase in halos larger than $10^{13}\,\mathrm{M}_{\odot}$.

The formation of the hot halo not only explains the flattening in the accretion rates onto galaxies, but also the gas accretion rates onto galaxies that do not have AGN activity, due to the fact that the rate of gas cooling from the hot halo is larger in the absence of AGN activity. We compare our semi-analytic model of gas accretion with the galaxy accretion rates calculated from the simulations in various redshift ranges and found excellent agreement.

7.2 Future work

The work presented in this thesis opens new questions and motivates further improvement. In the following items we discuss practical applications of the models presented throughout the thesis, and propose further possible investigations we plan to address in the near future.

- Modelling of warm dark matter halo accretion histories. In Chapter 2 we analysed the cosmology dependence of the halo MAH using the analytic model. We varied the cosmological parameters and showed that in an Einstein-de Sitter universe the halo MAH is characterized by an exponential function at all redshifts, and in universes with larger power spectrum index, larger matter density ($\Omega_{\mathrm{m},0}$) or larger hubble parameter, halos collapse earlier and thus have different accretion histories. We further tested the cosmology dependence using cosmological simulations (Chapter 3) and concluded that the model is successful in multiple CDM cosmologies. However, the structure and accretion histories of halos in non-CDM universes is unclear. Of interest to us are the models with truncated power-spectra, such as those expected for 'warm' dark matter (WDM), due to recent claims of detection (e.g. Malyshev et al. 2014; Anderson et al. 2015) and recent observations of dark matter dominated dwarf galaxies of the Local Group (Lovell et al. 2015) for evidence of dark matter decay (Jeltema & Profumo 2015). By extending the analytic halo MAH model to include different scenarios of WDM, we will be able to provide detailed predictions of structure growth for future lensing experiments, that have the potential to strongly constrain dark matter particle phenomenology (e.g. Vegetti et al. 2012).

- Analysing the impact of environment on halo concentrations. In Chapter 3 we showed how the surrounding environment of halos regulates their accretion rates via assembly bias by using the semi-analytic model for the halo MAH. We found

that strongly clustered halos, that reside in preferentially denser environments and form earlier, have lower accretion rates at $z = 0$, than late-forming halos of the same mass. For a better connection between the halo MAH and environment we plan to derive an additional dependence of the formation time, z_{-2}, on clustering. Such dependence can be quantified in terms of the relative strength of the two-point correlation function of young and old halos (see e.g. Gao et al. 2005). By extending the semi-analytic model for the halo MAH we can recalculate halo concentrations (as done in Chapter 4) in terms of clustering, and potentially alleviate the longstanding tension between cluster concentrations derived from simulations and observational measurements (e.g. Umetsu et al. 2015). Part of this study has already been carried. In a private communication with Umetsu et al., we compared our model with their data. We assumed formation times that capture the extreme values within the scatter of the formation time-halo mass relation, changed the halo mass histories and obtained concentrations in very good agreement with Umetsu et al. (2015) best-fit relation.

- Investigating the dependence of halo accretion histories on galactic conformity. Galactic conformity refers to correlations between star formation rates of nearby galaxies. The physical origin of galactic conformity has been topic of recent debate (e.g. Hearin et al. 2015; Kauffmann 2015). It has been suggested that it can potentially be driven by the correlation of dark matter halos formation times. But it is still not clear how star formation changes between galaxies that are within halos of same mass but different formation times. To analyse the impact of halo assembly bias on galaxies we plan to apply the semi-analytic model for galaxy gas accretion. By changing the halo formation times, and so the halo accretion rates from the semi-analytic MAH model, we will predict how gas accretion onto galaxies changes due to clustering, and investigate possible scenarios of galactic conformity.

Throughout this thesis we have focussed on large-scale structures, that are mainly governed by dark matter interacting gravitationally, and moved to small-scale structures, where the inclusion of gas physics has made numerical simulations an essential tool to this research. Although our theoretical understanding of the universe is rapidly improving, both through more refined numerical simulations and observational probes, it is still lacking on many basic levels. Simulations are unable to reproduce basic observables at all redshifts, and obervational techniques are not effective enough to be able to trace the real galaxy growth over time. Improvement in these fields will provide many strict test to the theories discussed in this thesis. In the mean time, we will continue to work towards a better understanding of structure formation and galaxy evolution.

A

On the computation of halo MAH and $c - M$ relations

This appendix presents a step-by-step description on how to compute the halo mass histories following the analytic model derived in Chapter 2, the extended analytic model derived in Chapter 4 and the semi-analytic model presented in Chapter 3. It also includes a step-by-step description on how to calculate the concentration-mass relations derived in Chapter 4. In addition, this appendix provides a short guide on how to use the COncentration-Mass relation and Mass Accretion Histories (COMMAH) code. COMMAH is available online in IDL and python, and calculates the $c - M$ relations and halo MAHs following the extended analytic MAH model and the semi-analytic model for the $c - M$ relation.

A.1 Step-by-step guide to compute halo mass histories

A.1.1 Analytic MAH model

This section provides a step-by-step procedure that details how to calculate the halo mass histories using the analytic model presented in Chapter 2:

1. Calculate the linear power spectrum $P(k)$. In this work we use the approximation of Eisenstein & Hu (1998).
2. Perform the integral

$$S(R) = \frac{1}{2\pi^2}\int_0^\infty P(k)\hat{W}^2(k;R)k^2\mathrm{d}k, \tag{A.1}$$

where $\hat{W}^2(k;R)$ is the Fourier transform of a top hat window function and R defines S in a sphere of mass $M = (4\pi/3)\rho_{\mathrm{m},0}R^3$, where $\rho_{\mathrm{m},0}$ is the mean background density today.

3. Given M_0, the halo mass today, calculate the mass history by first obtaining $\tilde{z}_\mathrm{f}$

$$\tilde{z}_\mathrm{f} = -0.0064(\log_{10} M_0)^2 + 0.0237(\log_{10} M_0) + 1.8837 \quad \text{and} \quad q = 4.137\tilde{z}_\mathrm{f}^{-0.9476}. \tag{A.2}$$

4. Use the parameter q to calculate $f(M_0)$, the function that relates the power spectrum to the mass history through the mass variance S,

$$f(M_0) = 1/\sqrt{S(M_0/q) - S(M_0)}. \tag{A.3}$$

5. Finally, the mass history can be calculated as follows,

$$M(z) = M_0(1+z)^{af(M_0)}e^{-f(M_0)z}, \tag{A.4}$$

$$a = \left[1.686(2/\pi)^{1/2}\frac{\mathrm{d}D}{\mathrm{d}z}|_{z=0} + 1\right], \tag{A.5}$$

where $\mathrm{d}D/\mathrm{d}z$ is the derivative of the linear growth factor, which can be computed by performing the integral $D(z) \propto H(z)\int_z^\infty \frac{1+z'}{H(z')^3}\mathrm{d}z'$, where $D(z)$ is normalized to unity at the present.

The above model is suitable for any adopted cosmology and halo mass range.

A.1.2 Semi-analytic MAH model

This Appendix provides a step-by-step procedure that outlines how to calculate the halo mass histories using the numerical model presented in Section 4.4:

1. First assume a cosmology and choose a concentration-mass relation from the literature. For instance, the Duffy et al. (2008) relation, $c = 6.67(M_0/2\times10^{12}h^{-1}\mathrm{M}_\odot)^{-0.092}$, is suitable for the WMAP5 cosmology, whereas Neto et al. (2007) is suitable for WMAP1:
2. Calculate the formation time,

$$z_{-2} = \left(\frac{200}{A_{\rm cosmo}}\frac{c(M_0)^3Y(1)}{\Omega_{\rm m}Y(c(M_0))} - \frac{\Omega_\Lambda}{\Omega_{\rm m}}\right)^{1/3} - 1. \tag{A.6}$$

   Note that the value of $A_{\rm cosmo}$ in the above equation is cosmology dependent. $A_{\rm WMAP5} = 900$ is suitable for the WMAP5 cosmology. In this work we obtained $A_{\rm WMAP1} = 787$, $A_{\rm WMAP3} = 850$, $A_{\rm WMAP9} = 820$ and $A_{\rm Planck} = 798$.
3. Calculate the parameters α and β,

$$\alpha = [\ln(Y(1)/Y(c)) - \beta z_{-2}]/\ln(1+z_{-2}), \tag{A.7}$$
$$\beta = -3/(1+z_{-2}). \tag{A.8}$$

4. Finally, the mass history can be calculated as follows,

$$M(z) = M_0(1+z)^\alpha e^{\beta z}. \tag{A.9}$$

The above model is suitable for any cosmology (as long as the concentration-mass relation and the value of $A_{\rm cosmo}$ correspond to the desire cosmology) and is valid over the halo mass range for which the concentration-mass and the $z_{-2}-M_0$ relations, obtained from simulations, are valid (e.g. $10^{10}-10^{14}\mathrm{M}_\odot$ for Duffy et al. 2008).

A.2 Step-by-step guide to compute $c-M$ relations

A.2.1 Fitting functions for the $c-M$ relation

In this Section we provide fitting functions for the $c-M$ relation in the high-z and low-z regimes for Planck cosmology. The following expression is suitable for the low-redshift regime ($z \leq 4$) and at all halo masses,

$$\begin{aligned}
\log_{10} c &= \alpha + \beta \log_{10}(M/\,\mathrm{M}_\odot)[1+\gamma(\log_{10} M/\,\mathrm{M}_\odot)^2], \\
\alpha &= 1.7543 - 0.2766(1+z) + 0.02039(1+z)^2, \\
\beta &= 0.2753 + 0.00351(1+z) - 0.3038(1+z)^{0.0269}, \\
\gamma &= -0.01537 + 0.02102(1+z)^{-0.1475}.
\end{aligned}$$

In the high-redshift regime the $c-M$ relation can be fitted using only two parameters. The following expression is suitable for $z > 4$ and at all halo masses,

$$\begin{aligned}
\log_{10} c &= \alpha + \beta \log_{10}(M/\,\mathrm{M}_\odot), \\
\alpha &= 1.3081 - 0.1078(1+z) + 0.00398(1+z)^2, \\
\beta &= 0.0223 - 0.0944(1+z)^{-0.3907}.
\end{aligned}$$

A.3 COMMAH code

The concentration-mass relation model presented in this work, as well as the halo mass accretion history model, are included in the code named `COMMAH` for COncentration-Mass relation and Mass Accretion History, available at *https://bitbucket.org/astroduff/commah* and *http://astro.physics.unimelb.edu.au/* in Research/Public-Data-Releases/COMMAH. The code is available in both the python and IDL languages. Also, `COMMAH` is in the PyPi python package, to install it type 'pip install commah'. In this section we present a short overview of `COMMAH`.

`COMMAH` is a routine that follows the analytic model described in Section 4.2 to calculate the MAH of a halo of mass M_0 at $z = 0$ in any given redshift interval (e.g. $M(z)$ between $z = 0 - 10$). Also, `COMMAH` calculates halo concentrations following the semi-analytic model described in Section 4.3, and outputs the $c-M$ relation at any given redshift. In addition, it also computes the dark matter accretion rate, the rms of the density field, peak height, and the integral of the NFW density profile (see eq. 4.21), suitable for DM annihilation calculations. `COMMAH` calculates concentration solving eqns. (4.16) and (4.18) by performing a Levenberg-Marquardt method. As described in the previous section, commah is suitable for any cosmology.

B

Bibliography

Aalseth C. E., Barbeau P. S., Colaresi J., Collar J. I., Diaz Leon J., Fast J. E., Fields N. E., Hossbach T. W., Knecht A., Kos M. S., et al. 2013, Phys. Rev. D, 88, 012002

Agertz O., Moore B., Stadel J., Potter D., Miniati F., Read J., Mayer L., Gawryszczak A., Kravtsov A., Nordlund Å., Pearce F., Quilis V., Rudd D., Springel V., Stone J., Tasker E., Teyssier R., Wadsley J., Walder R., 2007, MNRAS, 380, 963

Anderhalden D., Diemand J., 2013, J. Cosmol. Astropart. Phys., 4, 9

Anderson M. E., Bregman J. N., 2011, ApJ, 737, 22

Anderson M. E., Churazov E., Bregman J. N., 2015, MNRAS, 452, 3905

Angloher G., Bauer M., Bavykina I., Bento A., Bucci C., Ciemniak C., Deuter G., von Feilitzsch F., Hauff D., Huff P., et al. 2012, European Physical Journal C, 72, 1971

Aprile E., et al. 2012, Physical Review Letters, 109, 181301

Aramaki T., Boggs S., Bufalino S., Dal L., von Doetinchem P., Donato F., Fornengo N., Fuke H., Grefe M., Hailey C., et al. 2015, ArXiv e-prints

Avila-Reese V., Firmani C., Hernández X., 1998, ApJ, 505, 37

Babcock H. W., 1939, Lick Observatory Bulletin, 19, 41

Bardeen J. M., Bond J. R., Kaiser N., Szalay A. S., 1986, ApJ, 304, 15

Barnes J., Hut P., 1986, *Nature*, 324, 446

Behroozi P. S., Marchesini D., Wechsler R. H., Muzzin A., Papovich C., Stefanon M., 2013, ApJL, 777, L10

Behroozi P. S., Wechsler R. H., Conroy C., 2013, ApJ, 770, 57

Bennett C. L., Hill R. S., Hinshaw G., Nolta M. R., Odegard N., Page L., Spergel D. N., Weiland J. L., Wright E. L., Halpern M., et al. 2003, ApJS, 148, 97

Benson A. J., Bower R., 2011, MNRAS, 410, 2653

Benson A. J., Kamionkowski M., Hassani S. H., 2005, MNRAS, 357, 847

Berger M. J., Colella P., 1989, Journal of Computational Physics, 82, 64

Bergstrom L., 2012, ArXiv e-prints

Bernabei R., Belli P., Cappella F., Caracciolo V., Castellano S., Cerulli R., Dai C. J., d'Angelo A., d'Angelo S., Di Marco A., et al. 2013, European Physical Journal C, 73, 2648

Bertschinger E., 1985, ApJS, 58, 39

Binney J., 1977, ApJ, 215, 483

Birnboim Y., Dekel A., 2003, MNRAS, 345, 349

Birnboim Y., Dekel A., Neistein E., 2007, MNRAS, 380, 339

Blumenthal G. R., Faber S. M., Flores R., Primack J. R., 1986, ApJ, 301, 27

Blumenthal G. R., Faber S. M., Primack J. R., Rees M. J., 1984, *Nature*, 311, 517

Bond J. R., Cole S., Efstathiou G., Kaiser N., 1991, ApJ, 379, 440

Bower R. G., 1991, MNRAS, 248, 332

Bower R. G., Benson A. J., Malbon R., Helly J. C., Frenk C. S., Baugh C. M., Cole S., Lacey C. G., 2006, MNRAS, 370, 645

Brooks A. M., Governato F., Quinn T., Brook C. B., Wadsley J., 2009, ApJ, 694, 396

Bryan G. L., Norman M. L., 1998, ApJ, 495, 80

Bryan S. E., Kay S. T., Duffy A. R., Schaye J., Dalla Vecchia C., Booth C. M., 2013, MNRAS, 429, 3316

Bullock J. S., Kolatt T. S., Sigad Y., Somerville R. S., Kravtsov A. V., Klypin A. A., Primack J. R., Dekel A., 2001, MNRAS, 321, 559

Carroll S. M., Press W. H., Turner E. L., 1992, ARA&A, 30, 499

CDMS Collaboration Agnese R., Ahmed Z., Anderson A. J., Arrenberg S., Balakishiyeva D., Basu Thakur R., Bauer D. A., Billard J., Borgland A., et al. 2013, ArXiv e-prints

Chabrier G., 2003, ApJL, 586, L133

Cirelli M., Iocco F., Panci P., 2009, J. Cosmol. Astropart. Phys., 10, 9

Cole S., Helly J., Frenk C. S., Parkinson H., 2008, MNRAS, 383, 546

Cole S., Lacey C. G., Baugh C. M., Frenk C. S., 2000, MNRAS, 319, 168

Correa C. A., Wyithe J. S. B., Schaye J., Duffy A. R., 2015a, MNRAS, 450, 1514

Correa C. A., Wyithe J. S. B., Schaye J., Duffy A. R., 2015b, MNRAS, 450, 1521

Correa C. A., Wyithe J. S. B., Schaye J., Duffy A. R., 2015c, MNRAS, 452, 1217

Couchman H. M. P., 1991, ApJL, 368, L23

Cousin M., Lagache G., Bethermin M., Guiderdoni B., 2015, A&A, 575, A33

Crain R. A., McCarthy I. G., Frenk C. S., Theuns T., Schaye J., 2010, MNRAS, 407, 1403

Crain R. A., Schaye J., Bower R. G., Furlong M., Schaller M., Theuns T., Dalla Vecchia C., Frenk C. S., et al. 2015, MNRAS, 450, 1937

Creasey P., Theuns T., Bower R. G., Lacey C. G., 2011, MNRAS, 415, 3706

Croton D. J., Springel V., White S. D. M., De Lucia G., Frenk C. S., Gao L., Jenkins A., Kauffmann G., Navarro J. F., Yoshida N., 2006, MNRAS, 365, 11

Cullen L., Dehnen W., 2010, MNRAS, 408, 669

Dalal N., Lithwick Y., Kuhlen M., 2010, ArXiv e-prints:1010.2539

Dalla Vecchia C., Schaye J., 2008, MNRAS, 387, 1431

Dalla Vecchia C., Schaye J., 2012, MNRAS, 426, 140

Davis M., Efstathiou G., Frenk C. S., White S. D. M., 1985, ApJ, 292, 371

De Young D. S., 2010, ApJ, 710, 743

Dekel A., Birnboim Y., 2006, MNRAS, 368, 2

Dekel A., Birnboim Y., Engel G., Freundlich J., Goerdt T., Mumcuoglu M., Neistein E., Pichon C., Teyssier R., Zinger E., 2009, *Nature*, 457, 451

Dekel A., Devor J., Hetzroni G., 2003, MNRAS, 341, 326

Dekel A., Krumholz M. R., 2013, MNRAS, 432, 455

Diemer B., Kravtsov A. V., 2014, ApJ, 789, 1

Diemer B., Kravtsov A. V., 2015, ApJ, 799, 108

Diemer B., More S., Kravtsov A. V., 2013, ApJ, 766, 25

Dolag K., Borgani S., Murante G., Springel V., 2009, MNRAS, 399, 497

Dolag K., Borgani S., Schindler S., Diaferio A., Bykov A. M., 2008, Space Science Reviews, 134, 229

Dubinski J., 1994, ApJ, 431, 617

Dubois Y., Devriendt J., Slyz A., Teyssier R., 2012, MNRAS, 420, 2662

Dubois Y., Pichon C., Devriendt J., Silk J., Haehnelt M., Kimm T., Slyz A., 2013, MNRAS, 428, 2885

Duffy A. R., Schaye J., Kay S. T., Dalla Vecchia C., 2008, MNRAS, 390, L64

Duffy A. R., Schaye J., Kay S. T., Dalla Vecchia C., Battye R. A., Booth C. M., 2010, MNRAS, 405, 2161

Dunkley J., Hlozek R., Sievers J., Acquaviva V., Ade P. A. R., Aguirre P., Amiri M., Appel J. W., Barrientos L. F., et al. 2011, ApJ, 739, 52

Dunkley J., Komatsu E., Nolta M. R., Spergel D. N., Larson D., Hinshaw G., Page L., Bennett C. L., Gold B., Jarosik N., et al. 2009, ApJS, 180, 306

Durier F., Dalla Vecchia C., 2012, MNRAS, 419, 465

Dutton A. A., Macciò A. V., 2014, MNRAS, 441, 3359

Efstathiou G., 2000, MNRAS, 317, 697

Einasto J., 1965, Trudy Astrofizicheskogo Instituta Alma-Ata, 5, 87

Eisenstein D. J., Hu W., 1998, ApJ, 496, 605

Eisenstein D. J., Zehavi I., Hogg D. W., Scoccimarro R., Blanton M. R., Nichol R. C., Scranton R., Seo H.-J., Tegmark M., Zheng Z., et al. 2005, ApJ, 633, 560

Eke V. R., Navarro J. F., Steinmetz M., 2001, ApJ, 554, 114

Erb D. K., Shapley A. E., Pettini M., Steidel C. C., Reddy N. A., Adelberger K. L., 2006, ApJ, 644, 813

Fabian A. C., Sanders J. S., Taylor G. B., Allen S. W., Crawford C. S., Johnstone R. M., Iwasawa K., 2006, MNRAS, 366, 417

Fakhouri O., Ma C.-P., Boylan-Kolchin M., 2010, MNRAS, 406, 2267

Fardal M. A., Katz N., Gardner J. P., Hernquist L., Weinberg D. H., Davé R., 2001, Apj, 562, 605

Faucher-Giguère C.-A., Kereš D., Ma C.-P., 2011, MNRAS, 417, 2982

Feldmann R., Mayer L., 2015, MNRAS, 446, 1939

Friedmann A., 1922, Zeitschrift fur Physik, 10, 377

Furlanetto S. R., Oh S. P., Pierpaoli E., 2006, Phys. Rev. D, 74, 103502

Furlong M., Bower R. G., Theuns T., Schaye J., Crain R. A., Schaller M., Dalla Vecchia C., Frenk C. S., et al. 2014, ArXiv e-prints:1410.3485

Gabor J. M., Bournaud F., 2014, MNRAS, 437, L56

Gabor J. M., Davé R., 2012, MNRAS, 427, 1816

Gamow G., 1970, My world line: An informal autobiography.

Gao L., Navarro J. F., Cole S., Frenk C. S., White S. D. M., Springel V., Jenkins A., Neto A. F., 2008, MNRAS, 387, 536

Gao L., Springel V., White S. D. M., 2005, MNRAS, 363, L66

Gao L., White S. D. M., 2007, MNRAS, 377, L5

Genel S., Bouché N., Naab T., Sternberg A., Genzel R., 2010, ApJ, 719, 229

Gingold R. A., Monaghan J. J., 1977, MNRAS, 181, 375

Giocoli C., Tormen G., Sheth R. K., 2012, MNRAS, 422, 185

Gunn J. E., 1977, ApJ, 218, 592

Guth A. H., Pi S.-Y., 1982, Physical Review Letters, 49, 1110

Haardt F., Madau P., 2001, in Neumann D. M., Tran J. T. V., eds, Clusters of Galaxies and the High Redshift Universe Observed in X-rays Modelling the UV/X-ray cosmic background with CUBA. p. 64

Harrison E. R., 1970, Phys. Rev. D, 1, 2726

Hayashi E., White S. D. M., 2008, MNRAS, 388, 2

Hearin A. P., Behroozi P. S., van den Bosch F. C., 2015, ArXiv e-prints

Hinshaw G., Larson D., Komatsu E., Spergel D. N., Bennett C. L., Dunkley J., Nolta M. R., Halpern M., Hill R. S., Odegard N., et al. 2013, ApJS, 208, 19

Hobson M. P., Efstathiou G. P., Lasenby A. N., 2006, General Relativity

Hockney R. W., Eastwood J. W., 1988, Computer simulation using particles

Hopkins P. F., 2013, MNRAS, 428, 2840

Hopkins P. F., Bundy K., Hernquist L., Ellis R. S., 2007, ApJ, 659, 976

Hu C.-Y., Naab T., Walch S., Moster B. P., Oser L., 2014, MNRAS, 443, 1173

Hubble E., 1929, Proceedings of the National Academy of Science, 15, 168

Hubble E., Humason M. L., 1931, ApJ, 74, 43

Huss A., Jain B., Steinmetz M., 1999, ApJ, 517, 64

Hutchings R. M., Thomas P. A., 2000, MNRAS, 319, 721

Ishiyama T., 2014, ApJ, 788, 27

Jeltema T. E., Profumo S., 2015, ArXiv e-prints

Jenkins A., Frenk C. S., White S. D. M., Colberg J. M., Cole S., Evrard A. E., Couchman H. M. P., Yoshida N., 2001, MNRAS, 321, 372

Johansson P. H., 2013, in Thomas D., Pasquali A., Ferreras I., eds, IAU Symposium Vol. 295 of IAU Symposium, Assembly Histories and Observational Properties of Simulated Early-type Galaxies. pp 354–357

Kant I., 1755, Allgemeine Naturgeschichte und Theorie des Himmels

Katz N., Keres D., Dave R., Weinberg D. H., 2003, in Rosenberg J. L., Putman M. E., eds, The IGM/Galaxy Connection. The Distribution of Baryons at z=0 Vol. 281 of Astrophysics and Space Science Library, How Do Galaxies Get Their Gas?. p. 185

Kauffmann G., 2015, MNRAS, 454, 1840

Kauffmann G., Haehnelt M., 2000, MNRAS, 311, 576

Kay S. T., Pearce F. R., Jenkins A., Frenk C. S., White S. D. M., Thomas P. A., Couchman H. M. P., 2000, MNRAS, 316, 374

Keisler R., Reichardt C. L., Aird K. A., Benson B. A., Bleem L. E., Carlstrom J. E., Chang C. L., Cho H. M., Crawford T. M., et al. 2011, ApJ, 743, 28

Kereš D., Katz N., Fardal M., Davé R., Weinberg D. H., 2009, MNRAS, 395, 160

Kereš D., Katz N., Weinberg D. H., Davé R., 2005, MNRAS, 363, 2

Klypin A., Yepes G., Gottlober S., Prada F., Hess S., 2014, ArXiv e-prints:1411.4001

Klypin A. A., Trujillo-Gomez S., Primack J., 2011, ApJ, 740, 102

Komatsu E., Dunkley J., Nolta M. R., Bennett C. L., Gold B., Hinshaw G., Jarosik N., Larson D., Limon M., Page L., et al. 2009, ApJS, 180, 330

Komatsu E., Smith K. M., Dunkley J., Bennett C. L., Gold B., Hinshaw G., Jarosik N., et al. 2011, ApJS, 192, 18

Komatsu E., Smith K. M., Dunkley J., Bennett C. L., Gold B., Hinshaw G., Jarosik N., Larson D., Nolta M. R., Page L., et al. 2011, ApJS, 192, 18

Kowalski M., et al. 2008, ApJ, 686, 749

Kuhlen M., Strigari L. E., Zentner A. R., Bullock J. S., Primack J. R., 2005, MNRAS, 357, 387

Lacerna I., Padilla N., 2011, MNRAS, 412, 1283

Lacerna I., Padilla N., 2012, MNRAS, 426, L26

Lacey C., Cole S., 1993, MNRAS, 262, 627

Larson D., Dunkley J., Hinshaw G., Komatsu E., Nolta M. R., Bennett C. L., Gold B., Halpern M., Hill R. S., et al. 2011, ApJS, 192, 16

Lavalle J., Salati P., 2012, Comptes Rendus Physique, 13, 740

Lavalle J., Yuan Q., Maurin D., Bi X.-J., 2008, A&A, 479, 427

Li L.-X., 2008, MNRAS, 388, 1487

Li Y., Mo H. J., Gao L., 2008, MNRAS, 389, 1419

Li Y., Mo H. J., van den Bosch F. C., Lin W. P., 2007, MNRAS, 379, 689

Lin Y.-T., Mohr J. J., Stanford S. A., 2003, ApJ, 591, 749

Lovell M. R., Bertone G., Boyarsky A., Jenkins A., Ruchayskiy O., 2015, MNRAS, 451, 1573

Lu Y., Mo H. J., Katz N., Weinberg M. D., 2006, MNRAS, 368, 1931

Lu Y., Mo H. J., Wechsler R. H., 2015, MNRAS, 446, 1907

Lucy L. B., 1977, AJ, 82, 1013

Ludlow A. D., Navarro J. F., Angulo R. E., Boylan-Kolchin M., Springel V., Frenk C., White S. D. M., 2014, MNRAS, 441, 378

Ludlow A. D., Navarro J. F., Boylan-Kolchin M., Bett P. E., Angulo R. E., Li M., White S. D. M., Frenk C., Springel V., 2013, MNRAS, 432, 1103

Ludlow A. D., Navarro J. F., Li M., Angulo R. E., Boylan-Kolchin M., Bett P. E., 2012, MNRAS, 427, 1322

Ludlow A. D., Navarro J. F., Springel V., Vogelsberger M., Wang J., White S. D. M., Jenkins A., Frenk C. S., 2010, MNRAS, 406, 137

Lynden-Bell D., 1967, MNRAS, 136, 101

Ma X., Hopkins P. F., Faucher-Giguere C.-A., Zolman N., Muratov A. L., Keres D., Quataert E., 2015, ArXiv e-prints

Macciò A. V., Dutton A. A., van den Bosch F. C., 2008, MNRAS, 391, 1940

Macciò A. V., Dutton A. A., van den Bosch F. C., Moore B., Potter D., Stadel J., 2007, MNRAS, 378, 55

Mack K. J., 2014, MNRAS, 439, 2728

Malyshev D., Neronov A., Eckert D., 2014, Phys. Rev. D, 90, 103506

Mangano G., Miele G., Pastor S., Peloso M., 2002, Physics Letters B, 534, 8

Mannucci F., Cresci G., Maiolino R., Marconi A., Pastorini G., Pozzetti L., Gnerucci A., Risaliti G., Schneider R., Lehnert M., Salvati M., 2009, MNRAS, 398, 1915

Manrique A., Raig A., Salvador-Solé E., Sanchis T., Solanes J. M., 2003, ApJ, 593, 26

Martizzi D., Teyssier R., Moore B., 2012, MNRAS, 420, 2859

McBride J., Fakhouri O., Ma C.-P., 2009, MNRAS, 398, 1858

McKee C. F., Ostriker E. C., 2007, ARA&A, 45, 565

Mo H. J., Mao S., White S. D. M., 1998, MNRAS, 295, 319

Monaghan J. J., 1992, ARA&A, 30, 543

Muñoz-Cuartas J. C., Macciò A. V., Gottlöber S., Dutton A. A., 2011, MNRAS, 411, 584

Murray N., Quataert E., Thompson T. A., 2005, ApJ, 618, 569

Navarro J. F., Frenk C. S., White S. D. M., 1996, ApJ, 462, 563

Navarro J. F., Frenk C. S., White S. D. M., 1997, ApJ, 490, 493

Navarro J. F., Hayashi E., Power C., Jenkins A. R., Frenk C. S., White S. D. M., Springel V., Stadel J., Quinn T. R., 2004, MNRAS, 349, 1039

Navarro J. F., Ludlow A., Springel V., Wang J., Vogelsberger M., White S. D. M., Jenkins A., Frenk C. S., Helmi A., 2010, MNRAS, 402, 21

Neistein E., Dekel A., 2008, MNRAS, 388, 1792

Neistein E., van den Bosch F. C., Dekel A., 2006, MNRAS, 372, 933

Nelson D., Genel S., Pillepich A., Vogelsberger M., Springel V., Hernquist L., 2015, ArXiv e-prints

Nelson D., Genel S., Vogelsberger M., Springel V., Sijacki D., Torrey P., Hernquist L., 2015, MNRAS, 448, 59

Nelson D., Vogelsberger M., Genel S., Sijacki D., Kereš D., Springel V., Hernquist L., 2013, MNRAS, 429, 3353

Neto A. F., Gao L., Bett P., Cole S., Navarro J. F., Frenk C. S., White S. D. M., Springel V., Jenkins A., 2007, MNRAS, 381, 1450

Ng K. C. Y., Laha R., Campbell S., Horiuchi S., Dasgupta B., Murase K., Beacom J. F., 2014, Phys. Rev. D, 89, 083001

Nusser A., Sheth R. K., 1999, MNRAS, 303, 685

Ocvirk P., Pichon C., Teyssier R., 2008, MNRAS, 390, 1326

Oppenheimer B. D., Davé R., Kereš D., Fardal M., Katz N., Kollmeier J. A., Weinberg D. H., 2010, MNRAS, 406, 2325

Penzias A. A., Wilson R. W., 1965, ApJ, 142, 419

Percival W. J., Baugh C. M., Bland-Hawthorn J., Bridges T., Cannon R., Cole S., Colless M., Collins C., Couch W., Dalton G., et al. 2001, MNRAS, 327, 1297

Percival W. J., Reid B. A., Eisenstein D. J., Bahcall N. A., Budavari T., Frieman J. A., Fukugita M., Gunn J. E., Ivezić Ž., Knapp G. R., et al. 2010, MNRAS, 401, 2148

Pieri L., Bertone G., Branchini E., 2008, MNRAS, 384, 1627

Pinzke A., Pfrommer C., Bergström L., 2011, Phys. Rev. D, 84, 123509

Planck Collaboration 2015, ArXiv e-prints

Planck Collaboration Ade P. A. R., Aghanim N., Armitage-Caplan C., Arnaud M., Ashdown M., Atrio-Barandela F., Aumont J., Baccigalupi C., Banday A. J., et al. 2014, A&A, 571, A16

Power C., Navarro J. F., Jenkins A., Frenk C. S., White S. D. M., Springel V., Stadel J., Quinn T., 2003, MNRAS, 338, 14

Prada F., Klypin A. A., Cuesta A. J., Betancort-Rijo J. E., Primack J., 2012, MNRAS, 423, 3018

Press W. H., Schechter P., 1974, ApJ, 187, 425

Price D. J., 2008, Journal of Computational Physics, 227, 10040

Price D. J., 2012, Journal of Computational Physics, 231, 759

Pritchard J. R., Loeb A., 2012, Reports on Progress in Physics, 75, 086901

Reed D. S., Bower R., Frenk C. S., Jenkins A., Theuns T., 2007, MNRAS, 374, 2

Rees M. J., Ostriker J. P., 1977, MNRAS, 179, 541

Riess A. G., Filippenko A. V., Challis P., Clocchiatti A., Diercks A., Garnavich P. M., Gilliland R. L., Hogan C. J., Jha S., et al. 1998, AJ, 116, 1009

Rogstad D. H., Shostak G. S., 1972, ApJ, 176, 315

Rosas-Guevara Y. M., Bower R. G., Schaye J., Furlong M., Frenk C. S., Booth C. M., Crain R., Dalla Vecchia C., et al. 2013, ArXiv e-prints

Rubin V. C., Ford W. K. J., . Thonnard N., 1980, ApJ, 238, 471

Rubin V. C., Thonnard N., Ford Jr. W. K., 1978, ApJL, 225, L107

Saab T., 2013, in Schmaltz M., Pierpaoli E., eds, World Scientific Publishing Co. . pp 711–738

Salvador-Solé E., Viñas J., Manrique A., Serra S., 2012, MNRAS, 423, 2190

Sánchez Almeida J., Elmegreen B. G., Muñoz-Tuñón C., Elmegreen D. M., 2014, A&A Rev., 22, 71

Sánchez-Conde M. A., Prada F., 2014, MNRAS, 442, 2271

Sanders R. L., Shapley A. E., Kriek M., Reddy N. A., Freeman W. R., Coil A. L., Siana B., Mobasher B., Shivaei I., Price S. H., de Groot L., 2015, ApJ, 799, 138

Schaller M., Frenk C. S., Bower R. G., Theuns T., Jenkins A., Schaye J., Crain R. A., Furlong M., Dalla Vecchia C., McCarthy I. G., 2015, MNRAS, 451, 1247

Schaye J., 2004, ApJ, 609, 667

Schaye J., Crain R. A., Bower R. G., Furlong M., Schaller M., Theuns T., Dalla Vecchia C., Frenk C. S., et al. 2015, MNRAS, 446, 521

Schaye J., Dalla Vecchia C., 2008, MNRAS, 383, 1210

Schaye J., Dalla Vecchia C., Booth C. M., Wiersma R. P. C., Theuns T., Haas M. R., Bertone S., Duffy A. R., McCarthy I. G., van de Voort F., 2010, MNRAS, 402, 1536

Schutz B., 2009, A First Course in General Relativity

Shaw L. D., Weller J., Ostriker J. P., Bode P., 2006, ApJ, 646, 815

Shen J., Abel T., Mo H. J., Sheth R. K., 2006, ApJ, 645, 783

Sheth R. K., Lemson G., 1999, MNRAS, 305, 946

Sheth R. K., Tormen G., 2004, MNRAS, 349, 1464

Sievers J. L., Hlozek R. A., Nolta M. R., Acquaviva V., Addison G. E., Ade P. A. R., Aguirre P., Amiri M., Appel J. W., Barrientos L. F., et al. 2013, J. Cosmol. Astropart. Phys., 10, 60

Sijacki D., Springel V., Di Matteo T., Hernquist L., 2007, MNRAS, 380, 877

Silk J., Rees M. J., 1998, Aap, 331, L1

Smoot G. F., Bennett C. L., Kogut A., Wright E. L., Aymon J., Boggess N. W., Cheng E. S., de Amici G., Gulkis S., Hauser M. G., et al. 1992, ApJL, 396, L1

Sofue Y., Rubin V., 2001, ARA&A, 39, 137

Somerville R. S., Kolatt T. S., 1999, MNRAS, 305, 1

Spergel D. N., Bean R., Doré O., Nolta M. R., Bennett C. L., Dunkley J., Hinshaw G., Jarosik N., Komatsu E., 2007, AjPS, 170, 377

Spergel D. N., Verde L., Peiris H. V., Komatsu E., Nolta M. R., Bennett C. L., Halpern M., Hinshaw G., Jarosik N., Kogut A., et al. 2003, ApJS, 148, 175

Springel V., 2005, MNRAS, 364, 1105

Springel V., 2010, MNRAS, 401, 791

Springel V., Di Matteo T., Hernquist L., 2005, MNRAS, 361, 776

Springel V., White M., Hernquist L., 2001, ApJ, 549, 681

Steidel C. C., Rudie G. C., Strom A. L., Pettini M., Reddy N. A., Shapley A. E., Trainor R. F., Erb D. K., Turner M. L., Konidaris N. P., Kulas K. R., Mace G., Matthews K., McLean I. S., 2014, ApJ, 795, 165

Stone J. M., Norman M. L., 1992, ApJS, 80, 753

Suresh J., Bird S., Vogelsberger M., Genel S., Torrey P., Sijacki D., Springel V., Hernquist L., 2015, MNRAS, 448, 895

Syer D., White S. D. M., 1996, ArXiv Astrophysics e-prints

Tasitsiomi A., Kravtsov A. V., Gottlöber S., Klypin A. A., 2004, ApJ, 607, 125

Tegmark M., Eisenstein D. J., Strauss M. A., Weinberg D. H., Blanton M. R., Frieman J. A., Fukugita M., Gunn J. E., Hamilton A. J. S., Knapp G. R., et al. 2006, Phys. Rev. D, 74, 123507

Thacker R. J., Tittley E. R., Pearce F. R., Couchman H. M. P., Thomas P. A., 2000, MNRAS, 319, 619

Tozzi P., Norman C., 2001, ApJ, 546, 63

Tremonti C. A., Heckman T. M., Kauffmann G., Brinchmann J., Charlot S., White S. D. M., Seibert M., Peng E. W., Schlegel D. J., Uomoto A., Fukugita M., Brinkmann J., 2004, ApJ, 613, 898

Übler H., Naab T., Oser L., Aumer M., Sales L. V., White S. D. M., 2014, MNRAS, 443, 2092

Umetsu K., Zitrin A., Gruen D., Merten J., Donahue M., Postman M., 2015, ArXiv e-prints

van de Voort F., Schaye J., 2012, MNRAS, 423, 2991

van de Voort F., Schaye J., Booth C. M., Haas M. R., Dalla Vecchia C., 2011, MNRAS, 414, 2458

van den Bosch F. C., 2002a, MNRAS, 331, 98

van den Bosch F. C., 2002b, MNRAS, 331, 98

van den Bosch F. C., Jiang F., Hearin A., Campbell D., Watson D., Padmanabhan N., 2014, MNRAS, 445, 1713

van Dokkum P. G., Leja J., Nelson E. J., Patel S., Skelton R. E., Momcheva I., Brammer G., Whitaker K. E., Lundgren B., Fumagalli M., et al. 2013, ApJL, 771, L35

Vegetti S., Lagattuta D. J., McKean J. P., Auger M. W., Fassnacht C. D., Koopmans L. V. E., 2012, *Nature*, 481, 341

Vogelsberger M., Sijacki D., Kereš D., Springel V., Hernquist L., 2012, MNRAS, 425, 3024

Voit G. M., Donahue M., 2005, ApJ, 634, 955

Wang H., Mo H. J., Jing Y. P., 2009, MNRAS, 396, 2249

Wang P., Abel T., 2007, ArXiv Astrophysics e-prints

Wechsler R. H., Bullock J. S., Primack J. R., Kravtsov A. V., Dekel A., 2002, ApJ, 568, 52

Wechsler R. H., Zentner A. R., Bullock J. S., Kravtsov A. V., Allgood B., 2006, ApJ, 652, 71

Weinberg S., 1972, Gravitation and Cosmology: Principles and Applications of the General Theory of Relativity

Weinmann S. M., van den Bosch F. C., Yang X., Mo H. J., 2006, MNRAS, 366, 2

Wendland H., 1995, Advances Comput. Math., 4, 389

Wetzel A. R., Nagai D., 2015, ApJ, 808, 40

White S. D. M., 1996, in Schaeffer R., Silk J., Spiro M., Zinn-Justin J., eds, Cosmology and Large Scale Structure Formation and Evolution of Galaxies. p. 349

White S. D. M., Frenk C. S., 1991, ApJ, 379, 52

White S. D. M., Rees M. J., 1978, MNRAS, 183, 341

Wiersma R. P. C., Schaye J., Smith B. D., 2009, MNRAS, 393, 99

Wiersma R. P. C., Schaye J., Theuns T., Dalla Vecchia C., Tornatore L., 2009, MNRAS, 399, 574

Williams L. L. R., Babul A., Dalcanton J. J., 2004, ApJ, 604, 18

Wong A. W. C., Taylor J. E., 2012, ApJ, 757, 102

Woods R. M., Wadsley J., Couchman H. M. P., Stinson G., Shen S., 2014, MNRAS, 442, 732

Wright T., 1750, An original theory or new hypothesis of the universe : founded upon general phaenomena of the visible creation; and particularly the Via the laws of nature, and solving by mathematical principles : the Lactea ...compris'd in nine familiar letters from the author to his friendand : illustrated with upward of thirty graven and mezzotinto plates ...

Wu H.-Y., Hahn O., Wechsler R. H., Mao Y.-Y., Behroozi P. S., 2013, ApJ, 763, 70

Wu H.-Y., Rozo E., Wechsler R. H., 2008, ApJ, 688, 729

Zahid H. J., Kewley L. J., Bresolin F., 2011, ApJ, 730, 137

Zeldovich Y. B., 1972, MNRAS, 160, 1P

Zentner A. R., Hearin A. P., van den Bosch F. C., 2014, MNRAS, 443, 3044

Zhang J., Fakhouri O., Ma C.-P., 2008, MNRAS, 389, 1521

Zhao D. H., Jing Y. P., Mo H. J., Börner G., 2009, ApJ, 707, 354

Zhao D. H., Mo H. J., Jing Y. P., Börner G., 2003, MNRAS, 339, 12

Zwicky F., 1937, ApJ, 86, 217